

REDUCED-ORDER MODELING AND PARAMETERIZED OPTIMIZATION OF
BIO-INSPIRED ADAPTIVE STRUCTURES

A Dissertation

by

PEDRO BATISTA CAMARA LEAL

Submitted to the Graduate and Professional School of
Texas A&M University
in partial fulfillment of the requirements for the degree of
DOCTOR OF PHILOSOPHY

Chair of Committee,	Darren J. Hartl
Committee Members,	Junuthula N. Reddy
	Richard J. Malak Jr.
	Ergun Akleman
Head of Department,	Srinivas Rao Vadali

August 2021

Major Subject: Aerospace Engineering

Copyright 2021 Pedro Batista Camara Leal

ABSTRACT

Any aircraft wing design configuration is primarily intended to maximize performance during the predominant flight condition (e.g., cruise in transport aircraft) while control surfaces (e.g., flap and slats) permit necessary wing reconfigurations to transition between phases of flight. Control surfaces lead to higher performance during required maneuvers but are not without drawbacks. Due to their structural and mechanical complexity, they occupy volume inside the wing, which might displace valuable fuel storage and add weight. Due to the use of discontinuous surfaces, extra drag and acoustic noise are also generated for all flight conditions. These disadvantages motivate using alternative adaptive technologies, such as conformal wing morphing, that do not introduce discontinuities to the flow. Adaptive components (e.g., shape memory alloy and piezoelectric actuators) are a key to bioinspired locomotion, but there are unknowns regarding engineering and operational aspects (e.g., how to utilize, control, and design). The operation of a shape memory alloy (SMA) component is first explored for bi-pedal locomotion to demonstrate it operates as an *artificial muscle*, functioning as an actuator, a brake, or a spring. The following study shows the controllability, robustness, and scalability of an SMA-based *morphing wing*. Further considerations in how to design involve how to represent the morphed geometry, and new *parameterization methods* are developed to represent the aircraft topology. Current state-of-the-art methods in this field generally consider only one adaptive technology or do not consider structural restrictions (e.g., the necessary rigid spars and ribs) during the design process. It is proposed herein that a universal tool based on kinematic equations can be used to model morphing structures independent of the actuator technology used. An intuitive parameterization method is proposed that considers kinematic constraints to efficiently generate *structurally consistent* (i.e., all internal structural constraints are satisfied) morphed configurations with a limited number of design variables. The structurally consistent parameterization method is further implemented to *optimize* subsonic morphing wings using low-fidelity fluid solvers. Small changes to the wing outer mold line can result in significant noise reduction and drag loss; thus, a method to *accurately* and *efficiently* describe the deformed aircraft

geometry is developed that allows universal parameterization, including topological representations developed in this work.

DEDICATION

Para o meu tio Delsinho.

CONTRIBUTORS AND FUNDING SOURCES

Contributors

This work was supported by a dissertation committee consisting of Professor Darren Hartl and Professors Junuthula Reddy and Richard Malak of the Department of Mechanical Engineering and Professor Ergun Akleman of the Department of Visualization.

The prototypes and tests from chapters 2 and 3 were performed with the help of Hannah Stroud, Trent White, Emery Sheahan, Marcela Cabral, Hannah Jerdon, Sam Murley, and Mitchell Mu. The algorithms development in chapter 4 were aided by Ted Giblette, Antoine Baldo, and Timothee Coudour. Finally, the work in chapter 7 was done in collaboration with Dr. Jonathan Weaver-Rosen.

Funding Sources

Graduate study was supported by the US Air Force Office of Scientific Research under a grant number FA9550-16-1-0087, titled *Avian-Inspired Multifunctional Morphing Vehicles* monitored by Dr. BL Lee. The later work was also supported by the NASA *University Leadership Initiative* (ULI) program under federal award number NNX17AJ96A, titled *Adaptive Aerostructures for Revolutionary Civil Supersonic Transportation*.

NOMENCLATURE

a	A gain scheduling coefficient	—
\mathbf{a}^c	Independent child shape function coefficients	—
\mathbf{a}^p	Independent parent shape function coefficients	—
A	Active shape function coefficient	—
\mathbb{A}	Domain of feasible active shape coefficients	—
A^c	Child active shape function coefficient	—
A_f	Austenite final transformation temperature	C
A^p	Parent active shape function coefficient	—
A_s	Austenite start transformation temperature	C
α	Angle of attack	—
α_l	Left leg pitch angle	—
α_r	Right leg pitch angle	—
b	A gain scheduling coefficient	—
\mathbf{b}	Backwards restriction vector	—
\mathbf{B}	Backwards function matrix	—
β_1	Curvilinear coordinate tangent to OML	m
β_2	Curvilinear coordinate normal to OML	m
c	Voltage input defined by the controller	V
C	Class function	—
CST	Class/Shape Transformation	
D	Drag	N
ΔT	Temperature amplitude	C

e	Spring stiffness	N/m
E	Young modulus	N/m ²
ϵ	Strain	—
ϵ_b	Difference between a reference and process values	m
η	Non-dimensional coordinate in the parameterized domain	—
EBM	Energy-Based Model	
η_m	Master η -coordinate in the parameterized domain	—
η_o	η -reference coordinate in the parameterized domain	—
η_s	Slave η -coordinate in the parameterized domain	—
f	Forwards restriction vector	—
F	Forwards function matrix	—
f_r	Reference value factor for PID	—
F_x	x -component of the reaction force imposed on the leg	—
F_y	y -component of the reaction force imposed on the leg	—
g	Gravity	m s ²
g	Curvilinear coordinate system	—
G	Shear modulus	N m
G_A	Austenite shear modulus	N m
$\bar{\gamma}$	Effective shear strain	—
$\bar{\gamma}^t$	Effective transformation shear strain	—
G_M	Martensite shear modulus	N/m ²
h	Length of rigid spar	m
H	Shape function coefficient	—
H^{cur}	Current effective transformation strain	—
H^{min}	Minimum effective transformation strain	—

H^{\max}	Maximum effective transformation strain	—
\mathbf{i}	Global/assembly coordinate basis vectors	—
I	Global/assembly coordinate system	—
J	Cost function	—
J^*	Non-dominated cost function	—
\tilde{J}	Expected value	—
\bar{k}	Correction factor	—
K_c	Controller gain for PID	—
$k_{\text{leg},l}$	Left leg stiffness	—
$k_{\text{leg},r}$	Right leg stiffness	—
k_{swing}	Elastic torsional spring stiffness	—
κ	Position components in assembly coordinate system	m
\mathbf{l}	Local/part coordinate basis vectors	—
l_l	Deformed length of left compression spring	—
l_o	Undeformed length of compression spring	—
l_r	Deformed length of right compression spring	—
l_x	x -component of the spring length	—
L	Lift	N
L^*/D	Optimum lift-to-drag ratio	—
Λ	Local/part coordinate system	—
m	number of piecewise CST equations	—
\mathbf{M}	Moment vector	N m
M_b	Main body mass of the robot	kg
M_E	Moment distribution from external sources	N m
M^e	Moment distribution vector from spring interactions	N m

M_f	Martensite final transformation temperature	C
M_I	Moment distribution from internal sources	N m
M_l	Leg mass of the robot	kg
M^q	Moment distribution from concentrated forces Q	N m
M^r	Moment distribution from reaction forces R	N m
M_s	Martensite start transformation temperature	C
M^t	Moment distribution from applied torques T	N m
M^w	Moment distribution from pressure distribution w	N m
n	Order of Bernstein polynomial	—
\mathbf{n}	Normal vector to OML in physical domain	—
N	Total number of integration points	—
N_c	Number of coils	—
n^e	Number of spring forces	—
N_i	Class functions coefficient	—
n_i	i -th hardening parameter	—
n^q	Number of concentrated forces	—
NURBS	Non-Uniform Rational B-Splines	
n^r	Number of reaction forces	—
ω	Equality constraint	—
ω_{swing}	Angular frequency of the leg motion	m
OML	Outer mold line	
p	Probability density function	—
P	Passive shape function coefficient	—
P^p	Parent passive shape function coefficient	—
P^c	Child passive shape function coefficient	—

\mathbb{P}^c	Domain of child passive shape coefficients	—
ϕ	Rotation angle of curvilinear basis relate to cartesian	—
Φ_{fwd}	Forwards transformation function	—
Φ_{rev}	Reverse transformation function	—
ψ	Non-dimensional coordinate in the parameterized domain	—
ψ_A^c	Child ψ -coordinate	—
ψ_m	Master ψ -coordinate in the parameterized domain	—
ψ_o	ψ -reference coordinate in the parameterized domain	—
ψ_s	Slave ψ -coordinate in the parameterized domain	—
\mathbf{Q}	Force vector	N
R	Spring radius	m
r	Wire radius	m
\mathbf{r}	Position vector in the assembly domain	m
\mathbf{r}_m	Master position vector in the assembly domain	m
\mathbf{r}_n^p	Parent position along neutral line	m
\mathbf{r}_n^c	Child position along neutral line	m
\mathbf{r}_o	Rigid body translation tensor	m
r_s	Spearman correlation factor	—
\mathbf{r}_s	Slave position vector in the assembly domain	m
\mathbb{R}	Total beam residual	m
\mathbb{R}_l	Total beam residual for lower beam	m
\mathbb{R}_u	Total beam residual for upper beam	m
\mathbb{R}^*	Minimum total beam residual	m
\mathbf{R}_{l-i}	Rigid body rotation tensor from physical to assembly	—
s	Curvilinear coordinate tangent to OML	m

S	Shape function	—
SST	Supersonic transport	
\mathbf{t}	Tangent vector to OML in physical domain	—
T	Temperature	C
\mathbf{T}	Twist tensor	—
$\bar{\tau}$	Effective shear stress	N/m ²
τ_{crit}	Shear stress that transformation strain starts in Martensite	N/m ²
T_i	Integral time for PID	—
T_d	Derivative time for PID	—
$\boldsymbol{\theta}$	Parameters	—
θ_r	Phase offset	—
\mathbf{u}	Displacement vector	m
V	Velocity	m/s
V_p	Process value	m
V_r	Reference value	m
V_{range}	Reference value range	m
w	Displacement components in global coordinate system	m
W	pressure distribution	m
x	Coordinate in the physical domain	m
X	ψ -scaling factor from parameterized to intermediate domain	m
\bar{x}	x -component of the position on the neutral line	m
\hat{x}	Coordinate in the intermediate domain	m
ξ	Martensitic volume fraction	—
Ξ	Knot	—
ξ^r	Martensitic volume fraction at transformation reversal	—

x_{shear}	x -component of shear vector	m
y	Coordinate in the physical domain	m
Y	η -scaling factor from parameterized to intermediate domain	m
\hat{y}	Coordinate in the intermediate domain	m
y_{shear}	y -component of shear vector	m
z	Coordinate in the physical domain	m
Z	ζ -scaling factor from parameterized to intermediate domain	m
\bar{z}	z -component of the position on the neutral line	m
\hat{z}	Coordinate in the intermediate domain	m
ζ	Non-dimensional coordinate in the parameterized domain	—
ζ_A^c	Child ζ -coordinate	—
ζ_T^c	Non-dimensional child trailing edge thickness	—
ζ_o	ζ -reference coordinate in the parameterized domain	—
ζ_T	Non-dimensional trailing edge thickness	—

TABLE OF CONTENTS

	Page
ABSTRACT	ii
DEDICATION	iv
CONTRIBUTORS AND FUNDING SOURCES	v
NOMENCLATURE	vi
TABLE OF CONTENTS	xiii
LIST OF FIGURES	xvii
LIST OF TABLES	xxvi
1. INTRODUCTION AND LITERATURE REVIEW	1
1.1 Background	1
1.2 Artificial muscle	2
1.3 Morphing	4
1.4 Parameterized representation	5
1.5 Structural analysis	6
1.6 Design of morphing structures	8
1.7 This study	10
2. EXPERIMENTS WITH BIRD AND ARTIFICIAL MUSCLES	13
2.1 Background	13
2.2 Methods	14
2.2.1 SMA artificial muscle setup	14
2.2.2 Bipedal compass model	15
2.2.3 Spring model	17
2.2.4 SMA model	18
2.3 Results	21
2.3.1 Artificial vs. natural muscles	21
2.3.2 Robotics application to multifunctional SMA components	25
2.4 Remarks	30
3. EXPERIMENTAL STUDY OF MORPHING WINGS	33
3.1 Background	33

3.2	SMA composite actuator.....	35
3.2.1	Design and fabrication	37
3.2.2	Actuator characterization	38
3.3	Single-actuator platform	40
3.3.1	Fabrication of avian-inspired prototype	41
3.3.2	Controls	42
3.3.2.1	PID	43
3.3.2.2	Reinforcement learning	44
3.3.3	Setup and instrumentation	46
3.3.4	Results	47
3.3.4.1	Open-loop.....	47
3.3.4.2	Closed-loop: PID.....	49
3.3.4.2.1	Disturbance Response	49
3.3.4.2.2	Reference Value Response	50
3.3.4.3	Closed-loop: reinforcement learning.....	52
3.4	Multi-actuator platform	54
3.4.1	Material characterization	56
3.4.2	Design and fabrication	56
3.4.3	Setup and instrumentation	60
3.4.4	Results	62
3.4.4.1	Aerodynamics: non-morphing.....	62
3.4.4.2	Aerodynamics: single actuation cycle.....	64
3.4.4.3	Aerodynamics: multiple actuation cycles	66
3.4.4.4	Thermomechanical Results	67
3.5	Remarks	71
4.	PARAMETERIZATION OF MULTI-COMPONENT AIRCRAFT ASSEMBLY*	72
4.1	Modified Class/Shape Transformation	72
4.1.1	Parameterized domain	73
4.1.2	Physical and intermediate domain	76
4.1.3	Assembly domain	77
4.2	Geometric representation capability.....	79
4.2.1	Two-dimensional CST	79
4.2.2	Three-dimensional CST.....	80
4.2.3	Fuselage.....	82
4.2.4	Wing	83
4.3	Spline CST	86
5.	PARAMETERIZATION OF MORPHING STRUCTURES*	92
5.1	Two-dimensional camber morphing.....	92
5.2	Nomenclature for skin-based camber morphing.....	93
5.3	Assumptions for structurally consistent skin-based camber morphing	94
5.4	Forwards calculation	97
5.4.1	Constant length for forwards calculation.....	100

5.4.2	Constant angles assumptions for forwards calculation	101
5.4.3	Discussion and summary for forwards calculation	102
5.4.4	Finite Element Analysis validation of forwards calculation	103
5.5	Backwards calculation	108
5.5.1	Constant length and angles assumptions for backwards calculation	110
5.5.2	Discussion and summary for backwards calculation	112
5.6	Conclusions.....	116
6.	DESIGN AND OPTIMIZATION OF MORPHING STRUCTURES*	117
6.1	Methodology	117
6.1.1	Parametric optimization	118
6.1.2	Non-linear constraint	120
6.1.3	Expected value.....	120
6.1.4	Concept selection.....	122
6.2	Results	124
6.2.1	Parametric optimization of NACA 4415	124
6.2.2	Concept selection for four parent airfoils	126
6.2.3	Similarity of morphing OML to existing airfoils	131
6.3	Comments	134
7.	FINITE-DEFLECTION REVERSION BEAM THEORY	135
7.1	Overview	136
7.1.1	Motivation	136
7.1.2	Case studies	137
7.2	Finite-deflection Euler-Bernoulli derivation	138
7.2.1	Simplifications	145
7.3	Methodology	146
7.3.1	Previous methods.....	146
7.3.2	The proposed reversion method	148
7.3.3	Kinematic constraints and boundary conditions	151
7.3.4	Beam interactions	157
7.4	Implementation.....	160
7.4.1	Spline beam element and spline beam.....	161
7.4.2	Multi-beam assembly	167
7.5	Case studies	170
7.5.1	Case studies A: beam spline element.....	170
7.5.2	Case studies B: CST spline beam.....	176
7.5.3	Case studies C: multi-beam assembly	179
7.6	Comments	181
8.	CONCLUSIONS AND FUTURE WORK.....	183
8.1	Summary and conclusions	183
8.2	Future work.....	186

REFERENCES 188

APPENDIX A. DERIVATION OF ACTUATION FREQUENCY TO BODY MASS RATIO . 211

APPENDIX B. CST DERIVATIVES 213

 B.1 First derivative 214

 B.2 Second derivative 214

 B.3 Curvature radius 215

LIST OF FIGURES

FIGURE	Page
1.1 Overview of contributions to reduced-order modeling and applications addressed in this dissertation categorized by the utilization of geometric parameterization, kinematics, mechanics, and optimization.	3
1.2 Curvilinear basis vectors along the neutral line of a beam. For the neutral surface, the vectors are orthogonal and equivalent to the normal and tangent vectors.	8
1.3 Comparison between FEA, CAD, and the proposed Euler-Bernoulli model (EBM). .	8
1.4 Shock flow field for an F-5E and a modified F-5E developed as part of DARPA's QSP [72]. The modified aircraft decreased loudness 6.1% while significantly increasing drag. A morphing aircraft would enable OML adaptation to minimize fuel consumption or satisfy noise regulations (two conflicting objectives).	10
1.5 Overview of the main contributions of this dissertation. SMA components are experimentally and numerically evaluated for bio-inspired maneuvering. The first study consists of a bi-pedal robot with varying gaits as a function of thermal stimuli. The second study is of a camber morphing wing with skin-embedded SMA components that morph as a function of thermal stimuli. The experimental studies are followed by numerical analysis of the morphing wing including kinematics and constitutive response. A structurally consistent framework is optimized to explore the design domain of morphing wings. Moreover, a beam model that incorporates kinematics and constitutive response is developed. Overall, the numerical tools aid the design of future morphing structures.	12
2.1 Setup for experiments with humerotriceps muscles of pigeons and SMA actuators. a , the humerotriceps muscle originates on the head of the humerus, and the insertion was attached to a servo motor arm for work loop measurements. The dorsal branch of the brachial nerve was draped over two hooked electrodes and received electrical impulses to stimulate the muscle [75]. b , the engineering actuator consists of an equiatomic nickel-titanium wire attached to a loading frame responsible for the strain stimuli via insulated grips on each side. c , schematic of the electric and mechanical inputs for work-loop studies. d , isometric twitch of the pigeon humerotriceps muscle (7) and block force of a nitinol wire reveal similar asymmetry in force onset versus force offset.	14

2.2	Modeling framework of an adaptive bipedal robot from systems to material level with examples. Concept analysis requires the coupling of the following models: a , a dynamic model for the transient bipedal locomotion for a variable stiffness spring (parameters: $k_{leg,l}$, $k_{leg,r}$, k_{swing} , and M), b , a phenomenological model coupling local strain to spring displacements (parameters: r , R , and N), and c , a one-dimensional constitutive model for the thermomechanical response of the SMA material. d , the resultant states for systems- (location and velocity of the robot), actuator- (force and displacement), and material-levels (stress, strain, and temperature) for a constant temperature ($T = 390$ K), and e , for a cyclic thermal stimuli ($T_o = 387.8571$, $\Delta T = 2.8571$, $\theta_r = 0.5143$, $\theta_l = 0.9000$, and frequency of $0.7429/\sqrt{l_o g}$ Hz)	16
2.3	In situ work loops reveal the humerotriceps muscles of pigeons and SMA actuators are both capable of multifunctional roles through phase offset of stimuli. a , work-loops for pigeon humerotriceps specimen at 6.1 Hz and 50% stimulus duty cycle [75] and b , at 10.1 Hz and 50% stimulus duty cycle [75]. c , work-loops for SMA component at 29 mHz and 50% stimulus duty cycle and d , at 48 mHz and 50% stimulus duty cycle. Percentages indicate phase offset of the stimulus (relative to peak strain). Arrows on work loop traces depict the direction of the loops, with counterclockwise loop directionality indicates that the net work is positive (orange fill); clockwise directionality indicates net work is negative (blue fill). e , Power output for the pigeon humerotriceps and the SMA actuator in response to phase offset.	22
2.4	Cyclic response of SMA wire for 69% duty cycle, 0.04 Hz, and 0% phase. Similar data is available for all experiments in the Supplementary Information documents. a , the implied mechanical and electrical stimuli. b , resultant stress as a function of time. c , stress and strain evolution for the last three cycles. The counterclockwise loop directionality characterizes energy added to the system.	23
2.5	Scalability of the SMA-based robot in regards to dimensions, mass, and frequency. a , relation between leg length to body mass for: birds [105], 1.1-4.7 year-old humans [106], and 5-21 year-old humans [107]. Robot leg length is selected to satisfy the correlation from Daley and Birn-Jeffrey, $l_o = 0.2M^{0.4}$. Fredriks <i>et al.</i> did not provide information regarding the body mass of the studied population. Still the metric is estimated based on Body Mass Index (BMI) data for ages 5-19 provided by the World Health Organization (WHO). b , maximum actuation frequency of SMA spring relative to robot body mass for bi-pedal locomotion. The relation between both metrics is derived in appendix A.	26

2.6	Example of how shape memory alloys afford multifunctionality that can tune performance. a , Graphical representation of a simplified bi-pedal locomotion model utilizing SMA springs to either drive or add compliance to the system. b , thermal stimuli for SMA springs on the right and left legs. c , mechanical output for each leg with the respective volume fractions depicted. During the first cycle of locomotion, the right leg functions as an actuator followed by the left leg that operates as a brake. The operation of each leg is dependent on applied thermal stimuli. d , various states of the transient locomotion of the robot. The mechanical output for each state is also denoted in panel c.	27
2.7	Operational tunability of shape memory alloy is a function of thermal amplitude and phase offset. a , influence of right leg phase offset θ_r and thermal amplitude ΔT on power output from each leg. Frequency, left phase offset, and mean temperature are held constant $1/\sqrt{l_0g}$, 0, and 390 K. b , examples of how SMA power output affects robot horizontal velocity (e.g., two actuators increase velocity and two brakes decrease velocity).	28
2.8	Mechanical response for all explored stimuli inputs (cf. figure 2.7) as function of stride. All explored gaits have the same initial conditions for the left leg. a , stress, strain, and specific power bounds for gaits classified by the SMA spring response as an actuator or a brake. b , mechanical response of the bi-pedal robot with a linear spring and Young's Modulus equivalent to E_A . c , difference between modified gaits (i.e., actuator and brake) relative to the linear spring.....	29
2.9	Muscles and shape memory alloys exhibit similar capability for braking and actuation under different stimulus phases, despite substantial differences in actuation frequency and power phase dependency. We compare the performance of shape memory alloy, including from a previous study of thin wire SMA [89], with those found in previous studies of muscles that also examined the effects of phase-offset to timed stimuli: hawkmoth dorsolongitudinal [115], zebra finch pectoralis [116], and pigeon humerotriceps [75] muscles. Hawkmoth frequency range attained from Willmot and Ellington [117]. To mitigate the influence of outliers, only the average of each cyclic experiment is considered.	31
3.1	Overview of requirements, prototypes, and tests. A different prototype and set of tests are utilized to demonstrate each of the following requirements: tunability, controllability, and scalability. A composite actuator concept is tested to demonstrate that the generated force from the SMA component can be tuned via simple geometric properties. Control laws are developed for a 3D printed prototype with an SMA actuator in a wind tunnel environment to demonstrate controllability. Finally, a 6-foot wing with 12 actuators is tested to demonstrate scalability.	35
3.2	Concept of the composite SMA actuator.	36
3.3	Molds to fabricate composite SMA actuator.	38

3.4	The fabricated composite SMA actuator.	38
3.5	Force generated by SMA wire (experimental) and composite actuator (theoretical). .	39
3.6	Blocked force testing.	40
3.7	Hawk-inspired airfoil (F0808) [119].	41
3.8	Prototype of avian wing with an SMA embedded actuator.	42
3.9	Control framework for the morphing wing.	43
3.10	Overview of reinforcement learning algorithm.	45
3.11	Deep neural network architecture that maps the current wing configuration to control inputs.	45
3.12	Single-actuator platform on 1' x 1' wind tunnel.	47
3.13	Results of morphing wing utilizing SMA composite actuators.	48
3.14	Voltage applied to maintain 10 mm deflection for varying velocities.	49
3.15	Output voltage response compared to the velocity profile.	50
3.16	Wing tip displacement as a function of time for three flow velocities (15, 20, and 25 m/s) for four angles of attack (0°, 4°, 8°, and 12°).	51
3.17	Wing tip displacement as a function of time without flow.	52
3.18	Training on the Wind Tunnel: solid blue lines show the true displacement and red dashed lines the desire shape.	53
3.19	Displacement and temperature changes over time.	54
3.20	Training of Deep reinforcement learning controller performance after 1500 episodes.	55
3.21	Ashby [154] chart for material utilized for wing manufacturing.	57
3.22	Explored design domain. Highlighted design is was manufactured.	58
3.23	Selected design for morphing wing	58
3.24	Machined foam core of morphing wing.	59
3.25	Assembled morphing wing prototype.	59
3.26	Wing with applied speckle pattern.	61

3.27	Schematic of test setup (not to scale).....	61
3.28	Avian wing prototype and obtained results in wind tunnel: Lift coefficient v. angle of attack.....	63
3.29	Trailing edge displacement of morphing wing.....	64
3.30	Aerodynamic metrics for morphing wing.....	65
3.31	Pressure distribution before and after morphing.....	65
3.32	Transient signal for displacement and voltage under flow conditions.....	66
3.33	Transient response for aerodynamic metrics.....	67
3.34	Pressure distribution of the actuated and non-actuated configurations during cycling.....	68
3.35	Deflection contour mapped onto shape data from DIC imaging of a heating and cooling cycle with no flow.....	68
3.36	Mapped IR contour onto shape data from DIC imaging of a heating and cooling cycle with no flow.....	69
3.37	Mapped IR contour onto shape data from DIC imaging of a heating and cooling cycle with flow (third cycle).....	70
3.38	Temperature along a chordwise slice during heating and cooling.....	70
4.1	Overview of parameterizing a physically meaningful wing using the CST framework.....	73
4.2	Example of varying class function along span for a constant shape function.....	74
4.3	Example of the effects of parameters over class and shape function.....	75
4.4	Example of 3D shape function where $H_i(\eta)$ is a 2D shape function. The resultant shape is the tensor product of two 2D CST functions.....	75
4.5	Wing example demonstrating the framework capability to portray twist, camber, and dihedral changes along the span.....	77
4.6	Intersection of JWB wing and fuselage.....	79
4.7	Curve fitting of shape coefficients demonstrating the capability to various airfoils....	80
4.8	JAXA Wing Body (JWB) as an example of an aircraft assembly represented using the framework.....	81
4.9	Overview of the calibration process.....	82

4.10	Convergence study of CST calibration for JWB fuselage.	84
4.11	JWB fuselage parameterized and original geometries.	84
4.12	Simplified schematic of a B787-800 with linear mappings and respective physical meaning.	85
4.13	JWB wing parameterized and original geometries.	87
4.14	Spline and derivatives in the physical domain for $\Xi = (0, 0.2, 0.6, 1.0)$ and $\mathbf{A} = (0, 1.14, 2.28, 7.34, 6.47, 5.574, 3.69, 2.80) \times 10^{-2}$	89
4.15	CST basis for derivatives and positions in the parameterized domain for $\Xi = (0, 0.2, 0.6, 1.0)$ and $\mathbf{A} = (0, 1.14, 2.28, 7.34, 6.47, 5.574, 3.69, 2.80) \times 10^{-2}$	91
5.1	Structurally consistent airfoils based on a parent F0808 airfoil for calculation with actuators on lower surface; note the change in total chord due to assumed length preservation in non-actuated upper surface.	93
5.2	Map of the two morphing possibilities considered in the developed framework.	94
5.3	Structurally consistent airfoils based on a parent F0808 airfoil for backwards calculation with actuators on lower surface; note the change in total chord due to assumed length preservation in non-actuated upper surface.	95
5.4	Examples of compliant ribs: (a) Fishbone [169], (b) Jointed, (c) Voronoi [7]	95
5.5	Schematic of airfoils and their respective spars for example backwards calculation with actuator on the lower surface. The complement angles of β' are depicted for better visualization.	97
5.6	Conservation of spar heights and relative angles for forwards calculation.	98
5.7	Example of structurally consistent forwards calculation with a NACA0008 as the parent airfoil.	105
5.8	Schematic description of the finite element model for the morphing wing section showing permitted degrees of freedom.	106
5.9	Numerical validation of structurally consistent CST via refined FEA for forwards calculation with actuators on lower surface.	107
5.10	Description of backwards calculation in the case of an avian-inspired airfoil.	111
5.11	Influence of P_0^c over upper surface OML and chord of children airfoil sections for backwards calculation (actuators on lower surface). Note the conservation of arc length.	112

5.12	Influence of P_0^c over spars direction and height for parent geometry for backwards calculation with actuator on lower surface. Spars are vertical in the strain-free parent configuration.	113
5.13	Example of structurally consistent backwards calculation considering an F0808 airfoil [165] as parent (i.e., as the morphed shape).	115
6.1	Non-linear constraint to impose only existing airfoil solutions for morphed configurations.....	121
6.2	Flight condition probability of a Cessna 172 based on ADS-B measurements.....	123
6.3	Overview of concept selection methodology incorporating operation condition probability of an aircraft and parametric optimization of a morphed airfoil to select the ideal parent airfoil.	124
6.4	Lift-to-drag ratio results considering altitude at 10,000 ft. (a) Non-dominated surface for the morphing NACA 4415 and the aerodynamic results of the fixed configuration (b) Comparison between the performance of the morphing NACA 4415 and the fixed NACA 0012, NACA 4415, NACA 64 ₁ -212, and UAG 88-143/20 airfoils. ..	125
6.5	The non-dominated surface and the three cluster centers are depicted along with airfoil shape coefficients, designed flight condition, and lift-to-drag ratio for NACA 4415.	126
6.6	Aerodynamic performance of the fixed configuration and the non-dominated surface for the morphed configuration with the following parent airfoils: (a) NACA 0012, (b) NACA 4415, (c) NACA 64 ₁ -212, and (d) UAG 88-143/20.	128
6.7	Aerodynamic performance of (a) the fixed configuration and (b) the non-dominated surface for the morphed configuration with the following parent airfoils: NACA 0012, NACA 4415, NACA 64 ₁ -212, and UAG 88-143/20.	129
6.8	Cluster centers of the non-dominated surfaces and airfoils with the most significant degree of similarity for each concept.	132
6.9	Probability mass function for similar airfoils for the support vectors of the four evaluated concepts.....	133
7.1	Distinction between a geometrically feasible solution and the stable solution under specific loads.....	135
7.2	Nomenclature regarding superscripts and superscripts utilized for any variable in this chapter (e.g., x , M , and s)	136

7.3	Traditional methodology vs. universal parameterization methodology, where EBM stands for Euler-Bernoulli method. A universal parameterization method enables higher accuracy analysis without approximating the topology with a mesh of low-order piecewise polynomials.....	137
7.4	The different categories of beam models studied in this chapter: (A) spline element beam, (B) spline beam, and (C) multi-beam assembly. (A) requires C^0 pressure distributions, while (B) and (C) do not. (C) includes incorporates the interactions between different beams.	138
7.5	Curvilinear and Cartesian coordinate systems for bending beam.	139
7.6	Definitions of position vectors for the beam.	141
7.7	A summary of methods from Table 7.1 that consider a combinations of the following: arbitrary initial geometry, arbitrary loads, and parametric representation. Previous publication only consider up to one or two of these attributes, but this work considers the synthesis of all three.	149
7.8	Interactions between beams. For all three investigated interactions, the relation between reaction forces and lengths for parent and children configuration differ.....	158
7.9	Nested beam models.	160
7.10	An example of a beam with four knots and varying number of integration points per spline beam element.....	161
7.1	Main algorithm for CST and CST spline beam models.	163
7.2	Algorithm to calculate dependent variables for CST spline ($m \neq 1$) and CST ($m = 1$) beams.	164
7.3	Algorithm to determine parent and child geometries for CST spline ($m \neq 1$) and CST element ($m = 1$) beams.	165
7.4	Algorithm to determine bending moments.	166
7.5	Algorithm for coupled CST spline beams.....	168
7.6	Main algorithm to determine the solution of a multi-beam assembly.....	169
7.11	Schematics of loads, boundary conditions, and initial geometries for an example from each case study.	170
7.12	Schematics of loads, boundary conditions, and initial geometries considered in case studies A. Studies A3-A6 result in finite deflections.	172

7.13	Results of case studies A with a power series basis. All case studies returned low RMSE ϵ and residuals \mathbb{R} with no error exceeding 0.43% of the maximum deflection magnitude.	174
7.14	Results of case studies A with CST basis. All case studies returned low RMSE ϵ and residuals \mathbb{R} with no error exceeding 0.53% of the maximum deflection magnitude.	175
7.15	Schematics of loads, boundary conditions, and initial geometries for case studies B (independent shape coefficients are depicted).	177
7.16	Results of case studies B with CST basis. All case studies returned low RMSE ϵ and residuals \mathbb{R} with no error exceeding 0.05% of the maximum deflection magnitude.	178
7.17	Schematics loads, boundary conditions, and initial geometries of case studies C.	179
7.18	Results of case studies C with CST basis. All case studies returned satisfactory RMSE ϵ and residuals \mathbb{R} with no error exceeding 0.37% of the maximum deflection magnitude.	180
7.19	Motivation to utilize CST spline for beam representation in lieu of a single CST. The highlighted regions demonstrates that a single spline element is unable to capture the discontinuous bending moment. The bending moments differ at the root because the reaction force calculation is dependent on the geometric representation as will be shown in Section 7.3.4.	181

LIST OF TABLES

TABLE	Page
2.1 List of parameters utilized for numerical simulations.	20
5.1 Forward calculation: algorithm to compute dependent shape coefficients for child airfoil.	104
5.2 Backwards calculation: algorithm to calculate dependent shape coefficients for child airfoil.	114
6.1 Shape coefficients for parent (reference) airfoils considered in this work from which all morphed configurations are generated.	119
6.2 Summary of maximum and expected lift-to-drag ratios for fixed and morphed airfoils. Selected concepts are highlighted.	130
7.1 A review of implementations of beam theory.	146
7.2 Number of degrees of freedom to define a parent geometry α^p and child configuration α^c . Because of the imposed constraints, the number of degrees of freedom vary according to the imposed continuity at the knots. n is the order of the polynomial, m is the number of polynomial domains, and t is the number of locations with an applied torque.	157
7.3 All explored features for case studies A.	171
7.4 Residual and RMSE for case studies A with power series and CST.	173
7.5 All explored features for case studies B.	176
7.6 All explored features for case studies C.	179

1. INTRODUCTION AND LITERATURE REVIEW

1.1 Background

In pursuit of developing the next generation of high-performance aircraft, researchers are exploring the use of morphing aerodynamic surfaces. The implementation of morphing could increase the lift-to-drag ratio for subsonic flight [1] and mitigate the perceived loudness from sonic booms [2]. It is of particular interest that actuators embedded within the wing skin because of the very low volume impact and surface continuity advantages realized during activation [3]. Solutions utilizing high specific actuation energy density materials are desirable because of the restrictions imposed on actuator dimensions. Possible active materials that have been implemented experimentally include piezoelectrics [4], shape memory alloys [5], and combinations of both [6]. Beyond having external surfaces that are themselves actively deforming, conformed reconfiguration can also be enabled by features such as corrugated surfaces [7] or bistable structures [4]. Therefore, the technology for camber morphing exists, but a thorough analysis to determine desirable outer mold lines (OMLs) for different stages of a flight envelope is necessary to fully explore the potential of morphing wings. High-fidelity models utilizing constitutive models and finite element analysis may be highly enabling to forming design intuition and even accurate predictions, but their high computational cost can be prohibitive during preliminary design as one seeks to freely explore feasible designs towards understanding performance ranges; thus, the development of a low cost, structurally consistent morphing wing generator may be enabling and is proposed in this dissertation for the first time.

Irrespective of morphing motivations, there has been an increasing interest in airfoil optimization methods over the last two decades, motivated by the possibility of improving the aerodynamic performance of aircraft [8] and wind turbine blades [9]. This work builds on those successes, but with a focus on reconfigurable geometries. To effectively optimize the OML of an aircraft, it is necessary to employ a reliable and efficient method to represent the geometry. As a consequence,

several parameterization methods for airfoils and other geometries have been introduced. Each method has been developed for a specific application or to mitigate the weaknesses of other methods [10]. Consequently, there is great benefit in utilizing a universal shape parameterization such as the Class/Shape Transformation (CST) method [11] to represent 2D or 3D OMLs. Moreover, the CST method can be used to represent feasible morphed configurations if kinematic constraints are considered [12] and is a valuable *reduced-order model* for designing morphing aircraft.

Far beyond static representations, material and geometric non-linearities can be leveraged to improve performance and are the essence of aero-structural “morphing”. Although non-linearities are often considered undesirable for engineering analysis and design, birds and other animals have evolved to exploit non-linear responses to increase the range of their physical capabilities across a wide range of environmental conditions. Therefore, the research into avian flight inspires the concept of conformal wings and the means for manipulating such a morphing system via “artificial muscles.” Although wing flapping is beyond the scope of this dissertation and also unsuitable for high speed flight, the same functional flexibility can be observed in quasi-static reconfiguration or in the simple dynamic study of bipedal locomotion with a shape memory alloy (SMA) providing the non-linear actuation. Regarding geometric non-linearity, a “parameterized beam” formulation that allows for an arbitrary initial shape and large deflections is developed and used to explore the atypical design domain. When fully developed in Chapter 6, this new framework allows for seamless communication between geometric description and structural analysis, enabling the full exploration of material, geometric, and eventually surrounding aerodynamic behavior. Overall, the distinct efforts in this dissertation can be classified based on the utilization of kinematics, mechanics, and geometric parameterization as shown in Fig. 1.1.

1.2 Artificial muscle

SMA components, usually formed from nickel and titanium alloys (nitinol), generate and recover large strains (displacements) under large stresses (forces) and dissipate energy when undergoing phase transformation between austenite and martensite [13]. Depending on the initial state and thermomechanical loading, different phenomena can be observed. When not transforming,

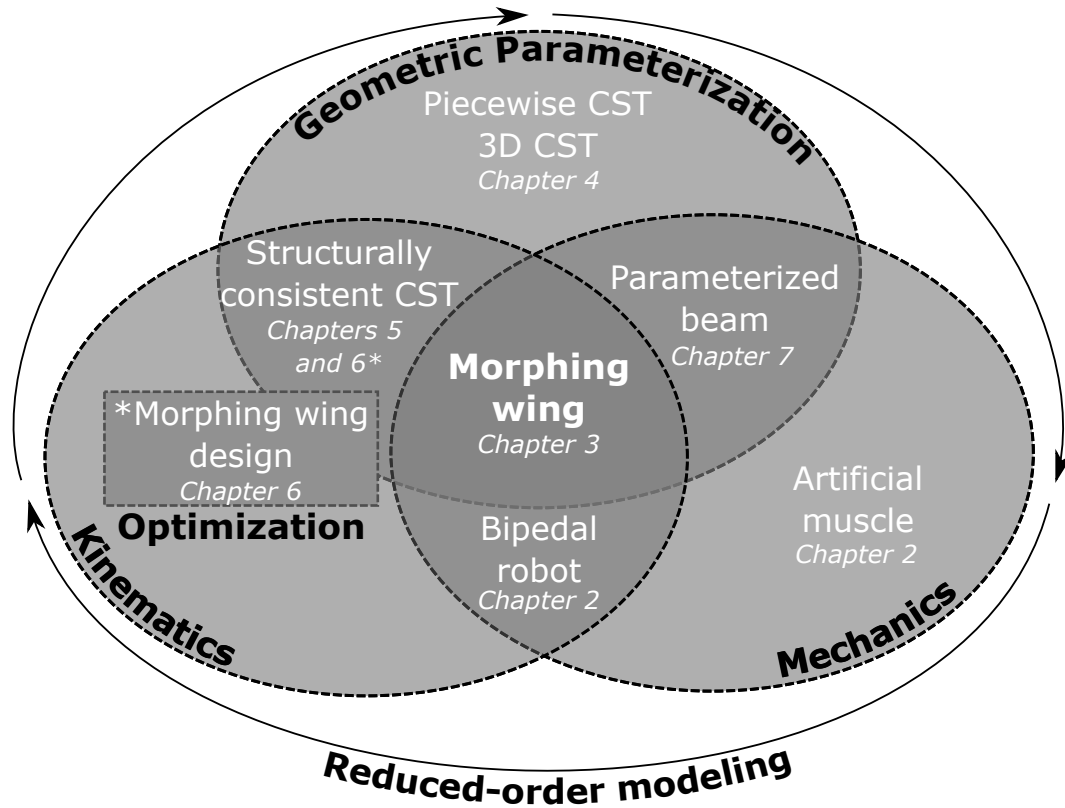


Figure 1.1: Overview of contributions to reduced-order modeling and applications addressed in this dissertation categorized by the utilization of geometric parameterization, kinematics, mechanics, and optimization.

SMA components are linearly elastic and can be used as structural members. However, if sufficiently mechanically loaded, an initially austenitic nitinol specimen will transform and deform toward a microstructural configuration of oriented martensite variants in a macroscopically non-linear fashion and then fully recover the austenitic configuration when unloaded. This is known as the pseudoelastic effect, and it can be highly dissipative. A specimen in an oriented martensite state can also be heated until it transforms into austenite state and recovers large strains under high stresses in a non-linear manner known as the shape memory effect. SMA actuators can generate positive mechanical work given the appropriate timings of supplied thermal energy [3]. Collectively, these features of SMAs point to their potential use as an artificial muscle [14] with tunable mechanical performance [15], but it is unknown whether SMAs can replicate the breadth of multi-functional capability shown by natural skeletal muscle, especially given cyclic stimuli.

Dynamic variation in functional demands is common to all forms of animal locomotion, but is an extreme feature of powered flight [16]. Birds dynamically adjust the shape and position of their wings to tailor performance to atmospheric conditions such as high winds [17, 18], and while capturing prey and gliding [19]. Insight into “wing morphing” adaptations that accommodate changing conditions is a major design target for improving aircraft performance. Skeletal muscle provides a compact solution for performing multiple tasks under diverse operational conditions, a capability lacking in many current engineered systems. In Chapter 2, it is evaluated if shape memory alloy (SMA) components can serve as artificial muscles with tunable mechanical performance.

1.3 Morphing

Morphing in aircraft is a concept at least partially inspired by how birds expand their performance envelope, enabling faster and longer flight and more effective maneuvering [20]. However, load-bearing structures and actuated control surfaces are typically distinct subsystems in aircraft while in a flying vertebrate the musculoskeletal system functions as both [21]. A morphing aircraft design [5] moves the former toward the latter by embedding the actuators into the skin. This actuating material often acts as a structural component, but under the appropriate stimulus the actuators function similar to muscles, leading to displacements that are constrained by the internal structure (i.e., ribs and spars) in similar fashion to how bird wing movements are restricted by stiff the skeletal system. In the literature, many works that address camber morphing mechanisms [22] incorporate solutions for alleviating strain in a morphed airfoil section such as rolling leading edge skin [23], corrugated skins [24–26], sliding skin [27], shape memory alloy actuators [28] and flexible skin [29–34]. In Chapter 5, it is shown that the Class/Shape Transformation (CST) method can be modified to represent feasible morphed airfoil configurations considering internal kinematic constraints regardless of actuation technology [3]. This framework is defined as “structurally consistent” since the OML must be consistent with the initial and rigid internal structure. This is a valuable tool to predict designs of morphing aircraft that can be used for structural and aerodynamic analysis.

In typical aircraft design, the selected OML is fixed and must have satisfactory performance

for all flight conditions [35]. For example, rudder dimensions are driven by Federal Aviation Association (FAA) regulations [36] that state that an aircraft must be able to execute a safe landing in the presence of crosswind, perhaps with either the right or left wing-mounted engine inoperative. Outside of this specific flight condition, the rudder is oversized and induces a drag penalty; clearly a more adaptive tail structure that minimized drag losses during the vast majority of flight operations. To overcome analogous performance losses, several methods exist to adapt them according to freestream conditions or changing performance requirements. The most common is the inclusion of rigid hinged control surfaces, which permit the reconfiguration of the wing necessary to transition from takeoff to cruise to landing [37]. These mechanisms lead to higher performance during required maneuvers but are not without drawbacks. Due to their structural and mechanistic complexity, they occupy volume inside the wing which might displace valuable fuel storage and would clearly add weight. Discontinuous surfaces also generate extra drag and noise. These disadvantages motivate the use of alternative adaptive technologies, such as conformal wing morphing via implementation of shape memory alloys or other active materials [38].

1.4 Parameterized representation

Regardless of the OML addressed and its ability to reconfigure, a representation of the surface, two- or three-dimensional, is necessary for both structural and aerodynamic analysis; the coupled results of which are essential to robust aircraft design. Parameterized representations are highly preferred over discrete ones due to the benefits of a continuous analytical geometric representation and seamless communication between various analyses regardless of mesh requirements. The main difference between parameterization methods is the quantity of degrees of freedom required to accurately represent a geometry. Usually there is a compromise between performance for a specific problem and computational performance for a general shape [39]. The most utilized parameterization methods include: the PARSEC method [40], Bezier curves [41], NURBS (Non-Uniform Rational B-Splines), Joukowski transformation, Hicks-Henne method [42], and Ferguson's method [43]. The PARSEC, Bezier curves, and modified Bezier curves seem to be the most widely used methods for wings [9, 44–47]. The PARSEC method is exclusive to 2-D air-

foil geometry and cannot be utilized for 3D bodies, while Bezier curves represent a generalization approach that requires several control points to represent an aircraft geometry. Kulfan [11] developed a universal shape representation known as the Class/Shape Transformation (CST) method that can mathematically define different geometries such as nacelles, fuselages, and subsonic [44] and supersonic wings [48]. Moreover, Sripawadkul et al. [10] established that among all methods evaluated, the CST method performs the best regarding the five desirable properties for airfoil representation: parsimony, orthogonality, completeness, flawlessness, and intuitiveness. Thus, the CST parameterization method provides desirable attributes in its generation of unique smooth geometries via physically meaningful variables, as will be further explored in Chapter 4.

Currently, free-form deformations (FFD) are used by multiple research groups to modify the mesh of pre-existing objects [49]. The method consists of establishing a grid of NURBS curves defining affine transformations that deform the geometry. The key advantage of this method is the capability of evaluating multiple configurations without requiring mesh generation. However, FFD is not an intuitive parameterization method (i.e., free variables do not have physical meaning), adding a layer of complexity to an already existing parameterization method. Applying kinematic constraints are essential when considering morphing *outer* surfaces enclosing rigid *interior* structural members; this is not trivial for FFD because the perturbation methods and geometry representation methods are uncoupled. Because this work proposes implementation of the parameterization method with aerodynamic models, the advantages of FFD are not significant. Conversely, the CST method represents the geometry and perturbations without any post-processing and is used as a universal shape parameterization to represent 2D or 3D OMLs [11], especially given the spline version developed in this work that allows for varying degrees of continuity along the OML.

1.5 Structural analysis

Historically, the fields of Computer Aided Design (CAD) and Finite Element Analysis (FEA) have developed independently from each other and different mathematical descriptions of the geometry are used in both fields. This has led to a gap between design and analysis models that is overcome by two-way model conversion. Meshing is often the most time-consuming step in

the design-through-analysis process [50]. Additionally, this introduces so-called “discretization error”, which describes the difference between the design model and the analysis model. There are varied techniques to bridge the gap by using the same mathematical description for the design and the analysis model. In the past decade, Isogeometric Analysis (IGA) has proposed NURBS as basis functions of the Galerkin method instead of the more traditional Lagrange/Hermite polynomials [50]. Through the concept of *knots*, the global geometric representation can be subdivided into C^{n-1} local *knot spans* that satisfy the requirements of a basis function [51]. However, the tensor product structure of NURBS functions proves to be inefficient due to the global nature of refinement operations, and the high-order continuity offered by NURBS has a negative impact on the performance of direct solvers. [52]

A fundamental step in the structural analysis an object is the choice of coordinate system. The Cartesian coordinate system is sufficient for most rigid bodies and linear elasticity problems [53] but may not be adequate for arbitrarily shaped objects as exemplified in Fig. 1.2. As a result, multiple FEA elements are defined in curvilinear coordinate systems (i.e., basis vectors are not fixed in the spatial domain). Two commonly used curvilinear coordinate systems are the cylindrical (e.g., as in curved beams [54]) and spherical (e.g., as in shell elements [55]). However, both frames assume a geometry to the object or a subset of the element (e.g., uniform radius along element). IGA methods are claimed to be more accurate than traditional FEA because a unique parameterized representation is used for the whole object across multiple applications [50]. However, other methods are also capable of a unique representation method for design and structural analysis [56]. As long as the implemented parameterization technique can represent all deformed configurations, accurate alternative structural models can be modeled [57].

An alternative to FEA is to utilize energy methods such as Ritz methods [58], principle of virtual work [59], or principle of minimum total potential energy [60]. Peraza Hernandez *et al.* have shown that all three methods can be used to accurately solve adaptive structure problems [57, 61,62]. The principle of minimum potential energy postulates that the configuration that minimizes the potential energy, calculated via Hamilton’s principle, is the stable configuration [60]. The

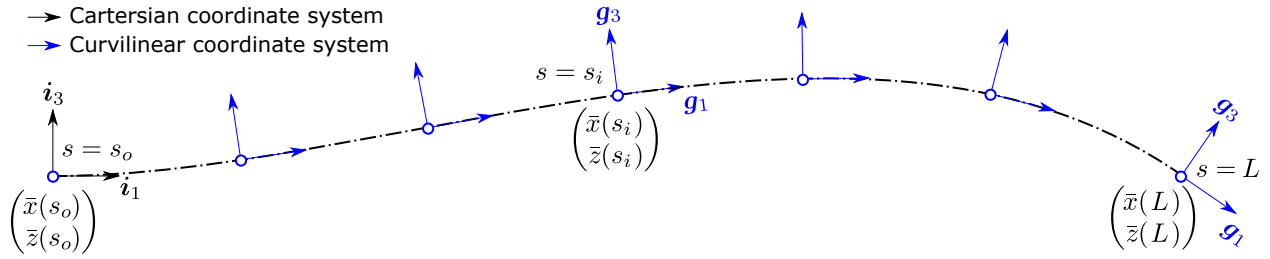


Figure 1.2: Curvilinear basis vectors along the neutral line of a beam. For the neutral surface, the vectors are orthogonal and equivalent to the normal and tangent vectors.

principle of virtual work is also based on Hamilton’s principle where a continuum body is in equilibrium if and only if the virtual work of all forces acting over any local virtual displacement of the stabilized body is zero, but assumes quasi-static deformations [58]. Ritz methods require a priori knowledge of the potential stable solutions, but have low computational cost [63]. A method inspired by the principle of minimum potential energy and Ritz methods is proposed because it enables the utilization of a universal parameterization similar to IGA as shown in Fig. 1.3. Similar approaches have been previously considered for beam angle [64–66], but applied here to CST parameterizations for the first time, leading to a unique aerodynamic-centric method for analyzing aerostructures in a preliminary manner. This is essential to the design of such systems.

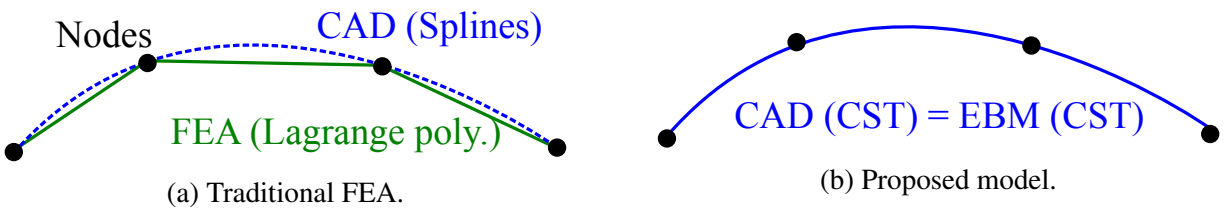


Figure 1.3: Comparison between FEA, CAD, and the proposed Euler-Bernoulli model (EBM).

1.6 Design of morphing structures

Although there has been extensive work in optimizing an aircraft OML to improve overall performance, most methods have one of the following three drawbacks:

- (i) lack of structural constraints [45, 46, 67, 68],
- (ii) lack of a set of analytical C^1 geometric representation [49, 68], and/or
- (iii) design is optimized for a limited number of flight conditions [3, 9, 42, 46, 48, 67, 68].

Optimized configurations for models that do not consider problem (i) will result in thin airfoils that are infeasible to manufacture while problem (ii) hinders the implementation of gradient-based methods or sensitivity analyses. The solution for problem (i) usually involves thickness [9, 68] and volume [42, 49] constraints on the OML that reproduce internal structural restrictions. High-fidelity CFD and FEA models accurately portray the physics of the problem, but this approach suffers from high computational cost [69]. The structurally consistent CST approach demonstrated herein addresses the first two problems.

Problem (iii) leads to designs that are highly sensitive to flight condition perturbations and are likely to underperform for a non-analyzed set of parameters (e.g., angle of attack, altitude, and aircraft velocity). The last challenge is solved both by explicitly considering morphing as part of the design search and by utilizing a parametric optimization (e.g., via P3GA [70]) that calculates the set of non-dominated solutions for a continuous set of varying parameters (i.e., flight conditions). Parametric optimization has the potential to become the standard procedure when optimizing morphing structures as it determines and describes how the optimum changes as a function of the parameters. Therefore, the performance efficiency of a morphing wing can be evaluated for all flight conditions and all mission objectives on flight regime and compared to traditional airfoils, verifying the advantages of adaptive structures relative to their possibly higher costs, weight, and complexity.

Morphing provides a solution to these design drawbacks by enabling multiple OMLs optimized for different flight conditions [3]. General aviation can benefit of this technology by increasing aircraft maneuverability [71] or minimizing drag [3] and noise [72] as shown in Fig. 1.4. Therefore, it is advantageous for an aircraft to adapt the OML for different flight conditions to satisfy acceptable performance requirements. This in part motivates the case study of a Cessna 172 with morphing

wings. The aircraft is suitable testing platform as information regarding the aerodynamic performance (e.g. lift coefficients) and mission profiles (e.g. frequency distribution of airspeed and angle of attack) are publicly available. A reduced-order model of the structural consistent CST equations with an aerodynamic solver is utilized with parametric optimization to determine the optimal performance for all relevant flight conditions simultaneously. Finally, flight data is leveraged to aid in the selection of the best concept (i.e., initial geometry).

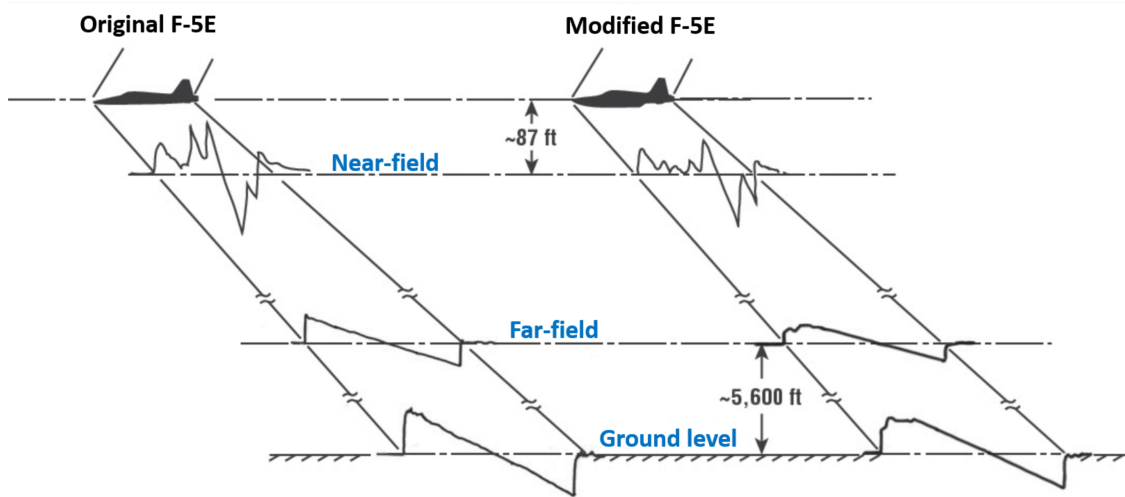


Figure 1.4: Shock flow field for an F-5E and a modified F-5E developed as part of DARPA's QSP [72]. The modified aircraft decreased loudness 6.1% while significantly increasing drag. A morphing aircraft would enable OML adaptation to minimize fuel consumption or satisfy noise regulations (two conflicting objectives).

1.7 This study

Considering the previously mentioned challenges in the development of morphing structures, the following contributions depicted in Fig. 1.5 are proposed herein:

- (i) demonstration of an SMA component as an *artificial muscle* that can be utilized as an actuator, brake, or spring,
- (ii) manufacturing and testing of a *morphing wing* that is controllable and robust performance

- for various environmental conditions,
- (iii) formulation of a modified CST Transformation model for *multi-component assembly*,
 - (iv) derivation and verification of a two-dimensional *structurally consistent framework* as a reduced-order model for morphing structures,
 - (v) *structural optimization* of subsonic adaptive wings and determination of the need of morphing technology, and
 - (vi) development of a *finite-deflection reversion beam theory* for any geometric parameterization method.

The remainder of this dissertation is summarized here. Chapter 2 presents experimental and numerical results for SMA-based artificial muscles that motivate their utilization as the driving component for morphing wings in Chapter 3. After verifying the feasibility of a morphing wing with experimental results, models are developed to enable efficient and accurate designs of morphing wings. The first step is to improve the CST equations to fully represent an aircraft with multiple components and discontinuities (i.e., splines) in Chapter 4. The second step is to incorporate the kinematic constraints into the parameterization method to develop structurally consistent CST equations in Chapter 5. The structurally consistent equations enable exploration of the morphing wing design domain that was not possible in Chapter 3, allowing for performance quantification of adaptive wings for various flight conditions and initial geometries in Chapter 6. The design studies motivate future analysis capabilities that incorporate material mechanics and use any parameterization method (e.g., CST, CST splines, and power series) to determine the feasible deformed solution in Chapter 7.

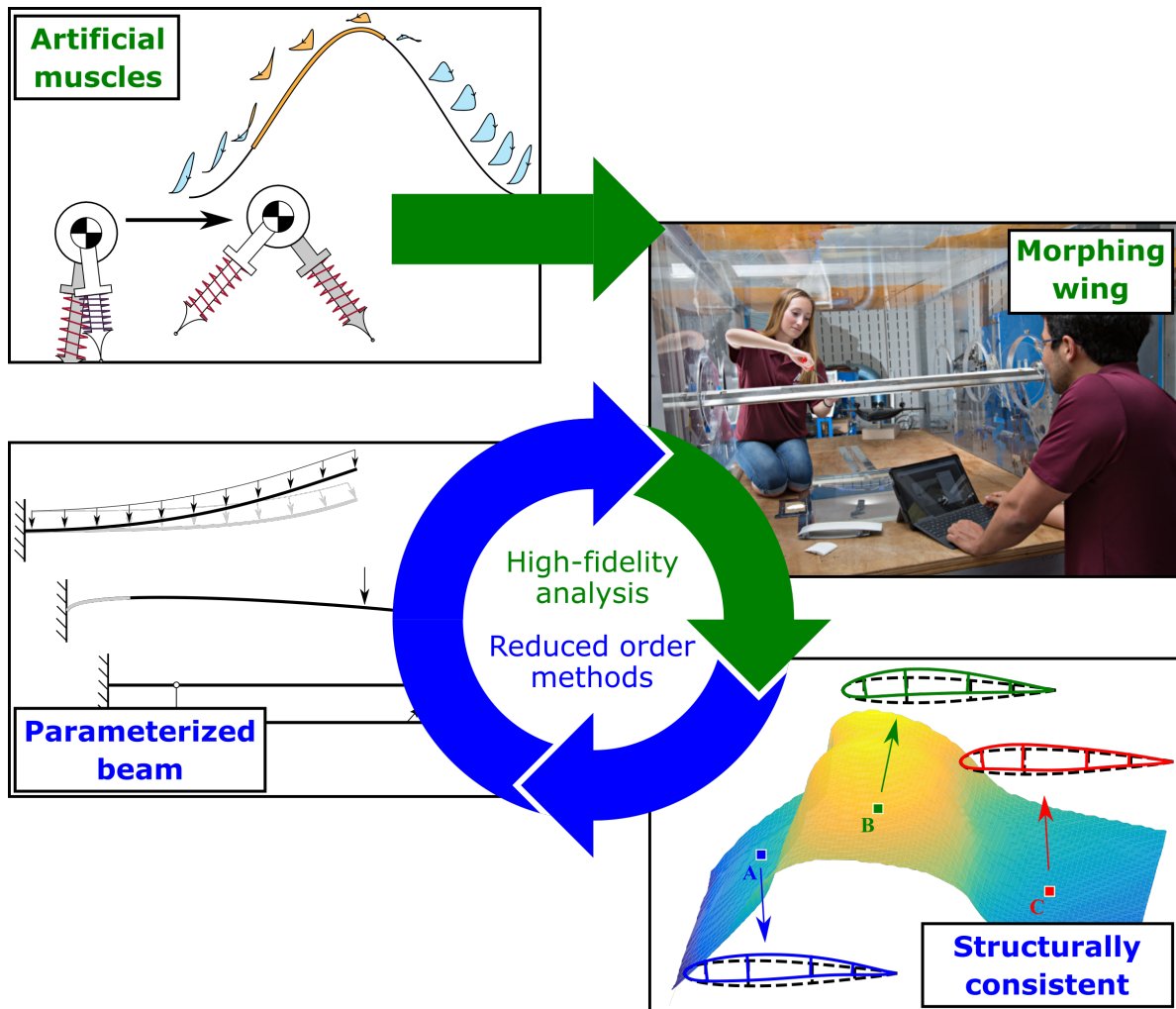


Figure 1.5: Overview of the main contributions of this dissertation. SMA components are experimentally and numerically evaluated for bio-inspired maneuvering. The first study consists of a bi-pedal robot with varying gaits as a function of thermal stimuli. The second study is of a camber morphing wing with skin-embedded SMA components that morph as a function of thermal stimuli. The experimental studies are followed by numerical analysis of the morphing wing including kinematics and constitutive response. A structurally consistent framework is optimized to explore the design domain of morphing wings. Moreover, a beam model that incorporates kinematics and constitutive response is developed. Overall, the numerical tools aid the design of future morphing structures.

2. EXPERIMENTS WITH BIRD AND ARTIFICIAL MUSCLES

2.1 Background

In traditional engineered systems, actuators, brakes, and structural members represent distinct components. In contrast, when an animal moves through its environment, all such functions can be performed by a single integrated musculoskeletal system [73]. Dynamic variation in functional demands is common to all forms of animal locomotion, but is an extreme feature of powered flight [16]. Birds dynamically adjust the shape and position of their wings to tailor performance to atmospheric conditions such as high winds [17, 18], and while capturing prey and gliding [19]. Insight into “wing morphing” adaptations that accommodate changing conditions is a major design target for improving aircraft performance. An important mechanism believed to be responsible for shape change in the wing is the elbow motion [74] driven by two triceps muscles, the humerotriceps and scapulothorax. Theriault *et al.* [75] determined that in the humerotriceps muscles of pigeons (*Columba livia*), the timing of neural stimuli relative to the muscle length cycle (hereafter “phase offset”) affected the production of mechanical power (Fig. 2.1a). Electrically stimulating the muscle just before attaining peak length resulted in actuation, whereas nearly all other phase offsets resulted in either dissipation (a brake) or low hysteresis (a spring). This observed multi-functional capability of a single wing muscle raises the question of whether human-designed systems can be designed to shift among functional roles with minimal changes to applied stimuli.

The design gap between natural and engineered systems [76] can be bridged by using smart materials such as shape memory alloys (SMAs). Because the functional role of skeletal muscle is dependent on phase offset [77–79], we sought to determine how SMA systems respond to phase offset of supplied thermal stimuli. We first performed experimental studies to measure the mechanics inherent to an SMA system. This revealed that an SMA system can have negative, neutral, and positive work-loops in a fashion that emulates those shown by skeletal muscle, namely the humerotriceps muscles of pigeons [75]. We performed numerical investigations to determine

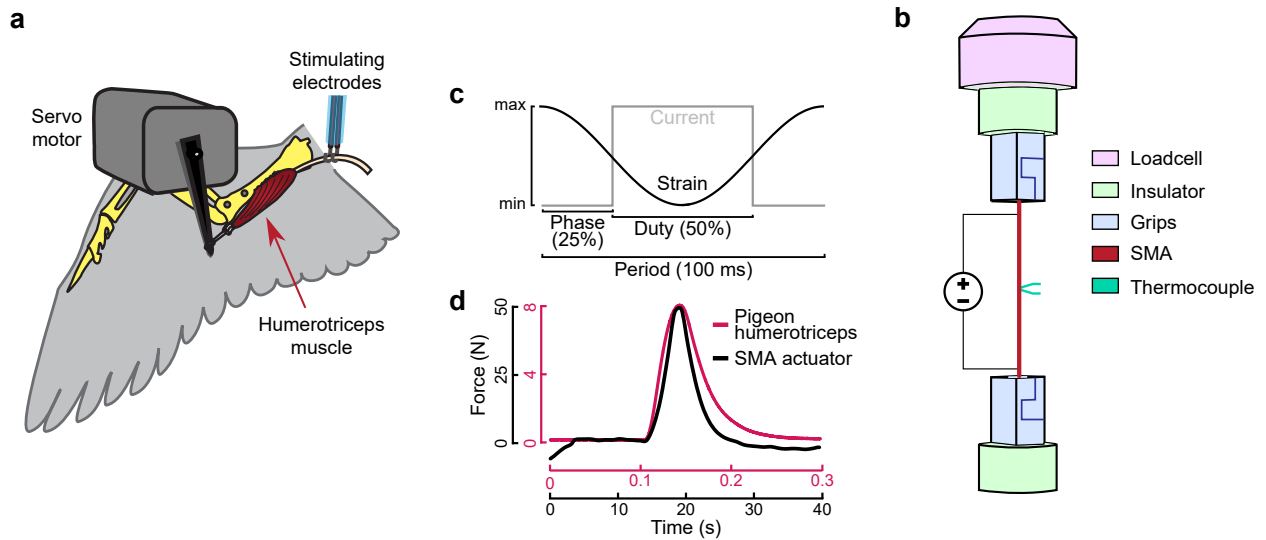


Figure 2.1: Setup for experiments with humerotriceps muscles of pigeons and SMA actuators. **a**, the humerotriceps muscle originates on the head of the humerus, and the insertion was attached to a servo motor arm for work loop measurements. The dorsal branch of the brachial nerve was draped over two hooked electrodes and received electrical impulses to stimulate the muscle [75]. **b**, the engineering actuator consists of an equiatomic nickel-titanium wire attached to a loading frame responsible for the strain stimuli via insulated grips on each side. **c**, schematic of the electric and mechanical inputs for work-loop studies. **d**, isometric twitch of the pigeon humerotriceps muscle (7) and block force of a nitinol wire reveal similar asymmetry in force onset versus force offset.

what potential advantages are available for engineering applications by tuning the force dynamics of shape memory alloys, a common mechanism found in nature [80].

2.2 Methods

2.2.1 SMA artificial muscle setup

All experiments utilize the setup depicted in Fig. 2.1 and are here described. Two stimuli, an electrical and a mechanical, were imposed on the SMA wire. The *electrical stimulus* in the form of voltage was directly applied to the wire to increase temperature via Joule heating; cooling is provided via natural convection. Type-K thermocouples are utilized to measure temperature, and two ABS 3D-printed connectors were used to electrically insulate the load frame from the nitinol wire. The *mechanical stimuli* in the form of displacement were controlled through an MTS Insight tensile testing machine, and a 100 N loadcell measured force. The strain is defined as a cosine

wave with the same frequency as the electric pulse wave, which is further defined by duty, phase offset, and amplitude. Five cycles are imposed for each work-loop, and only the last three are studies to remove outliers.

2.2.2 Bipedal compass model

A notable model explaining the natural motions resulting from the interplay of gravity, inertia, and elasticity is a spring-loaded inverted pendulum model that closely reproduces running gaits [81, 82]. Specifically, we utilized the model by Remy and coworkers, as shown in Fig. 2.2a, which has extensively been utilized for various gait problems [83–85]. Incorporated into this is the high-fidelity SMA constitutive model for the leg components [13, 86] (see section 2.2.4) in spring form (see section 2.2.3).

The SLIP model consists of the main body with mass M_b , two legs with mass M_l and stiffnesses $k_{\text{leg},l}$ and $k_{\text{leg},r}$, and an elastic torsional spring between both legs with stiffness k_{swing} (omitted from the figure). Leg mass is neglected, and each leg has an SMA compression spring element of length, l_l and l_r , and undeformed length l_o . The system is defined by the coordinates (x, y) of the center of mass as well as the pitch angles α_l and α_r for the left and right legs. As typical for bipedal locomotion, all results are normalized based on body size dimensions [87]. If no energy is dissipated, an angular frequency ω_{swing} of the leg motion is guaranteed by defining the torsional spring stiffness as:

$$k_{\text{swing}} = \omega_{\text{swing}}^2 M_l l_o^2. \quad (2.1)$$

During locomotion, at most one foot at a time can be in contact with the ground, and no-slip conditions are assumed. During contact, the angle and length of leg i is defined through $\alpha_i = \arctan[(l_{x,i} - x)/y]$ and $l_i = \sqrt{(x - l_{x,i})^2 + y^2}$, where $l_{x,i}$ is the x -component of the spring length, and the reaction forces are:

$$\begin{aligned} F_x &= k_{\text{leg},l}(l_l - l_o) \sin \alpha_l + k_{\text{leg},r}(l_r - l_o) \sin \alpha_r, \\ F_y &= k_{\text{leg},l}(l_l - l_o) \cos \alpha_l + k_{\text{leg},r}(l_r - l_o) \cos \alpha_r. \end{aligned} \quad (2.2)$$

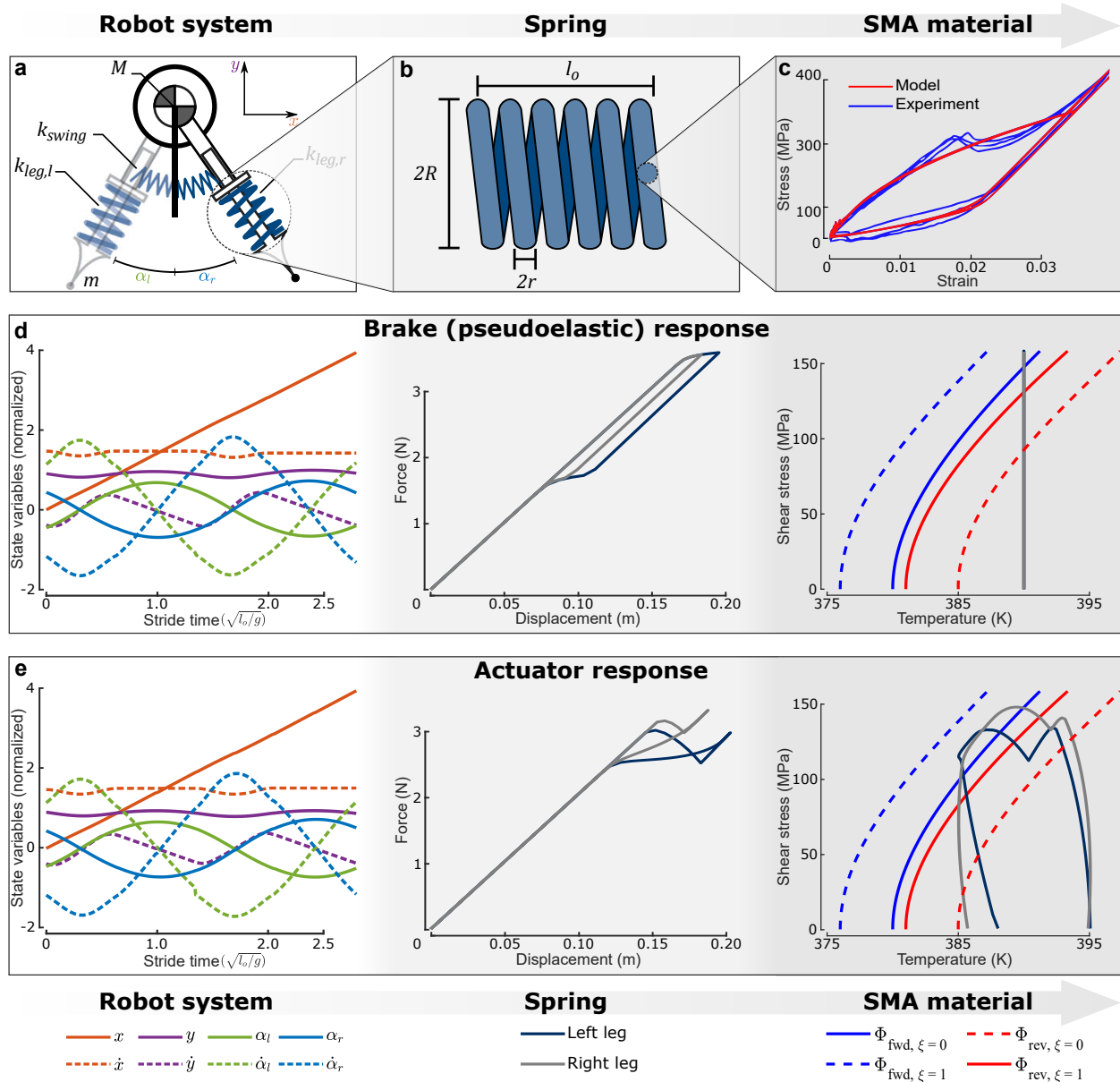


Figure 2.2: Modeling framework of an adaptive bipedal robot from systems to material level with examples. Concept analysis requires the coupling of the following models: **a**, a dynamic model for the transient bipedal locomotion for a variable stiffness spring (parameters: $k_{\text{leg},l}$, $k_{\text{leg},r}$, k_{swing} , and M), **b**, a phenomenological model coupling local strain to spring displacements (parameters: r , R , and N), and **c**, a one-dimensional constitutive model for the thermomechanical response of the SMA material. **d**, the resultant states for systems- (location and velocity of the robot), actuator- (force and displacement), and material-levels (stress, strain, and temperature) for a constant temperature ($T = 390$ K), and **e**, for a cyclic thermal stimuli ($T_o = 387.8571$, $\Delta T = 2.8571$, $\theta_r = 0.5143$, $\theta_l = 0.9000$, and frequency of $0.7429/\sqrt{l_o g}$ Hz)

However, when not in contact, the leg is assumed to be at the rest length l_o . The transition in between contact and no-contact is defined by Gan *et al.* through a series of events (e.g., take-off and touchdown) [83].

The trajectory of the robot center of mass in the state space was not imposed to understand the dynamic interplay of all acting physical phenomena and their role in generating efficient mechanics observed in gait [88]. Contrary to the experiments in Figs. 2.1 and 2.3, the strain and stress paths were not known a priori and were calculated as the robot advanced. The governing equations are the following 2nd-order ordinary differential equations: [83–85]

$$\begin{aligned}
\ddot{x} &= F_x/M_b, \\
\ddot{y} &= F_y/M_b - g, \\
\ddot{\alpha}_l &= \frac{1}{l_o^2 M_l} [-\ddot{x} M_l l_o \cos \alpha_l - (g + \ddot{y}) M_l l_o \sin \alpha_l - k_{\text{swing}} \alpha_l], \\
\ddot{\alpha}_r &= \frac{1}{l_o^2 M_l} [-\ddot{x} M_l l_o \cos \alpha_r - (g + \ddot{y}) M_l l_o \sin \alpha_r - k_{\text{swing}} \alpha_r].
\end{aligned} \tag{2.3}$$

In the state space, the four governing equations can be constructed in the canonical form of eight 1st-order differential equations that are fully defined by $\{x, \dot{x}, y, \dot{y}, \alpha_l, \dot{\alpha}_l, \alpha_r, \dot{\alpha}_r\}$ and integrated via a 4th-order Runge-Kutta scheme, calculating all states variables as shown in the first column of Figs. 2.2(d) and 2.2(e). The initial conditions were taken from the work of Gan *et al.* [83], and the resultant elastic gait is classified as a “running forward symmetrical single stance.” The robot parameters and initial conditions are provided in Table 2.1. Spring stiffnesses are calculated for each instance of time for the instantaneous thermomechanical states, as is explained in the following sections.

2.2.3 Spring model

Nitinol can only generate at most 6% recoverable extensional strain [89] and would not provide sufficient compliance if formed into the most common wire/rod configurations [90]. An SMA spring was utilized among any possible options for balancing force against displacement [91]. The

nitinol components along an SMA spring are undergoing pure shear that is not uniform along the wire radius. For engineering purposes, the constitutive model for the cross-section of the SMA wire is defined based on an effective shear stress $\bar{\tau}$ and strain $\bar{\gamma}$ via:

$$\bar{\tau} = G\bar{\gamma} \quad (2.4)$$

where G is the shear modulus. Force F and displacement u at the systems level are associated to the local $\bar{\tau}$ and $\bar{\gamma}$ of the SMA springs through: [91]

$$\begin{aligned} F &= \frac{2\pi r^3}{3R} \bar{\tau}, \\ u &= \frac{8\pi N_c R^2}{3r} \bar{\gamma}, \end{aligned} \quad (2.5)$$

where R is the spring radius, r is the wire radius, and N_c is the number of coils; alongside the undeformed length l_o , these four parameters fully define the spring geometry as shown in Fig. 2.2*b*; the selected parameter values are depicted in Table 2.1. Examples of spring force and displacement when functioning as a brake or an actuator are provided in the second column of Figs. 2.2(*d*) and 2.2(*e*).

2.2.4 SMA model

The constitutive model elaborated by Lagoudas *et al.* [13] is implemented to describe the SMA response. The lumped-parameter model originally developed for tension [90] is modified for shear strain. The model considers three external state variables: effective shear stress $\bar{\tau}$, effective shear strain $\bar{\gamma}$, and absolute temperature T . Two internal state variables are also considered: effective inelastic transformation strain $\bar{\gamma}^t$ and martensitic volume fraction ξ . For this chapter, temperature is known, while stress is calculated through linear and angular momentum conservation. Considering that the shear modulus for austenite and martensite phases are different, the effective shear is given by:

$$\bar{\gamma} = \left[\frac{1}{G_A} + \xi \left(\frac{1}{G_M} - \frac{1}{G_A} \right) \right] \bar{\tau} + \bar{\gamma}^t. \quad (2.6)$$

Crystal structure transformation only takes place at specific thermomechanical states according to the transformation direction, *forwards* from austenite ($\xi = 0$) to martensite ($\xi = 1$) or *reverse* from martensite to austenite. The region where transformation is possible is defined through transformation functions Φ_{rev} and Φ_{fwd} as depicted in the third column in Figs. 2.2(d) and 2.2(e). The relation between the evolution of effective transformation strain $\bar{\gamma}^t$ and evolution of martensitic volume fraction is given as:

$$\dot{\bar{\gamma}}^t = \dot{\xi} \begin{cases} \text{sgn}(\bar{\tau}) H^{\text{cur}}(|\bar{\tau}|) & \dot{\xi} > 0 \\ \bar{\gamma}^{t-r} / \xi^r & \dot{\xi} \leq 0 \end{cases}, \quad (2.7)$$

where $\bar{\gamma}^t$ is the effective transformation strain at transformation reversal, ξ^r is the martensitic volume fraction at transformation reversal, and $H^{\text{cur}}(|\bar{\tau}|)$ is the current effective transformation strain. The current effective transformation strain is given by the following piecewise equation:

$$H^{\text{cur}}(|\bar{\tau}|) = \begin{cases} H_{\text{min}} & |\bar{\tau}| > \tau_{\text{crit}} \\ H_{\text{min}} + (H_{\text{max}} - H_{\text{min}}) (1 - e^{-\kappa(|\bar{\tau}| - \tau_{\text{crit}})}) & |\bar{\tau}| \leq \tau_{\text{crit}} \end{cases}, \quad (2.8)$$

where H_{min} , H_{max} , κ , and τ_{crit} are material parameters. Other parameters considered in the model are: the transformation temperatures (A_s , A_f , M_s , and M_f) that determine where transformation occurs when load-free, the slopes of the reverse and forwards transformation surfaces (C_A and C_M), and the hardening parameters (n_1 , n_2 , n_3 , and n_4) that determine the smoothness in the transition between transformation and thermoelastic loading. An in-depth description of each variable is provided by Lagoudas *et al.* [13], and selected parameter values are provided in Table 2.1.

Compass-gait parameters	M	10 kg
	g	9.81 kg m/s ²
	l_o	1 m
	ω_{swing}	7
Spring parameters	r	1.8 mm
	R	5.5 mm
	N	113
SMA constitutive model parameters	G_A	14.4 GPa
	G_M	34.2 GPa
	M_s	380 K
	M_f	376 K
	A_s	381 K
	A_f	385 K
	C_A	7.20 MPa/K
	C_M	7.95 MPa/K
	H_{min}	0
	H_{max}	0.055
	κ	4.68 GPa ⁻¹
	τ_{crit}	0 Pa
	n_1	0.18
	n_2	0.18
n_3	0.15	
n_4	0.29	
Compass-gait initial conditions (non-dimensional)	x_o	0
	\dot{x}_o	1.4709
	y_o	0.9053
	\dot{y}_o	-0.3840
	$\alpha_{l,o}$	-0.4528
	$\dot{\alpha}_{l,o}$	1.1412
	$\alpha_{r,o}$	0.4387
	$\dot{\alpha}_{r,o}$	-1.1684
SMA initial conditions (both springs)	ξ_o	0
	ϵ_o^t	0
	σ_o	0
	ϵ_o	0

Table 2.1: List of parameters utilized for numerical simulations.

2.3 Results

2.3.1 Artificial vs. natural muscles

The experimental setup for the investigation of artificial muscles includes an equiatomic nitinol wire subject to tensile loading via an MTS Insight tensile testing machine and electrical stimuli via Joule heating as depicted in Fig. 2.1*d*. This setup is capable of timed mechanical and electrical stimuli to the SMA wire, reproducing the studied stimuli on humerotriceps muscles [75].

We first assessed the transient response of SMA systems to electrical stimuli (Fig. 2.1*d*). Similar to the isometric twitch investigation performed by Theriault *et al.* [75], we subjected SMA specimens to a block force test; here, the specimen lengths were held constant while a pulse of electrical stimulus was applied. This initial assessment indicated clear similarities between nitinol wire and pigeon triceps muscle responses, particularly in the asymmetry in force onset vs. offset, which then motivated the investigation of other shared functionalities.

In cyclic operation (Fig. 2.1*c*), a stimulated muscle contracts and produces force, which can either provide positive work by shortening or can provide negative works as it resists lengthening [77]. Muscle performance in animals is influenced by muscle length, velocity, stimulation intensity and timing, and imposed force change during a cycle [16]. *In situ* work-loops, as depicted in Fig. 2.3*a* and 2.3*b*, estimate the *in vivo* output work for biological muscles. Varying the phase offset between the mechanical and electrical cyclic stimuli alters the net work produced. A positive work cycle, counterclockwise in the force-displacement (stress-strain) space, corresponds to the muscle functioning as an actuator. Negative work, clockwise in stress-strain space, equates to a dissipative brake. Although not considered explicitly herein, the muscle can also result in zero net work cycles similar to a spring if its stress-strain response is non-hysteretic. Therefore, the humerotriceps can function as a brake, actuator, or a spring with variable compliance depending on activation properties [75].

The exploration of work-loops in the SMA wire expanded upon the previous block force testing by instead imposing a cyclic strain with an amplitude of 0.02 within each of three frequency treat-

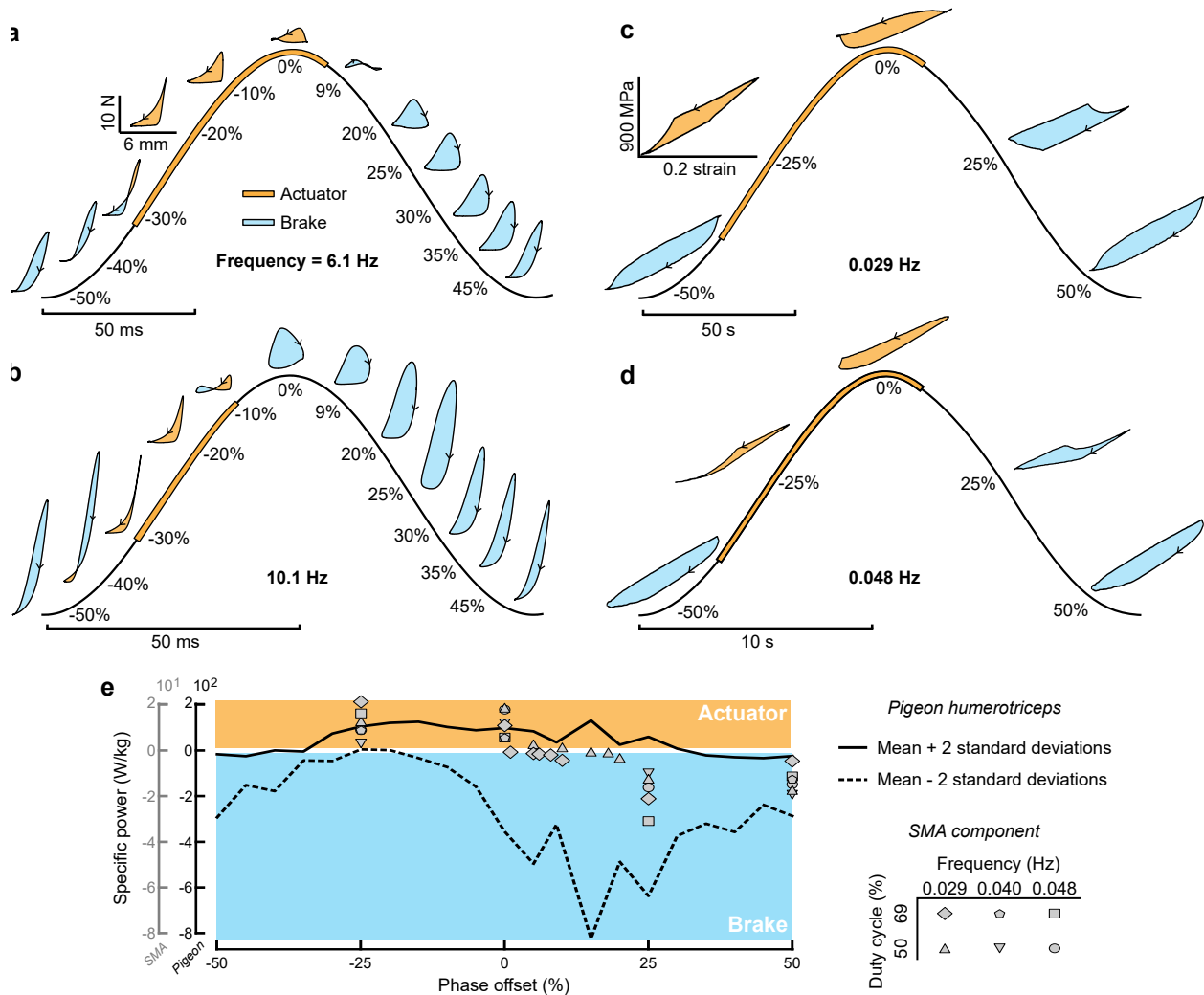


Figure 2.3: In situ work loops reveal the humerotriceps muscles of pigeons and SMA actuators are both capable of multifunctional roles through phase offset of stimuli. **a**, work-loops for pigeon humerotriceps specimen at 6.1 Hz and 50% stimulus duty cycle [75] and **b**, at 10.1 Hz and 50% stimulus duty cycle [75]. **c**, work-loops for SMA component at 29 mHz and 50% stimulus duty cycle and **d**, at 48 mHz and 50% stimulus duty cycle. Percentages indicate phase offset of the stimulus (relative to peak strain). Arrows on work loop traces depict the direction of the loops, with counterclockwise loop directionality indicates that the net work is positive (orange fill); clockwise directionality indicates net work is negative (blue fill). **e**, Power output for the pigeon humerotriceps and the SMA actuator in response to phase offset.

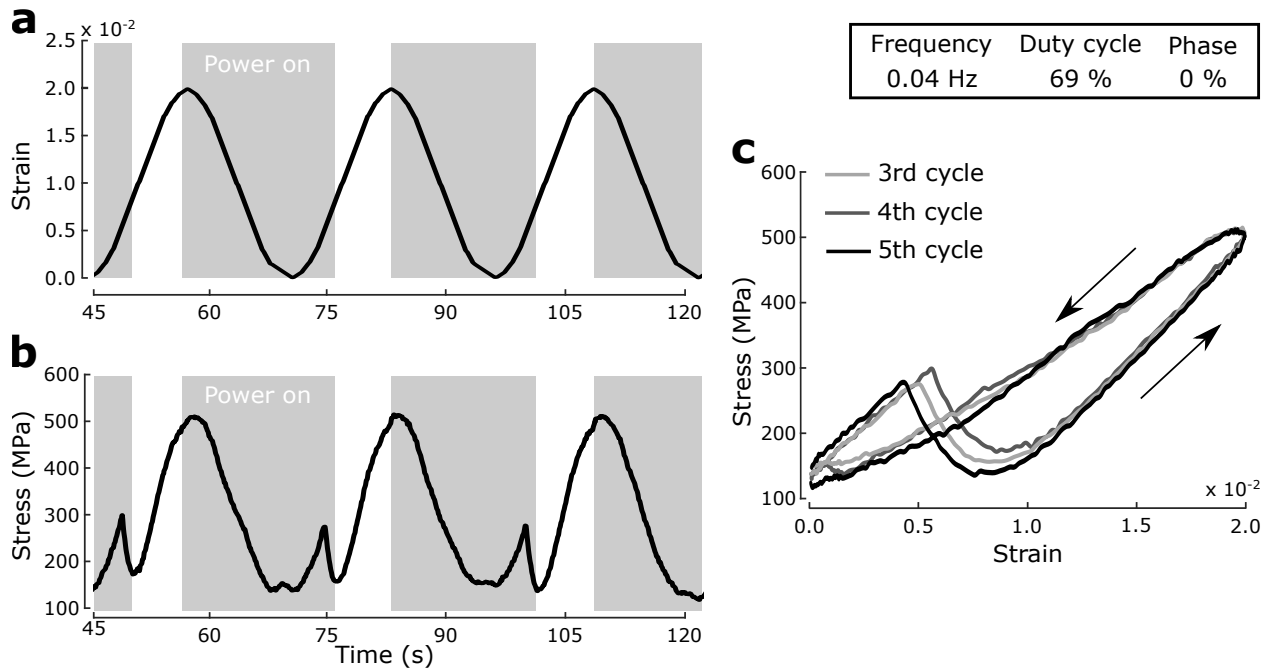


Figure 2.4: Cyclic response of SMA wire for 69% duty cycle, 0.04 Hz, and 0% phase. Similar data is available for all experiments in the Supplementary Information documents. **a**, the implied mechanical and electrical stimuli. **b**, resultant stress as a function of time. **c**, stress and strain evolution for the last three cycles. The counterclockwise loop directionality characterizes energy added to the system.

ments. Timed Joule heating represented the imposed actuation stimulus while cooling occurred via forced convection. The stimuli frequencies studied were based on the explored frequencies by Theriault *et al.* [75] and adjusted to consider the intrinsically different time scales between the natural and artificial muscle responses (cf. Fig. 2.1d). Considering this setup, the influence of frequency (29, 40, and 48 mHz), duty cycle (50 and 69%), and phase offset (-25, 0, 25, and 50%) were experimentally explored. The mechanical results for one of the evaluated cases are depicted in figure 2.4 to demonstrate the cyclic response as a function of time. Similar to Theriault *et al.* [75], the first two cycles are neglected to consider results with reproducible heat transfer (i.e., the same temperature at the end of each cycle). The majority of experiments lead to reproducible cycles, whereas the case here depicted has the most variability. The applied stimuli, figure 2.4a, result in the stress output depicted in figure 2.4b and 2.4c. The net work for the depicted work-loop is positive, characterizing an actuator.

It was expected that the SMA wire would behave as a brake for most explored cycles given the dissipative nature of many mechanic cycles previously explored [92]. This behavior was observed for phase offsets 25% and 50% for the work-loop cycles depicted in Figs. 2.3c and 2.3d. However, if the electrical stimuli was timed to phase offsets between -25% and 0%, the work-loops evolve in a counterclockwise manner, corresponding to positive net work output. Therefore, it is possible to utilize the same SMA wire as a brake, structural member, and actuator solely as a function of thermal stimuli.

The overall similarity in work loop shape and direction motivated us to determine how strong the phase offset effects are on power output in both natural and artificial materials. We evaluated the non-linear monotonic relationship between stimulus parameters and net work using the Spearman rank correlation factor r_s [93].* Similar to natural muscle systems, the phase offset of the thermal stimuli on SMA is strongly correlated to the resultant power output with $r_s = -0.75$. The effects of frequency and duty cycles were not significant for the explored ranges[†] with respective Spearman rank correlations of -0.03 and -0.04. This predominant dependency on stimuli phase offset is similar to that observed by natural systems [75]. For the pigeon humerotriceps, the Spearman values for phase offset, frequency, and duty cycle were -0.49, -0.30, and -0.01. Considering all the experimental results for natural and artificial muscles, the same trends are noticeable regarding specific power. Fig. 2.3e depicts the data for varying frequencies, duty cycles, and phase offsets solely as a function of phase offset and specific power. Both systems are mostly dependent on the phase offset and act as an actuator for approximately the same phase ranges, a similarity that motivated us to further explore the use of SMA components as artificial muscles.

* $r_s \in [-1, 1]$ where negative values indicate an inversely proportional relationship. Correlations are qualified as “very weak” ($r_s \in \pm[0.0, 0.2]$), “weak” ($r_s \in \pm[0.2, 0.4]$), “moderate” ($r_s \in \pm[0.4, 0.6]$), “strong” ($r_s \in \pm[0.6, 0.8]$), and “very strong” ($r_s \in \pm[0.8, 1.0]$).

[†]Higher values of frequency and duty cycles were not explored because they would lead to higher temperatures, and, as a result, the nitinol wire would predominantly act as an elastic structural component.

2.3.2 Robotics application to multifunctional SMA components

All results hitherto indicate that SMA components enable tailored structural properties in cyclic applications. Previous studies have aspired to develop various potential engineered systems mimicking biological counterparts and have implemented SMA components in biomimetic jellyfish [94,95], birds [28,90], earthworms [96], human-like anatomical systems [97], and others. However, previous studies did not explore the multifunctional potential of SMA components as inspired by natural musculoskeletal systems. We examined the prospect of SMA for non-smooth systems [98], specifically bipedal locomotion [99]. This locomotor mode is of interest for bio-inspired engineering because in animals it allows for the exploration of challenging habitats that are not currently accessible by wheeled and tracked vehicles [100]. Simple rigid bipedal robots can achieve some necessary gaits [101, 102], but timed and tailored compliance plays an essential role in nature [103] by allowing energy storage and release as well as improving passive adaptability [104].

The compass gait model from Gan *et al.* [83] is non-dimensional, but a leg length and body mass of 0.526 m and 10 kg are assumed for calculating the mechanical state of the SMA wire cross section. The leg length of the 10 kg robot was selected based on the avian leg length to body mass correlation from the work of Daley and Birn-Jeffrey [105] as shown in figure 2.5a. The utilized leg length is 50 % above that of a child with equivalent body mass. For the selected dimensions, the SMA component can achieve actuation frequencies beyond the robot stride frequency with the proper combination of parameters as shown in figure 2.5b. The maximum actuation frequency is inversely proportional to the body mass times a coefficient A as derived in appendix A. As the body mass of the robot increases, the maximum actuation frequency decreases for the same coefficient A , corresponding to a constant set of parameters (e.g., heat transfer, spring design, operation, and others). Parameters such as the spring index C , typically between 4 and 25, can significantly impact the maximum actuation frequency as shown by the gray line in figure 2.5b. The developed frequency-mass relation, Eq. A.7, and the Daley and Birn-Jeffrey correlation can be combined to determine the maximum actuation frequency for the selected robot parameters as a function of

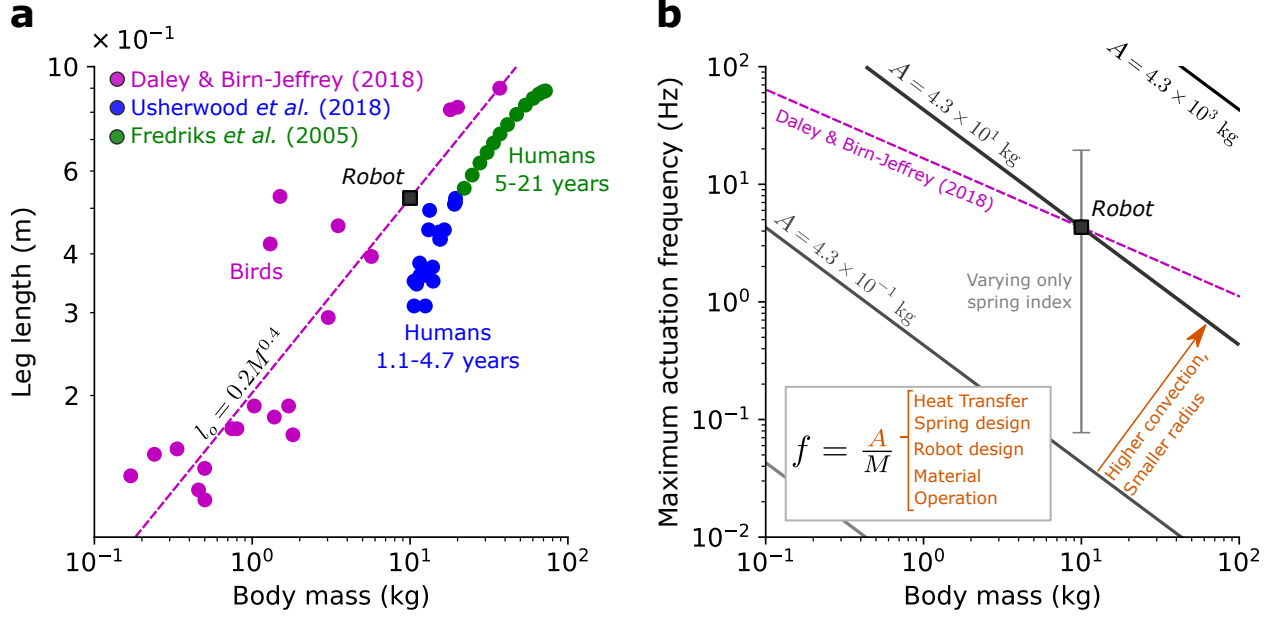


Figure 2.5: Scalability of the SMA-based robot in regards to dimensions, mass, and frequency. **a**, relation between leg length to body mass for: birds [105], 1.1-4.7 year-old humans [106], and 5-21 year-old humans [107]. Robot leg length is selected to satisfy the correlation from Daley and Birn-Jeffrey, $l_o = 0.2M^{0.4}$. Fredriks *et al.* did not provide information regarding the body mass of the studied population. Still the metric is estimated based on Body Mass Index (BMI) data for ages 5-19 provided by the World Health Organization (WHO). **b**, maximum actuation frequency of SMA spring relative to robot body mass for bi-pedal locomotion. The relation between both metrics is derived in appendix A.

mass as shown by the magenta line in figure 2.5b. Overall, SMA components can function for bipedal locomotion for the explored frequency, body mass, and leg length domains.

In the field of robotics, sinusoidal stimuli can generate gaits that are similar to those found in nature (e.g., running of a cockroach [108]). Moreover, sine wave inputs have also been employed for natural muscles (e.g., angle extensors in wild turkeys [78]). Therefore, we used sinusoidal thermal stimuli for our robot prototype [78]. The sinusoidal temperature imposed on each leg has the same frequency, amplitude ΔT , and mean temperature, but the phase offsets, θ_r and θ_l , are different. A solution where the SMA components have opposite functions (i.e., actuator vs. brake) is depicted in Fig. 2.6b and 2.6c. As the robot walks, the martensitic volume fraction ξ of the springs varies when in contact with the ground. All cases explored represent only partial transformation ($\xi < 20\%$), which is beneficial to the component fatigue life [109, 110], and thus

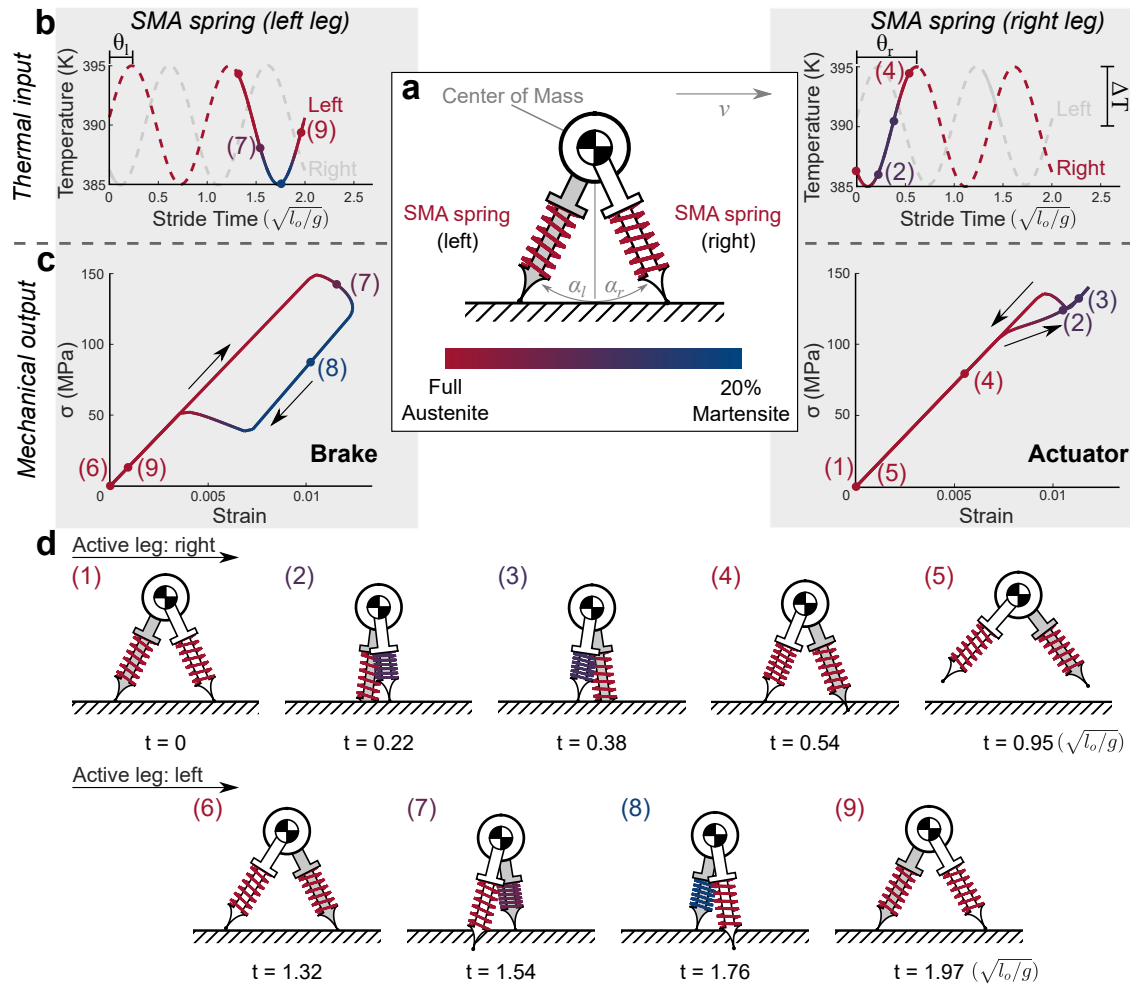


Figure 2.6: Example of how shape memory alloys afford multifunctionality that can tune performance. **a**, Graphical representation of a simplified bi-pedal locomotion model utilizing SMA springs to either drive or add compliance to the system. **b**, thermal stimuli for SMA springs on the right and left legs. **c**, mechanical output for each leg with the respective volume fractions depicted. During the first cycle of locomotion, the right leg functions as an actuator followed by the left leg that operates as a brake. The operation of each leg is dependent on applied thermal stimuli. **d**, various states of the transient locomotion of the robot. The mechanical output for each state is also denoted in panel c.

utilize only a fraction of the contracting capability of the artificial muscle (10%) similar to muscle fibers constrained by joints (20%) [15]. These results demonstrate that an SMA component can preserve or dissipate energy to achieve more natural gaits with a simple mechanism, not requiring the use of other components such as latches [111].

The real value of utilizing SMA components is the tuning capability [112] resulting from phase

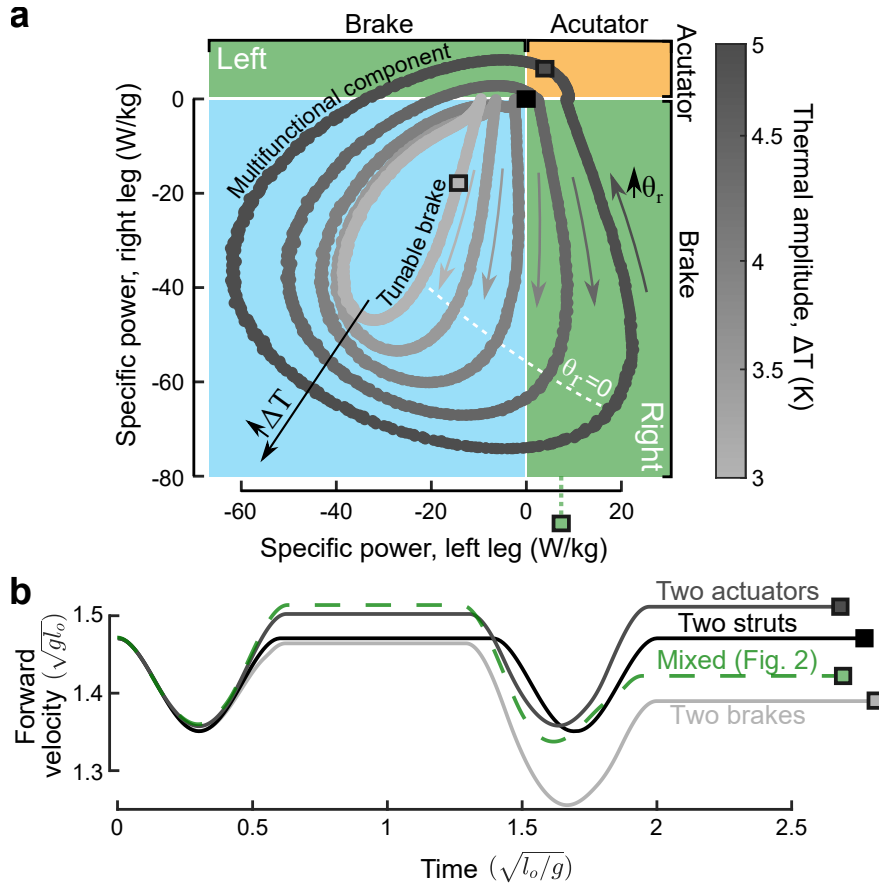


Figure 2.7: Operational tunability of shape memory alloy is a function of thermal amplitude and phase offset. **a**, influence of right leg phase offset θ_r and thermal amplitude ΔT on power output from each leg. Frequency, left phase offset, and mean temperature are held constant $1/\sqrt{l_0 g}$, 0, and 390 K. **b**, examples of how SMA power output affects robot horizontal velocity (e.g., two actuators increase velocity and two brakes decrease velocity).

transformation; this is elucidated in Fig. 2.7. Changes in time-variant temperature stimuli can result in different features than those depicted in Fig. 2.6. If the thermal amplitude is fixed at $\Delta T = 5 K$ and only the right leg phase offset is varied, the compression springs operate as various combinations of brakes, structural members, and actuators, as shown in Fig. 2.7a. Therefore, the thermal stimuli can be modified such that energy is provided to drive locomotion or dissipated based on environmental conditions (e.g., terrain and gust) or maneuver objectives (e.g., trajectory and velocity requirements). Some applications only require a dissipative functionality, but benefit from varying dissipation magnitude [112]. By decreasing the thermal stimuli amplitude, multiple tunable

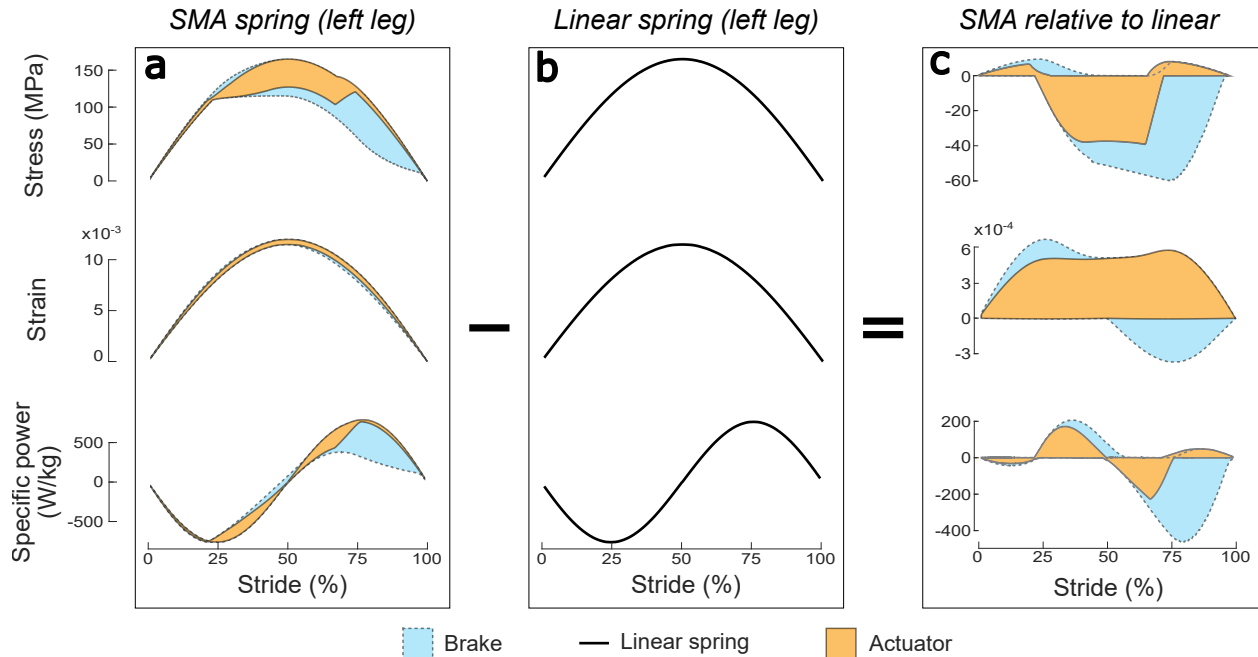


Figure 2.8: Mechanical response for all explored stimuli inputs (cf. figure 2.7) as function of stride. All explored gaits have the same initial conditions for the left leg. **a**, stress, strain, and specific power bounds for gaits classified by the SMA spring response as an actuator or a brake. **b**, mechanical response of the bi-pedal robot with a linear spring and Young’s Modulus equivalent to E_A . **c**, difference between modified gaits (i.e., actuator and brake) relative to the linear spring.

brake configurations are possible that are a function of a single parameter. A direct consequence of varying the net cyclic system energy is a decrease or increase of the robot instantaneous velocity, as depicted in Fig. 2.7b. Note that all results herein depicted (cf. Figs. 2.6 and 2.7) are for specific robot and spring specifications; more general design studies may identify other responses of interest.

The obtained mechanical results in figure 2.7 can also be utilized to provide insight on how the mechanical states (i.e., stress, strain, and power) change along with the stride and the reason why the SMA component acts as a brake or an actuator. The upper and lower bounds of all evaluated SMA responses are provided in figure 2.8a in a similar fashion as the bird gait study by Higham *et al.* [113]. While the actuator and brake strains are similar, the stress significantly differs at the end of the stride, from 70% to 95%. As a consequence, less power is generated at the end of the stride for a brake SMA component. Any stimuli combination will add or subtract energy throughout the

stride regardless of whether the net work is positive or negative. Even for the case of a linear spring where the net work is zero, negative and positive instantaneous power is experienced as shown in figure 2.8*b*. Comparing the actuator and brake performances relative to the linear spring as shown in figure 2.8*c* provides further insight why some stimuli result in actuators. Actuator solutions do not decrease the strain and stress at the end of the cycle relative to the zero-work performance, resulting in more energy being added rather than subtracted as for most brakes. Therefore, the SMA spring can increase power at specific points of the stride provided timely stimulus is applied, leading to a narrow set of solutions with net positive work.

2.4 Remarks

That skeletal muscle can achieve multifunctionality, transitioning between actuator, brake, or spring-like behavior, via changes to stimulus phase has been well established [16, 75, 78, 79]. Despite engineering efforts to mathematically characterizing biological systems capable of this multifunctionality [114], no study had heretofore reproduced this feature for an engineered system. We explored the capabilities of shape memory alloys as artificial muscles based on the similarity of the mechanical response of phase transformation with muscle fiber phenomenology [15]. Through experimental and numerical studies, we observed highly similar trends in work and power output in response to the phase offset by skeletal muscles and SMA-based artificial muscles. Both systems' work-loops were highly sensitive to the phase offset of the electrical input, indicating that energy output can be tailored during operation by shifting the stimulus phase.

Comparing the performance capabilities of skeletal muscle and shape memory alloy reveals these materials have a similar capacity for braking and actuation under different stimulus phases, despite substantial differences in actuation frequency. In Fig. 2.9, we provide a comparison of work-related properties of SMA and skeletal muscles that have been examined in the context of phase offset to timed stimuli: hawkmoth dorsolongitudinal [115], zebra finch pectoralis [116], and pigeon humerotriceps [75] muscles. Although the SMA specimens examined herein operated at slower strain rates than typical skeletal muscle, thin-wire preparations of SMA [89] allow higher frequency oscillations that approach the operating frequencies of skeletal muscles. The work and

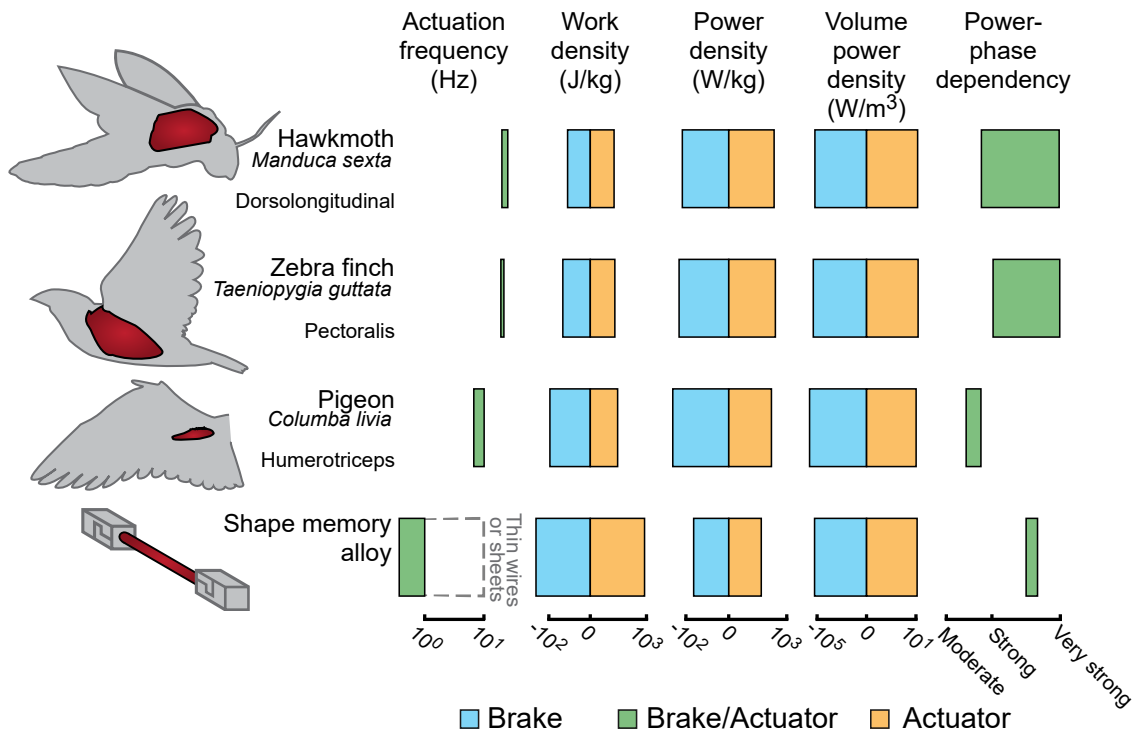


Figure 2.9: Muscles and shape memory alloys exhibit similar capability for braking and actuation under different stimulus phases, despite substantial differences in actuation frequency and power phase dependency. We compare the performance of shape memory alloy, including from a previous study of thin wire SMA [89], with those found in previous studies of muscles that also examined the effects of phase-offset to timed stimuli: hawkmoth dorsolongitudinal [115], zebra finch pectoralis [116], and pigeon humerothriceps [75] muscles. Hawkmoth frequency range attained from Willmot and Ellington [117]. To mitigate the influence of outliers, only the average of each cyclic experiment is considered.

power output of SMA shows as broad a range as that for skeletal muscles, albeit with a slightly narrower range of work density (J/kg) and a slightly broader range of power density (W/kg). Moreover, SMA shows as strong of a tunability via phase compared to the primary muscles that power flight in hawkmoths and birds, and a stronger relationship between power and phase than that in the pigeon's humerotriceps. Collectively, each of these materials affords control authority over functional output, which can be tuned via phase offset adjustments. What is especially promising is that shape memory alloys show a greater range of work per unit mass over studied ranges, indicating that SMA is a valuable material if adaptive changes to the magnitude of force or work production are the design target.

3. EXPERIMENTAL STUDY OF MORPHING WINGS*

3.1 Background

The allure of morphing wings is their potential to increase overall aircraft aerodynamic performance. Replacing traditional control surface actuators with morphing components can lead to a 6.5% increase in the lift-to-drag ratio relative to discrete surface actuators [8]. Furthermore, concepts that consider morphing wings in the design of glider wing sections have been predicted to increase the lift-to-drag ratio by approximately 30% [8]. However, technical limitations such as high energy requirements, manufacturing difficulties, and modeling complications have hindered the adoption of the concept. In the context of actuating morphing, shape memory alloys (SMAs) are an enabling material due to their high energy density [118]. The current state of the art for monolithic and composite SMA actuators offers the possibility to overcome previous shortcomings. Therefore, a novel composite SMA actuator and multiple wind-tunnel tested prototypes are developed to explore the morphing concept once again.

A conformal surface enables different outer mold lines (OMLs) that are favorable to specific flight conditions, allowing for non-traditional designs such as avian-inspired airfoils. Most bird wings are the result of natural selection where the evolutionary objectives include reduced energy consumption via aerodynamic efficiency [119]. The work of Bansmer *et al.* [119] and Liu *et al.* [120] developed avian-inspired airfoils based on the wing section geometry of ducks, seagulls, mergansers, teals, owls, and hawks. Although all species differ regarding aspect ratios, wingspan, and other geometric properties, all studies indicate that bird and insect wings have low-efficiency factors at high Reynolds numbers compared to conventional airfoils [121]. Therefore, the use of such wing geometries with high camber and maximum thickness so close to the leading edge is

*Reprinted with permission from: (1) "Skin-based camber morphing utilizing shape memory alloy composite actuators in a wind tunnel environment" by Leal, P., Stroud, H., Sheahan, E., Cabral, M., and Hartl, D., 2018, AIAA Scitech; (2) "Experimental and computational assessment of a shape memory alloy based morphing wing incorporating linear and non-linear control" by Leal, P., Goecks, V., White, T., Valasek, J., and Hartl, D., 2018, AIAA Scitech; and (3) "Experimental multiphysical characterization of an SMA driven, camber morphing owl wing section" by Stroud, H., Leal, P., and Hartl, D., 2018, SPIE.

unsuitable for the typical cruise velocity of modern aircraft. A method to change the OML during flight is necessary to enable avian wing use for a large aircraft designed for high-speed flight conditions. Because of these advantages, morphing capabilities are explored for avian-inspired platforms.

Previous experimental work from Strelec *et al.* [122] indicates that SMA wires can be utilized for morphing the OML. However, in that example, substantial structural compliance of the airfoil section was required to enable morphing, and the actuator mechanism occupied a large portion of the wing volume. Monolithic SMA actuators embedded at the wing skin minimizes the loss of internal volume while also maintaining wing rigidity. As the SMA wires are heated, the contraction of the actuators modifies the outer mold line of the wing; the new geometry will improve aerodynamic performance in other flight conditions. A similar concept is explored in this chapter, but composite actuators are utilized instead for various reasons.

This chapter intends to demonstrate the feasibility of morphing wings through experimental testing of various prototypes in multiple controlled environments, as shown in 3.1. Each experiment is performed to satisfy one of the following requirements:

- *Design flexibility* (section 3.2): the actuator embedded in the skin shall have a tailorable thermomechanical response for each application. There is a trade-off between generated force and displacement or input energy. Therefore, a tailorable composite actuator is proposed, manufactured, and tested. All following prototypes utilize versions of the composite actuator.
- *Controllability* (section 3.3): the mechanical response of the morphing wing has geometric and constitutive nonlinearities, posing a challenge to traditional control algorithms. A single-actuator, rapid prototype wing shall demonstrate controllability and robustness to environmental fluctuations. Two non-linear control strategies are developed.
- *Scalability* (section 3.4): the morphing wing concept shall function independently of the scale of the prototype, the number of actuators, the airfoil, and the material composition of

Requirement-driven exploration

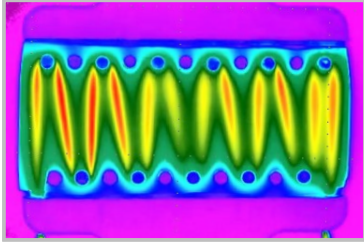
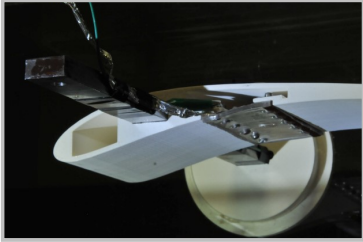
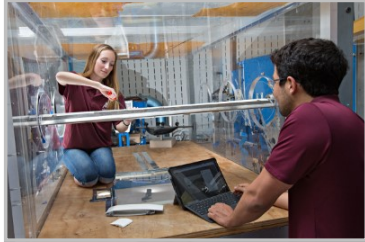
	1) Tunability	2) Controllability	3) Scalability
			
Platform:	Composite actuator	Single-actuator, 3D printed wing	Multi-actuator, composite wing
Environment:	Tensile frame	1' x 1' wind tunnel	6' x 4' wind tunnel
Sensors:	Load cell, IR camera, and thermocouple	Laser sensors and thermocouple	Load cells, IR camera, DIC cameras, laser sensor, pressure transducer, and thermocouples
Tests:	Block force test	Open- and closed-loop control for various conditions	Open-loop control for multiple cycles

Figure 3.1: Overview of requirements, prototypes, and tests. A different prototype and set of tests are utilized to demonstrate each of the following requirements: tunability, controllability, and scalability. A composite actuator concept is tested to demonstrate that the generated force from the SMA component can be tuned via simple geometric properties. Control laws are developed for a 3D printed prototype with an SMA actuator in a wind tunnel environment to demonstrate controllability. Finally, a 6-foot wing with 12 actuators is tested to demonstrate scalability.

the platform. Therefore, a 4 ft long composite avian-inspired wing that utilizes 12 actuators is manufactured, instrumented, and tested in a wind tunnel environment.

3.2 SMA composite actuator

A robust actuator is required to produce the desired morphing effect on the wing. This actuator must generate a force capable of inducing necessary displacements to achieve the desired OML. Other requirements for the actuators are that they must be easily attached to the wing itself, present a continuous and smooth OML, be easy to manufacture, and allow local tailoring of actuator thermomechanical properties. The use of elastomers embedded with SMA wires proposed by Peraza Hernandez *et al.* [57] enables design flexibility of generated force and power consumption to the local actuation needs. As a consequence of the inherent advantages of these composite actuators and morphing, the fabrication and implementation of the actuators depicted in Fig. 3.2 are assessed.

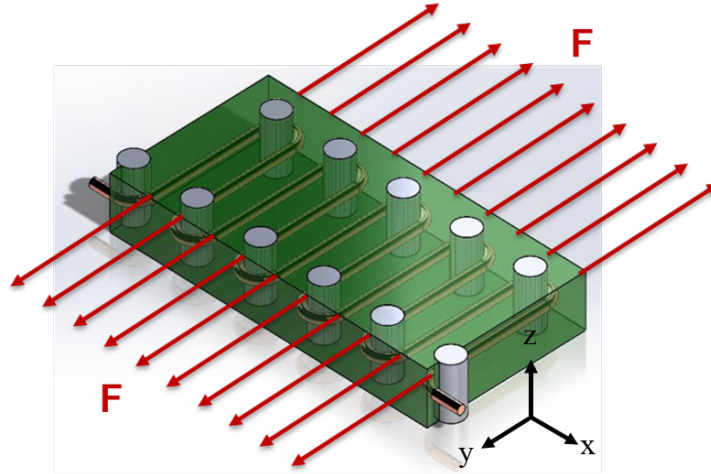


Figure 3.2: Concept of the composite SMA actuator.

Shape memory alloys have a high energy density and high actuation stress, but they also have poor energy efficiency, and thermal management can be difficult at the system level. Therefore, for applications that do not require high force, minimizing the volume of SMA while generating enough strain is essential [5]. Integrating an insulating matrix with SMA components to form a unique composite structure also decreases total actuator density and power requirements relative to a monolithic SMA component [118]. There is a great diversity of possible matrix materials for embedded SMA composites such as aluminum honeycomb [123], silicone [124], graphite-Epoxy [125], Epoxy-Kevlar [126, 127], Epoxy-glass [128], Polydimethylsiloxane (PDMS) [129], and bulk Epoxy [130, 131]. Therefore, an engineer has multiple options to select a material matrix that tailors actuator properties such as stiffness-to-weight ratio and thermal conductivity [118]. PDMS elastomer matrix does not hinder the generation of actuation strain but is not suitable for applications with high shearing forces [118]. Because the force requirements for the morphing wing are not high, PDMS is utilized as the matrix material.

There are a plethora of papers about SMA composite applications in the pursuit of variable natural frequencies [127, 128] and stiffness [131] of a structure. Similar to the current effort, some authors have explored the use of SMA composites for morphing. Villanueva *et al.* [124] embedded SMA wires into a jellyfish-inspired structure, where the matrix material was RTV silicone. Choi

et al. [130] explored the advantages of active buckling for an epoxy beam with an embedded SMA wire. Balta *et al.* [126] demonstrated the capabilities of strain-stabilizing feedback control for an Epoxy-Kevlar composite. Despite all previous work, this is the first time an active SMA composite is utilized for morphing the outer mold line (OML) of a wing.

3.2.1 Design and fabrication

The SMA composite actuator is manufactured using a mold casting method. The cast part is designed so that its outer surface is flush with the wing surface when installed and also features a method of attachment to the wing via dowel pins. A fixed (cf. Fig. 3.3a) and adjustable (cf. Fig. 3.3b) molds were designed and fabricated. The pins are inserted into the mold through a clearance fit hole, allowing them to be easily removed for cured part removal from the mold. SMA wire is cooled to ensure a complete martensite state before it is wrapped around the dowels, manually tensioned, and secured. Once secure, liquid PDMS is poured into the mold and set to cure as depicted in Fig. 3.3a, forming a compliant matrix that surrounds the wire tensile actuators. The curing process is accelerated by heating the casting in an oven at 60°C, a temperature that increases curing speed but is insufficient to actuate the SMA wires. The cured part is then released from the mold by depressing the dowels fully through the aluminum mold and separating the cured composite actuator from the mold. The final result is depicted in Fig. 3.4a. The manufactured actuator is stiff along the intended actuation direction and compliant in the transverse direction.

The active component composed of a nitinol wire embedded in a PDMS matrix is depicted in Fig. 3.4. The pre-tensioned SMA wire wraps around rows of metal dowels to form a web configuration that allows ease of manufacturing and installation. The pre-tensioning of the wires is necessary so that the individual segments are straightened, but the SMA is not detwinned. This concept also allows for design flexibility such that the force and deflection provided by the actuator vary based on the distance between dowels. Decreasing the distance between dowels leads to an increase in effective SMA cross-section within the actuator and increased generated force. On the other hand, increasing the distance between the dowels increases the in-plane angle between SMA wires, increasing the resultant actuator strain. This design also allows for ease of assembly in that

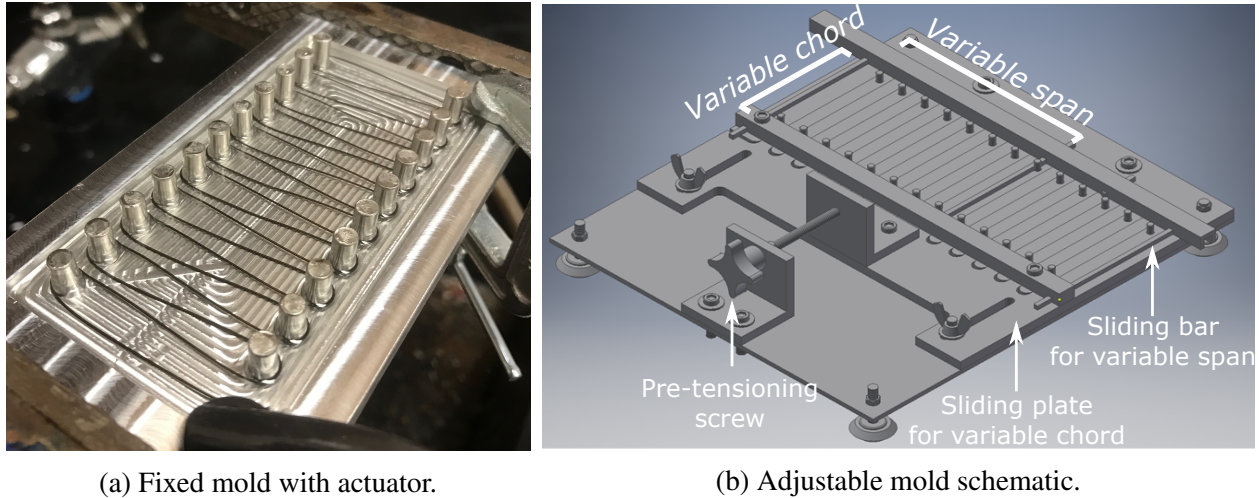


Figure 3.3: Molds to fabricate composite SMA actuator.

the wing has matching metal dowels to allow the actuator to be installed on the final morphing wing.

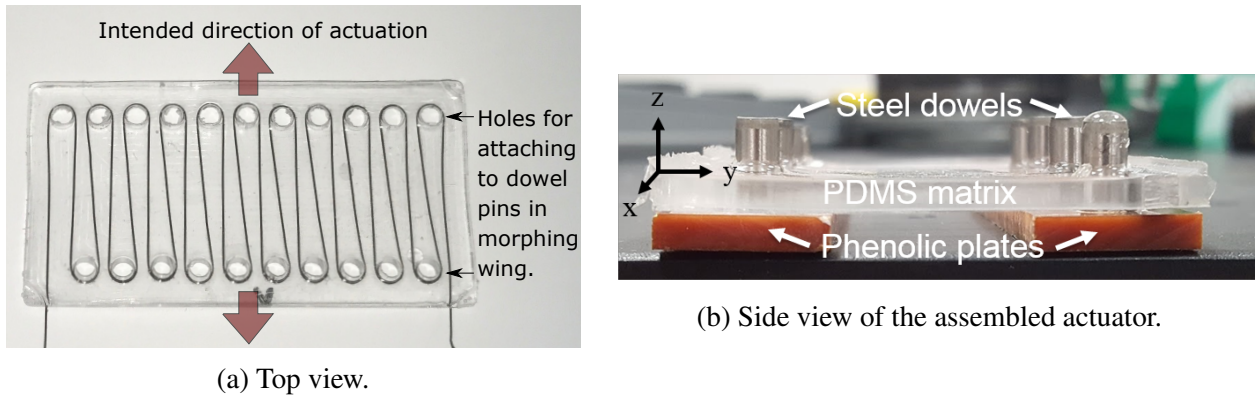


Figure 3.4: The fabricated composite SMA actuator.

3.2.2 Actuator characterization

Material characterization of the SMA wire, actuator, foam, and composite material was performed to determine the properties needed to develop a high-fidelity model of the wing for the structural analysis-driven design of the actuator configuration and placement. Differential scan-

ning calorimetry (DSC) was executed to estimate the zero stress transformation temperatures as M_f at 5.6°C, M_s at 29.9°C, A_s at 58.9°C, and A_f at 77.1°C. Because the final martensitic transformation temperature is below room temperature pre-stress, it is necessary to have an actuator with repeatable, cyclic stroke. The SMA wires were provided by SAES [132], have a 0.5 mm diameter and can generate up to 33 N when fully actuated. The tests consisted of heating the SMA to a temperature sufficient to ensure a fully austenitic phase, loading to the desired stress level (e.g., 100 MPa in Fig. 3.5a), cycling the temperature back down to martensite below M_f , and then back to well above A_f once again. The SMA wire was subjected to constant force tests, shown in Fig. 3.5a, as described in ASTM WK55902 [133]. Utilizing the SMA wire force as nominal, the total theoretical force and displacement of the composite actuator is determined by the number of dowels and the distance in between dowels, as shown in Fig. 3.5b. The selected dimensions for the composite actuators are 25.4 cm (10 in) in the spanwise direction and 20.2 cm (8 in) in the chordwise direction (e.g., SMA wire).

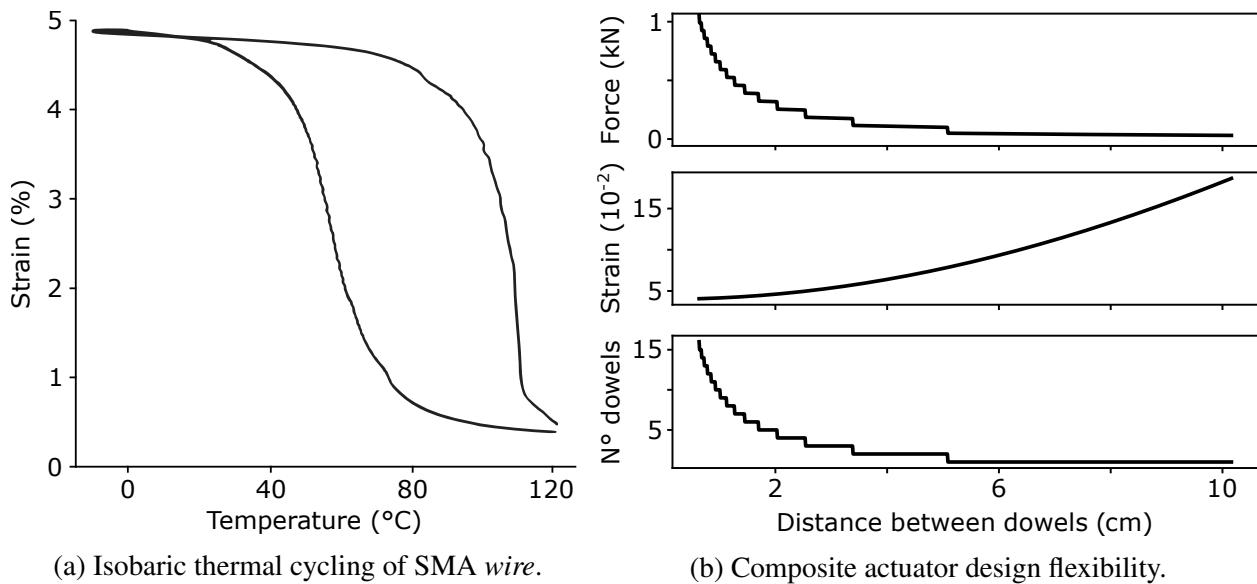
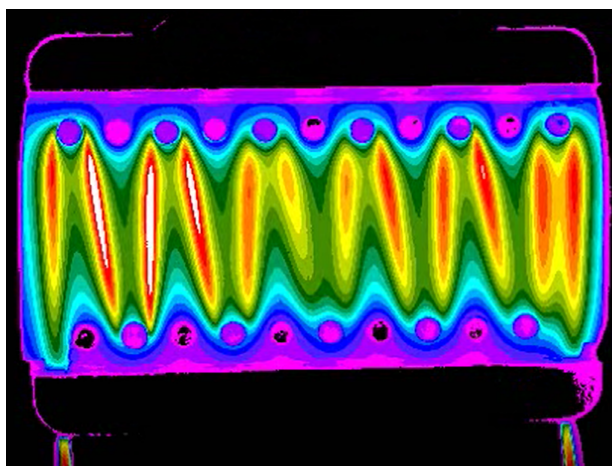


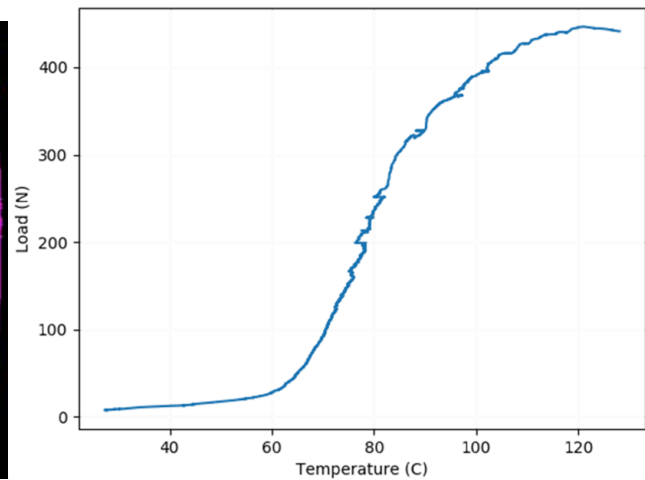
Figure 3.5: Force generated by SMA wire (experimental) and composite actuator (theoretical).

After performing thorough material characterization for the wire, it was important to test its

performance when embedded into the composite. Thus, the same tensile tests mentioned for the SMA wire were performed for an actuator. At the same stress level of 100 MPa and temperature ranges, the martensite and austenite effective Young's modulus were obtained ($E_M = 32.96$ GPa and $E_A = 67.18$ GPa). These results showed very little difference from those for the SMA wire. Further testing was undertaken to evaluate how much force each actuator could generate in similar conditions to the intended application. The actuator displacement was fixed, and the wires were heated via an electric current. The resultant temperature field can be observed via IR cameras as shown in Fig. 3.6a. The results at Fig. 3.6b indicate that even an actuator with a sparse amount of wire can generate more than 400 N.



(a) Infrared measurement of actuator surface.



(b) One heating cycle.

Figure 3.6: Blocked force testing.

3.3 Single-actuator platform

The morphing wing concept theory is first verified using one actuator before considering the multi-actuator design. This more straightforward platform serves to evaluate the ability of the actuators to morph the wing and to evaluate control strategies. Partial transformation, as opposed to full transformation between two OML configurations, allows morphing wings to be fully lever-

aged. Popov *et al.* [134] effectively explored the partial transformation of two SMA wires attached to a flexible wing surface in a wind tunnel environment to obtain distinct outer mold lines according to flight conditions. Consequently, a control scheme that enables morphing between several outer mold lines is desirable.

3.3.1 Fabrication of avian-inspired prototype

The avian-inspired wing considered utilizes the F0808 airfoil developed by Bansmer *et al.* [119] as depicted in Fig. 3.7. Compared to other airfoils such as the seagull-inspired SG04 [119] and SD7003 [135] airfoils, there is a larger range of angles of attack for which the hawk airfoil performs well, even up to 15° .

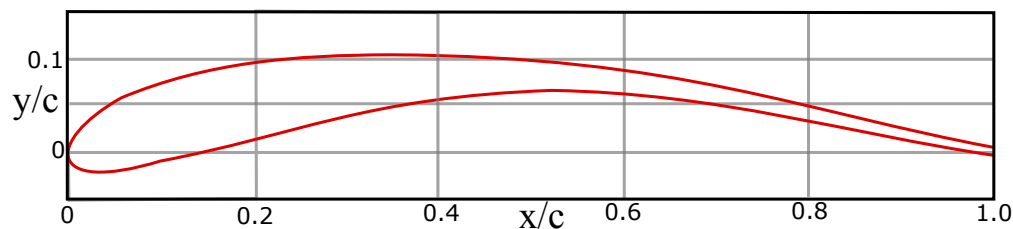


Figure 3.7: Hawk-inspired airfoil (F0808) [119].

The morphing wing section prototype is additively manufactured using Fused Filament Fabrication (FFF) and an Acrylonitrile butadiene styrene (ABS) filament. The modifications are made to accommodate for the actuator, as shown in Fig. 3.8. Part of the wing skin is removed to fit the actuator without creating a discontinuity at OML. Two cavities are placed to allow the passage of SMA wires to the voltage source, and two additional inner surfaces extend from the lower surface to attach the actuator to the wing structure. Dowel pins are driven into the inner surfaces, allowing the actuator to be mounted easily by pressing each of the molded holes over the dowel pins. Because FFF characteristically results in "ridging" along the build axis of the part, resulting in non-negligible surface roughness, some amount of post-processing was required in fabricating the wing. The surface is therefore sanded with the appropriate grit until a satisfactory finish was

achieved.

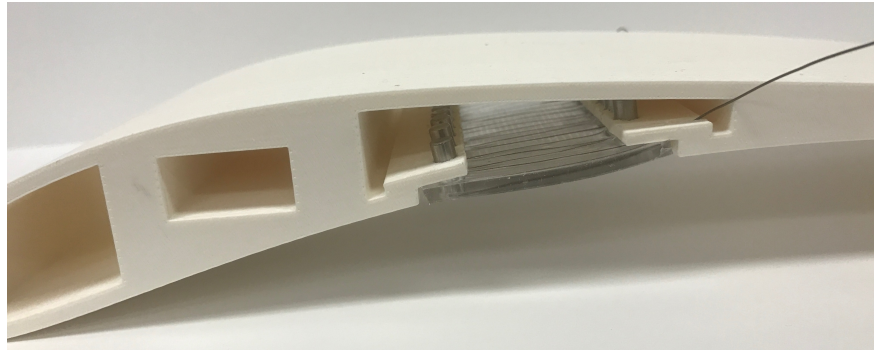


Figure 3.8: Prototype of avian wing with an SMA embedded actuator.

3.3.2 Controls

SMA actuators exhibit strong thermomechanical coupling and have a hysteresis during phase transformation. A model that fully describes the response of most SMA actuators does not have a simple analytical solution, and multiple experiments are necessary to calibrate it [89]. Consequently, most work related to the control of SMA actuators is experimental or simplifies material mechanics for a specific application. Velazquez and Pissaloux [136] demonstrated that for rapid heating, the hysteresis can be neglected, and linear algorithms such as P, PI, and PID are effective. Ikuta *et al.* [137] and Ma *et al.* [138] calibrated a electric resistance feedback controller for actuator systems utilizing SMA wires and springs via a linear simplification [137] or a neural network [138]. Moghadas *et al.* [139] showed that reinforcement learning can be used to control the bending angle of a self-folding sheet with SMA wires. The advantage of the last method is adaptability. Despite an initially expensive training process, the algorithm is capable of lifelong learning and adapting to changes. Reinforcement learning is explored because a morphing wing will likely be subject to unknown flight conditions, and SMA properties can change with time. Consequently, the two control algorithms, gain scheduled PID and reinforcement learning, are implemented for an SMA system that is exposed to aerodynamic pressure and forced convection.

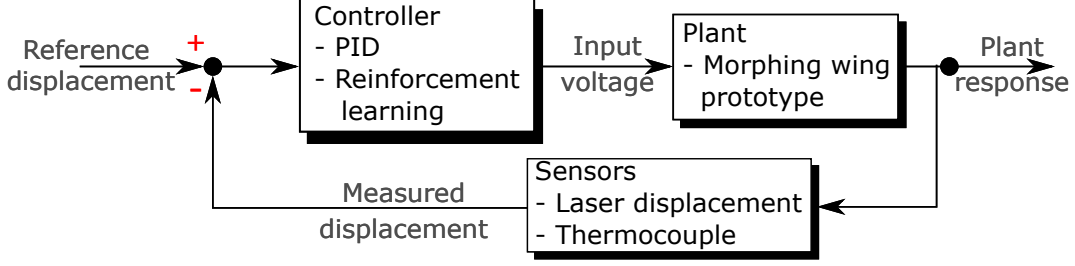


Figure 3.9: Control framework for the morphing wing.

As depicted in Fig. 3.9, after the measured displacement is processed through the PID controller, the resulting control output (i.e., a voltage) is applied via the voltage sources. The voltage supplied, or their lack of, stimulates the actuator, thus controlling the trailing edge displacement. The laser sensor then measures the new displacement to complete the feedback loop, and this process is continually repeated to attain the desired reference displacement.

3.3.2.1 PID

Proportional-integral-derivative (PID) controllers are the standard for linear feedback control algorithms. Many researchers have explored their use for shape memory alloys because of their simplicity and implementation in tools such as Matlab. Experimental work from Balta *et al.* [126] demonstrated that a PID controller suffices to maintain system equilibrium of SMA wires embedded in an epoxy matrix. If incorporated with a *gain scheduling*, a linear PID can be utilized for non-linear systems in various environments.

A conventional PID algorithm minimizes the error ϵ_b between a reference value (V_r) and a measured process variable (V_p), which correspond to the reference wing tip displacement and the measured wing tip displacement, respectively [140]. The resultant control input c is computed through LabVIEW's built-in Advanced PID algorithm that is of the form:

$$c(t) = K_c(V_r) \left(\epsilon_b(t) + \frac{1}{T_i} \int_0^t \epsilon_b(\tau) d\tau + T_d \frac{d\epsilon_b}{dt} \right), \quad (3.1)$$

where K_c is the controller gain, T_i is the integral time, T_d is the derivative time, and $\epsilon_b(t)$ is

calculated via

$$\epsilon_b(t) = (f_r V_r - V_p(t)) \frac{|f_r V_r - V_p(t)|}{V_{\text{range}}}, \quad (3.2)$$

where V_{range} is the reference value range, and f_r is the reference value factor. The default range of V_r was used, and the values of T_i and T_d were found empirically and fixed; however, K_c employs a form of gain scheduling [141] for which the reference value acts as the scheduling variable. Through experimentation and least-squares regression analysis, an approximated analytical relationship between the controller gain and reference value was discovered to be of the form:

$$K_c(V_r) = a^{bV_r}, \quad (3.3)$$

where a and b are coefficients determined by the least-squares regression. The difference between LabVIEW's Advanced PID Algorithm and the conventional PID algorithm is the reference value factor and linearity factor. The reference value factor, ranging from zero to one, enables the controller to be more adaptive to reference value response. A value of one maximizes the controller response to reference value changes, and a value of zero minimizes reference value changes to favor load-disturbance response. The linearity factor, ranging from zero to one (i.e., with a value of one generating linear control action), yields a non-linear controller gain that increases as the error between the reference value and the measured process variable increases. A reference value factor of one was sufficient to manage load disturbances. However, in actual flight conditions, a reference value factor less than one would be more appropriate to address the more substantial load disturbances from turbulence that are not as pronounced in wind tunnel conditions.

3.3.2.2 Reinforcement learning

Reinforcement learning, a sub-field of machine learning, considers a class of algorithms where an agent interacts with the environment to learn a policy that maps states to actions to maximize a numerical reward signal, as depicted in Fig. 3.10 [142]. The goal of the learning algorithm is to adapt the deep neural network parameters that represent the controller to successfully map the

input deflections to output voltages necessary to move from any arbitrary wing configuration to another. For the application considered, the agent is the controller, the reward is the aerodynamic performance, the environment is the morphing wing, states are the readings from the sensors (i.e., displacement), and actions are the voltage inputs for the actuators. The authors refer the reader to Sutton and Barto [142] for in-depth coverage of the topic.

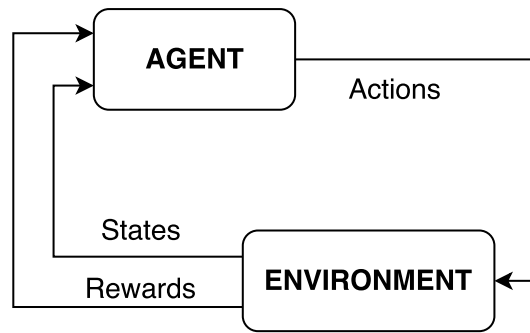


Figure 3.10: Overview of reinforcement learning algorithm.

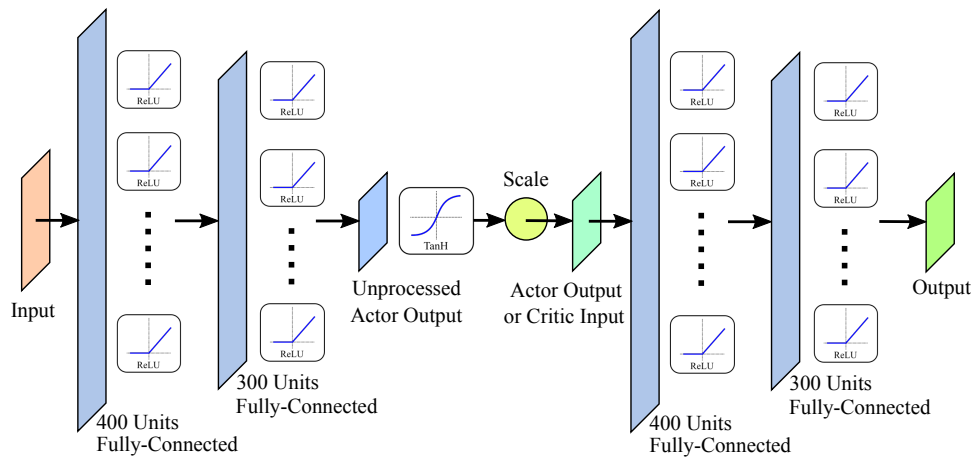


Figure 3.11: Deep neural network architecture that maps the current wing configuration to control inputs.

The network architecture consists of neurons organized as hidden layers. The neural network

implemented is depicted in Figure 3.11 which also shows how these neurons are connected between layers, the specific activation functions used after each layer output, and additional operations to transform the network output. The learning algorithm is evaluated based on the control effort required to morph, time to go from the initial to the final configuration, and the number of iterations required to train the learning algorithm to achieve the best performance.

3.3.3 Setup and instrumentation

Experiments were undertaken to evaluate the actuation of the fabricated prototype to demonstrate the capabilities of the SMA composite actuator and the morphing wing concept for open-loops. The prototype for the open-loop testing was fixed to an optic table via a grip at the quarter-chord location, as will be later shown in Fig. 3.13. The free SMA wire ends were connected to a voltage source. A laser displacement sensor and a ruler are also placed on the optic table to measure the trailing edge displacement.

The prototype in close-loop experiments is utilized in conjunction with a laser sensor to measure the trailing edge displacement, a thermocouple to measure the temperature of the SMA wire, and a voltage source to heat the SMA wire via Joule heating. Experimentation of the prototype is conducted in a 1' x 1' subsonic wind tunnel that is water-cooled to maintain an approximate constant stream temperature. A steel spar is fitted through to the rectangular cavity shown in Fig. 3.8 and mounted to two end caps inserted into the wind tunnel wall. It should be noted that the dowels holding the actuator are electrically isolated from the ABS, so current only flows through the wire and dowels. The mounted wing setup can be seen in Fig. 3.12. The thermocouple is wrapped in aluminum tape that acts as a grounded Faraday's Cage to eliminate the electromagnetic noise emitted by the wind tunnel electric motor. A single National Instruments Data Acquisition Module (DAQ) is employed to interface the hardware (e.g., the laser sensor and thermocouple) to the controller

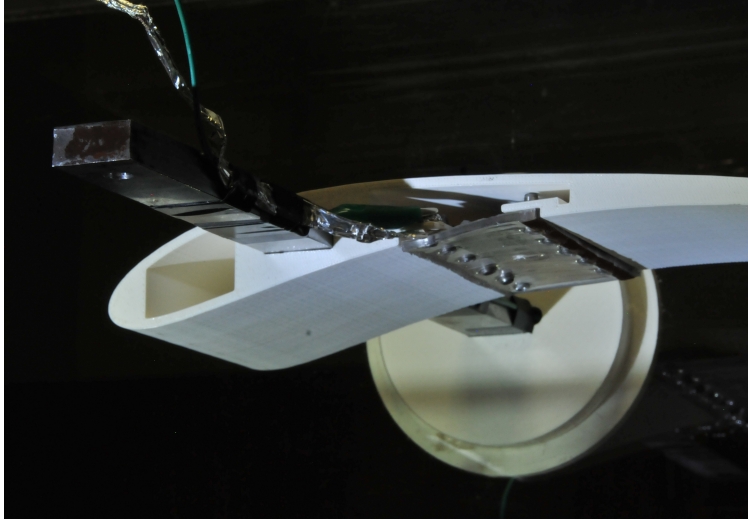
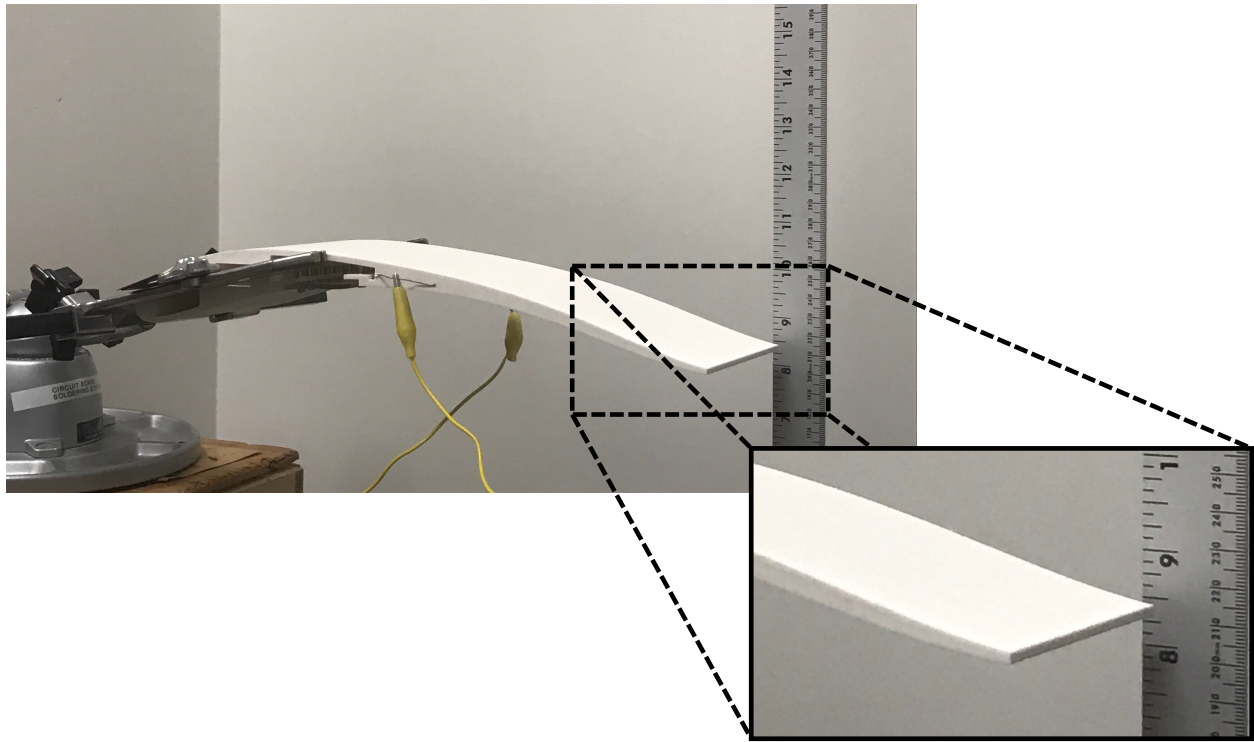


Figure 3.12: Single-actuator platform on 1' x 1' wind tunnel.

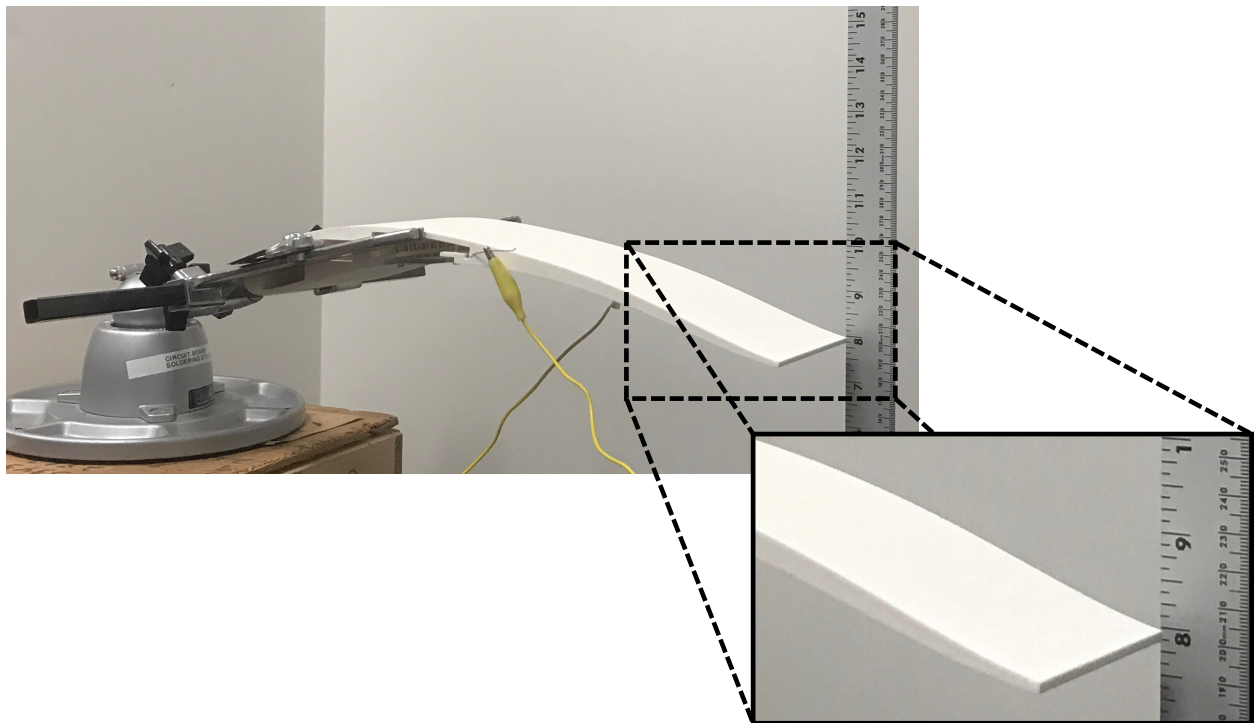
3.3.4 Results

3.3.4.1 *Open-loop*

The results obtained are depicted in Fig. 3.13. After four seconds with voltage applied, the original configuration in Fig. 3.13a morphs into the configuration in Fig. 3.13b. The obtained trailing edge displacement is 0.5 in (12.7 mm), which is 3.5% of the chord. After 40 seconds cooling down, the prototype recovers the initial configuration (c.f. Fig. 3.13). Compared to an equivalent monolithic actuator, the heat necessary for full actuation is considerably smaller because the SMA wires are a small fraction of the total actuator volume, and PDMS is a poor thermal conductor. As a result, most of the power utilized is used to heat the SMA wires. The cooling process was also considerably fast because SMA wires have a high area-to-volume ratio, and the wires are directly exposed to air at room temperature (the wires are located at the surface).



(a) Before actuation.



(b) After actuation.

Figure 3.13: Results of morphing wing utilizing SMA composite actuators.

3.3.4.2 Closed-loop: PID

As stated previously, robustness is a necessary aspect for algorithms implemented for control surfaces. Robustness is qualified herein as managing to achieve reference values under fluctuations in aerodynamic loading and convection under dynamic flow conditions. As such, gain scheduling is calibrated to guarantee that the PID control algorithm can perform various environmental conditions. Additionally, SMA behavior during a complete cycle of actuation is characterized by a unique hysteresis loop when comparing strain and temperature of the SMA, where strain in the scope of this topic can be equated to the trailing edge displacement. Suppose the PID controller is robust enough to manage the non-linearity of SMA. In that case, it is expected that the displacement-temperature curve from measured laser and thermocouple data also exhibits the hysteresis behavior. Fig. 3.14 shows that the constitutive relationship between displacement (i.e., strain) and temperature is upheld by demonstrating full and partial transformation cycles.

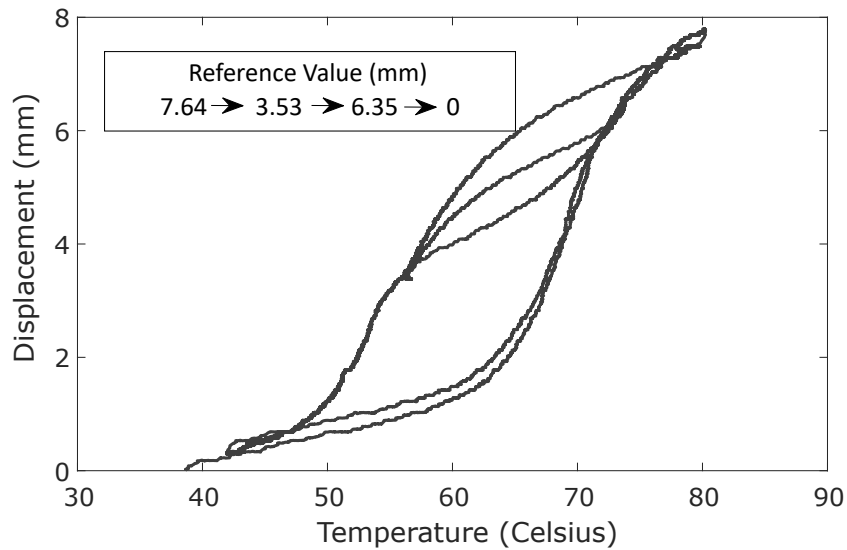


Figure 3.14: Voltage applied to maintain 10 mm deflection for varying velocities.

3.3.4.2.1 Disturbance Response The controller was set to hold a reference displacement of 10 mm for various flow velocities to demonstrate the PID's ability to manage perturbations through

voltage output adjustment. As shown in Fig. 3.15, the controller regulated the output voltage synchronous to changes in flow velocity. Though the measured displacement is not presented in the figure, the controller’s timely responsiveness to both changes in the convective state of the flow on the SMA and the lift-induced moment on the trailing edge enabled the actuator to maintain a constant displacement at the wingtip.

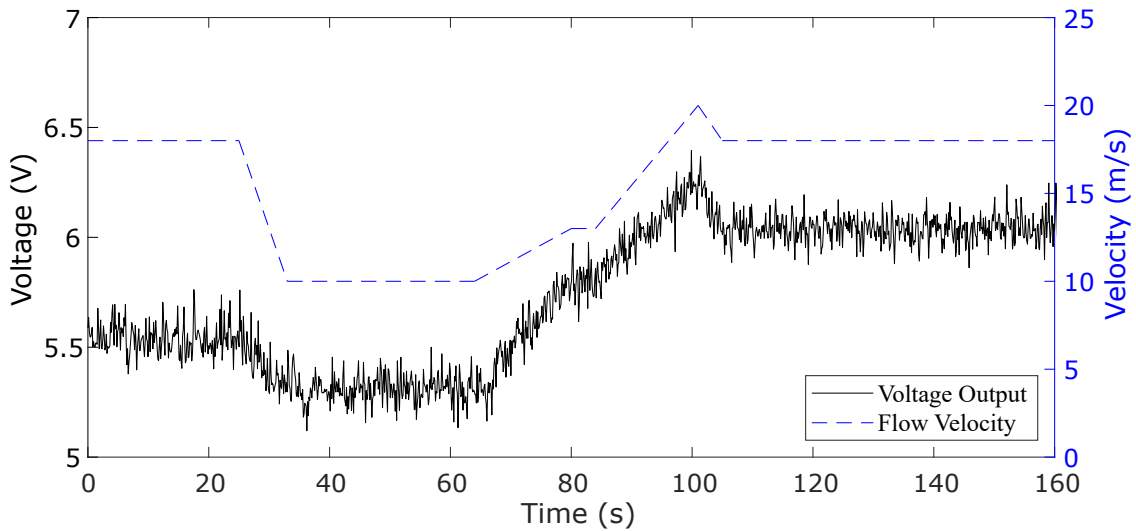


Figure 3.15: Output voltage response compared to the velocity profile.

3.3.4.2.2 Reference Value Response To further evaluate the robustness of the PID controller, the performance of the wing was analyzed at 0° , 4° , 8° , and 12° angles of attack at wind tunnel velocities of 15 m/s, 20 m/s, and 25 m/s. A five-sequence set of reference displacements was chosen using a random number generator constrained between 0 and 10 mm, eliminating bias from familiarity with controller performance. The results for reference values 8.3 mm, 6.9 mm, 3.3 mm, 9.3mm, and 1.7 mm are shown in Fig. 3.16. From these results, it is shown that the PID controller not only actuates to the reference displacements at each angle of attack and stream velocity but that the controller performs consistently across all test cases. The difference in performance is nearly indistinguishable. For minor changes, flow conditions have a negligible effect between test cases;

however, for more significant displacement decreases, the flow velocity does affect the amount of time required to reach the reference displacement.

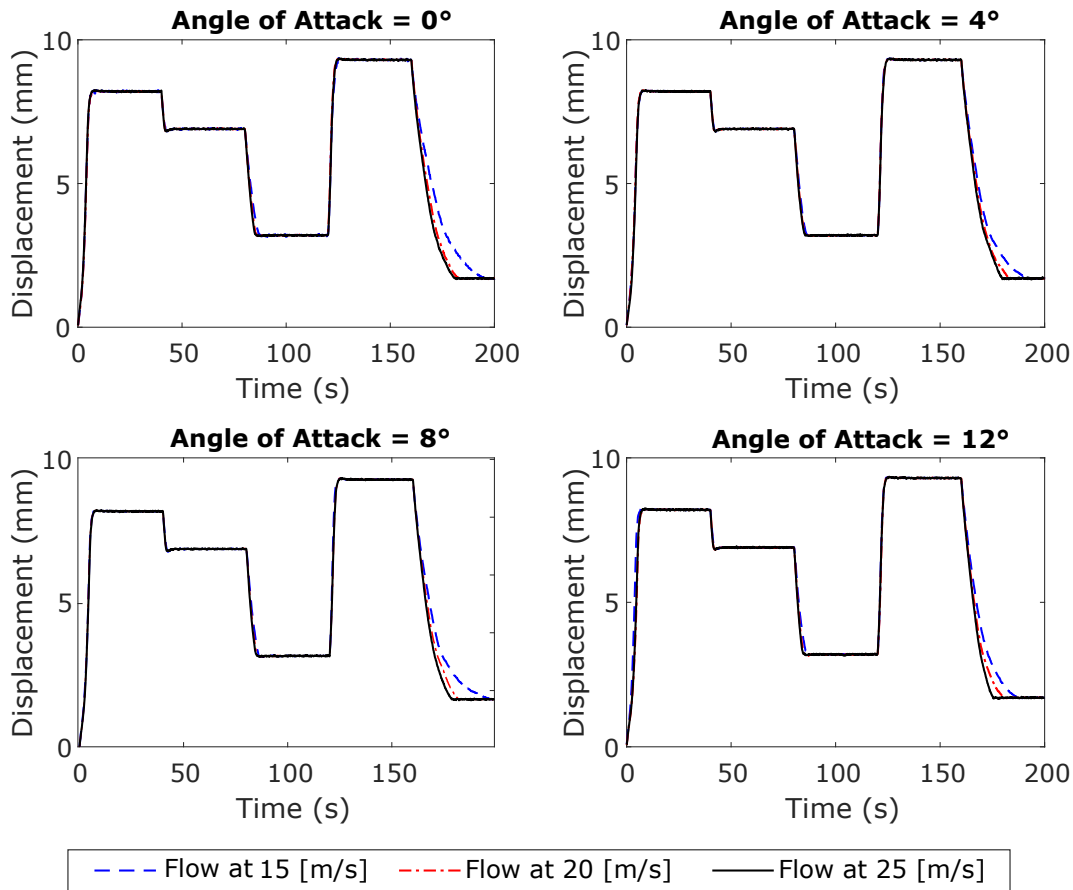


Figure 3.16: Wing tip displacement as a function of time for three flow velocities (15, 20, and 25 m/s) for four angles of attack (0° , 4° , 8° , and 12°).

Suppose there is no flow, as displayed in Fig. 3.17. In that case, displacement recovery requires significantly more time to attain the reference displacement, especially for the last sequence where the test was terminated because of the time necessary to reach a displacement of 0.28 mm. However, when comparing the camber morphing sequences, the response is nearly identical between flow and without flow, further presenting that the PID controller is robust within the actuator abilities scope. Additionally, it is also observed that introducing flow to the wing section, thus

increasing convection, inherently improves the overall reference displacement response.

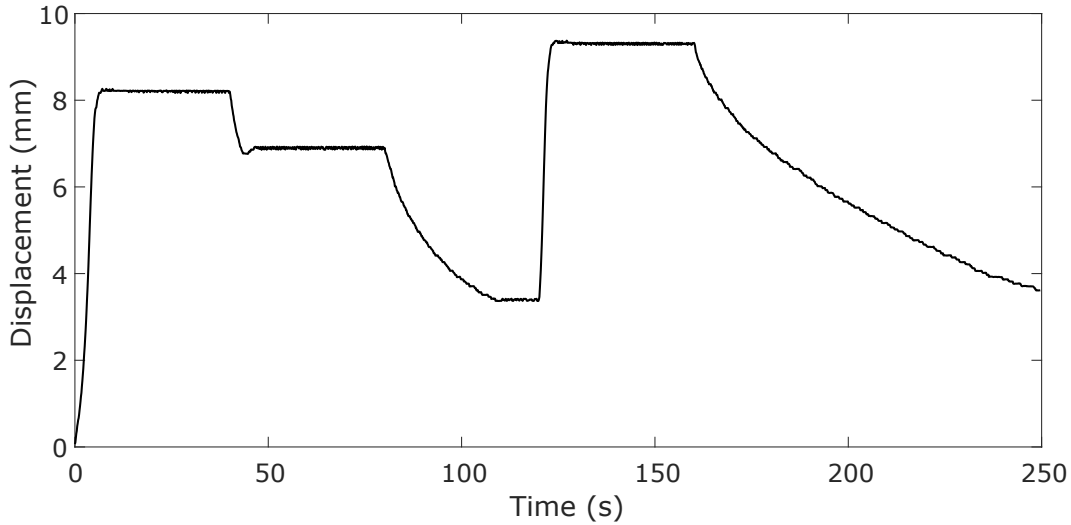


Figure 3.17: Wing tip displacement as a function of time without flow.

3.3.4.3 Closed-loop: reinforcement learning

The deep reinforcement learning algorithm was deployed to the hardware platform to train the neural network. The learning process is separated into episodes that can be considered as separate training sessions where the algorithm can change parameters between episodes. The algorithm ran in the wind tunnel for more than 300 episodes over two days. Every 200 seconds, the desired reference displacement is randomly changed, and the learning algorithm has to adapt the applied voltage to match the reference value. Results achieved after 100 episodes are shown in Fig. 3.18. Although the number of episodes was not sufficient to obtain equivalent performance of a PID, the trained policy is sufficient to approximately obtain the reference displacement.

Applying data-driven learning algorithms directly to hardware is challenging. Deep reinforcement learning algorithms are well known to depend heavily on multiple graphic and central processing units (GPUs and CPUs, respectively) [143–146] and training time on the order of days [143, 147] to achieve meaningful results. Simple continuous tasks (e.g., controlling a two-link

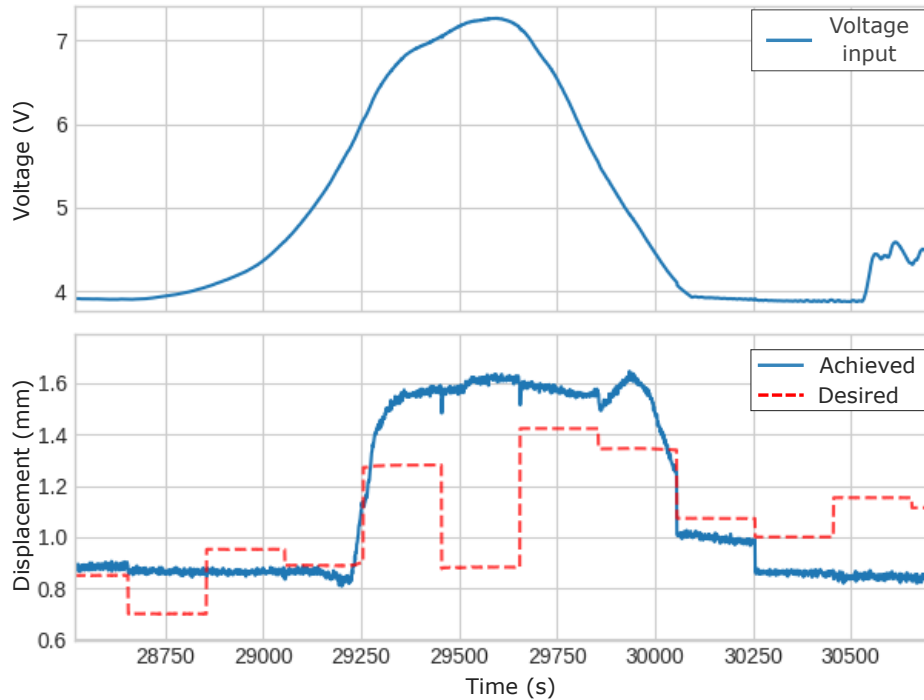


Figure 3.18: Training on the Wind Tunnel: solid blue lines show the true displacement and red dashed lines the desire shape.

robotic arm) require on average more than 2.5 million steps [148] and more complex operations (e.g., control of a humanoid robot or robots with multiple degrees of freedom), requires on average 25 million steps using different reinforcement learning algorithms [149]. Since it was infeasible to perform a wind tunnel test for weeks, it was desired to create a model with the same dynamics of the avian-inspired airfoil section actuated by an SMA wire under a wind tunnel test. A deep neural network was implemented using initial wind tunnel data to learn to approximate the hardware dynamics as a solution. Figure 3.19 shows the learned model compared to the truth model in terms of temperature and displacement.

The learning algorithm was also tested using a simulated wing model based on data collected from the wind tunnel. The algorithm ran for 1500 episodes. Every 200 time steps the commanded setpoint was randomly changed, and the learning algorithm had to adapt the applied voltage to match the commanded value. Figure 3.20 shows the controller performance after 900 and 1500 episodes of training. After 900 episodes, there is still a steady-state error between the current and

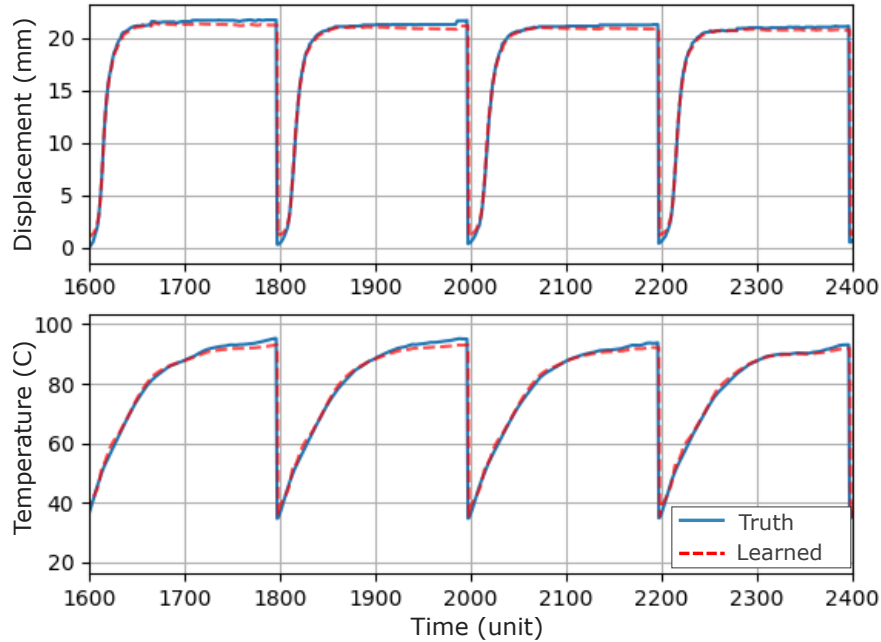


Figure 3.19: Displacement and temperature changes over time.

commanded displacement. After 1500 the deep reinforcement learning algorithm can complete the task multiple times in a row for different commanded morphing shapes.

A trade-off between both algorithms is expected; nevertheless, both controllers are expected to achieve the reference displacement for the experimental tests. As shown by the experimental results, the PID is robust enough to manage the aerodynamic loading and convection fluctuations on the SMA for tested cases. It can be stated that a PID controller is sufficient for controlling a wing section consisting of a single SMA composite actuator for the test conditions evaluated. As a more complex wing with multiple actuators is eventually addressed in a wind tunnel environment, the relevance of reinforcement learning over linear controllers will become evident.

3.4 Multi-actuator platform

The overall goal of this section is to demonstrate that the skin-embedded morphing wing concept is scalable. As such, a four-foot long camber morphing wing is designed, fabricated, and tested. A significant modification from the single-actuator platform is using a foam-core fiberglass skinned wing instead of a 3D printed plastic wing. The motivation behind this change is the sub-

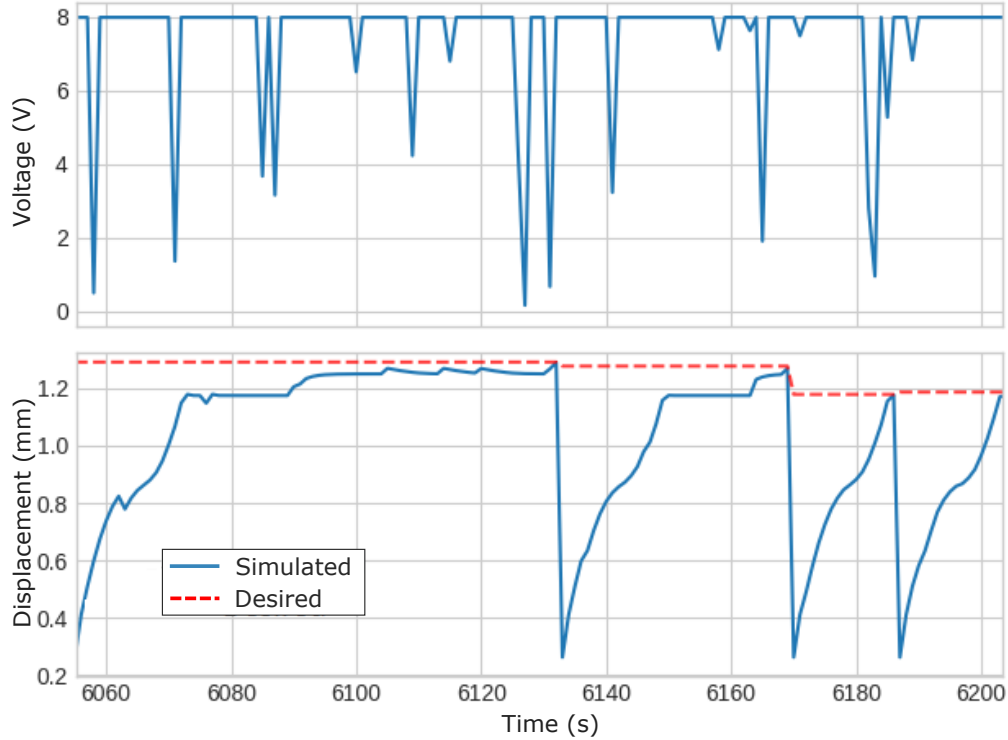


Figure 3.20: Training of Deep reinforcement learning controller performance after 1500 episodes.

stantial increase in the stiffness-to-weight ratio, which could enable implementation on a commercially available UAV. The structural components of the wing (i.e., all parts except the actuators and actuator attachment components) are comprised of six primary materials: cross-linked polyethylene foam, polystyrene foam, fiberglass-epoxy composite, aluminum, steel, and filler primer for a smooth, finished surface. The selected airfoil is from the wing cross-section of a Tawny owl in the gliding phase of flight obtained by a group of researchers from the Royal Veterinary College led by Dr. Richard Bomphrey [150]. The platform is tested in a wind tunnel environment for various operating conditions to demonstrate the repeatable aerodynamic performance change.

Traditional engineering sensors, such as strain gauges and thermocouples, are robust and reliable for most applications. However, these methods are intrusive (i.e., influence the system response) and provide information for only a localized region. For morphing wings, it is relevant to measure the displacement and temperature of the whole OML, not just a single point (e.g., trailing edge) [151] to fully explore the advantages of conformal shape change. A non-intrusive method is

necessary to obtain 3D continuous temperature and strain measurements in a wind tunnel environment. This section also utilizes state-of-the-art technology for the multiphysical characterization of an SMA actuated morphing wing under both thermomechanical and aerodynamic loads in a wind tunnel environment.

3.4.1 Material characterization

The foam core of the morphing wing must be resilient (i.e., must be able to absorb energy when it is deformed elastically and release that energy upon unloading) so that all generated strain is recovered while it must simultaneously be stiff. For this use, 2 lb cross-linked polyethylene is used, where the density for foam is defined for dimensions of a cube 12" x 12" x 12". According to compression tests, which is the standard characterization method for foam [152], the Young's modulus (assuming linear elasticity) is 305 kPa, and the material fully recovers all deformation up to 10% strain. The fiberglass composite was characterized as well. Four plies in a quasi-isotropic configuration were shaped into rectangular specimens at various orientations 0°, 45°, or 90°, cured, and mechanically evaluated. The 0° and 90° orientations did not show a concerning difference in their Young's modulus (14.7 GPa and 13.9 GPa). But the 45° orientation plies showed a much smaller Young's modulus of 4.7 GPa. Using the methodology from Glaser and Caccese [153], the shear modulus was calculated to be 1.4 GPa, assuming Poisson's Ratio of $\nu_{AB} = 0.21$ and $\nu_{BA} = 0.23$.

The chart in Fig. 3.21 summarizes all the mechanical properties of the materials used for fabricating the prototype. As can be seen, there is a significant difference in stiffness and density based on the function that the material components have for the morphing wing.

3.4.2 Design and fabrication

A finite element analysis (FEA) model is developed utilizing the material properties from the previous section and consists of two parts: the first part consists of hexahedral elements and represents the foam and the two SMA actuators on the bottom surface; the second part consists of shell elements and represents the quasi-isotropic four-layer fiberglass. The model is integrated into an

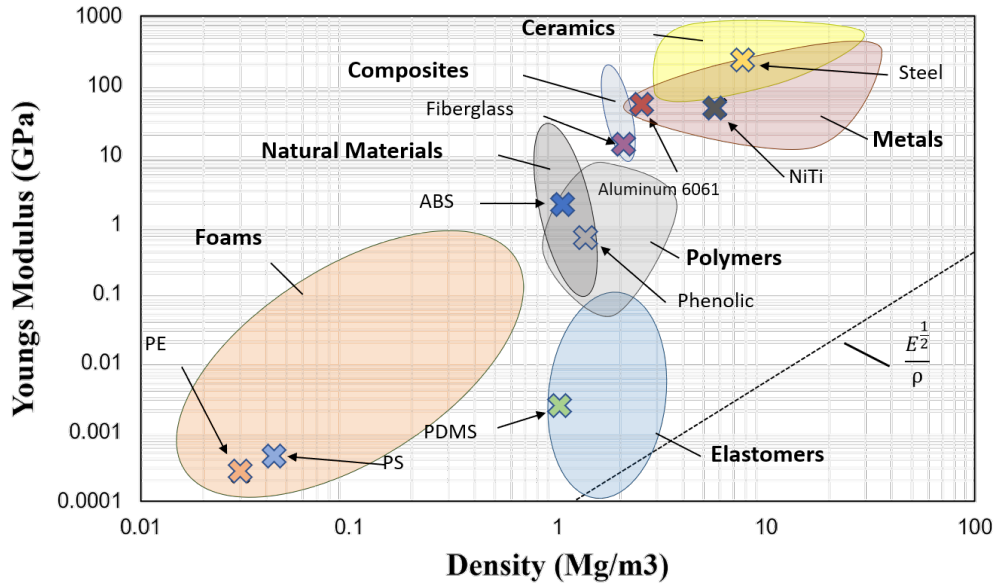


Figure 3.21: Ashby [154] chart for material utilized for wing manufacturing.

in-house developed Fluid-Structure Interaction (FSI) framework connecting Abaqus and Xfoil [8]. Since the SMA components generate more force than necessary to bend the composite wing, the constitutive model is simplified so that the actuator consistently achieves full stroke regardless of stress. The design variables of the model are the location and lengths of the two actuators. The objective metrics are the lift coefficient and the total length of the actuators, which are related to power consumption. The model is used in the Latin hypercube sampling strategy to explore the domain of feasible designs as depicted in Fig. 3.22. Because of manufacturing constraints, a non-dominant design was chosen instead of a solution on the Pareto frontier. In this context, the Pareto frontier is the set of solutions that minimize power and maximize lift. The selected configuration is represented in Fig. 3.23; it leads to a trailing edge displacement of 3.8 cm and lift coefficient equal to 2.35.

Regarding manufacturing, polyethylene foam (XLPE) and polystyrene are utilized for the foam core that gives the wing its shape. Except for the half-span section, all the foam core is XLPE because of its stiffness and resilience. Polystyrene is used for the half-span section for the pressure ports because it is easier to machine than XLPE. Two 23-inch long sections of XLPE are machined

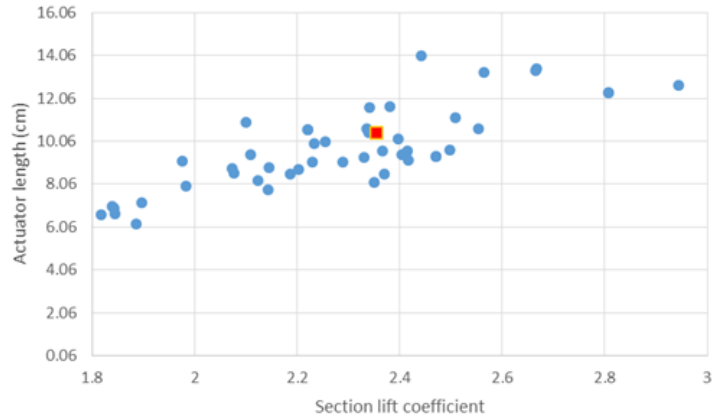


Figure 3.22: Explored design domain. Highlighted design is was manufactured.

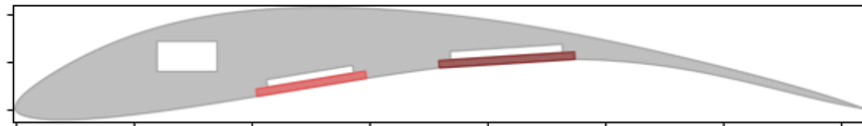


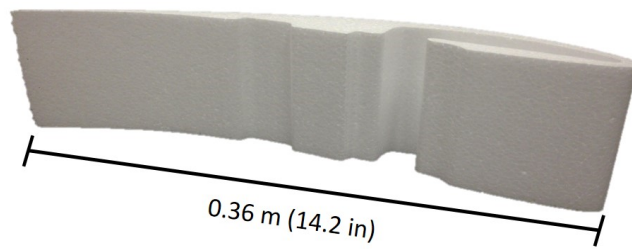
Figure 3.23: Selected design for morphing wing

using a CNC mill to the owl airfoil, as seen in Fig. 3.24a. A two-inch polystyrene section is hot-wired with a hollow interior at the leading edge to allow pressure tubes to be inserted easily into the assembled wing. Two machined aluminum fixtures are placed at the cutouts on the XLPE foam sections following the curvature of the leading edge; the fixtures serve as the attachment points between the wing and two eight-inch steel spars that connect the wing to the wind tunnel load cells.

The foams and the aluminum fixtures are epoxied together before four plies of fiberglass-epoxy composite in a $[0, +/-45, 90]$ orientation scheme are laid up and cured over the OML of the entire four-foot surface. The surface of the composite is filled and sanded successively with filler primer to ensure a smooth surface. Once the structural assembly is complete, the actuator elements are added to the wing, as shown in Fig. 3.25a. Sections of phenolic sheet are cut to size, drilled to reflect the dowel pattern of the actuators, and epoxied to the actuator-sized recesses on the lower surface of the wing. Actuator attachment was analyzed previously with the morphing wing section



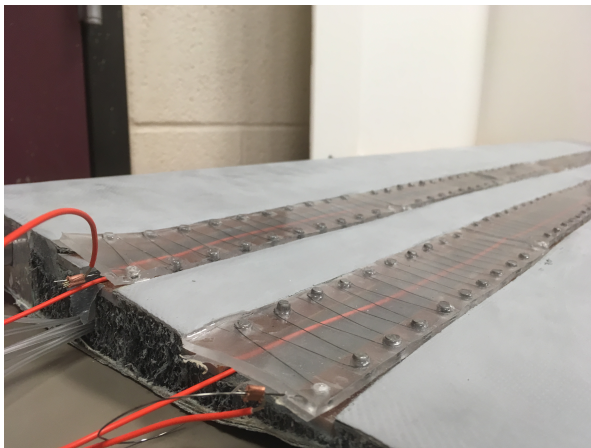
(a) 2lb XLPE machined foam core



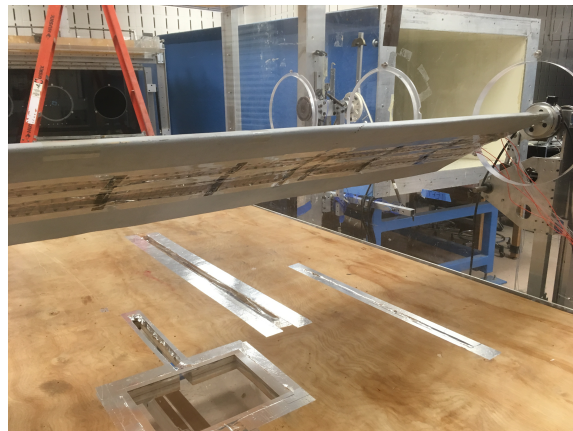
(b) Polystyrene hot-wired foam core

Figure 3.24: Machined foam core of morphing wing.

prototype, yielding a design that relied on dowel pins embedded in a recessed surface that allows the actuator to sit flush with the OML after applying speed tape as seen in Fig. 3.25b. This assembly is not only convenient for actuator attachment and removal but for actuator manufacturing as well, as the mold relies on identical dowels to secure the SMA wire inside the PDMS matrix.



(a) Fabricated actuators attached to the bottom surface of the wing



(b) Assembled wing in wind tunnel test section

Figure 3.25: Assembled morphing wing prototype.

Two rows of actuators run along the span of the lower surface with dimensions and positioning to obtain maximum trailing edge deflection with minimal power consumption. The actuation system consists of twelve actuators total. Sets of three actuators are wired in series, and the four sets are wired together in parallel. The actuators are connected to a voltage source and resistively heated. The current prototype allows for control of each set of actuators if separate voltage sources are used. However, for this experiment, only simple, simultaneous actuator heating achieved by a single voltage source is required.

3.4.3 Setup and instrumentation

As previously discussed, Digital Image Correlation (DIC) is utilized as a non-interferometric optical technique for gathering full-field strain and displacement data [155]. Moreover, the temperature field on the actuators is heterogeneous because of non-uniform heating and convection, and conventional methods for temperature data acquisition result only in local indication [156]. Therefore, infrared (IR) thermography is utilized in conjunction with the DIC to map the full field, thermomechanical description of the sample [157]. Simultaneously using both full-field measurement techniques enables a multiphysical profile to be developed for a section and allows for determination and visualization of correlations between temperature variation and regional deflection in multiple directions. For experiments utilizing DIC, the sample must have a visible, high-contrast pattern that the system can track, known as a speckle pattern; therefore, a new coating with a speckled pattern is applied at the surface for thermomechanical tests as shown in Fig. 3.26.

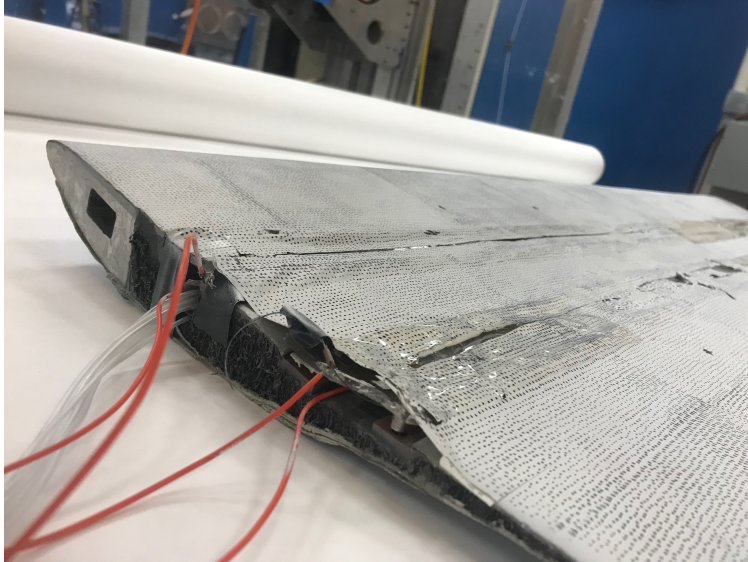


Figure 3.26: Wing with applied speckle pattern.

This experiment was performed in a 3' x 4' test section of a low speed wind tunnel. Fig. 3.27 depicts a 2D schematic of the instruments utilized and relative locations within the test setup.

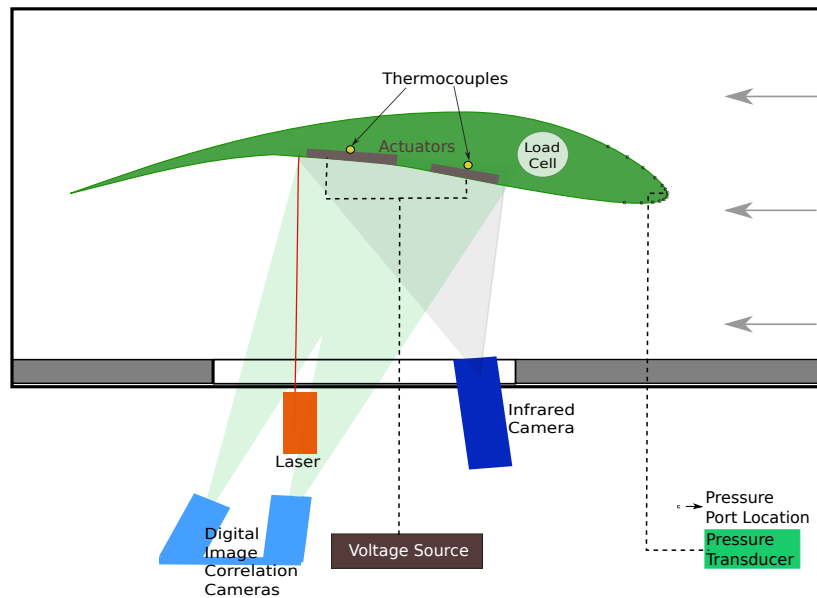


Figure 3.27: Schematic of test setup (not to scale).

The wing is mounted to two three-axis load cells to collect aerodynamic loading data during the test, and a pressure transducer acquires pressure data at the surface of the wing in 13 discrete locations at half span. To obtain the surface temperature of the actuator, two thermocouples are attached to each actuator at the surface not exposed to flow. A FLIR A655sc infrared camera mounted and sealed into the floor of the tunnel views both actuators and obtains thermal data through a hole sized to the camera lens. Two Correlated Solutions Grasshopper3 GS3-U3-23S6M DIC cameras equipped with Nikon Nikkor 60 mm lenses view the lower surface of the wing in stereo through a plexiglass section in the floor of the tunnel for DIC. A Keyence Intelligent-L laser sensor is directed at the lower surface of the wing at the aft-most point of the field of view of the cameras in order to correlate one-dimensional displacement data with the three-dimensional data acquired from the DIC. Field of view was maximized while working within space constraints beneath the tunnel, and the final area visible to the system was 5 " x 7.5 ". Since the chord of the wing is larger than the possible field of view length, the area of focus is the area that encompasses the forward and aft actuators and includes the closest possible point to the trailing edge. To instigate actuation, a voltage source is connected to the actuators. The maximum voltage and current outputs of this voltage source are 40 V and 12 A respectively.

3.4.4 Results

To fully evaluate the fabricate platform, the following quantitative characterizations are undertaken: aerodynamic characterization (experimental and numerical) of the wing without morphing in Section 3.4.4.1, wind tunnel testing of the morphing wing for a single actuation cycle in Section 3.4.4.2, wind tunnel testing of the morphing wing for multiple actuation cycles in Section 3.4.4.3, and thermomechanical characterization of the lower OML during morphing in Section 3.4.4.4.

3.4.4.1 Aerodynamics: non-morphing

The platform is initially tested in a wind tunnel without actuation (Fig. 3.25b) and compared to numerical fluid analysis to verify that the fabricated prototype has the intended aerodynamic

properties of the owl wing. The implemented low-fidelity potential fluid solver Xfoil [158] considers inviscid flow coupled with a built-in semi-empirical correction for viscous effects. Although the model is of lower fidelity and limited to conditions prior to stall, it has a low computational cost and is a robust tool for preliminary design. For high fidelity results, a Reynolds-averaged Navier-Stokes (RANS) simulation utilizing CRADLE [159] is employed. In each case, the boundary conditions used are: inlet fluid velocity at 15, 23, or 30 m/s, static pressure at the outlet is zero, and no-slip conditions on airfoil walls. A $k-\omega$ turbulence model is used with a time step of 0.02 milliseconds, air density of 0.9398 kg/m^3 , and dynamic viscosity $1.6922 \text{ Pa}\cdot\text{s}$. The fluid dimensions are 11×8 chords. The mesh consists of three mesh regions to refine the mesh near the airfoil while enabling a coarse mesh far from the airfoil. In total, 665,052 elements were utilized.

The lift coefficient results from the RANS, Xfoil, and wind tunnel experiments for wind velocities 15, 23, and 30 m/s are depicted in Fig. 3.28. All methods obtained similar lift curves demonstrating that the fabricated prototype, despite manufacturing uncertainties, has a similar performance to expected.

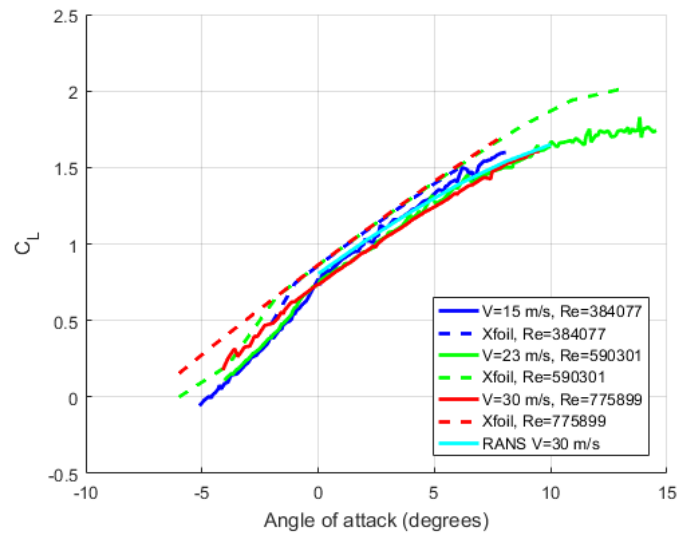


Figure 3.28: Avian wing prototype and obtained results in wind tunnel: Lift coefficient v. angle of attack.

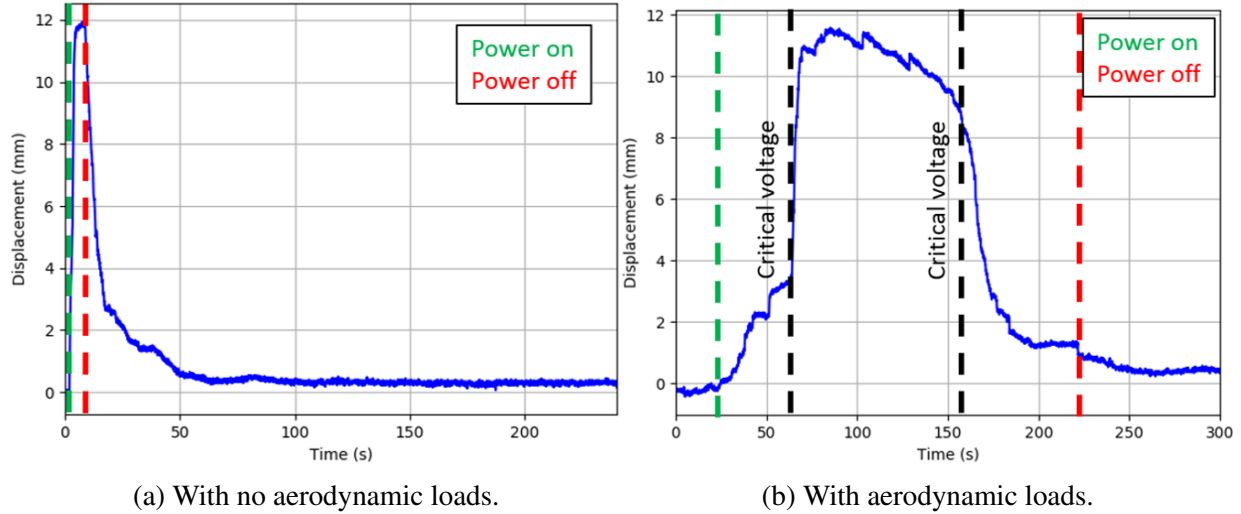
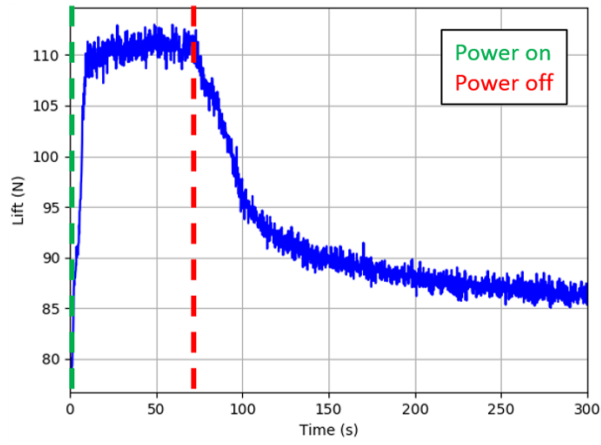


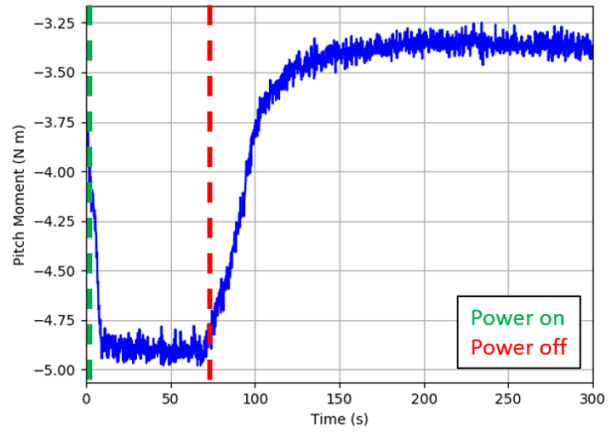
Figure 3.29: Trailing edge displacement of morphing wing.

3.4.4.2 Aerodynamics: single actuation cycle

An initial actuation cycle was done before turning the wind tunnel on and is depicted in Fig. 3.29a. The trailing edge of the wing displaced 12 mm (32% of the theoretical capacity) when actuated and fully recovered during cooling. However, the cooling path is much slower than heating because Joule heating is intrinsically a faster phenomenon than convection. With the wind tunnel at an average speed of 16 m/s, the displacement is marginally smaller than the wind-off actuation, but the actuation authority is increased as depicted in Fig. 3.29b. It should be noted that there are critical voltages between voltage bounds at which the rate of actuation rapidly increases or decreases, as denoted in Fig. 3.29b. The lift and pitching moment coefficients during the actuation cycle are depicted in Fig. 3.30. As the wing morphs, camber increases; consequently, lift and pitching moments increase 40% and 30% in magnitude. Finally, the pressure distributions before and after morphing are measured (c.f. Fig. 3.31). Overall, the morphed, highly cambered airfoil has higher pressure magnitude in all of the pressure ports installed. In conclusion, considerable camber morphing of a composite wing is not only feasible but yields significant changes in aerodynamic performance.



(a) Lift.



(b) Pitching Moment.

Figure 3.30: Aerodynamic metrics for morphing wing.

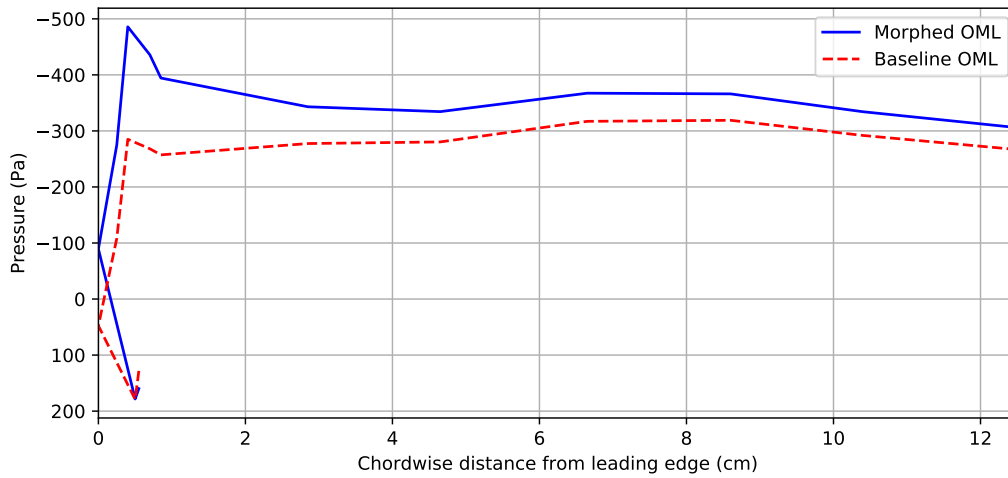


Figure 3.31: Pressure distribution before and after morphing.

3.4.4.3 Aerodynamics: multiple actuation cycles

After further improvements of the skin roughness and actuator improvements, more tests were performed to evaluate performance robustness for multiple actuation cycles. Even minor modifications of the airfoil can lead to significant variations in metrics such as lift, drag, and pitching moment. The morphing wing actuators undergo four actuation cycles preceded by a normalizing cycle. Each cycle consists of 150 seconds of the voltage at 40 V and 450 seconds with zero voltage. The data collected from the laser sensor, Fig. 3.32, shows that a 4 mm displacement is generated when voltage is applied. A negative deflection for the reference system implies a downwards deflection of the point of interest. A positive deflection indicates upwards deflections usually caused by aerodynamic loads. After the initial voltage application, the system only has slight variations in deflection during heating. Once the voltage is turned off, convection and aeroelastic effects dominate, eventually recovering to a displacement slightly above the previous reference displacement. This increase is related to residual deformation of the compliant wing structure.

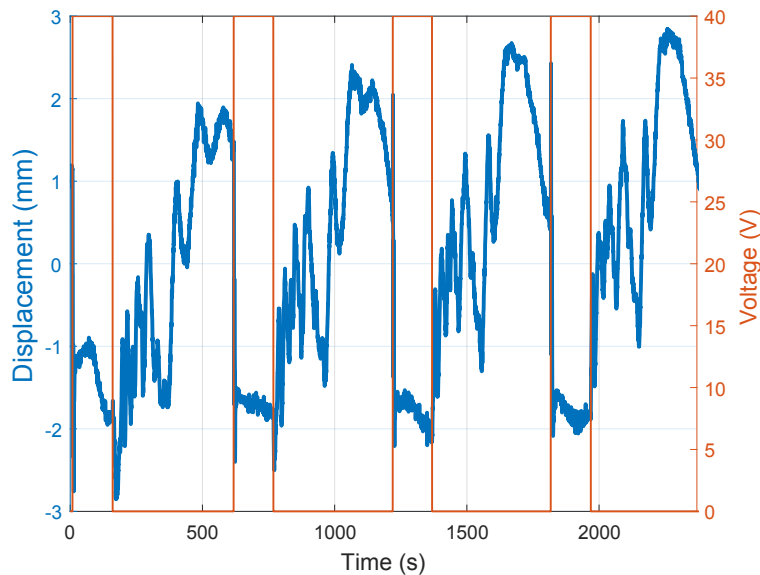


Figure 3.32: Transient signal for displacement and voltage under flow conditions.

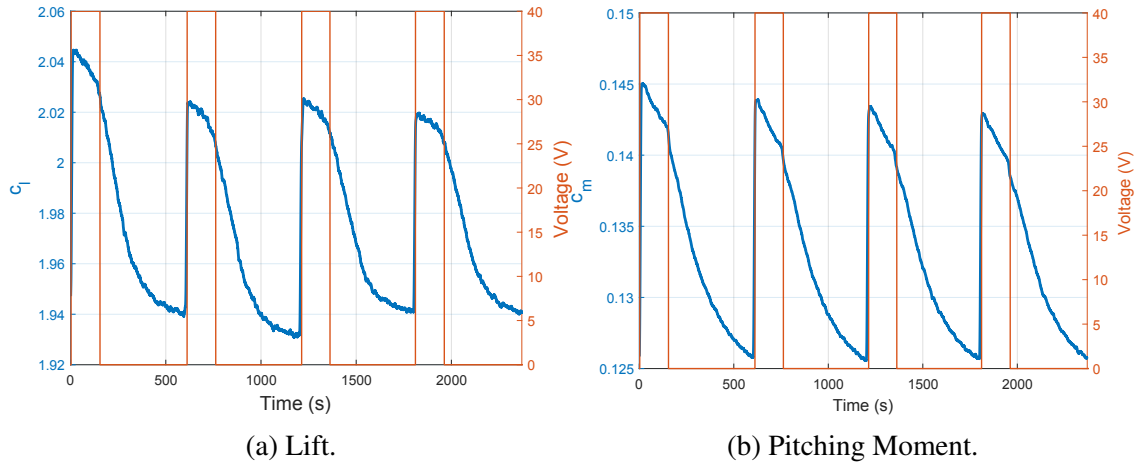


Figure 3.33: Transient response for aerodynamic metrics.

The lift and pitching moment coefficients, Figs. 3.33a and 3.33b, show that a consistent change in aerodynamic performance is achieved via morphing. The partial transformation of the composite actuators generated a 5% lift increase and 12% pitching moment increase. Another relevant aerodynamic metric is the pressure distributions showed in Fig. 3.34. As expected, the magnitude of the measured pressures increased for locations on the top surface. Because the generated deformations are smaller than for the single cycle test, the magnitude of the pressure distribution of the morphed configuration is smaller than Fig 3.31. The pressure distributions for all cycles are similar, indicating that similar aerodynamic properties obtained before and after heating.

3.4.4.4 Thermomechanical Results

While single-point data acquisition helps characterize thermomechanical interactions, this method does not provide the full field description of an area of interest. DIC and IR imagery shows properties of the whole surface of a sample and can validate these single-point measurements. In a no-flow environment, laser extensometer readings show the aft-most point in the field of view deflecting 4.5 mm when fully actuated. DIC deflection data reflects comparable results for the same point of interest, with deflection of the same point measured at 4.1 mm (an 8% difference); a full wind off, heating and cooling cycle is depicted in Fig. 3.35.

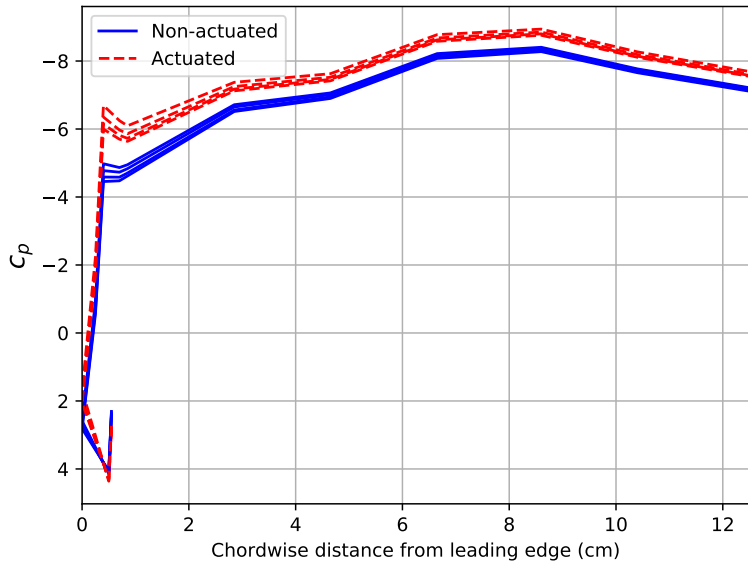


Figure 3.34: Pressure distribution of the actuated and non-actuated configurations during cycling.

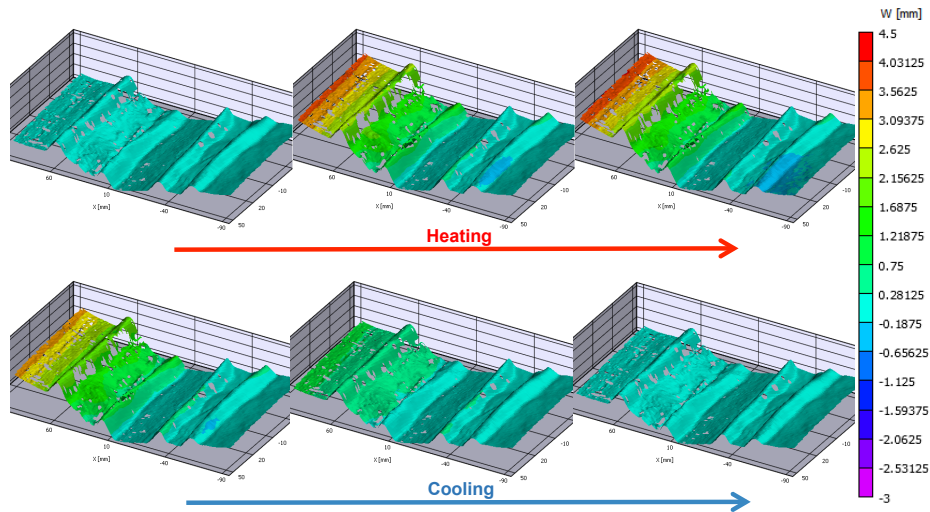


Figure 3.35: Deflection contour mapped onto shape data from DIC imaging of a heating and cooling cycle with no flow.

The temperature contours are mapped to the wing shape providing a 3D view of the displacement and temperature fields. As the wing morphs, a full-field description of thermal activity allows for a greater understanding of the resulting shape change than single-point measurements. Fig. 3.36

shows the temperature contour mapped onto the wing shape at the same points in time as the deflection mapping in Fig. 3.35. From this imagery, the temperature differential between the SMA wires and the rest of the wing can be seen as well as the disparity in actuator heating resulting from the difference in actuator size. Actuator sizes vary according to chord location as previously shown in Fig. 3.23. Because the actuators with the greater chord have more SMA wire and therefore more resistance per actuator, the current the aft actuators are exposed to is lower and less heat is generated.

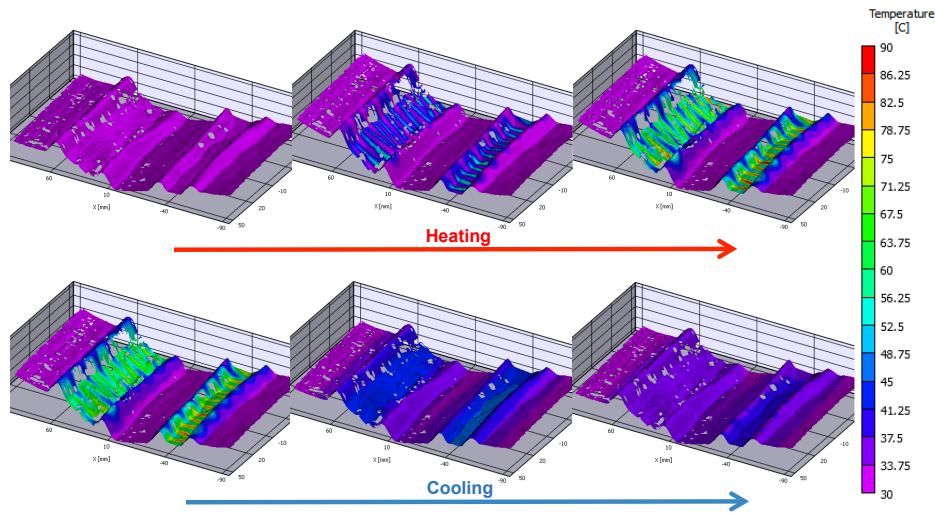


Figure 3.36: Mapped IR contour onto shape data from DIC imaging of a heating and cooling cycle with no flow.

The actuation of the wing is voltage-limited. Therefore, the wing does not actuate to its total capacity; this is especially relevant for the wind on condition as the flow generates pitching moments that hinder morphing, and more energy is dissipated via forced convection. Fig. 3.37 depicts the temperature mapping for the wing as exposed to the airflow of 15 m/s. The disparity in actuator heating is more visible in these images.

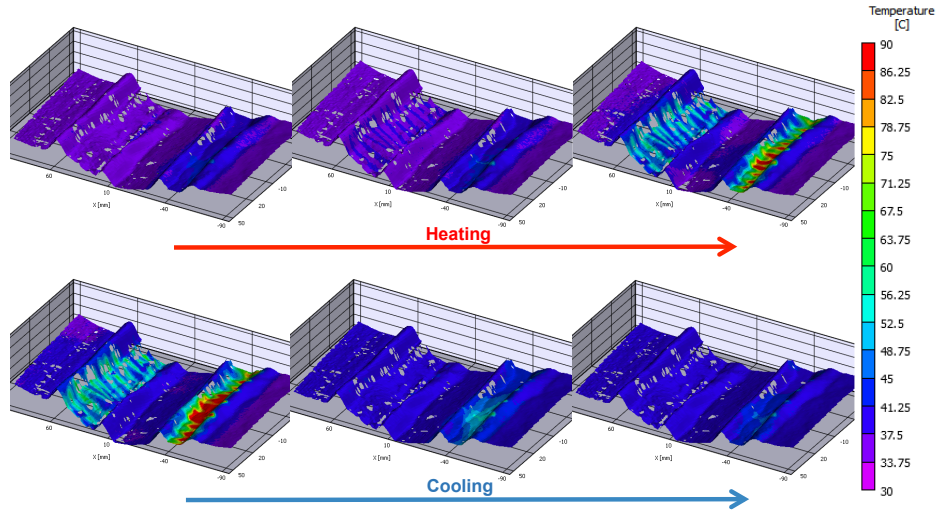


Figure 3.37: Mapped IR contour onto shape data from DIC imaging of a heating and cooling cycle with flow (third cycle).

Because the temperature profile is not uniform according to Fig. 3.37, quantitatively depicting temperature for points along the chord is essential. While thermocouple data shows the same temperature differential, without the IR camera validation, this could be attributed to sensor placement sensitivity. However, the full-field view of cooling and heating cycles in Fig. 3.38 shows that the actuators did achieve different temperatures at the maximum voltage.

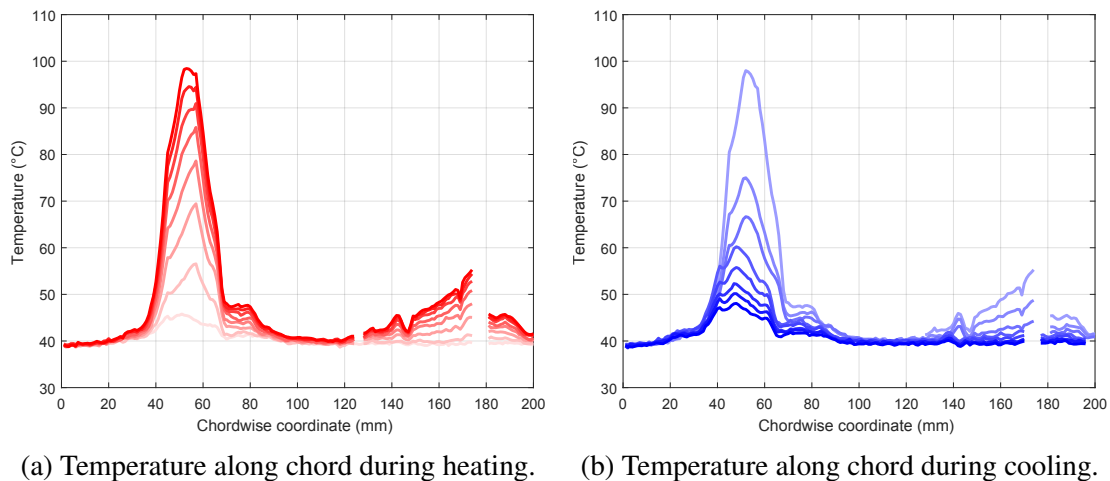


Figure 3.38: Temperature along a chordwise slice during heating and cooling.

3.5 Remarks

The concept of a morphing wing with composite SMA actuators embedded in the skin is proposed, modeled, fabricated, and tested as an alternative to increasing aircraft aerodynamic performance. Various prototypes were manufactured to demonstrate design flexibility, controllability, and scalability of the actuator implementation.

The concept of an SMA actuated skin-based morphing structure was initially validated with an additively manufactured, single-actuator section, achieving a 1.3 cm trailing edge deflection, corresponding to 3.5% of the chord. The aerodynamic benefits of morphing structures were further tested with a four-foot, composite morphing section with optimized actuator location maximizing trailing edge deflection with minimal power consumption. Wind tunnel experiments showed that with partial transformation (32% of the theoretical maximum trailing edge displacement) there was a 40% increase in lift compared to the original OML.

Two types of controllers, PID and deep reinforcement learning, are explored on the single-actuator wing prototype. The PID with gain scheduling is sufficiently robust to manage the aerodynamic loading and convection fluctuations on the SMA for tested cases. While the PID controller is sufficient for a wing section consisting of a single SMA composite actuator, the relevance of reinforcement learning over linear controllers is evident as a wing with multiple actuators.

Further testing of the four-foot span composite morphing wing is performed for multiple cycles and 3D DIC and IR cameras to obtain the thermomechanical properties in situ. The results obtained demonstrate that considerable change in aerodynamic coefficients, 5% for lift and 12% for pitching moment, are achieved with small deflections. The peak magnitude of the pressure coefficients also increases along the chord. Repeated actuation of the system showed that aerodynamic gains are consistent throughout cycles. Displacement data obtained using DIC corresponded to traditional methods within 8%, and full-field temperature readings obtained through IR thermography are mapped to the corresponding shape. The coupled 3D DIC and IR measurements enabled the visualization of manufacturing errors, the temperature profile, and a local correlation between displacement and temperature.

4. PARAMETERIZATION OF MULTI-COMPONENT AIRCRAFT ASSEMBLY*

The Class/Shape Transformation equations are utilized instead of other parameterization methods as it intuitively allows the specialization of geometries per aerospace industry requirements. The following improvements are incorporated to the CST equations initially proposed by Kulfan [11] in 2006: *i*) a more intuitive 3D representation where rigid body motion and geometry are decoupled, *ii*) the assembly of multiple intersecting CST objects, and *iii*) a spline representation where the basis functions are CST functions.

4.1 Modified Class/Shape Transformation

Inspired by discrete parameterization methods [160], the 3D CST method is expanded herein to include large rotations and the concept of shape coefficient functions. As shown in Fig. 4.1, the parameterized aircraft can be represented in the following three domains: parameterized, intermediate, and physical. In the *parameterized domain*, class and shape coefficients are used to define the general and local details of the OML, respectively. All geometries in the parameterized domain are normalized, facilitating operations such as mesh generation and numerical integration. In the *intermediate domain*, the geometry from the parameterized domain is linearly scaled to appropriate $x - y - z$ dimensions and features such as taper and span are considered). In this intermediate domain the leading and trailing edge are located on the $x - y$ plane, which is suitable for applying internal kinematic constraints. The *physical domain* builds upon the intermediate domain by introducing twist and shear (e.g., dihedral and sweep) mappings. This final domain is the most relevant from a design point of view since it represents the final built geometry and will be used for structural and aerodynamic analysis.

*Part of the data reported in this chapter is reprinted with permission from "Extended 3D Class/Shape Transformation equations for multicomponent aircraft assemblies" by Leal, P., Giblette, T., Hunsaker, D., and Hartl, D., 2019, AIAA Scitech.

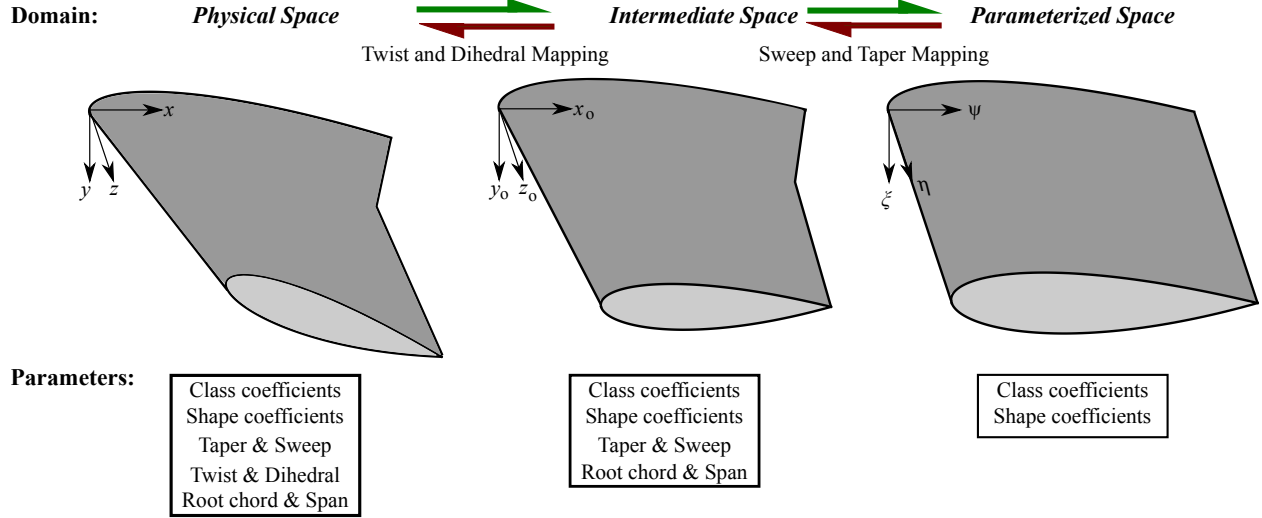


Figure 4.1: Overview of parameterizing a physically meaningful wing using the CST framework.

4.1.1 Parameterized domain

The CST method is a universal method to parameterize geometries that combines the concepts of a class function C and a shape function S . To facilitate the mathematical representation of the aircraft geometry, the physical domain $x - y - z$, wherein the aircraft is represented, is transformed into unique parameterized domains $\psi - \eta - \zeta$ for each major aircraft component via a bijective linear transformations such that $\psi \in [0, 1]$ and $\eta \in [0, 1]$. Defining $\zeta(\psi = 1, \eta) = \zeta_T$, which in general need not be zero, the general form for the CST equations is:

$$\zeta(\psi, \eta) = C(\psi, \eta)S(\psi, \eta) + \psi\zeta_T(\eta). \quad (4.1)$$

The concept of a class function is used, without any loss of generality, to define geometric characteristics inherent to given geometric forms common in an aircraft, e.g., nacelles, fuselages, and wings. The class function C , adjusted via parameters N_1 and N_2 , is

$$C(\psi, \eta) = \bar{k} \psi^{N_1(\eta)} (1 - \psi)^{N_2(\eta)}, \quad (4.2)$$

where \bar{k} is a correction factor so that the maximum cross-section thickness is always normalized

for shape functions equal to one and is given by:

$$\bar{k}(\eta) = \frac{(N_1 + N_2)^{N_1+N_2}}{N_1^{N_1} + N_2^{N_2}}. \quad (4.3)$$

The 2D [161] class functions are extended to 3D by allowing N_1 and N_2 to be defined as functions of the spanwise coordinate η as in Eq. 4.2. As depicted in Fig. 4.2, various geometry classes are obtained for different combinations of N_1 and N_2 and the values of these coefficients can change along the span. This feature allows the use of supersonic (sharp leading edge) and subsonic (blunt leading edge) airfoils on the same wing. The 3D shape functions further define the

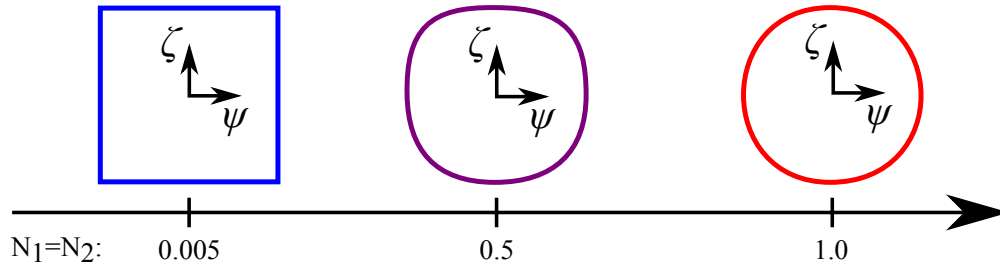


Figure 4.2: Example of varying class function along span for a constant shape function.

OML and are defined as Bernstein polynomials that are a linear combination of Bernstein basis polynomial each weighted by a shape coefficient $H_i(\eta)$ [162]. The shape coefficients for 2D are constants and have multiple applications for airfoils [8]. Similar to the class functions, the 3D shape functions are the same as for 2D with the exception that the shape coefficients are a function of the spanwise coordinate η . Specifically, the 3D shape function is formulated as follows:

$$S(\psi, \eta) = \sum_{i=0}^n H_i(\eta) \left[\frac{n!}{i!(n-i)!} \psi^i (1-\psi)^{n-i} \right], \quad (4.4)$$

where n is the order of the shape coefficients. The effects of the class and shape functions for 2D are depicted in Fig. 4.3.

The example in Fig. 4.4 demonstrates how the cross-section varies across the span based on the

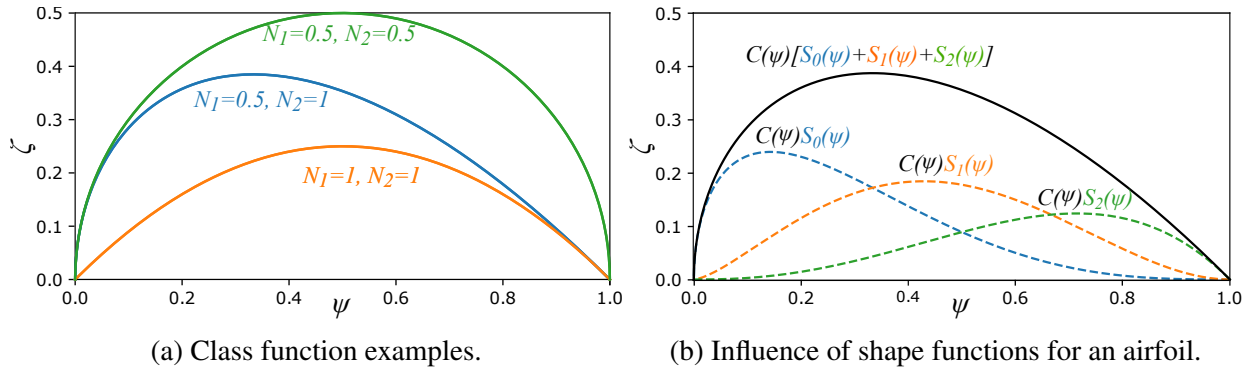


Figure 4.3: Example of the effects of parameters over class and shape function.

shape coefficient function. In this case, the shape coefficients are defined as Bernstein polynomials, resulting in smooth geometries originally defined by Kulfan [48]. $A_i(\eta)$ is a function defined by the user depending on the intended application. If the shape coefficients are constant, the resultant geometry has a constant cross-section. If $A_i(\eta)$ are piecewise linear functions, the resultant C^0 geometry consists of linear lofts between cross-sections defined along the span (cf., Fig. 4.1).

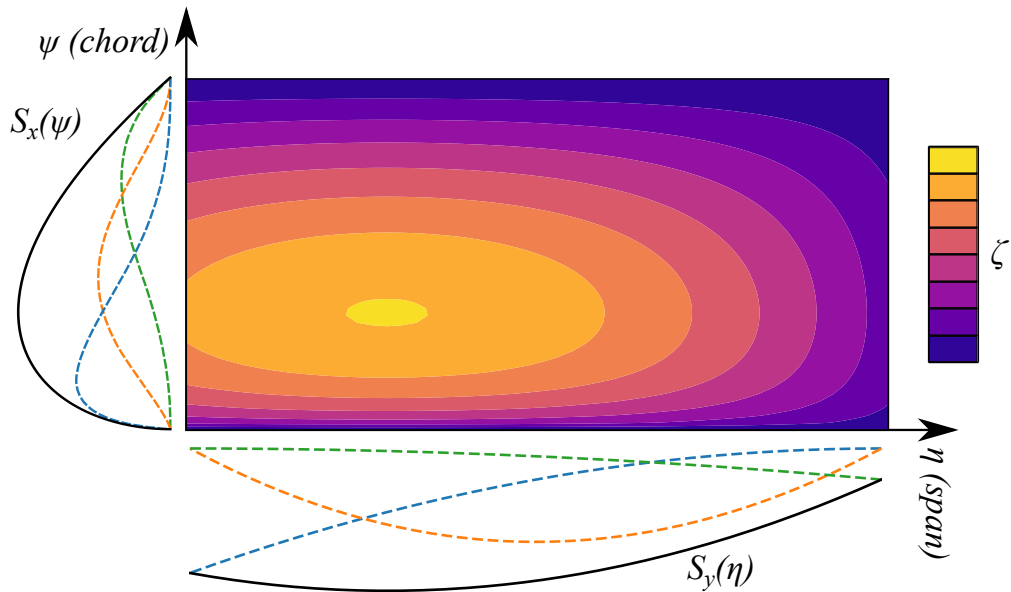


Figure 4.4: Example of 3D shape function where $H_i(\eta)$ is a 2D shape function. The resultant shape is the tensor product of two 2D CST functions.

4.1.2 Physical and intermediate domain

The model in the parameterized domain, defined by only shape and class coefficients, is a rectangular untapered, unswept wing with no dihedral and twist which is not typically useful for designing aircraft. However, other geometric properties can be introduced via linear mappings. The first step is to linearly scale the chordwise and spanwise dimensions to introduce the notions of the chord, taper, sweep, and span. The resultant design domain $\hat{x}-\hat{y}-\hat{z}$ is called the intermediate domain where the OML coordinates for both surfaces are given by:

$$\hat{x} = (\psi - \psi_o) X(\eta), \quad (4.5)$$

$$\hat{y} = (\eta - \eta_o) Y(\eta), \quad (4.6)$$

$$\hat{z} = (\zeta - \zeta_o) Z(\eta), \quad (4.7)$$

where $(\psi_o, \eta_o, \zeta_o)$ is the reference point in the parameterized domain, and $X(\eta)$, $Y(\eta)$, and $Z(\eta)$ are linear mappings. For a wing, $X(\eta)$ and $Y(\eta)$ are related to taper and span, and $Z(\eta) = X(\eta)$.

The full geometric representation in the physical domain as shown in Fig. 4.5 is obtained by including twist and shear, where shear mapping is defined as displacement along the plane perpendicular to η . Consequently, the leading edge and trailing edge are not necessarily on the $x - y$ plane. The upper surface coordinates in the physical domain $x - y - z$ are given by :

$$\begin{pmatrix} x \\ y \\ z \end{pmatrix} = \mathbf{T} \begin{pmatrix} \hat{x} \\ \hat{y} \\ \hat{z} \end{pmatrix} + \begin{pmatrix} x_{\text{shear}}(\eta) \\ 0 \\ z_{\text{shear}}(\eta) \end{pmatrix} \in \Lambda, \quad (4.8)$$

where x_{shear} is the x -component of the shear displacement (e.g., sweep for a wing), z_{shear} is the z -component of the shear displacement (e.g., dihedral for a wing), $\Lambda = \{\mathbf{l}_1, \mathbf{l}_2, \mathbf{l}_3\}$ is the local/physical vector space, and \mathbf{T} is the twist matrix that can take Euler angles, Euler vector, and

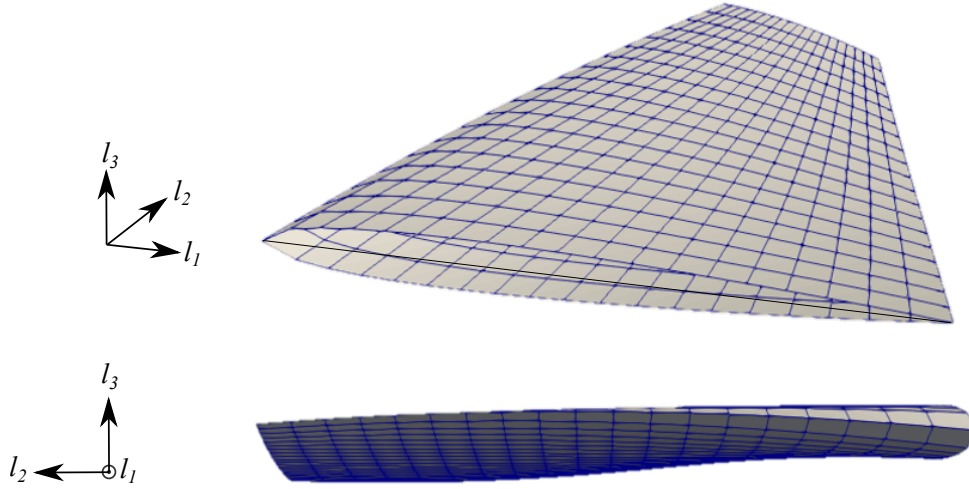


Figure 4.5: Wing example demonstrating the framework capability to portray twist, camber, and dihedral changes along the span.

quaternions as inputs [163].

4.1.3 Assembly domain

Despite the flexibility of the CST equations, it is inefficient to only use one set of CST equations to present complex structures such as an aircraft. As a solution, the structure is subdivided into smaller components (e.g., fuselage, wing, nacelle, and tail), each with a unique CST representation. Thereafter, all parts are included in the assembly domain as position vectors \mathbf{r} with a respective part origin and orientation. The transformation from local to global is attained via the following rigid body motion:

$$\mathbf{r} = \mathbf{R}_{1-i} \begin{pmatrix} x \\ y \\ z \end{pmatrix} + \mathbf{r}_o \in I, \quad (4.9)$$

where \mathbf{R}_{1-i} is the rotation matrix related to the part orientation, \mathbf{r}_o is the position vector of the part origin in the assembly domain, and $I = \{\mathbf{i}_1, \mathbf{i}_2, \mathbf{i}_3\}$ is global/assembly vector space.

Considering Eqs. B-4.9, the following relations are used to transform the coordinates from the parameterized domain to the assembly domain, resulting in a physically meaningful geometry based on a given mesh (e.g., set of points in the parameterized domain):

$$\mathbf{r} = \mathbf{R}_{i-1} \left[\mathbf{T} \begin{pmatrix} X(\psi - \psi_o) \\ Y(\eta - \eta_o) \\ Z(\zeta - \zeta_o) \end{pmatrix} + \begin{pmatrix} x_{\text{shear}} \\ 0 \\ z_{\text{shear}} \end{pmatrix} \right] + \mathbf{r}_o. \quad (4.10)$$

For model calibration and intersection calculations, it is also important to transform from the physical domain to the parameterized domain; the relation is given as:

$$\begin{pmatrix} \psi \\ \eta \\ \zeta \end{pmatrix} = \mathbf{T}^{-1} \left[\mathbf{R}_{i-1} (\mathbf{r} - \mathbf{r}_o) - \begin{pmatrix} x_{\text{shear}} \\ 0 \\ z_{\text{shear}} \end{pmatrix} \right] \begin{pmatrix} X^{-1} \\ Y^{-1} \\ Z^{-1} \end{pmatrix} + \begin{pmatrix} \psi_o \\ \eta_o \\ \zeta_o \end{pmatrix}. \quad (4.11)$$

The key technical challenge of subdividing the structure into smaller components is guaranteeing compatible OML representation at the intersections. Typically, intersections between 3D geometries are defined after mesh generation [164]. However, because all the surfaces herein utilized are analytically defined, the intersections are implicitly solved as the desired structured mesh for structural and aerodynamic analysis can be generated. When calculating the intersection for two parts utilizing the proposed algorithm, a *slave-master* relation exists to ensure convergence during iterations. The master is defined as the component to which the slave is attached, while the slave is the smaller component that defines the parametric coordinates ψ_s for the mesh. The position vectors \mathbf{r}_m and \mathbf{r}_s are associated with the master and slave components, respectively, at the intersection. For the case of an aircraft shown in Fig. 4.6, the fuselage is the master and the wing is the slave. The intersection algorithm summarized in Algorithm 1 consists of a fixed point iteration method to find the parameterized coordinate η_s that returns a norm of the difference between \mathbf{r}_m

and \mathbf{r}_s smaller than a given tolerance.

Algorithm 1: Intersection algorithm for CST objects.

Input: ψ_s ;

Result: \mathbf{r}_m and \mathbf{r}_s at intersections

$\eta_s = \eta_{s,o}$;

while $\|\mathbf{r}_m - \mathbf{r}_s\| < tol.$ **do**

 Determine assembly vector \mathbf{r}_s based on parameterized coordinates (ψ_s, η_s) - Eq. 4.10;

 Calculate parameterized coordinates (ψ_m, η_m) based on assembly vector \mathbf{r}_s - Eq. 4.11;

 Estimate assembly vector \mathbf{r}_m from parameterized coordinates (ψ_m, η_m) - Eq. 4.10;

end

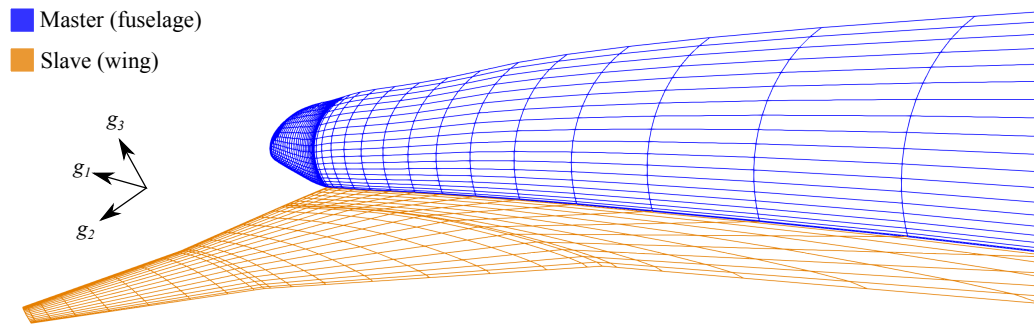


Figure 4.6: Intersection of JWB wing and fuselage.

4.2 Geometric representation capability

4.2.1 Two-dimensional CST

Two airfoils are considered as the primary *example* parent airfoils throughout this paper. The first airfoil is a conventional NACA0008, while the second one is the hawk-inspired F0808 airfoil [165]. Two sets of shape coefficients are calibrated to enable the CST method that best represents these airfoils. In this work, a genetic optimization algorithm is utilized that considers the Hausdorff distance, a metric to determine similarity between two geometries, as the objec-

tive function [166]. Resulting calibrations of the CST demonstrate that it can represent simple and challenging airfoil geometries equally well. As shown in Fig. 4.7, both airfoils are accurately represented by a fifth order CST function. For the NACA0008 airfoil: $\mathbf{D}_u = \mathbf{D}_l = \{0.1194, 0.0976, 0.1231, 0.0719, 0.1061, 0.1089\}$, $\Delta\xi_{TE} = 0$, and the final mean Hausdorff distance is 0.0013, or 0.13% of the chord. As for the F0808 airfoil: $\mathbf{D}_u = \{0.2399, 0.3447, 0.1813, 0.3537, 0.2441, 0.2572\}$, $\mathbf{D}_l = \{0.1889, -0.2469, 0.0776, -0.5478, -0.0047, -0.2399\}$, $\Delta\xi_{TE} = 0.0094$, and the final mean Hausdorff distance is 0.0028, or 0.28% of the chord.

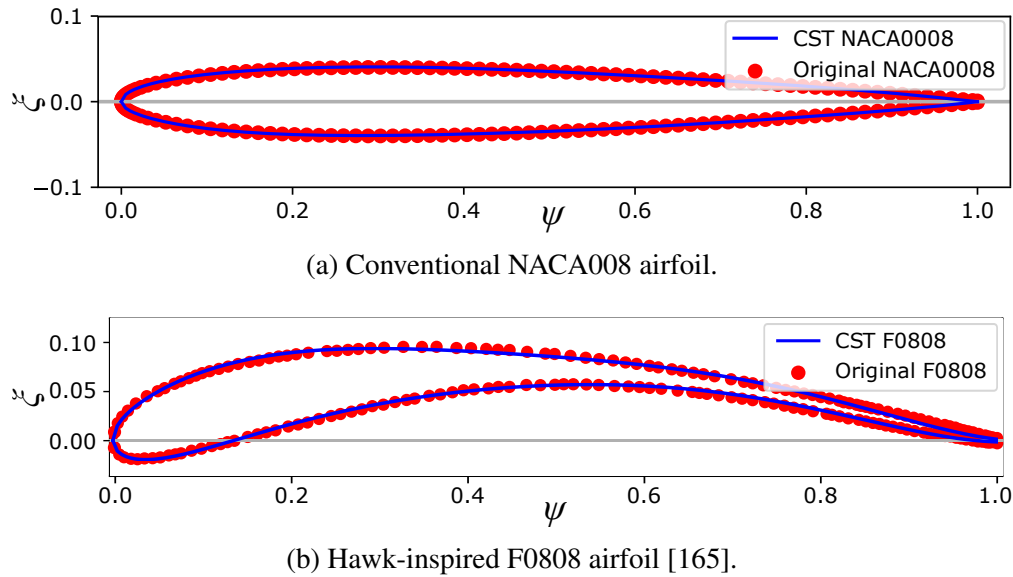


Figure 4.7: Curve fitting of shape coefficients demonstrating the capability to various airfoils.

4.2.2 Three-dimensional CST

3D CST is proposed as a method to accurately represent geometries; to this purpose, two sets of CST equations are calibrated to represent two distinct objects with disparate linear mappings, shape coefficient functions, and location/orientation in the assembly domain. The two parts considered are the fuselage and wing of the JAXA Wing Body (JWB) [160], an SST concept developed for low-boom signatures at ground level (cf., Fig. 4.8). Each component has distinct geometric features which makes it suitable to confirm the developed framework capabilities.

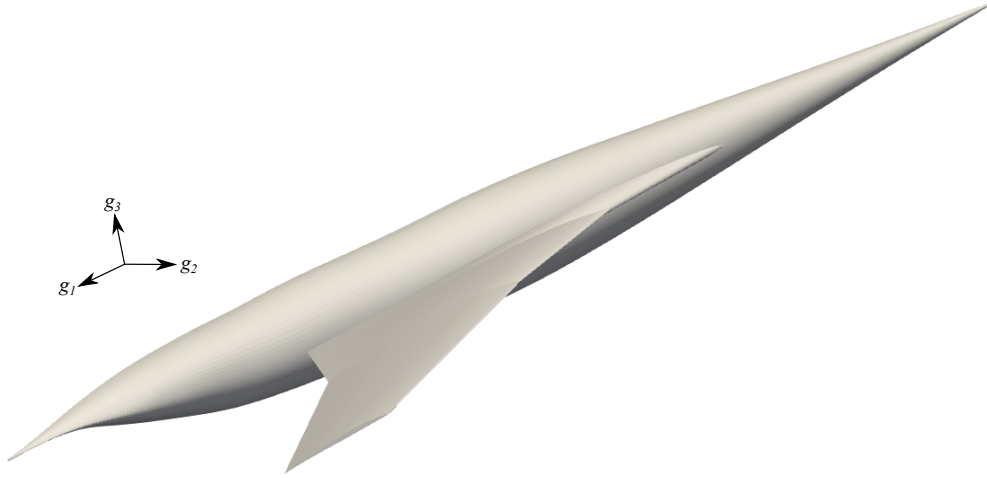


Figure 4.8: JAXA Wing Body (JWB) as an example of an aircraft assembly represented using the framework.

The calibration of the CST equations consists of a gradient-based minimization of the shape difference between the parameterized JWB and the original configuration [160]. The optimizer utilized is the Broyden-Fletcher-Goldfarb-Shanno (BFGS) algorithm, an unconstrained quasi-Newton method (i.e., the Hessian matrix is approximated by gradient evaluations). The shape difference metric implemented is the average of the *vector distance field* [167] defined as:

$$E = \frac{1}{N} \sum_{i=1}^N \|\mathbf{p}_i - \mathbf{r}(\mathbf{p}_i)\|^2, \quad (4.12)$$

where N is the number of points evaluated, \mathbf{p} is the position vector from the original JWB configuration and \mathbf{r} is the estimated position vector utilizing CST equations. \mathbf{r} is calculated for the parameterized coordinates ψ_i, η_i obtained from utilizing \mathbf{p} as an input for Eq. 4.10; thus, the error will be minimum only when the position vectors coincide. For the convergence studies, the normalized shape difference is also utilized and is defined as the shape difference relative to the optimized solution with the greatest shape difference.

The calibration of the CST equations is computationally intensive because of the high number of degrees of freedom and the need to calculate of the shape difference. However, the curve fitting

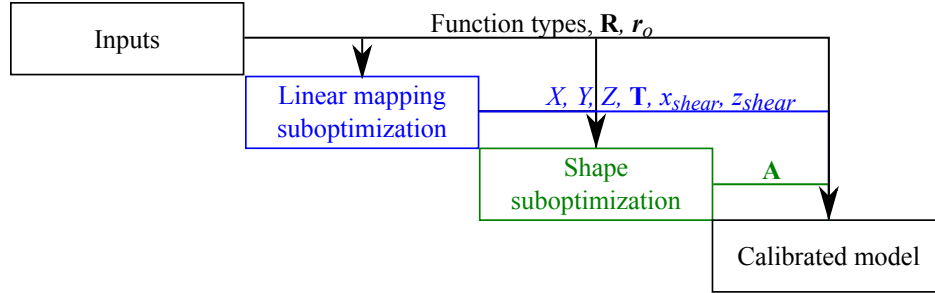


Figure 4.9: Overview of the calibration process.

process can be split into two sequential suboptimizations, mitigating the curse of dimensionality and the overall runtime. The first suboptimization is related to the linear mappings that transform the parameterized domain into the physical domain (Eq. 4.10) and only considers points at $\psi = 0$ and $\psi = 1$ for calculating the shape difference. The subsequent suboptimization is related to the shape coefficient functions and utilized the optimized linear mappings from the previous optimization. All the data from the original shape is utilized for the shape difference calculation.

4.2.3 Fuselage

The fuselage is the main body of an aircraft and is symmetric along the butt line; thus, only half of the fuselage is herein evaluated. The object is oriented such that the non-dimensional coordinates (ψ, η, ζ) are aligned with the water line, butt line, and reference line of the fuselage. The JWB fuselage is an atypical design because of the significant fuselage camber not usually found in current aircraft. Furthermore, because the geometry is achieved to mitigate boom, multiple small-scale features exist specially near the tail. As a consequence, high-order CST and Bernstein polynomials are utilized for an accurate representation. The mapping functions (c.f., Eq. 4.10)

utilized are:

$$X(\eta) = h_f S^b(\psi, \eta) C^b(\psi, \eta), \quad (4.13)$$

$$Y(\eta) = l_f, \quad (4.14)$$

$$Z(\eta) = w_f S^b(\psi, \eta) C^b(\psi, \eta), \quad (4.15)$$

$$A_i(\eta) = S^{d_i}(\psi, \eta), \quad (4.16)$$

$$x_{\text{shear}}(\eta) = S^f(\psi, \eta), \quad (4.17)$$

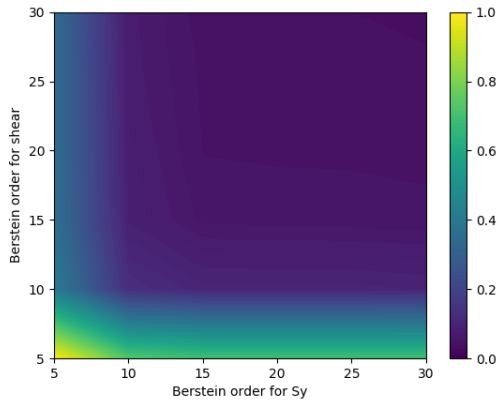
$$z_{\text{shear}}(\eta) = 0, \quad (4.18)$$

where h_f , l_f , w_f are the fuselage height, length, and width; S^b and S^f are the shape function for shape coefficients $\mathbf{A}^b \in \mathbb{R}^b$ and $\mathbf{A}^f \in \mathbb{R}^f$; S^{d_i} is the shape function for the i -th row of $\mathbf{A}^d \in \mathbb{R}^{d_1 \times d_2} \forall i \in [1, n]$; and C^b is the class function for parameters $N_1 = 0.75$ and $N_2 = 0$. The selected class coefficients are considered because it guarantees a conic geometry at the leading edge and minimizes the number of shape coefficients necessary to represent it.

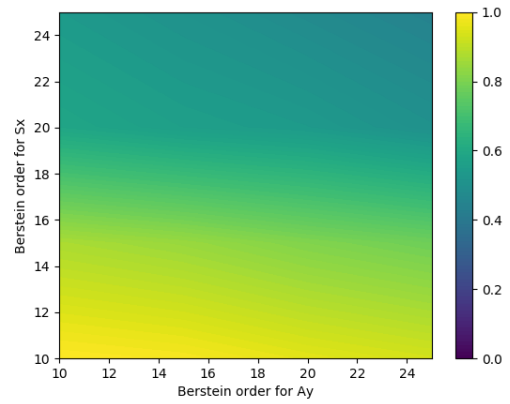
Following the calibration procedure described in Fig. 4.9, two suboptimizations are implemented to curve fit the CST equations for a JWB fuselage. Convergence studies are executed to evaluate the influence of the shape coefficient orders over the shape difference. The objective of the study is to determine the minimum order necessary for satisfactory OML representation. The results depicted in Fig. 4.10 show that an accurate representation of the fuselage is achieved with orders $b = 15$, $d_1 = 18$, $d_2 = 24$, and $f = 15$. The resulting parameterized geometry is depicted in Fig. 4.11.

4.2.4 Wing

Because of manufacturing and control surface constraints, aircraft wing OMLs consist of lofts between defined airfoil along the span. Compared to the design of a fuselage, the number of degrees of freedom is significantly reduced. Mathematically, lofting can be represented as a linear piecewise function. For a given set of known values $\{q_0, \dots, q_r\}$ at $\{\eta_0, \dots, \eta_r\}$, the interpolation



(a) Linear mapping suboptimization.



(b) Shape coefficient suboptimization.

Figure 4.10: Convergence study of CST calibration for JWB fuselage.

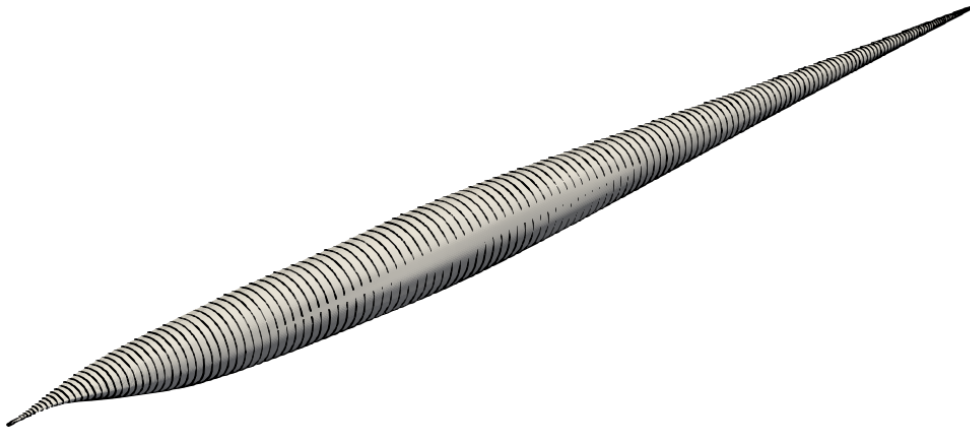


Figure 4.11: JWB fuselage parameterized and original geometries.

function is given by equation 4.19. An example of the characteristic lofting of aircraft wing is depicted in Fig. 4.12 for the case of a B787-800, where four sections are defined along the wing to accurately define functions for taper, sweep, and dihedral.

$$p(\eta) = \begin{cases} q_0 + \frac{\eta}{\eta_1}(q_1 - q_0), & \text{if } \eta_0 < \eta < \eta_1 \\ \dots & \\ q_i + \frac{\eta - \eta_i}{\eta_{i+1} - \eta_i}(q_{i+1} - q_i), & \text{if } \eta_i < \eta < \eta_{i+1} \\ \dots & \\ q_{r-1} + \frac{\eta - \eta_{r-1}}{\eta_r - \eta_{r-1}}(q_r - q_{r-1}), & \text{if } \eta_{r-1} < \eta < \eta_r \end{cases} \quad (4.19)$$

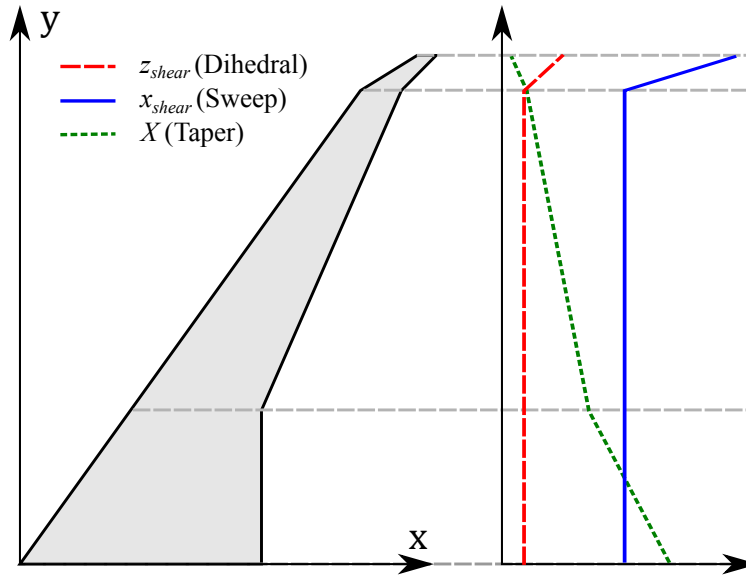


Figure 4.12: Simplified schematic of a B787-800 with linear mappings and respective physical meaning.

Two surface, an upper and lower, are necessary to represent the OML of a wing because CST mapping is bijective. The Z -mapping and shape coefficients for the upper surface are represented by Z_u and \mathbf{A}_u while for the Z -mapping and shape coefficients are represented by Z_l and \mathbf{A}_l . The

functions utilized for describing the linear mappings and shape coefficients are:

$$X(\eta) = c_{\text{root}} p^b(\eta), \quad (4.20)$$

$$Y(\eta) = b/2, \quad (4.21)$$

$$Z_u(\eta) = c_{\text{root}} S^u(\psi, \eta) p^b(\eta), \quad (4.22)$$

$$Z_l(\eta) = c_{\text{root}} S^l(\psi, \eta) p^b(\eta), \quad (4.23)$$

$$A_i^u(\eta) = p^{u_i}(\eta), \quad (4.24)$$

$$A_i^l(\eta) = p^{l_i}(\eta), \quad (4.25)$$

$$x_{\text{shear}}(\eta) = p^f(\eta), \quad (4.26)$$

$$z_{\text{shear}}(\eta) = p^g(\eta), \quad (4.27)$$

where c_{root} is the root chord root, b is the span, p^b , p^{u_i} , p^{l_i} , p^f , and p^g are linear interpolation functions for parameters $\mathbf{q}^b \in \mathbb{R}^b$, $\mathbf{q}^{u_i} \in \mathbb{R}^u$, $\mathbf{q}^{l_i} \in \mathbb{R}^l$, $\mathbf{q}^f \in \mathbb{R}^f$, and $\mathbf{q}^g \in \mathbb{R}^g$, and S^u and S^l are shape functions for shape coefficients \mathbf{A}^u and \mathbf{A}^l .

The same procedure for curve fitting the fuselage is herein utilized for the wing. The order of the piecewise linear equations and the Bernstein polynomials are known from the original JWB paper to be four and six. Therefore, there is not a need to do a convergence study. The resultant surface obtained by optimizing the CST equations for the wing is depicted with the original database in Fig. 4.13. Overall, the calibrated CST equations can represent the wing OML.

4.3 Spline CST

Despite the versatility of a CST representation, there are shape modeling situations for which it is not a suitable method. Because a CST requires the same degree of continuity for any point in the domain it spans (except for the bounds $\psi = 0$ and $\psi = 1$), it is an inefficient method capturing shapes that require discontinuities. The order n of the shape functions can be increased to approximately represent discontinuity, but this is inefficient as it requires a high number of shape coefficients to do so. This challenge is not unique to CST equations but is common to all continuous

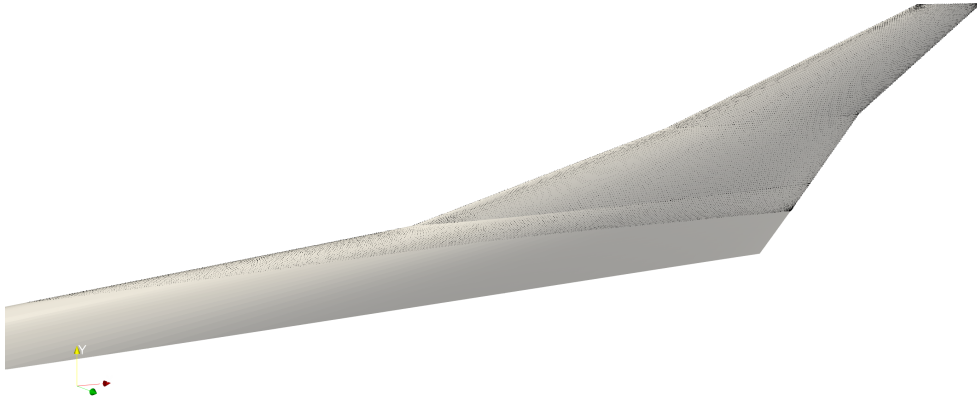


Figure 4.13: JWB wing parameterized and original geometries.

functions. A standard solution is to utilize a piecewise assemblage of polynomials or splines to satisfy the localized continuity requirements along the geometry [168]. An additional benefit of splines is that their use leads to topologically stable representations, avoiding the “waviness” inherent to high-order polynomials. The stability and flexibility of splines are the main reasons they are the default parametric representation for CAD software (e.g., NURBS, B-splines, and Bezier-splines). Therefore, it is evident that incorporating CST equations for use as the basis functions in such a well proven spline approach can be beneficial to this work. The CST splines are the foundation of the beam formulation in Chapter 7 for discontinuous bending moment distributions.

In general, a spline consists of m piecewise polynomials connected at points denoted as *knots*; the vector containing all the knot locations as the *knot vector* and the region in between knots as the *knot span* [50]. Each knot Ξ^k is defined by its arc-length coordinate s and the knot span (also denoted as a spline beam element in Chapter 7) is denoted as $\mathbf{s}^k = \{s : \Xi^{k-1} \leq s \leq \Xi^k\}$. The domain a knot span has the same degree of continuity, but discontinuities for line representation are allowed at the knots. In general, a 2D spline can be described in the parameterized domain as:

$$\zeta(s) = \prod_{l=1}^m \zeta^l, \quad (4.28)$$

and

$$\zeta^k(s) = \begin{cases} C^k(\psi^k)S^k(\psi^k) + (1 - \psi^k)\zeta_L^k + \psi^k\zeta_T^k & \text{if } \Xi^{k-1} \leq s < \Xi^k, \\ 1 & \text{otherwise,} \end{cases} \quad (4.29)$$

where

$$\psi^k = \frac{x(s) - x(\Xi^{k-1})}{c^k}. \quad (4.30)$$

and C^k , S^k , ζ_L^k , ζ_T^k , and c^k are the following properties respectively for the k -th knot span: class function, shape function, ζ at $\psi = 0$, ζ at $\psi = 1$, and chord.

The affine transformation from the parameterized to the physical domain (i.e., $(\psi, \zeta) \rightarrow (x, z)$) is given by:

$$\left. \begin{aligned} x &= \sum_{l=1}^{k-1} c^l + c^k(s)\psi^k(s) \\ z &= c(s)\zeta(s). \end{aligned} \right\} \text{ s.t. } \{c(s) = c^k | \Xi^{k-1} \leq s < \Xi^k\} \quad (4.31)$$

The arc-length of each knot span is calculated based on the chord c^k , hence

$$L^k = L_{k-1} + \int_0^{c^k} \sqrt{1 + \left[\frac{d\zeta}{d\psi}(s) \right]^2}. \quad (4.32)$$

Finally, degrees of continuity C^0 , C^1 , and C^2 at the knots can be satisfied by the following relations:

- C^0 is ensured if coordinates x and y at knot k for both knot spans, k and $k + 1$, are the same.

From Eqs. 4.29 and 4.31, the following relation must be satisfied:

$$c^k \zeta_T^k = c^{k+1} \zeta_L^{k+1}. \quad (4.33)$$

- C^1 is imposed if the first derivative at knot k for both knot spans, k and $k + 1$, are the same.

From Eqs. B.7 and B.9, the following relation must be satisfied if $N_1^k = N_2^{k-1} = 1$:

$$-\zeta_L^k - A_n^k + \zeta_T^k = -\zeta_L^{k+1} + A_0^{k+1} + \zeta_T^{k+1}. \quad (4.34)$$

- C^2 is guaranteed if the second derivative at knot k for both knot spans, k and $k + 1$. From Eqs. B.11 and B.12, the following relation must be satisfied if $N_1^k = N_2^{k-1} = 1$:

$$\frac{1}{c^k} [nA_{n-1}^k - (N_1 + n) A_n^k] = \frac{1}{c^{k+1}} [-(n+1)A_0^{k+1} - nA_1^{k+1}]. \quad (4.35)$$

Each knot span is represented by a different set of shape coefficients \mathbf{A}^k , but the continuity constraints can impose dependencies among the coefficients through ζ_T , ζ_L , and A_n . Therefore, the geometric properties (i.e., positions, angles, and derivatives) are calculated in series from the knot span at the root ($k = 1$) to the free end ($k = m$) when generating the spline. The collection of independent shape coefficients that define the spline is denoted as \mathbf{a} .

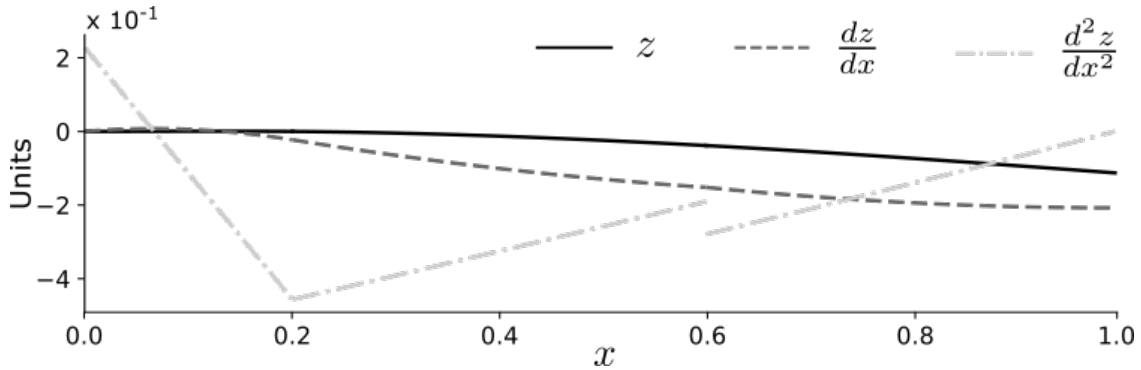


Figure 4.14: Spline and derivatives in the physical domain for $\Xi = (0, 0.2, 0.6, 1.0)$ and $\mathbf{A} = (0, 1.14, 2.28, 7.34, 6.47, 5.574, 3.69, 2.80) \times 10^{-2}$.

An example of a CST spline and the respective derivatives are depicted in Fig. 4.14. C^0 and C^1 continuities are imposed for all domains in the spline, and the domain is also C^3 except for the knots. The knot at $\Xi^1 = 0.2$ is C^2 continuous while the knot at $\Xi^2 = 0.6$ is only C^1 continuous.

The resultant geometry could not be represented using a continuous function (e.g., a single CST function).

While Fig. 4.14 depicts the spline and derivatives in the physical domain, understanding of a parameterized domain is also important. The spline and derivatives are again depicted in Fig. 4.15, but each knot span and the basis functions are shown separately in the parameterized domain. For any CST spline, $m(n + 1)$ bases or shape coefficients are used to represent the geometry (e.g., nine basis functions for the depicted spline as $n = 2$ and $m = 3$). Each basis function has a greater influence at a specific region of the knot span (e.g., ζ^0 is more relevant near $\psi^0 = 0$) and has localized influence on its respective knot span (e.g., ζ^0 does not influence the second knot span). Moreover, the implications of the continuity constraints are noticeable even in the parameterized domain as n -th basis function of a knot span is always continuous with the 0-th basis function of the following knot span. It is worth highlighting that the non-linear basis can represent linear geometries as shown for the second derivative in Fig. 4.15.

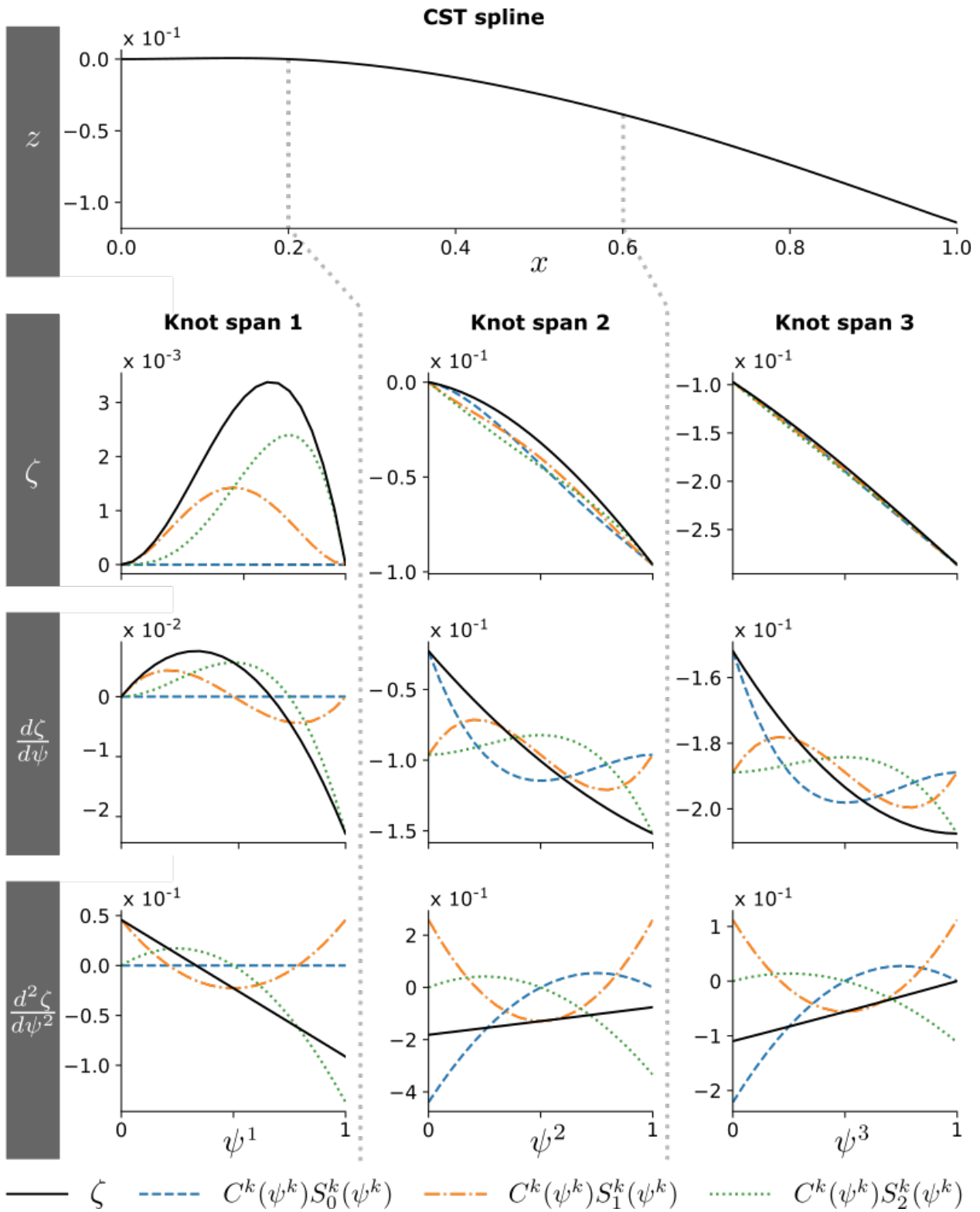


Figure 4.15: CST basis for derivatives and positions in the parameterized domain for $\Xi = (0, 0.2, 0.6, 1.0)$ and $\mathbf{A} = (0, 1.14, 2.28, 7.34, 6.47, 5.574, 3.69, 2.80) \times 10^{-2}$.

5. PARAMETERIZATION OF MORPHING STRUCTURES*

Regardless of any ability to morph, aircraft wings undergo a wide variety of flight loads and therefore must include stiff internal structural components. These components impose restrictions on feasible morphed shapes independent of the utilized technology. In general, a morphing structure problem considers a single reference state, a *parent* OML, and many derived or morphed states, the *children* OML. Every child configuration satisfies a set of essential internal structural constraints (e.g., ribs and spar stiffnesses) and is deemed *structurally consistent*. Designs derived from the parent that do not satisfy these constraints violate the laws of physics and are not considered children configurations. Here we propose modifications to the CST method that consider these kinematic constraints to generate all possible children OML based on a given parent OML. The framework is developed so that the parent configuration is the OML either before or after morphing; thus, the children OMLs are either the OMLs of a morphed parent airfoil or are the OMLs that, when morphed, will result in the parent OML. This enables the use of a robust shape parameterization method in problems where minimum internal volume or component dimensions are satisfied.

5.1 Two-dimensional camber morphing

Leal et al. [161] modified the CST equations so that children airfoils (e.g., morphed configuration) can be generated from any parent airfoil (e.g., original configuration) while considering kinematic constraints related to the internal structure; thus, all of the explored designs are feasible with regards to structural performance and manufacturability. Eq. 4.1 can be used to describe the children and parent configurations (denoted by a superscript c and p) by varying the values of the shape coefficients. Using an unconventional hawk-inspired airfoil as an example parent airfoil [28] and an internal structure consisting of five spars, different OMLs can be generated that preserve the spar dimensions as shown in Fig. 5.1. An assumption inherent in the framework as proposed is that

*Reprinted with permission from "Structurally consistent Class/Shape Transformation equations for morphing airfoils" by Leal, P., and Hartl D., 2018, Journal of Aircraft.

one surface/skin is passive (e.g., no strain) while the remaining surface is active (e.g., generates strain), each surface specified by shape coefficients A and P .

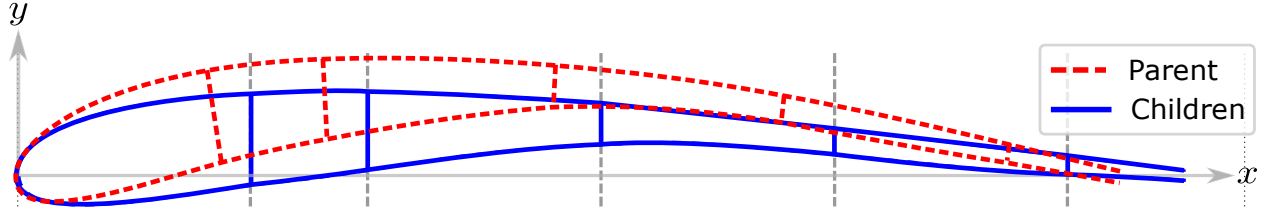


Figure 5.1: Structurally consistent airfoils based on a parent F0808 airfoil for calculation with actuators on lower surface; note the change in total chord due to assumed length preservation in non-actuated upper surface.

5.2 Nomenclature for skin-based camber morphing

Herein *morphing* is defined as the transformation of an airfoil section OML from a reference (e.g., strain-free) configuration toward any structurally consistent compatible deformed (e.g., actuated) configuration. The two OML surfaces, upper and lower, are defined as either *active* or *passive*. The active surface is both axially extended/compressed (e.g., actuated in the chord-wise direction) and bent as a consequence of this actuation; while the passive surface is purely bent. Therefore, Eq. 4.1 is rewritten to accommodate the notion of an active/passive dichotomy:

$$\xi_P(\psi) = \text{sgn}(\xi_P, \xi_A) \left[\psi^{N_1} (1 - \psi)^{N_2} \sum_{i=0}^n P_i K_{i,n} \psi^i (1 - \psi)^{n-i} + \psi \frac{\Delta \xi_{TE}}{2} \right], \quad (5.1)$$

$$\xi_A(\psi) = \text{sgn}(\xi_P, \xi_A) \left[\psi^{N_1} (1 - \psi)^{N_2} \sum_{i=0}^n A_i K_{i,n} \psi^i (1 - \psi)^{n-i} + \psi \frac{\Delta \xi_{TE}}{2} \right]. \quad (5.2)$$

where ξ_P and ξ_A are the ξ -coordinates for the passive and active surfaces respectively, $\Delta \xi = \xi_P(\psi) - \xi_A(\psi)$ for a $\psi \in (0, 1)$, and P_i and A_i are the shape coefficients for the passive and active surfaces.

Depending on the application, either the geometry of the reference (i.e., strain-free) OML or the geometry of the desired deformed (i.e., active surface actuators engaged) OML is taken

to be known while options for the other are explored. Two structurally consistent frameworks, defined as backwards and forwards, are then developed to account for each scenario. For *forwards* calculations possible deformed OMLs (children) are generated based on a known reference OML (parent). For *backwards* calculations, possible reference OMLs (children) are generated based on a known deformed OML (parent). This design flexibility is mapped in Fig. 5.2.

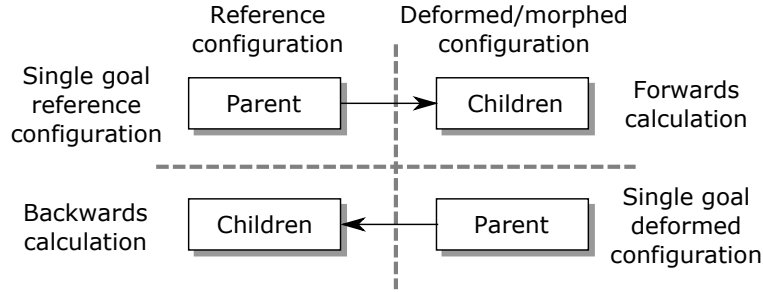


Figure 5.2: Map of the two morphing possibilities considered in the developed framework.

In this work, we specifically consider the restrictions imposed by the rigid, non-actuated internal structure when examining possible children (dependent) configurations generated via morphing of a parent (known). During camber-wise morphing, the chord length is not constant, as is depicted in Fig. 5.3. Geometric properties preserved in the dimensional domain $x - y$ are then not preserved in the non-dimensional domain $\psi - \xi$ because the chord of the child configuration c^c is not the same as that for the parent (c^p). Consequently, the full representation of the children configurations is known if and only if shape coefficients \mathbf{A}^c and \mathbf{P}^c as well as chord c^c are known. Finally, the following relation is used to convert the trailing edge thickness between the configurations with different chord lengths:

$$\Delta \xi_{TE}^c c^c = \Delta \xi_{TE}^p c^p. \quad (5.3)$$

5.3 Assumptions for structurally consistent skin-based camber morphing

In brief, the purpose of this work is to develop a new mathematical formulation to directly calculate the possible chord c^c and active shape coefficients \mathbf{A}^c for children configurations as func-

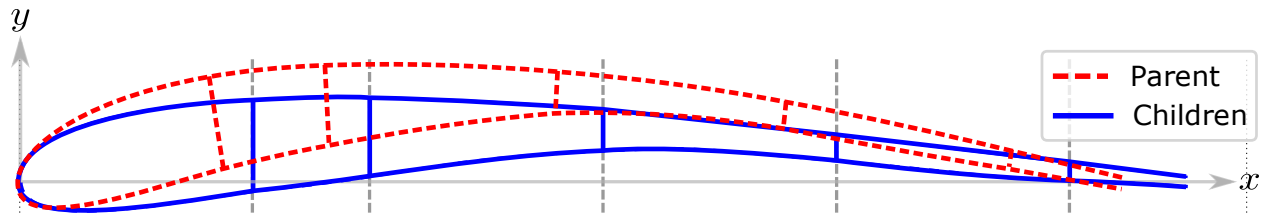


Figure 5.3: Structurally consistent airfoils based on a parent F0808 airfoil for backwards calculation with actuators on lower surface; note the change in total chord due to assumed length preservation in non-actuated upper surface.

tions of the parent configuration and any desired shape coefficients P^c . Generally, the functions describing c^c and A^c lead to an underdetermined system of equations. However, a unique closed-form solution for the child shape coefficients (e.g., child OML) is obtained given the following five assumptions:

- *Compliant ribs*: a traditional rib is chordwise stiff and hinders camber-wise morphing; it is assumed that a compliant rib is utilized so that the ribs do not act as structural constraints. As shown in Fig. 5.4, possible concepts for compliant ribs are Fishbone ribs [169], Jointed ribs, and Voronoi ribs [7].

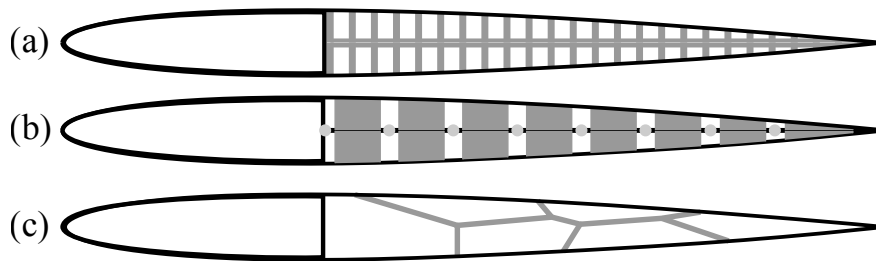


Figure 5.4: Examples of compliant ribs: (a) Fishbone [169], (b) Jointed, (c) Voronoi [7]

- *Rigid body spars*: no actuators are placed in the internal structure and spar deformations of any kind are assumed negligible. Consequently, spar dimensions are common to both children and parent airfoils as depicted in Figs. 5.3 and 5.5. In the non-dimensional domains,

the parent and child spar heights h_j^p and h_j^c are related via the following geometric relation for spars $j = 1, \dots, m$:

$$h_j^c c^c = h_j^p c^p. \quad (5.4)$$

- *Constant leading edge radius:* deformations at the leading edge are also neglected since no actuators are placed at the leading edge and conventional D-sections are often rigid; the leading edge radius is preserved as shown in Fig. 5.5. According to Kulfan [11], shape coefficients for $i = 0$ (P_0^c , A_0^c , P_0^p , and A_0^p) are related to the leading edge radius, and the relation between these shape coefficients for parent and children airfoils having a common leading edge radius is:

$$\begin{pmatrix} P_0^c \\ A_0^c \end{pmatrix} = \sqrt{\frac{c^p}{c^c}} \begin{pmatrix} P_0^p \\ A_0^p \end{pmatrix}. \quad (5.5)$$

- *Constant passive surface length:* the curvilinear length of the passive surface L_P is constant because this surface does not contain any active materials or actuators, the aerodynamic loading is moderate, and the active surface does not generate more than 4% strain, a common actuation stroke for shape memory alloys [5]. This assumption enables the determination of the children chords and a relation between children and parent spar locations. If L_P^c and L_P^p are the passive surface lengths for the children and parent configurations, the relation between lengths is simply:

$$L_P = L_P^c = L_P^p. \quad (5.6)$$

- *Constant angles between spars and passive surface:* the connection between the spars and the passive surface is assumed to be of high stiffness. Thus, it is assumed that angles β_j between the spars and the passive surface are constant, as depicted in Fig. 5.5. This assumption enables the determination of spar orientations in the deformed configuration. Once the spar

locations and angles are calculated, all geometric dimensions of both airfoils are known. If β_j^p and β_j^c are the angle values for the parent and children $j = 1, \dots, n$, the following is assumed:

$$\beta_j = \beta_j^c = \beta_j^p. \quad (5.7)$$

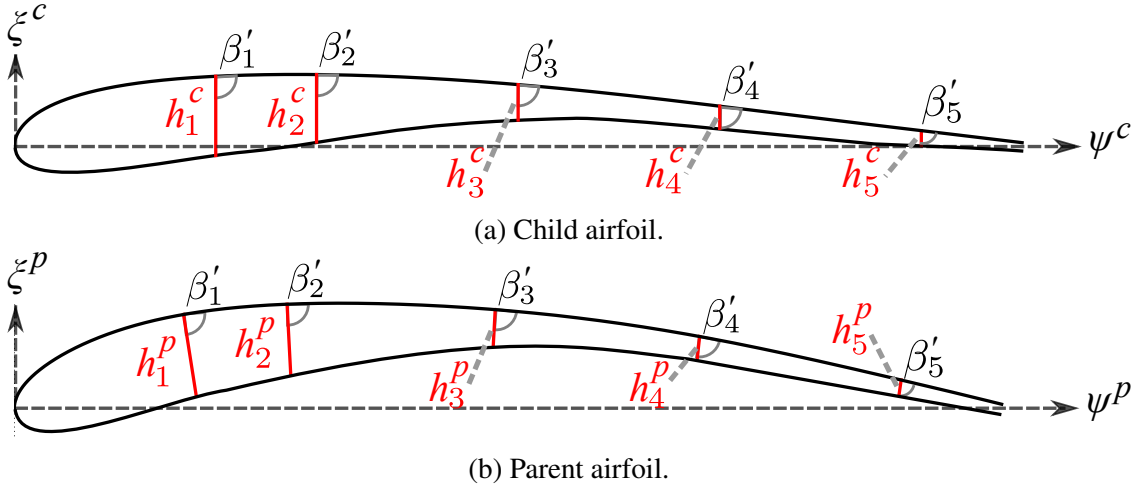


Figure 5.5: Schematic of airfoils and their respective spars for example backwards calculation with actuator on the lower surface. The complement angles of β' are depicted for better visualization.

Given the above assumptions applied to relations (5.1) and (5.2), the closed-form solution for the functions that define c^c and A^c can in general be found numerically. There are also two simplified cases where exact analytical solutions are possible as shown by Leal *et al.* [8, 12].

5.4 Forwards calculation

Forwards calculation is useful in designing wings where the reference (non-deformed) OML is optimal for the predominant flight condition, but multiple possible morphed OMLs that could improve performance for other flight conditions are unknown and of interest. As an example, Leal *et al.* [8] optimized an airfoil for high lift-to-drag ratio for cruise configuration (the parent) and also optimized a structurally consistent morphed landing OML (the child) based on the optimal cruise airfoil. Therefore, the wing was kinematically able to morph between two optimal

airfoils, and this was verified through high-fidelity finite element analysis. For forwards calculation, spar geometric dimensions including spar locations, heights, and orientations (spars are assumed vertical for the parent configuration) are given and an example is shown in Fig. 5.6. Consequently, the spar connection points (i.e, intersection between the spar and the OML) on the passive and active surfaces share the same ψ -coordinate ψ_j^p , and spar heights are clearly given as $h_j^p = \xi_u^p(\psi_j^p) - \xi_l^p(\psi_j^p) = |\xi_P^p(\psi_j^p) - \xi_A^p(\psi_j^p)|$ for the j^{th} spar. It follows from equations (5.1) and (5.2) that the child spar heights in the non-dimensional space for $\psi^c - \xi^c$ are simply renormalized for the modified chord to give:

$$h_j^c = \frac{c^p}{c^c} h_j^p = \frac{c^p}{c^c} |\xi_P^p(\psi_j^p) - \xi_A^p(\psi_j^p)| = \text{sgn}(\Delta\xi) \frac{c^p}{c^c} (\xi_P^p(\psi_j^p) - \xi_A^p(\psi_j^p)) . \quad (5.8)$$

Though vertical in the parent configuration, spars are rotated in the morphed children configurations to accommodate for morphing of the skin, and the coordinates of their end points must be calculated. For the children, the intersection of the j^{th} spar with the passive surface takes place at $\psi_{P,j}^c$, and the intersection with the active surface takes place at $\psi_{A,j}^c$.

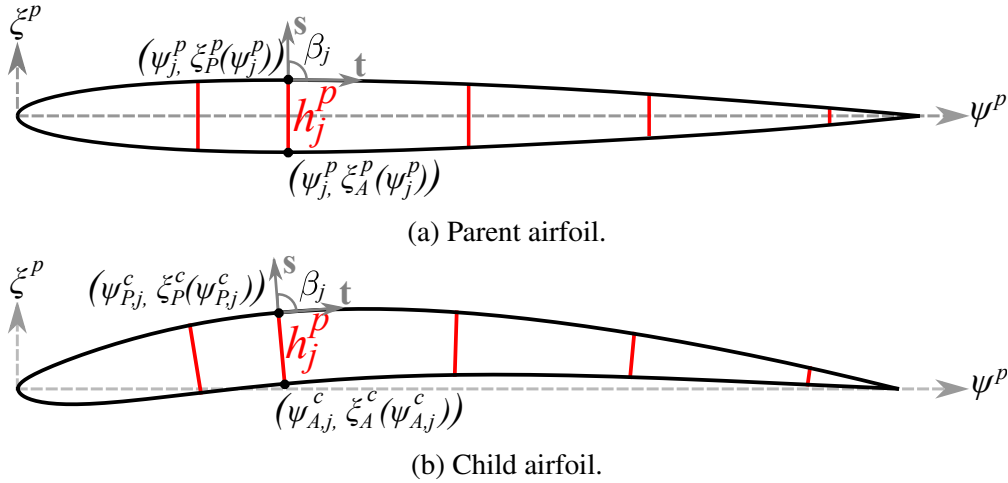


Figure 5.6: Conservation of spar heights and relative angles for forwards calculation.

For the chosen passive shape coefficients P^c , the conserved spar heights and leading edge are

known, but no other geometric properties of the children airfoils are known a priori. Considering that the leading edge radius for both airfoils are the same, the CST equation for the active surface (Eq. (5.2)) of the child configuration is rearranged to give:

$$\frac{2 \operatorname{sgn}(\Delta\xi) \xi_A^c(\psi_{A,j}^c) + \psi_{A,j}^c \Delta\xi_{TE}^c}{2\sqrt{\psi_{A,j}^c(\psi_{A,j}^c - 1)}} - A_0(1 - \psi_{A,j}^c)^n = \sum_{i=1}^n A_i K_{i,n}(\psi_{A,j}^c)^i (1 - \psi_{A,j}^c)^{n-i}. \quad (5.9)$$

This can also be represented as:

$$f_j = \sum_{i=0}^n F_{ji} A_i^c \quad \text{or} \quad \mathbf{f} = \mathbf{F} \mathbf{A}, \quad (5.10)$$

where \mathbf{A} is the active shape coefficient vector (n -dimensional), \mathbf{f} is the forwards restriction vector (m -dimensional)

$$f_j = \frac{2 \operatorname{sgn}(\Delta\xi) \xi_A^c(\psi_{A,j}^c) + \psi_{A,j}^c \Delta\xi_{TE}^c}{2\sqrt{\psi_{A,j}^c(\psi_{A,j}^c - 1)}} - A_0(1 - \psi_{A,j}^c)^n, \quad (5.11)$$

and \mathbf{F} is the forwards function matrix ($m \times n$ dimensional)

$$F_{ji} = K_{i,n}(\psi_{A,j}^c)^i (1 - \psi_{A,j}^c)^{n-i}. \quad (5.12)$$

\mathbf{F} is a non-negative tensor where all components are non-zero since there are no spars located at the leading or trailing edges. In the case where $n = m$ (e.g., number of spars equal to n), \mathbf{F} is a square tensor and invertible, and the solution for the linear system of equations is simply:

$$\mathbf{A} = \mathbf{F}^{-1} \mathbf{f}. \quad (5.13)$$

Through geometric constraints and the known values for the spar heights, \mathbf{f} and \mathbf{F} are calculated.

5.4.1 Constant length for forwards calculation

The passive surface is assumed to have constant length for aerodynamically applicable deformations because the skin-based actuators are placed on the active OML. The arc length of the passive surface L_P in the $x - y$ coordinate system valid for the child and parent airfoils is:

$$L_P = c \int_0^1 \sqrt{1 + \left(\frac{d\xi_P}{d\psi}\right)^2} d\psi, \quad (5.14)$$

where the derivative term is obtained from Eq. (B.4).

Since the chord c^p is known and the length of the passive OML for parent and children airfoils are the same (Eq. (5.6)), we have that:

$$L_P^c = c^c \int_0^1 \sqrt{1 + \left(\frac{d\xi_P^c}{d\psi^c}\right)^2} d\psi^c = c^p \int_0^1 \sqrt{1 + \left(\frac{d\xi_A^p}{d\psi^p}\right)^2} d\psi^p = L_A^p, \quad (5.15)$$

$$\therefore c^c = c^p \int_0^1 \sqrt{1 + \left(\frac{d\xi_P^p}{d\psi^p}\right)^2} d\psi^p \left[\int_0^1 \sqrt{1 + \left(\frac{d\xi_A^c}{d\psi^c}\right)^2} d\psi^c \right]^{-1}. \quad (5.16)$$

The derivative terms in Eq. (5.16) are functions of c^c after the dependency of the trailing edge thickness is a function of the chord c^c (Eq. (5.3)). Thus, Eq. (5.16) can be also represented as:

$$c^c = f(c^c). \quad (5.17)$$

Relation (5.17) is solved via a fixed-point iterative approach. This method converges to the correct solution if the initial guess is close to the actual chord and the derivative is smaller than one. This is generally true since chord changes are small and the child chord can easily be calculated for moderate deformations.

With c^c calculated, the value for the trailing edge $\Delta\xi_{TE}^c$ is known via Eq. (5.3). To apply the restrictions related to the spars, the spar locations for the child configuration are determined. Since

the arc lengths along the passive surface from the leading edge to each spar are the same for both configurations, the spar locations $\psi_{P,j}^c$ are numerically calculated for each spar via:

$$L_P^c(\psi_{P,j}^c) = c^c \int_0^{\psi_{P,j}^c} \sqrt{1 + \left(\frac{d\xi_P^c}{d\psi^c}\right)^2} d\psi^c = c^p \int_0^{\psi_j^p} \sqrt{1 + \left(\frac{d\xi_P^p}{d\psi^p}\right)^2} d\psi^p = L_P^p(\psi_j^p) \quad (5.18)$$

5.4.2 Constant angles assumptions for forwards calculation

The assumption of constant spar intersection angle with the passive surface is used to determine spar orientations. In forwards calculation, the parent spars are vertically aligned while the child spars must translate and rotate to accommodate camber morphing. Therefore:

$$\mathbf{s}^c(\psi_{P,j}^c) = \begin{pmatrix} s_1^c(\psi_{P,j}^c) \\ s_2^c(\psi_{P,j}^c) \end{pmatrix}, \quad (5.19)$$

$$\mathbf{s}^p(\psi_j^p) = \begin{pmatrix} 0 \\ 1 \end{pmatrix}. \quad (5.20)$$

As depicted in Fig. 5.6, the mathematical definition of the angle β_j between spar j and the passive OML is the internal product between a unit vector \mathbf{t}_j tangent to the airfoil surface and a unit vector \mathbf{s}_j affixed to the spar:

$$\cos(\beta_j) = \mathbf{s}_j \cdot \mathbf{t}_j, \quad (5.21)$$

where the normalized tangent vector at a point ψ_j for any surface is given by:

$$\mathbf{t}_j = \begin{pmatrix} t_{1,j} \\ t_{2,j} \end{pmatrix} = \frac{1}{\sqrt{1 + \left(\frac{d\xi(\psi_j)}{d\psi}\right)^2}} \begin{pmatrix} 1 \\ \frac{d\xi(\psi_j)}{d\psi} \end{pmatrix} \quad (5.22)$$

and the inner product between \mathbf{s}_j^p and \mathbf{t}_j^p at the passive surface for the parent airfoil is then:

$$\cos(\beta_j) = \mathbf{s}_j^p \cdot \mathbf{t}_j^p = \frac{1}{\sqrt{1 + \left(\frac{d\xi_P^p(\psi_j^p)}{d\psi}\right)^2}} \frac{d\xi_P^p(\psi_j^p)}{d\psi}. \quad (5.23)$$

From the definition of a unit vector and the inner product between the tangent and spar vectors for the child airfoil, the following system of equations is formulated to determine the components of vector \mathbf{s}_j^c :

$$\begin{aligned} s_1^c(\psi_{P,j}) t_1^c(\psi_{P,j}) + s_2^c(\psi_{P,j}) t_2^c(\psi_{P,j}) &= \cos(\beta_j), \\ s_1^c(\psi_{P,j})^2 + s_2^c(\psi_{P,j})^2 &= 1. \end{aligned} \quad (5.24)$$

Solving the system of equations (5.24) for $s_2^c(\psi_j^c)$, there are two solutions, but only one is physically meaningful. The unique solution is:

$$\begin{aligned} s_1^c(\psi_{P,j}) &= \frac{\cos(\beta_j) - t_2^c(\psi_{P,j})[t_2^c(\psi_{P,j}) \cos(\beta_j) + t_1^c(\psi_{P,j}) \sin(\beta_j)]}{t_1^c(\psi_{P,j})}, \\ s_2^c(\psi_{P,j}) &= t_2^c(\psi_{P,j}) \cos(\beta_j) + t_1^c(\psi_{P,j}) \sin(\beta_j). \end{aligned} \quad (5.25)$$

After calculating the location and orientation of the spars, these geometric properties are used to determine the intersection of the spars with the active surface $(\psi_{A,j}, \xi_A^c(\psi_{A,j}))$ via:

$$\begin{pmatrix} \psi_{A,j}^c \\ \xi_A^c(\psi_{A,j}^c) \end{pmatrix} = \begin{pmatrix} \psi_{P,j}^c \\ \xi_P^c(\psi_{P,j}^c) \end{pmatrix} + \text{sgn}(\Delta\xi) h_j^c \begin{pmatrix} s_1^c(\psi_{P,j}^c) \\ s_2^c(\psi_{P,j}^c) \end{pmatrix}. \quad (5.26)$$

With all the spar heights h_j known, the system of equations (5.13) is solved, and the dependent \mathbf{A}^c vector is calculated.

5.4.3 Discussion and summary for forwards calculation

A step-by-step algorithm for calculating the forwards structurally consistent airfoils is provided in Table 5.1. The conventional NACA0008 airfoil is used as the parent (reference) airfoil for a fifth order CST to demonstrate the capabilities of this framework. Fig. 5.7 contains four examples of

structurally consistent airfoils with actuators placed either on the lower or upper surface. According to the chosen passive shape coefficients P^c , negative and positive camber are generated from an initially symmetric airfoil during morphing. As the shape changes, the camber and spar orientations also change. This demonstrates the capabilities of this framework for forwards calculation.

5.4.4 Finite Element Analysis validation of forwards calculation

Finite element analysis (FEA) is used to numerically validate the structurally consistent CST equations. The model in Fig. 5.8 solely consists of shell elements. In this example, the active surface is the lower surface. Strains are defined for the active surface components to generate approximately equivalent strains to the deformed CST configuration. The FEA strains are not point-wise equivalent to the CST; instead the average strains for the six regions delimited by spars are used. For this model, the out of plane dimension is neglected and the converged mesh consists of 1734 S4R elements. The comparison between FEA and CST for varying strains is depicted in Fig. 5.9. For small deflections, e.g., strains $\leq 1.1\%$, the structurally consistent CST equations and the FEA model generate the same deformed OML as shown in Fig. 5.9a. The Hausdorff distance is 0.0022, which is quantitatively similar to the obtained values during initial curve fitting in Section 4.2.1 (0.0013 and 0.0028). However, the structurally consistent CST equations slightly underpredict the morphing calculated for greater deflections. A case with moderate deflections (strains $\leq 4\%$) was also analyzed as shown in Fig. 5.9b and a Hausdorff distance of 0.0069 was obtained. An additional case with even greater deflections (strains $\leq 5.5\%$) was evaluated as depicted in Fig. 5.9c and a Hausdorff distance of 0.0098 was obtained. Comparing the three morphing configurations, the assumption of constant passive surface length assumption appears to be invalid for strains exceeding 4%. In summary, the developed framework is accurate for strains up to 4% and provides good estimates for higher strains with only the use of kinematic relations.

1. Calculate chord until convergence (initial guess $c^c = c^p$)

a. Find shape coefficients satisfying constant leading edge radius assumption via Eq. (5.5)

$$\begin{pmatrix} P_0^c \\ A_0^c \end{pmatrix} = \sqrt{\frac{c^p}{c^c}} \begin{pmatrix} P_0^p \\ A_0^p \end{pmatrix}$$

b. Solve Eq. (5.16) via fixed point iteration to find children chord c^c satisfying assumptions

$$c^c = c^p \int_0^1 \sqrt{1 + \left(\frac{d\xi_P^p(\psi^p)}{d\psi^p} \right)^2} d\psi^p \left[\int_0^1 \sqrt{1 + \left(\frac{d\xi_P^c(\psi^c)}{d\psi^c} \right)^2} d\psi^c \right]^{-1}$$

where:

$$\frac{d\xi_P}{d\psi} = \sum_{i=0}^n P_i K_{i,n} \frac{\psi^i (1-\psi)^{n-i}}{2\psi^{0.5}} [-(3+2n)\psi + 1 + 2i] + \frac{\Delta\xi_{TE}}{2}$$

2. Spar location calculation

For each spar:

a. Find children configuration coordinate $\psi_{P,j}^c$ for spar j that satisfies Eq. (5.18)

$$c^p \int_0^{\psi_{P,j}^p} \sqrt{1 + \left(\frac{d\xi_P^p}{d\psi^p} \right)^2} d\psi^p = c^c \int_0^{\psi_{P,j}^c} \sqrt{1 + \left(\frac{d\xi_P^c}{d\psi^c} \right)^2} d\psi^c$$

b. Calculate angle β_j between spar and passive surface from parent airfoil via Eq. (5.23)

$$\cos(\beta_j) = \frac{1}{\sqrt{1 + \left(\frac{d\xi_P^c(\psi_{P,j}^c)}{d\psi^p} \right)^2}} \frac{d\xi_P^c(\psi_{P,j}^c)}{d\psi^p}$$

c. Use system of Eqs. (5.25) to find spar orientation components s_j^c and s_j^c for child airfoil

$$s_1^c(\psi_{P,j}^c) = \frac{\cos(\beta_j) - t_2^c(\psi_{P,j}^c)[t_2^c(\psi_{P,j}^c)\cos(\beta_j) + t_1^c(\psi_{P,j}^c)\sin(\beta_j)]}{t_1^c(\psi_{P,j}^c)},$$

$$s_2^c(\psi_{P,j}^c) = t_2^c(\psi_{P,j}^c)\cos(\beta_j) + t_1^c(\psi_{P,j}^c)\sin(\beta_j)$$

d. Find spar heights h_j^p for parent airfoil using Eq. (5.8)

$$h_j^p = |\xi_P^p(\psi_j^p) - \xi_A^p(\psi_j^p)|$$

e. Find spar intersections with active surface $(\psi_{A,j}^c, \xi_A^c(\psi_{A,j}^c))$ via Eq. (5.26)

$$\begin{pmatrix} \psi_{A,j}^c \\ \xi_A^c(\psi_{A,j}^c) \end{pmatrix} = \begin{pmatrix} \psi_{P,j}^c \\ \xi_P^c(\psi_{P,j}^c) \end{pmatrix} + \text{sgn}(\Delta\xi) h_j^c \begin{pmatrix} s_1^c(\psi_{P,j}^c) \\ s_2^c(\psi_{P,j}^c) \end{pmatrix}$$

3. Find active shape coefficients \mathbf{A} (Eq. (5.13))

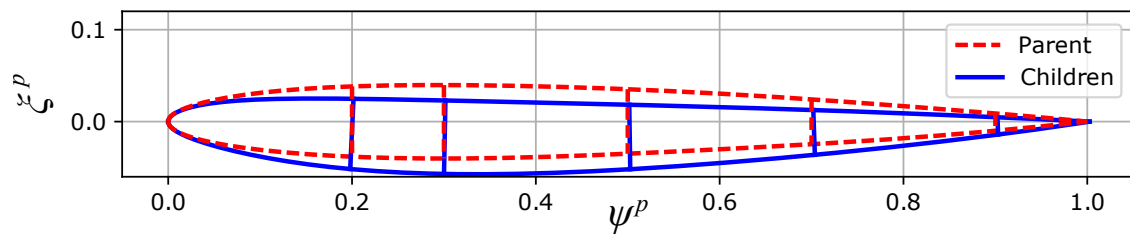
$$\mathbf{A} = \mathbf{F}^{-1}\mathbf{f}$$

where:

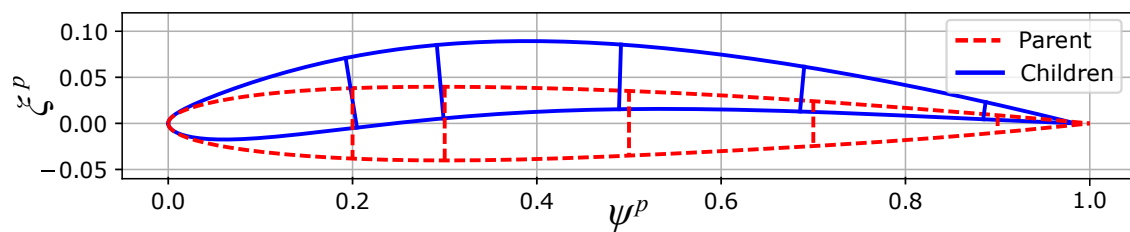
$$F_{ji} = K_{i,n}(\psi_{A,j}^c)^i(1-\psi_{A,j}^c)^{n-i}$$

$$f_j = \frac{2 \text{sgn}(\Delta\xi) \xi_A^c(\psi_{A,j}^c) + \psi_{A,j}^c \Delta\xi_{TE}^c}{2\sqrt{\psi_{A,j}^c(\psi_{A,j}^c - 1)}} - A_0(1-\psi_{A,j}^c)^n$$

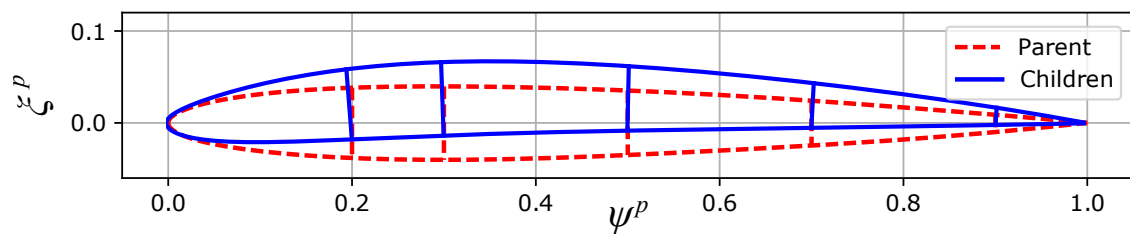
Table 5.1: Forward calculation: algorithm to compute dependent shape coefficients for child airfoil.



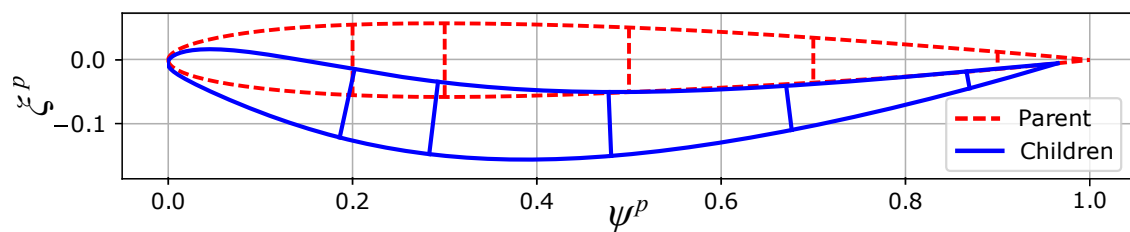
(a) Actuators expand lower surface; child OML with all passive shape coefficients equal to 0.05 except for P_0 .



(b) Actuators contract lower surface; child OML with all passive shape coefficients equal to 0.25 except for P_0 .



(c) Actuators expand upper surface; child OML with all passive shape coefficients equal to 0.02 except for P_0 .



(d) Actuators contract upper surface; child OML with all passive shape coefficients equal to 0.3 except for P_0 .

Figure 5.7: Example of structurally consistent forwards calculation with a NACA0008 as the parent airfoil.

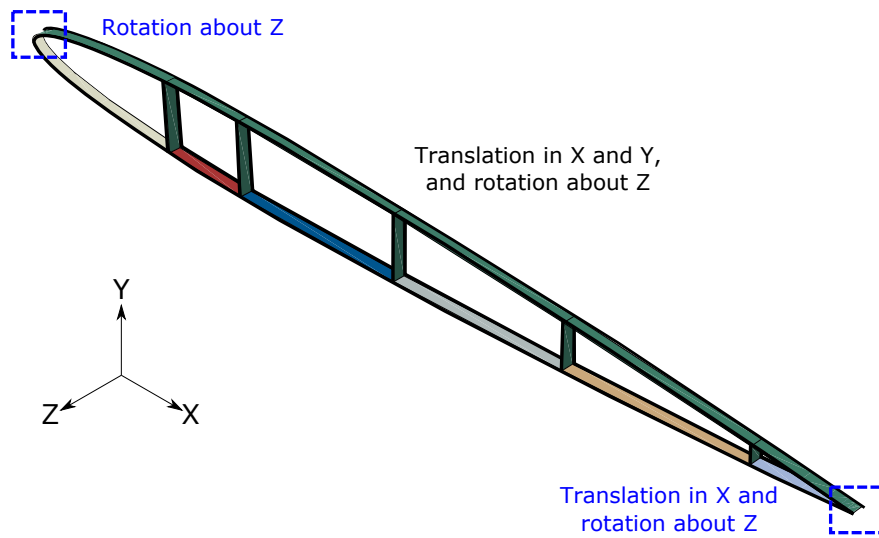
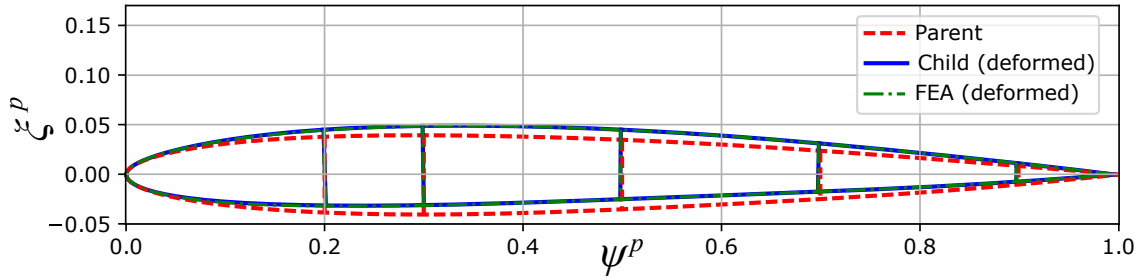
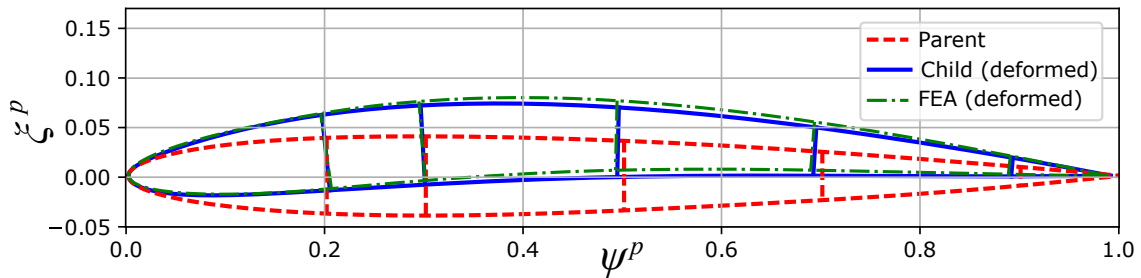


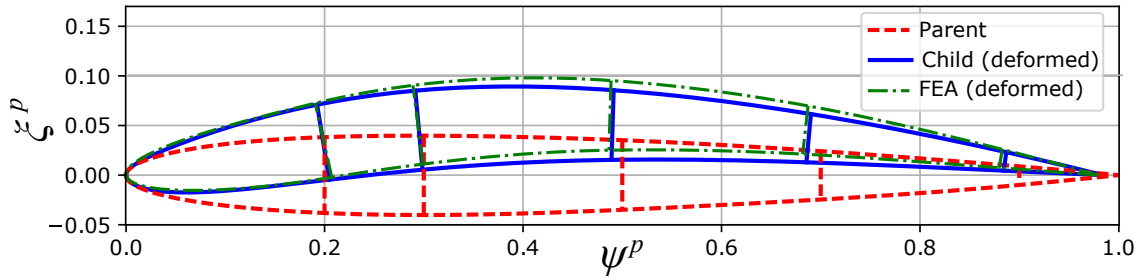
Figure 5.8: Schematic description of the finite element model for the morphing wing section showing permitted degrees of freedom.



(a) Comparison for $P^c = \{0.1113, 0.1487, 0.1084, 0.1508, 0.1092, 0.1284\}$ (Hausdorff distance of 0.0022).



(b) Comparison for $P^c = \{0.1117, 0.2187, 0.1784, 0.2208, 0.1792, 0.1984\}$ (Hausdorff distance of 0.0069).



(c) Comparison for $P^c = \{0.1097, 0.2500, 0.2500, 0.2500, 0.2500, 0.2500\}$ (Hausdorff distance of 0.0098).

Figure 5.9: Numerical validation of structurally consistent CST via refined FEA for forwards calculation with actuators on lower surface.

5.5 Backwards calculation

For backwards calculation, the parent design is the deformed configuration and the children designs represent all structurally feasible reference (i.e., strain-free) configurations. The implementation of backwards calculation is useful for designing high-performance reference airfoils that can morph into a desired OML for a given flight configuration. As an example, avian-inspired airfoils are highly cambered geometries that have been naturally selected for low Reynolds flight, but are unsuitable for use at high Reynolds [165]. Thus, to use such an airfoil efficiently, Leal *et al.* [170] optimized a low-camber cruise airfoil that could morph into an avian-inspired airfoil and validated the kinematic results using a high-fidelity finite element model. As mentioned before, the spanwise wing spars are assumed rigid and also play a major role in constraining the chordwise OML. This follows the mathematical formulation of Section 5.4, but is presented in some detail for completeness. The child airfoil spars are assumed vertical because aircraft are fabricated with vertical spars. Therefore, the connection points of the spar with upper and lower surfaces share the same ψ^c coordinates, and spar heights $h_j^c = \xi_u^c(\psi_j^c) - \xi_l^c(\psi_j^c) = |\xi_P^c(\psi_j^c) - \xi_A^c(\psi_j^c)|$ for spars $j = 1, \dots, m$. It follows from Eqs. (5.1) and (5.2) that the spar heights are:

$$h_j^c = |\xi_P^c(\psi_j^c) - \xi_A^c(\psi_j^c)| = \text{sgn}(\Delta\xi) \left[\sqrt{\psi_j^c(1 - \psi_j^c)} \sum_{i=0}^n (P_i^c + A_i^c) K_{i,n}(\psi_j^c)^i (1 - \psi_j^c)^{n-i} + \psi_j^c \Delta\xi_{TE}^c \right]. \quad (5.27)$$

It is convenient to define $P_i^c + A_i^c$ as a single variable \bar{A}_i so that Eq. (5.27) can be rewritten as:

$$h_j^c = \text{sgn}(\Delta\xi) \left[\sqrt{\psi_j^c(1 - \psi_j^c)} \sum_{i=0}^n \bar{A}_i K_{i,n}(\psi_j^c)^i (1 - \psi_j^c)^{n-i} + \psi_j^c \Delta\xi_{TE}^c \right]. \quad (5.28)$$

We have from Eq. (5.28) that for a Bernstein polynomial of n -order, the OML can only be subject to a maximum of n thickness constraints. It is possible to obtain an analytical solution for Bernstein polynomial of order one [3]. However, an analytical solution is impractical or even infeasible for n -order Bernstein polynomial equations with m restrictions (i.e., m spars). Never-

theless, the linear system of equations can be numerically solved. Considering that the leading edge radius for both airfoils are the same (Eq. (5.5)), the thickness restriction function (Eq. (5.28)) is modified so that only components with unknown variables \bar{A}_i are on the right-hand side:

$$\frac{\text{sgn}(\Delta\xi) h_j^c - \psi_j^c \Delta\xi_{TE}^c}{\sqrt{\psi_j^c(1 - \psi_j^c)}} - \bar{A}_0(1 - \psi_j^c)^n = \sum_{i=1}^n \bar{A}_i K_{i,n} (\psi_j^c)^i (1 - \psi_j^c)^{n-i}, \quad (5.29)$$

which can be also represented as:

$$b_j = \sum_{i=1}^m B_{ji} \bar{A}_i \quad \text{or} \quad \mathbf{b} = \mathbf{B} \bar{\mathbf{A}}, \quad (5.30)$$

where $\bar{\mathbf{A}}$ is the equivalent shape coefficient vector (n dimensional), \mathbf{b} is the backwards thickness restriction vector (m dimensional), given by

$$b_j = \frac{\text{sgn}(\Delta\xi) h_j^c - \psi_j^c \Delta\xi_{TE}^c}{\sqrt{\psi_j^c(1 - \psi_j^c)}} - \bar{A}_0(1 - \psi_j^c)^n, \quad (5.31)$$

and \mathbf{B} is the backwards shape function matrix ($m \times n$ dimensional), given as

$$B_{ji} = K_{i,n} (\psi_j^c)^i (1 - \psi_j^c)^{n-i}. \quad (5.32)$$

\mathbf{B} is a non-negative tensor where all components are non-zero since no spars are located at the leading ($\psi = 0$) or trailing edges ($\psi = 1$). In the case where $n = m$, \mathbf{B} is a square tensor. Since \mathbf{B} is invertible, the solution for the linear system of equations is:

$$\bar{\mathbf{A}} = \mathbf{B}^{-1} \mathbf{b}. \quad (5.33)$$

Except for defining spars as rigid, no other assumptions have been herein considered in this section. The trailing edge thickness $\Delta\xi_{TE}^c$ and spar heights h_j^c are still unknown since the spar location for the children configurations and the orientation for the parent configurations are unknown. The following sections will handle the calculation of \mathbf{b} and \mathbf{B} through the assumptions.

5.5.1 Constant length and angles assumptions for backwards calculation

Using the same assumptions for constant passive surface length and constant relative spar angles, the equations obtained for forwards and backwards calculation are similar. Only the most relevant steps that differ from backwards calculation are demonstrated here to avoid repetition. As indicated in Fig. 5.10, children airfoils have vertical spars in backwards calculation problems so the connection points of the spar with the passive and active surfaces have the same ψ -coordinate ψ_j^c , which is not true for the parent configuration. For the parent, the ψ -coordinate for the passive connection points are denoted as $\psi_{P,j}^p$ while for the active connection points they are denoted as $\psi_{A,j}^p$. From the constant passive surface length assumption, the arc length from the leading edge up to the spar location $\psi_{P,j}^p$ is the same for both configurations such that

$$L_P^c(\psi_j^c) = L_P^p(\psi_{P,j}^p), \quad (5.34)$$

and the unit vectors \mathbf{s}_j affixed to a spar j for the child and parent configurations are:

$$\mathbf{s}^c(\psi_j^c) = \begin{pmatrix} 0 \\ 1 \end{pmatrix}, \quad (5.35)$$

$$\mathbf{s}^p(\psi_{P,j}^p) = \begin{pmatrix} s_1^p(\psi_{P,j}^p) \\ s_2^p(\psi_{P,j}^p) \end{pmatrix}. \quad (5.36)$$

For backwards calculation, the inner product between the unit spar vector \mathbf{s} and the tangent vector \mathbf{t} is given by:

$$\cos(\beta_j) = \mathbf{s}_j^c \cdot \mathbf{t}_j^c = \frac{1}{\sqrt{1 + \left(\frac{d\xi_P^c(\psi_j^c)}{d\psi}\right)^2}} \frac{d\xi_P^c(\psi_j^c)}{d\psi}. \quad (5.37)$$

From the assumption of constant angles between spars and passive surfaces, the components

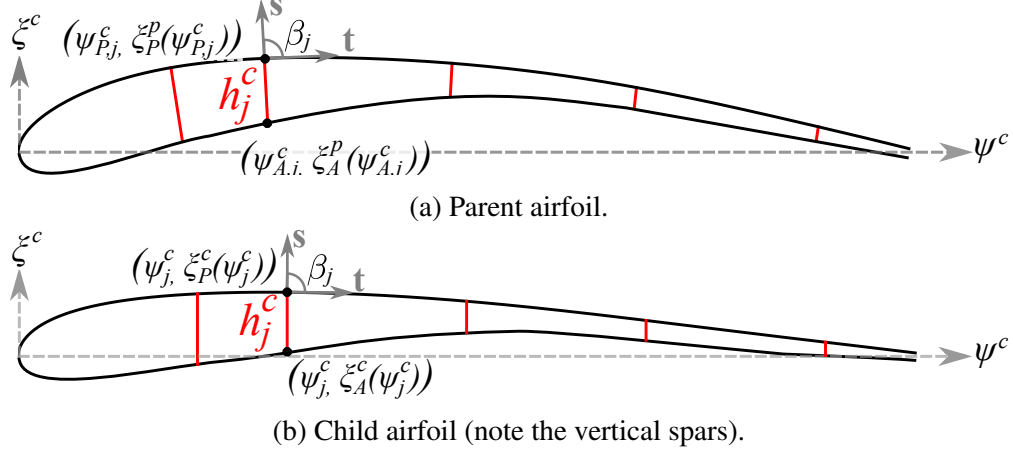


Figure 5.10: Description of backwards calculation in the case of an avian-inspired airfoil.

of the parent spar orientation vector are:

$$s_1^p(\psi_{P,j}^p) = \frac{\cos(\beta_j) - t_2^p(\psi_{P,j}^p)[t_2^p(\psi_{P,j}^p) \cos(\beta_j) + t_1^p(\psi_{P,j}^p) \sin(\beta_j)]}{t_1^p(\psi_{P,j}^p)}, \quad (5.38)$$

$$s_2^p(\psi_{P,j}^p) = t_2^p(\psi_{P,j}^p) \cos(\beta_j) + t_1^p(\psi_{P,j}^p) \sin(\beta_j).$$

After obtaining the location and orientation of the spars, the heights of the spars are calculated from the definition of the spar vector. From Fig. 5.10, the vector that connects $(\psi_{P,j}^p, \xi_P^p(\psi_{P,j}^p))$ and $(\psi_{A,j}^p, \xi_P^p(\psi_{A,j}^p))$ has unit vector \mathbf{s}_j and magnitude h_j . Therefore:

$$\begin{pmatrix} \psi_{P,j}^p \\ \xi_P^p(\psi_{P,j}^p) \end{pmatrix} - \text{sgn}(\Delta\xi) h_j \begin{pmatrix} s_1^p(\psi_{P,j}^p) \\ s_2^p(\psi_{P,j}^p) \end{pmatrix} = \begin{pmatrix} \psi_{A,j}^p \\ \xi_A^p(\psi_{A,j}^p) \end{pmatrix}. \quad (5.39)$$

The system of two Eqs. (5.39) for two unknowns h_j and $\psi_{A,j}^p$ can be manipulated to give:

$$\psi_{A,j}^p = \psi_{P,j}^p + \frac{s_1^p(\psi_{P,j}^p)}{s_2^p(\psi_{P,j}^p)} [\xi_A^p(\psi_{A,j}^p) - \xi_P^p(\psi_{P,j}^p)], \quad (5.40)$$

$$h_j = \text{sgn}(\Delta\xi) \frac{\xi_P^p(\psi_{P,j}^p) - \xi_A^p(\psi_{A,j}^p)}{s_2^p(\psi_{P,j}^p)}. \quad (5.41)$$

A fixed-point iterative method is used to solve Eq. (5.40) because it is an equation that defines $\psi_{A,j}^p$ implicitly. With all the spar heights h_j known, the system of Eqs. (5.33) is solved and the dependent \mathbf{A}^c vector is calculated based on the definition of the equivalent shape coefficient vector:

$$\mathbf{A}^c = \bar{\mathbf{A}} - \mathbf{P}^c. \quad (5.42)$$

5.5.2 Discussion and summary for backwards calculation

The step-by-step algorithm is summarized for the reader in Table 5.2. A first-order CST (i.e., single-parameter) is used to demonstrate the influence of child shape coefficient \mathbf{P}^c over the child chord. The trailing edge thickness is set to zero, the parent chord c^p is one, and the shape coefficients are all initially set to 0.2. From Eq. (5.16), c^c is inversely proportional to P_0^c as is depicted in Fig. 5.11. As camber increases the chord must decrease to maintain the same arc length for the child configuration. The parent OML is not affected by the change of shape coefficient, but the spar orientation and heights are modified as shown in Fig. 5.12. Since P_0^c increases, the ratio between the arc lengths from the leading edge to the spar and the spar to the trailing edge increases. Consequently, the spar is calculated to be closer to the trailing edge (i.e., $\psi_{P,j}^p$ increases according to Eq. (5.18)), and the spar orientation is rotated in a counterclockwise manner (i.e., β_j increases according to Eq. (5.37)).

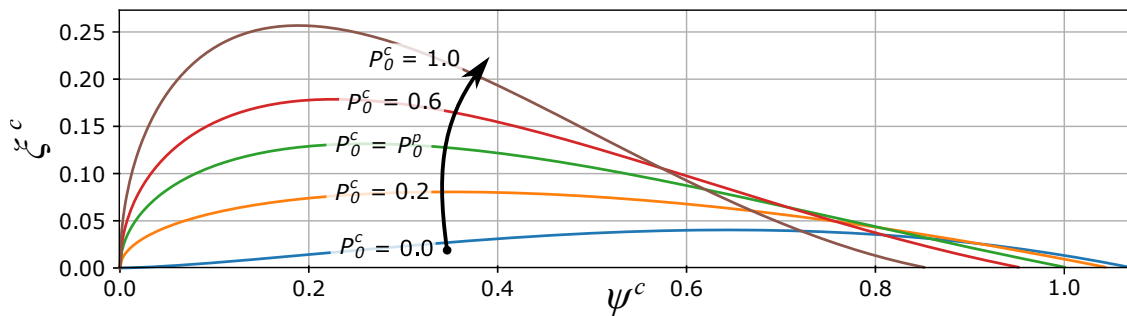


Figure 5.11: Influence of P_0^c over upper surface OML and chord of children airfoil sections for backwards calculation (actuators on lower surface). Note the conservation of arc length.

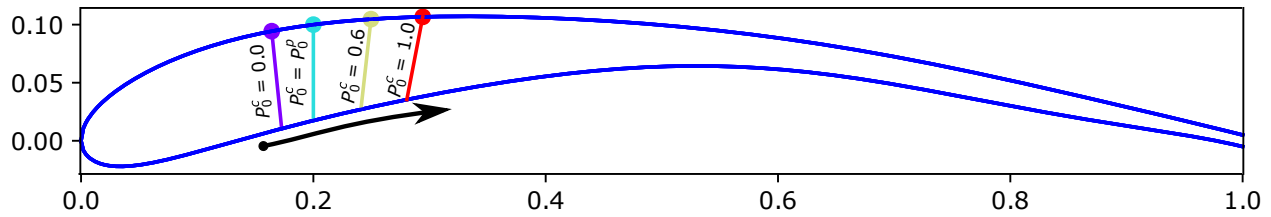


Figure 5.12: Influence of P_0^c over spars direction and height for parent geometry for backwards calculation with actuator on lower surface. Spars are vertical in the strain-free parent configuration.

Fig. 5.13 contains multiple examples for fifth-order CST equations representing the unorthodox, avian-inspired F0808 airfoil held as the parent (morphed) configuration. Actuators are assumed to be placed alternatively on the upper or lower surfaces in various sub-figures. Depending on the chosen children shape coefficients, an increase or decrease of camber and actuator lengths are generated while all geometric constraints remain satisfied, demonstrating the capabilities of the framework. Note how the location and direction of the spars change, but the spar heights do not. Furthermore, the airfoil chord is altered due to camber morphing, but the trailing edge thickness remains fixed. This novel airfoil parameterization allows for realistic reference configurations while allowing great flexibility in choosing shape parameters.

1. Calculate chord until convergence (initial guess $c^c = c^p$)

a. Find shape coefficients that satisfies constant leading edge radius assumption via Eq. 5.5

$$\begin{pmatrix} P_0^c \\ A_0^c \end{pmatrix} = \sqrt{\frac{c^p}{c^c}} \begin{pmatrix} P_0^p \\ A_0^p \end{pmatrix}$$

b. Solve Eq. (5.16) via fixed point iteration to find children chord c^c satisfying assumptions

$$c^c = c^p \int_0^1 \sqrt{1 + \left(\frac{d\xi_P^p(\psi^p)}{d\psi^p} \right)^2} d\psi^c \left[\int_0^1 \sqrt{1 + \left(\frac{d\xi_P^c(\psi^c)}{d\psi^c} \right)^2} d\psi^p \right]^{-1}$$

where:

$$\frac{d\xi_P}{d\psi} = \sum_{i=0}^n P_i K_{i,n} \frac{\psi^i (1-\psi)^{n-i}}{2\sqrt{\psi}} [-(3+2n)\psi + 1 + 2i] + \frac{\Delta\xi_{TE}}{2}$$

2. Spar height calculation

a. Find parent configuration coordinate $\psi_{P,j}^c$ for spar j that satisfies Eq. (5.18)

$$c^p \int_0^{\psi_{P,j}^p} \sqrt{1 + \left(\frac{d\xi_P^p(\psi^p)}{d\psi^p} \right)^2} d\psi^c = c^c \int_0^{\psi_{P,j}^c} \sqrt{1 + \left(\frac{d\xi_P^c(\psi^c)}{d\psi^c} \right)^2} d\psi^p$$

b. Find angle β_j between spar and passive surface for child airfoil using Eq. (5.37)

$$\cos(\beta_j) = \frac{1}{\sqrt{1 + \left(\frac{d\xi_P^c(\psi_{P,j}^c)}{d\psi^c} \right)^2}} \frac{d\xi_P^c(\psi_{P,j}^c)}{d\psi^c}$$

c. Use Eq. (5.38) to find spar orientation components s_j^p and t_j^p for parent configuration

$$s_1^p(\psi_{P,j}^p) = \frac{\cos(\beta_j) - t_2^p(\psi_{P,j}^p)[t_2^p(\psi_{P,j}^p) \cos(\beta_j) + t_1^p(\psi_{P,j}^p) \sin(\beta_j)]}{t_1^p(\psi_{P,j}^p)},$$

$$s_2^p(\psi_{P,j}^p) = t_2^p(\psi_{P,j}^p) \cos(\beta_j) + t_1^p(\psi_{P,j}^p) \sin(\beta_j)$$

d. Find spar coordinate $\psi_{A,j}^p$ via Eq. (5.40)

$$\psi_{A,j}^p = \psi_{P,j}^p + \frac{s_1^p(\psi_{P,j}^p)}{s_2^p(\psi_{P,j}^p)} [\xi_A^p(\psi_{A,j}^p) - \xi_u^p(\psi_{P,j}^p)]$$

e. Find spar heights h_j using Eq. (5.41)

$$h_j = \text{sgn}(\Delta\xi) \frac{\xi_P^p(\psi_{P,j}^p) - \xi_A^p(\psi_{A,j}^p)}{s_2^p(\psi_{P,j}^p)}$$

3. Solve system of equations (Eq. 5.33)

$$\bar{\mathbf{A}} = \mathbf{B}^{-1}\mathbf{b}$$

where:

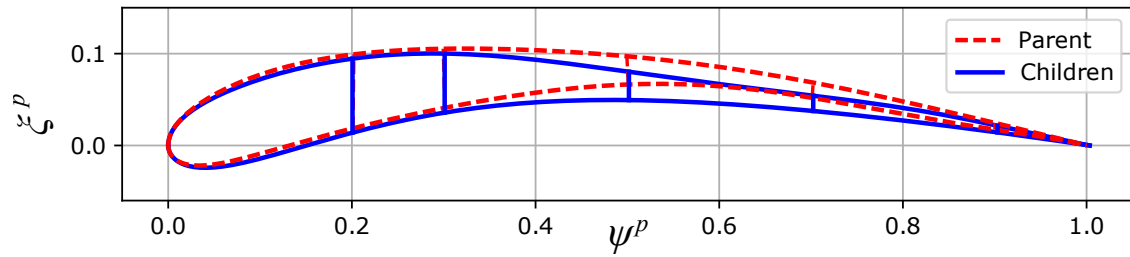
$$b_j = \frac{\text{sgn}(\Delta\xi) h_j^c - \psi_j^c \Delta\xi_{TE}^c}{\sqrt{\psi_j^c(1-\psi_j^c)}} - \bar{A}_0(1-\psi_j^c)^n,$$

$$B_{ji} = K_{i,n}(\psi_j^c)^i(1-\psi_j^c)^{n-i}$$

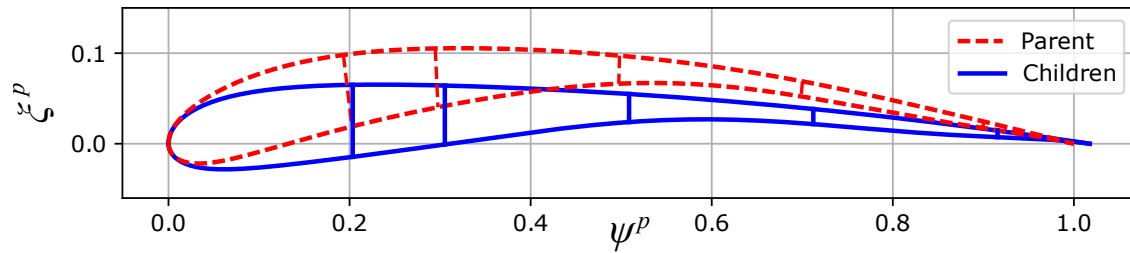
4. Find active shape coefficients \mathbf{A}^c via Eq. (5.42)

$$\mathbf{A}^c = \bar{\mathbf{A}} - \mathbf{P}^c$$

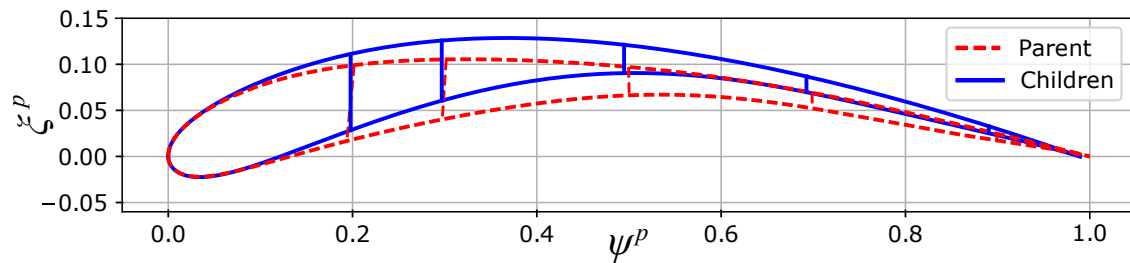
Table 5.2: Backwards calculation: algorithm to calculate dependent shape coefficients for child airfoil.



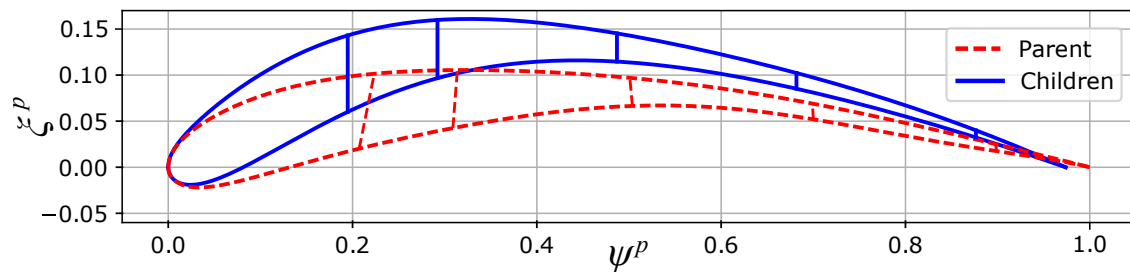
(a) Actuator placed on *lower* surface: Child OML with all independent passive shape coefficients equal to 0.15.



(b) Actuator placed on *upper* surface: Child OML with all independent passive shape coefficients equal to 0.15.



(c) Actuator placed on *lower* surface: Child OML with all independent passive shape coefficients equal to 0.35.



(d) Actuator placed on *upper* surface: Child OML with all independent passive shape coefficients equal to 0.35.

Figure 5.13: Example of structurally consistent backwards calculation considering an F0808 airfoil [165] as parent (i.e., as the morphed shape).

5.6 Conclusions

A novel structurally consistent kinematic model for skin-based camber morphing was developed herein based on appropriately constrained Class/Shape Transformation (CST) relations. Assumptions were made regarding the rigidity of the spars and of the active or passive nature of upper and lower skins. A designer invoking this framework can generate a wide range of feasible children configurations based on a parent configuration with little computational cost. The parent OML, assumed to be fully defined, can either be the reference strain-free OML (forwards calculation) or the final deformed OML (backwards calculation) according to the design application. Design features were explored using the examples of a NACA0008 (forwards calculation) and an avian-inspired F0808 airfoil (backwards calculation) as the parent airfoils. Results indicate that structurally consistent airfoils are obtainable for increasing and decreasing camber designs with actuators placed on either the lower or upper surfaces. Despite the restrictions of structural consistency, chord and spar orientations are necessarily altered as the structure morphs. The framework permits closed-form numerical solution, and even simpler analytical solutions can be developed for sufficiently simple CST formulations. When compared to an FEA model with equivalent average strains on the morphing skin selected, the structurally consistent CST equations accurately calculate morphing deflections for moderate deformations (strains $\leq 4\%$). Structurally consistent airfoils allow quick analysis of morphing wings without the need for full structural analysis for a preliminary assessment. Consequently, optimizations and other design processes that might suffer from the complexity of run time for the finite element model can now be performed.

The original CST methods were originally developed for 3D representations of aerospace forms. Therefore, the framework herein can be further expanded for fully 3D structurally consistent wings that include other structure restrictions such as ribs, control surfaces, and spanwise spar restrictions; this work is ongoing. Other future research will study the effects of morphing on aerodynamic improvements according to reference configuration, internal structure, and actuation technology.

6. DESIGN AND OPTIMIZATION OF MORPHING STRUCTURES*

The previous three chapters introduced the improved CST equations and the structurally consistent implementation. Herein, their implementation is proposed for preliminary rapid aircraft design. The design domain expanded by morphing is nontrivial and nonlinear, requiring tools such as design of experiments (DOE) and optimization frameworks. The main goal of the design exploration is not necessarily to achieve a final optimal design but to facilitate decision making. For this intent, a parameterized optimization algorithm is implemented. These features are beneficial to morphing structures, which are most advantageous when considering performance across multiple flight conditions. The methodology is implemented for a civil utility subsonic aircraft to demonstrate that a fixed airfoil is unable to reproduce the aerodynamic performance of a wing utilizing morphing.

In a typical aircraft design process, the designer is tasked with selecting an airfoil with acceptable performance throughout its flight. Concept selection typically happens in the earliest stages of design, and designers are asked to make preliminary design decisions with little information and much uncertainty [171]. To further pressure a designer, concept selection is a very consequential step of the design process and can affect everything that follows. Malak and Paredis [172] echo this sentiment stating that “no amount of detail engineering can compensate for a poorly chosen concept”. A sound concept selection method is vital to the success or failure of the design process. Therefore, a concept selection method is proposed for the design of morphing airfoils that considers many flight conditions.

6.1 Methodology

The current morphing aero-structural design problem can be formulated as a multi-parametric optimization problem, where the single objective is to maximize the lift-to-drag ratio. This ratio is

*Part of the data reported in this chapter is reprinted with permission from "Parametric Optimization for Morphing Structures Design: Application to Morphing Wings Adapting to Changing Flight Conditions" by Weaver-Rosen, J., Leal, P., Hartl, D., and Malak, R., 2020, Structural and Multidisciplinary Optimization.

determined by calculating the coefficients of lift and drag using XFOIL [158], a subsonic panel-method aerodynamic solver. The operational parameters considered are the angle of attack α and airspeed V , all of which vary during flight. For this design problem, the optimization variables are the shape coefficients of the child (morphed) airfoil P_i^c for $i = [1, 2, 3, 4]$, where each coefficient is spatially predominant in a different chordwise location. Together, the four shape coefficients define the airfoil shape. P_1^c and P_4^c dominate the leading and trailing edges, respectively, while P_2^c and P_3^c are most relevant for intermediate chordwise coordinates. All other aspects of the problem, such as the initial parent shape coefficients and spar locations, are held constant for each parametric optimization (see Table 6.1 for parent shape coefficients \mathbf{P}^p and \mathbf{A}^p). Thus, the mathematical problem formulation is:

$$J^*(\alpha, V) = \max_{\mathbf{P}^c} J(\mathbf{P}^c; \alpha, V),$$

Subject to:

$$\begin{aligned} \mathbf{A} &\in \mathbb{A}^c, \\ \begin{bmatrix} 0^\circ \\ 20 \text{ m/s} \end{bmatrix} &\leq \begin{bmatrix} \alpha \\ V \end{bmatrix} \leq \begin{bmatrix} 12^\circ \\ 65 \text{ m/s} \end{bmatrix}, \end{aligned} \tag{6.1}$$

where $J^*(\alpha, V)$ represents the maximum lift-to-drag ratio as a function of the parameters determined by the parametric optimization (section 6.1.1), \mathbb{A} is the domain of feasible active (i.e., lower) shape coefficients imposed by a non-linear constraint (section 6.1.2), and the objective function J represents the lift-to-drag ratio. Expected values, defined for this work as the convolution of aircraft performance with aircraft flight data (section 6.1.3) and other metrics are utilized to determine the “best” airfoil according to concept selection (section 6.1.4).

6.1.1 Parametric optimization

Parametric optimization is different from traditional optimization in that it solves an optimization problem as a function of some parameters that are currently unknown to or uncontrolled by

Table 6.1: Shape coefficients for parent (reference) airfoils considered in this work from which all morphed configurations are generated.

NACA 0012	P_0^p	P_1^p	P_2^p	P_3^p	P_4^p
	0.1828	0.1179	0.2079	0.0850	0.1874
	A_0^p	A_1^p	A_2^p	A_3^p	A_4^p
	0.1828	0.1179	0.2079	0.0850	0.1874
NACA 4415	P_0^p	P_1^p	P_2^p	P_3^p	P_4^p
	0.2590	0.3113	0.3033	0.2719	0.3530
	A_0^p	A_1^p	A_2^p	A_3^p	A_4^p
	0.1700	0.0750	0.0904	0.0315	0.0746
NACA 64 ₁ -212	P_0^p	P_1^p	P_2^p	P_3^p	P_4^p
	0.1469	0.1607	0.2394	0.1592	0.1237
	A_0^p	A_1^p	A_2^p	A_3^p	A_4^p
	0.1174	0.1098	0.1729	0.1023	0.0126
UAG 88-143/20	P_0^p	P_1^p	P_2^p	P_3^p	P_4^p
	0.2156	0.3757	0.2671	0.6060	0.2000
	A_0^p	A_1^p	A_2^p	A_3^p	A_4^p
	0.0777	0.0028	0.0389	0.0128	0.0157

the designer. The result is not an optimal point but rather a function describing the optimal point related to the parameters, also known as the “non-dominated surface.” The algorithm is well suited for problems with design variables \boldsymbol{x} and parameters $\boldsymbol{\theta}$ that can be formulated as:

$$J^*(\boldsymbol{\theta}) = \max_{\boldsymbol{P}^c \in \mathbb{P}^c} J(\boldsymbol{P}^c, \boldsymbol{\theta}) \quad \forall \boldsymbol{\theta} \in [\boldsymbol{\theta}_{lb}, \boldsymbol{\theta}_{ub}]. \quad (6.2)$$

where \mathbb{P}^c is the bounded domain of the optimization variables, and $\boldsymbol{\theta}_{lb}$ and $bm\boldsymbol{\theta}_{ub}$ are the lower and upper bounds of the parameter doain.

In the case of morphing aircraft, optimization variables include the variables that control wing OMLs (i.e., shape variables) during operation. Parameters consist of airspeed and angle of attack, but altitude, temperature, air density, and others could also be considered. In most cases, it is unlikely that a pilot will know all of these parameter values for a given flight plan at take-off, and many parameters are subject to change during flight. A pilot or a controls system utilizing the

generated non-dominated surface is always informed of all optimal lift-to-drag ratios and corresponding shape variables for a vector of parameters describing the flight condition.

The predictive parameterized Pareto genetic algorithm (P3GA) [70] has been applied to multiple engineering case studies [173–175]. P3GA has been shown to outperform a parameterized version of NSGA-II [176] when there are multiple parameters or many objectives as demonstrated on several test problems [174]. In that study, P3GA converged to a solution with an acceptable tolerance and found a solution at every operational parameter with improved performance compared to the undeformed OML. The results reinforce the idea that parametric optimization (and P3GA specifically) reduces the computational burden when compared to a grid of individual optimization loops due to shared information throughout the parameter space. For a more detailed description of parametric optimization as used in this work, see Ref. [70, 173–175, 177].

6.1.2 Non-linear constraint

The shape coefficients are conservatively constrained based on feasible, existing airfoil shapes to prevent generating OMLs that are either unreasonable or unsolvable with the panel method. This feasible set of active shape coefficients is denoted as \mathbb{A} . 1636 shape coefficient vectors are calculated for all the airfoils contained in a public database [135] to quantify this constraint. A thorough investigation of this four-dimensional data revealed that the feasible space would not be easily imposed via linear constraints. Instead, a Support Vector Domain Description (SVDD) is trained to fit the data and provide a single nonlinear constraint [172]. This SVDD is a one-class classifier that, once trained, predicts whether a new data point lies inside or outside of the class [178]. In this case, the class being trained is that of feasible airfoil shapes, as shown in Fig. 6.1. Outlier designs, outside of the 94% percentile, are not considered for the constraint.

6.1.3 Expected value

If the probability density functions (PDFs) of the parameters are known, the expected value \tilde{J} for the i -th concept is defined as: [177]

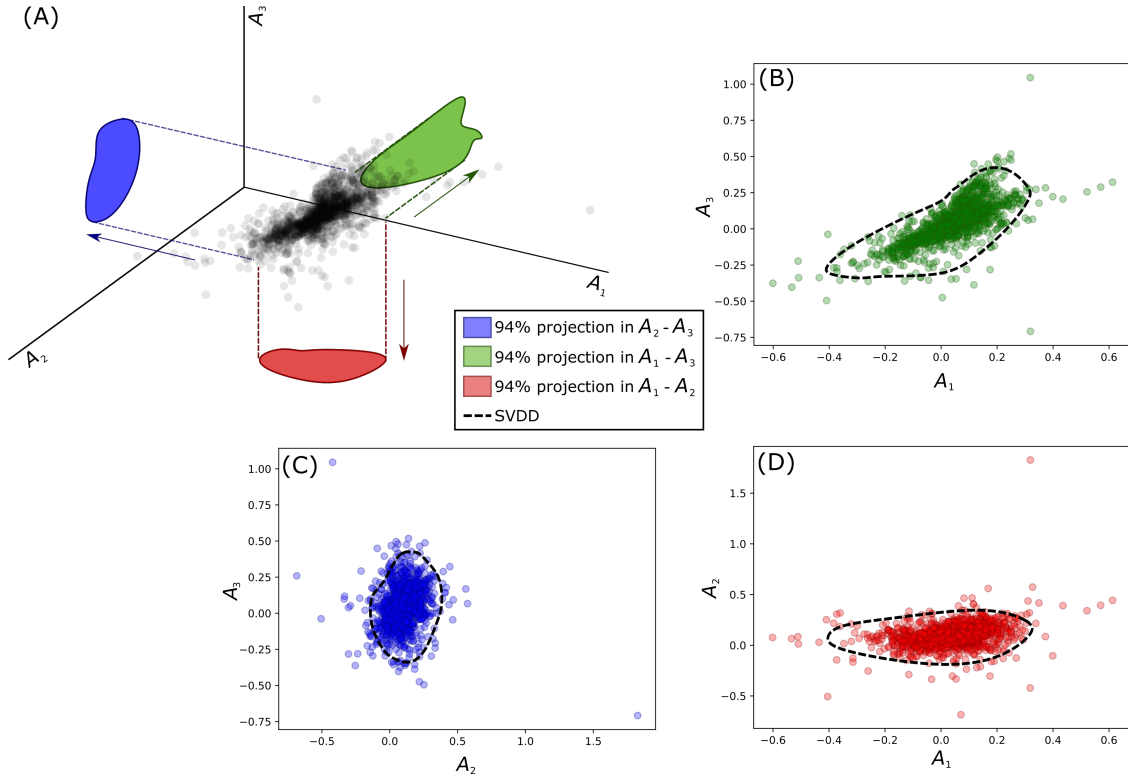


Figure 6.1: Non-linear constraint to impose only existing airfoil solutions for morphed configurations.

$$\tilde{J}_i = \int_{\theta_{lb}}^{\theta_{ub}} J_i^*(\theta) p(\theta) d\theta, \quad (6.3)$$

where $p(\theta)$ denotes the PDF of the parameters. Eq. (6.3) is the convolution of the performance information and parameter probabilities into a single expected value for use in oncept selection. Not all flight conditions evaluated by the parameterized optimization are of equal frequency and relevance. Therefore, a probability density function $p(\theta)$ is defined for the Cessna 172 models based on the following parameter-specific assumptions:

- *Velocity*: Historical data is obtained from a database with measurements from Automatic Dependent Surveillance-Broadcast (ADS-B), a surveillance technology in which an aircraft location is determined via satellite navigation. Most aircraft have an ADS-B due to FAA regulations. The data is utilized for training a kernel density estimation (KDE) to estimate

the probability density function for a specific velocity, which is assumed to be equivalent to the air velocity for a smaller aircraft.

- *Weight*: it is assumed that the aircraft weight has a uniform probability of being between the minimum W_f and maximum weights W_i .
- *Angle of attack*: Thin-airfoil theory is utilized to determine the angle of attack of the aircraft as a function of the aircraft weight W and airspeed V as shown by [37]:

$$\alpha = \frac{1}{C_{L\alpha}} \frac{2W}{\rho V^2 S} \frac{1}{\cos\alpha} - C_{L_0}, \quad (6.4)$$

where $C_{L\alpha}$ is the lift curve slope ($C_{L\alpha} = 5.143$), C_{L_0} is the lift coefficient at zero angle of attack ($C_{L_0} = 0.31$), and S is the planform ($S = 16.12 \text{ m}^2$) [179].

Finally, the Monte Carlo method, which consists of randomly sampling the design domain based on the the KDE distribution for angle of attack and uniform distribution for weight, is implemented to determine the probability density function of a specific flight condition, as shown in Fig. 6.2.

6.1.4 Concept selection

The solution of the concept selection algorithm is defined as:

$$\mathbf{x}^* = \operatorname{argmax}_{\mathbf{x} \in \mathbb{X}} \tilde{J}(\mathbf{x}), \quad (6.5)$$

where \mathbf{x} represents a design concept including shape coefficients for passive and active surfaces, \mathbb{X} is the set containing all concepts, \mathbf{x}^* represents the optimal design concept, and \tilde{J} denotes the metric, which can be a traditional or an expected value objective. Due to the nested nature of this problem, each design concept considered requires a parametric optimization loop. For problems whose objective functions can be time-consuming and where solving the parametric optimization problem is very costly, it is unlikely that the concept selection could be performed as a continuous

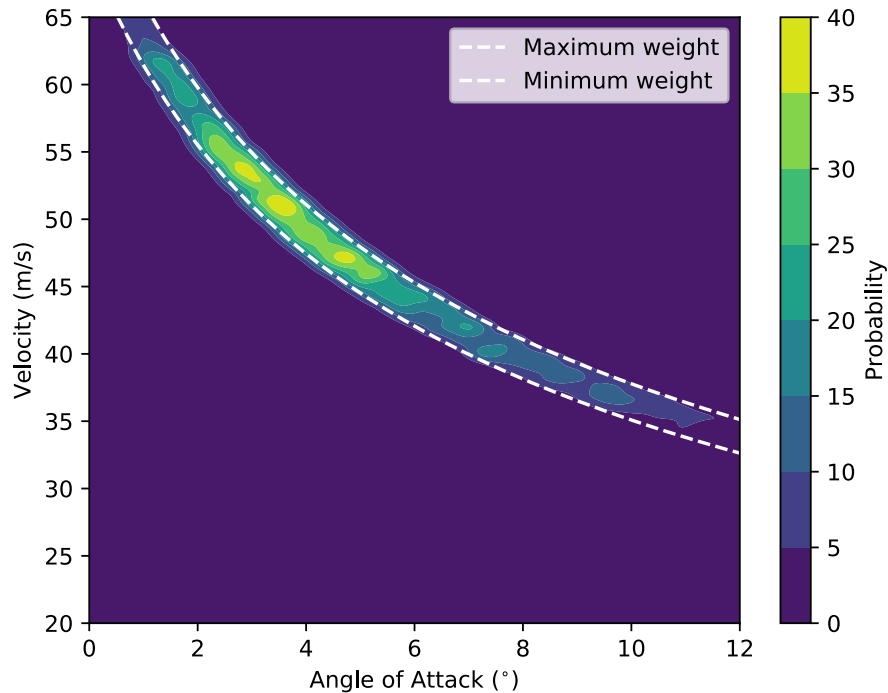


Figure 6.2: Flight condition probability of a Cessna 172 based on ADS-B measurements.

optimization problem promptly. Therefore, a case with a discrete set of design concepts in \mathbb{X} is considered. Each design concept can be quantitatively scored and compared based on expected values to determine the best design concept for the given situation.

The implemented concept selection methodology is depicted in Fig. 6.3. The problem formulation in Eq. 6.1 is solved in multiple instances for different parent airfoils, also denoted as concepts, via parametric optimization, returning the optimal morphed performance for all flight conditions. The non-dominated surface establishes the relationship between flight conditions and optimal lift-to-drag ratio. The maximum L/D calculated from the surface is a traditional metric for the aerospace industry and is also utilized for concept selection. However, existing flight data regarding the most relevant flight conditions allow for quantification of concept performance through expected values. Therefore, the parent airfoils can be ranked utilizing concept selection based on the traditional or expected metrics.

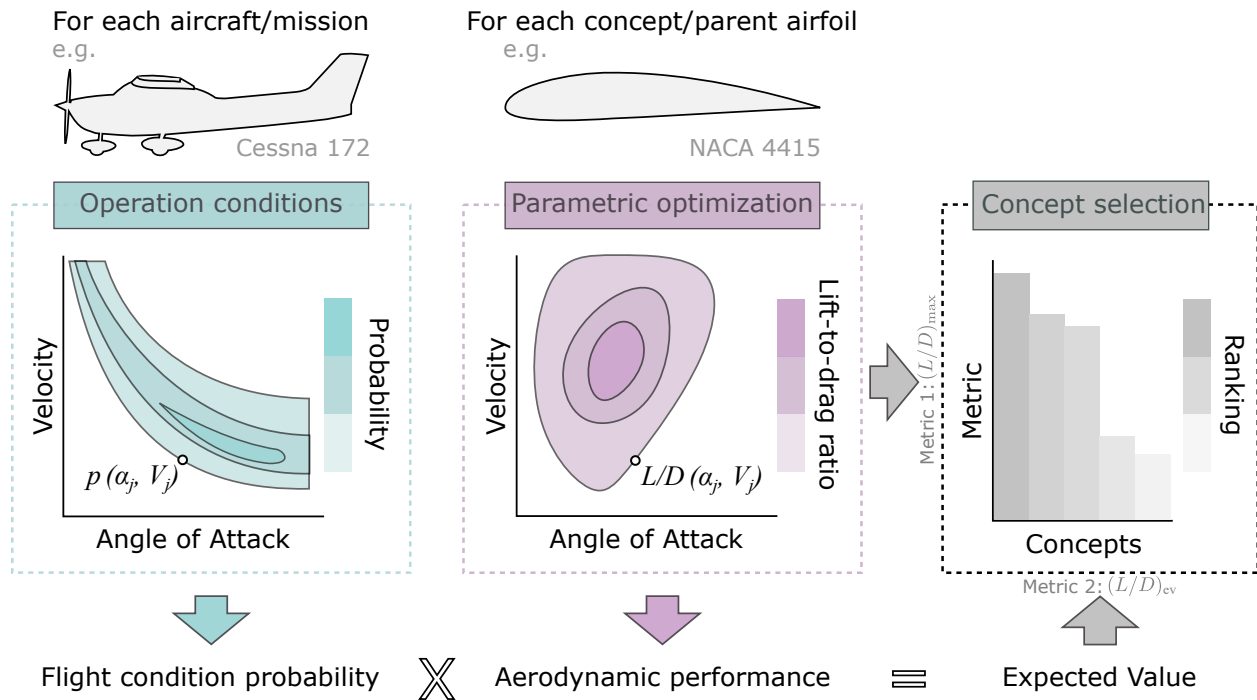


Figure 6.3: Overview of concept selection methodology incorporating operation condition probability of an aircraft and parametric optimization of a morphed airfoil to select the ideal parent airfoil.

6.2 Results

The parametric optimization method is first implemented in section 6.2.1 for a single parent airfoil, the NACA 4415, to demonstrate the capability of a parametric optimizer. The procedure is repeated for three additional airfoils (NACA 0012, NACA 64₁-212, and UAG 88-143/20), expected values are calculated, and concept selection is performed in section 6.2.2. Finally, the designs of the non-dominated surface are compared to a public airfoil database in section 6.2.3.

6.2.1 Parametric optimization of NACA 4415

Considering a fixed altitude of 10,000 ft, the non-dominated surface of the performance of a NACA 4415 over changing angle of attack and airspeed is illustrated in Fig. 6.4a. For the fixed airfoil case, parametric optimization is not necessary since there are no variables to change beyond the initial concept.

Depending on the parameter values, lift-to-drag ratios of up to 203^\dagger are achieved. Overall, the optimal lift-to-drag ratio monotonically increases with airspeed V . An increase in angle of attack for smaller angles ($\alpha \leq 6^\circ$) increases the objective function. However, for higher angles of attack ($\alpha > 6^\circ$), the lift-to-drag ratio decreases because of sensitivity to stalling [158]. Fig. 6.4b shows a comparison between the performance of the camber *morphing* NACA 4415 and four *fixed* airfoils for the same flight conditions. The benefits of using a morphing configuration are apparent at higher angles of attack where all fixed configurations underperformed. For lower angles of attack, the morphing alternative seems to be less advantageous as at least one airfoil, the UAG 88-143/20, has improved performance without requiring the additional complexity of morphing. Nevertheless, the morphing NACA 4415 outperforms most fixed airfoils for the considered flight parameters.

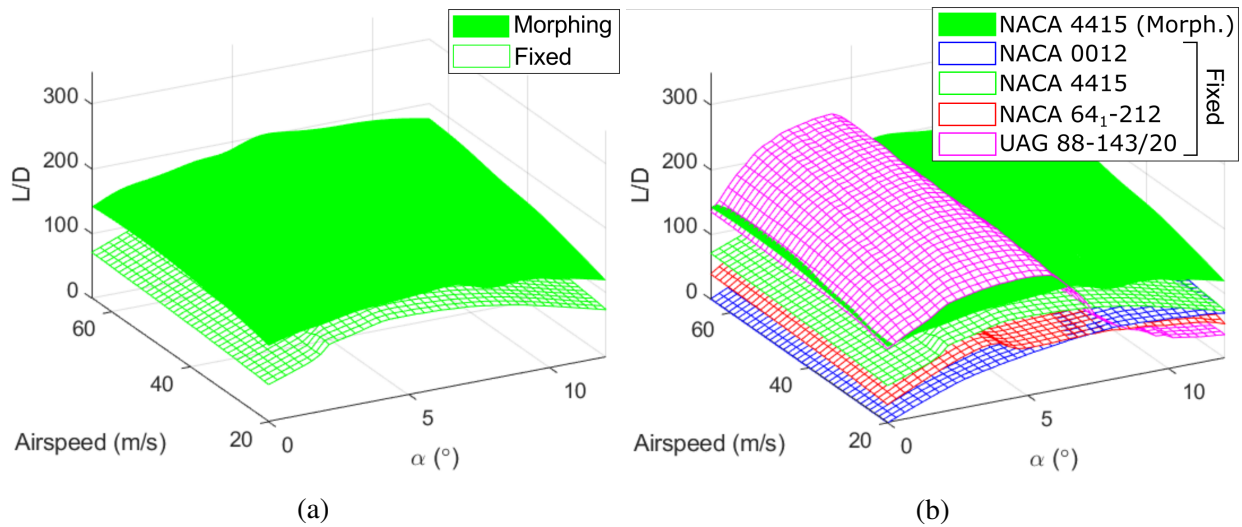


Figure 6.4: Lift-to-drag ratio results considering altitude at 10,000 ft. (a) Non-dominated surface for the morphing NACA 4415 and the aerodynamic results of the fixed configuration (b) Comparison between the performance of the morphing NACA 4415 and the fixed NACA 0012, NACA 4415, NACA 64₁-212, and UAG 88-143/20 airfoils.

The optimal morphed configuration changes with flight condition, but three distinct families can be clustered based on their topology [180]. Fig. 6.5 illustrates the non-dominated surface

[†]Conservatively, the values of the support vectors are utilized instead of the SVDD values.

together with cluster centers for each family of solutions [180]. At lower angles of attack ($\alpha < 4^\circ$), the morphed configurations (design A) are similar to traditional high-lift airfoils [181]. As angle of attack increases ($4^\circ \leq \alpha < 8^\circ$), the maximum camber location tends towards the leading edge, resulting in configurations (design B) similar to avian airfoils [119]. At the highest angles of attack, delaying boundary layer separation dominates the morphing design, leading to unorthodox designs (design C) known as reflexed airfoils [182]. Each of the identified designs is not acceptable for all flight conditions but is viable as one of many states of a morphing configuration.

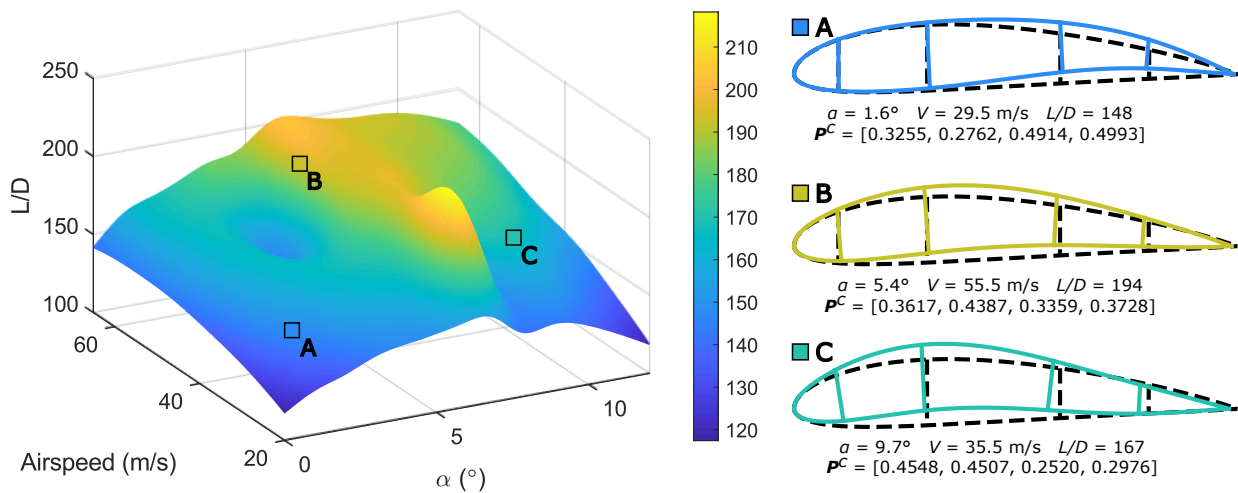


Figure 6.5: The non-dominated surface and the three cluster centers are depicted along with airfoil shape coefficients, designed flight condition, and lift-to-drag ratio for NACA 4415.

6.2.2 Concept selection for four parent airfoils

Another high-level objective of this chapter is to select the optimal parent airfoil. The optimization procedure implemented for the NACA 4415 is repeated for the NACA 0012, NACA 64₁-212, and UGA 88-143/20. The non-dominated surfaces for each morphing configuration and the aerodynamic performance of the fixed configuration are depicted in Fig. 6.6. For all airfoils, the morphing configuration outperforms or is equivalent to the originating configuration. However, different trends are observed for each concept due to the original OML and structural constraints:

- *NACA 0012* is the only symmetric airfoil (i.e., zero lift coefficient at zero angle of attack) of the evaluated concepts. The low performance of the parent airfoil did not restrict the morphing configuration to achieve lift-to-drag ratios as high as 200. At high angles of attack, the morphed configuration is equivalent to the original airfoil as airfoil symmetry is beneficial to delay boundary layer separation.
- *NACA 4415* is an outlier in regards to the performance insensitivity to flight conditions. The objective value for the fixed and morphed configurations shows the smallest variation among all airfoils for changing angle of attack and airspeed.
- *NACA 64₁-212* is designed for maximizing laminar flow and has a low lift-to-drag ratio for the fixed configuration. However, the morphing configuration resulted in the highest L/D of all concepts (the maximum took place for $\alpha = 0^\circ$ and $V = 60$ m/s). This result demonstrates that the aerodynamic performance of the parent airfoil does not directly correlate to the performance of the morphing configuration.
- *UAG 88-143/20* is the only airfoil that does not considerably increase performance at low angles of attack when incorporating morphing. The airfoil is intended for sailplanes and is already tailored for a maximum L/D for low α . However, morphing does improve performance at higher values of α .

When comparing fixed configurations, as shown in Fig. 6.7a, it is evident that the sailplane airfoil is best at low α while the *NACA 4415* is superior at high α . However, the same conclusions cannot be made when comparing the morphing configurations, as shown in Fig. 6.7b. Each concept has flight conditions where it has superior aerodynamic performance over the other three. Therefore, a formal process for concept selection is necessary and would benefit from a metric that weighs $J^*(\alpha, V)$ for the most relevant flight conditions.

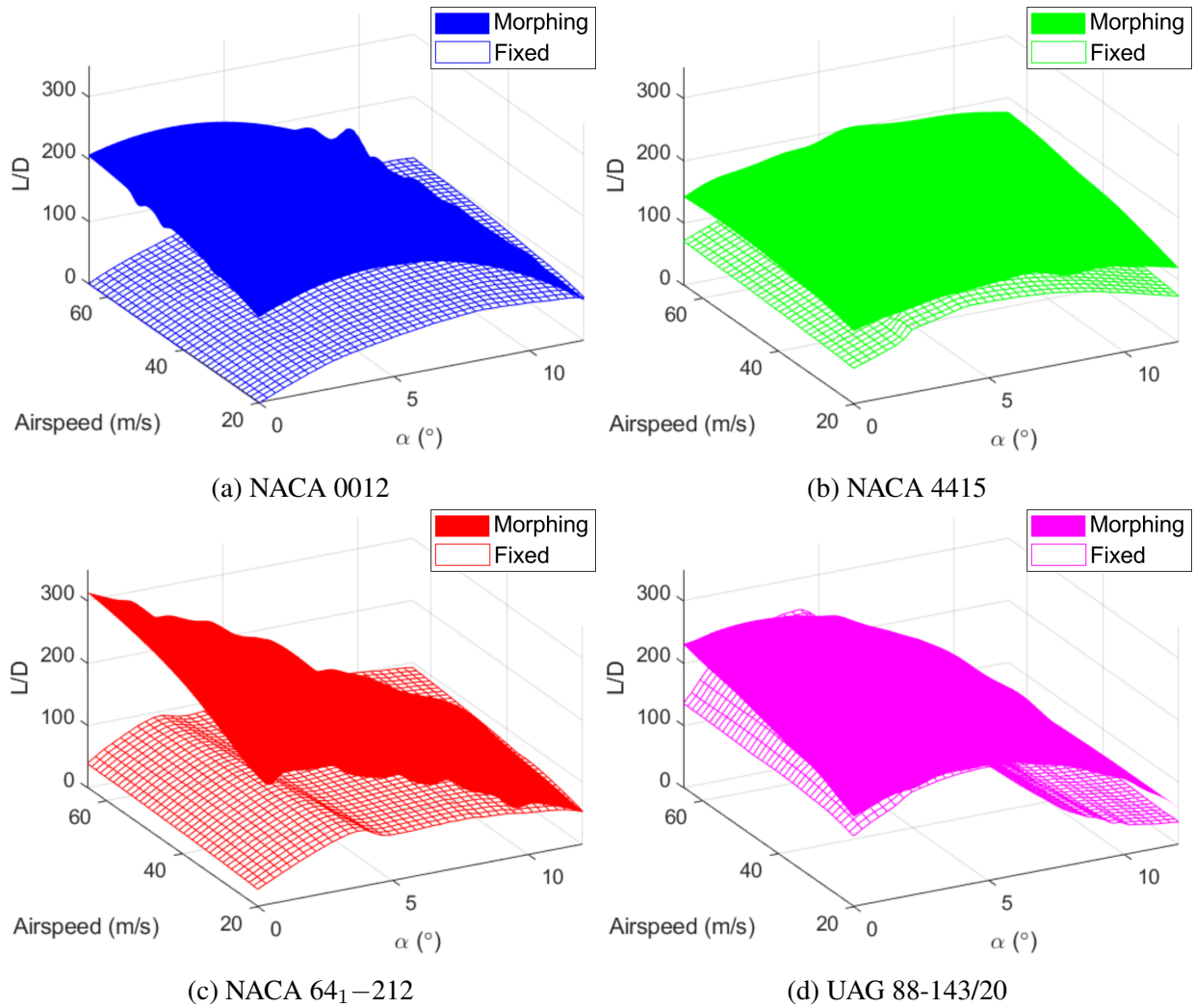
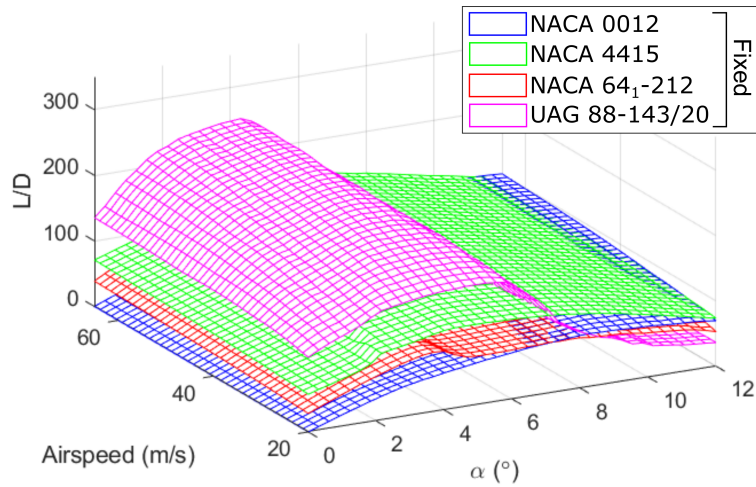
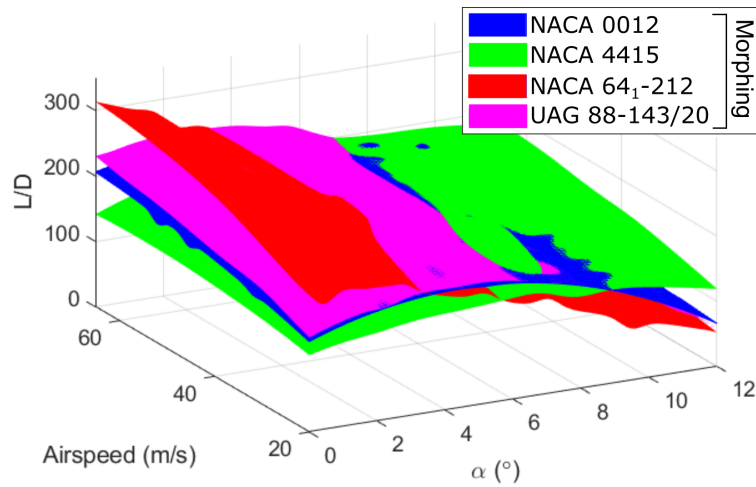


Figure 6.6: Aerodynamic performance of the fixed configuration and the non-dominated surface for the morphed configuration with the following parent airfoils: (a) NACA 0012, (b) NACA 4415, (c) NACA 64₁-212, and (d) UAG 88-143/20.



(a) Fixed



(b) Morphed

Figure 6.7: Aerodynamic performance of (a) the fixed configuration and (b) the non-dominated surface for the morphed configuration with the following parent airfoils: NACA 0012, NACA 4415, NACA 64₁-212, and UAG 88-143/20.

The expected value \tilde{J} considers optimal lift-to-drag ratios as a function of the operational parameters, angle of attack and airspeed, and the probability of each flight condition. The SVDD for each of the morphed configurations (i.e., $J^*(\alpha, V)$) is utilized to determine the optimal objective for each flight condition continuously. A margin of error of 2.8% is assumed for morphed configuration results based on the average error from a previous study [183]. As discussed in Appendix ??, the error does not affect expected lift-to-drag ratio, but is relevant for maximum lift-to-drag ratio. The compilation of all metrics is shown in Table 6.2. The optimal airfoil for fixed and morphed configurations varied according to the selected metric. Regarding the fixed configurations, the UAG 88-143/20 is the optimal airfoil according to the traditional metrics, but the NACA 4415 is determined optimal if utilizing the expected lift-to-drag ratio. Regarding the morphed concepts, the NACA 64₁-212 is best for the traditional metric and similar to the sailplane airfoil for the expected value. Hence, utilizing an expected value does not always imply a change of the selected concept. Except for the UAG 88-143/20, all morphing airfoils are aerodynamically superior to the fixed concepts for both metrics.

Conf.	Parent	Traditional (L/D) _{max}	Expected (L/D) _{ev}
Fixed	NACA 0012	104	85
	NACA 4415	151	126
	NACA 64(1)-212	103	86
	UAG 88-143/20	250	102
Morphed	NACA 0012	226 ± 6	208 ± 6
	NACA 4415	218 ± 6	169 ± 5
	NACA 64(1)-212	314 ± 9	216 ± 6
	UAG 88-143/20	247 ± 7	218 ± 6

Table 6.2: Summary of maximum and expected lift-to-drag ratios for fixed and morphed airfoils. Selected concepts are highlighted.

6.2.3 Similarity of morphing OML to existing airfoils

As discussed in section 6.1.2, a non-linear constraint is implemented such that the explored morphed airfoils resemble designs in existing airfoil databases. The development of aerodynamically favorable airfoils is a well-developed and active area of research and is not the goal of this chapter. All the airfoils on the non-dominated surface have a substantial degree of similarity (i.e., low RMSE) to existing airfoils, as shown in Fig. 6.8. The three previously mentioned clusters in Fig. 6.5, A, B, and C, are equivalent to the following Gottingen series airfoils: GOE 502, GOE 675, and GOE 503. This series of high-camber airfoils was created at Gottingen University in Germany in the early days of aviation, during the 1920s, and are not utilized in commercial aviation. The remaining concepts include typical sailplane airfoils such as the UAG 88-143/20, the Eppler 644 (ex), the Eppler 678, and the Quabeck HQ 2.5/12. In general, morphing allows altering the OML in between different well-known airfoils according to flight conditions rather than utilizing a sub-optimal airfoil for the whole flight mission.

An additional study is performed where the calculated support vectors, which can vary between 30 to 50 designs, for the non-dominated surface for each concept are compared to the airfoil database. Interpolation between the support vectors or the trained SVDDs could be utilized to evaluate more designs and obtain a more continuous distribution, but could also introduce errors. Fig. 6.9 depicts the probability mass function (i.e., the frequency distribution of discrete objects) of the five most common similar existing airfoils for the support vectors for each concept. This analysis provides insight on how many interchangeable airfoils would be necessary to obtain a similar aerodynamic performance as the non-dominated surface. Once again, out of the 20 airfoils, almost half are from the Gottingen series. The most frequent airfoil is the GOE 573. This result highlights that no existing fixed airfoil can obtain the same performance as a morphing airfoil.

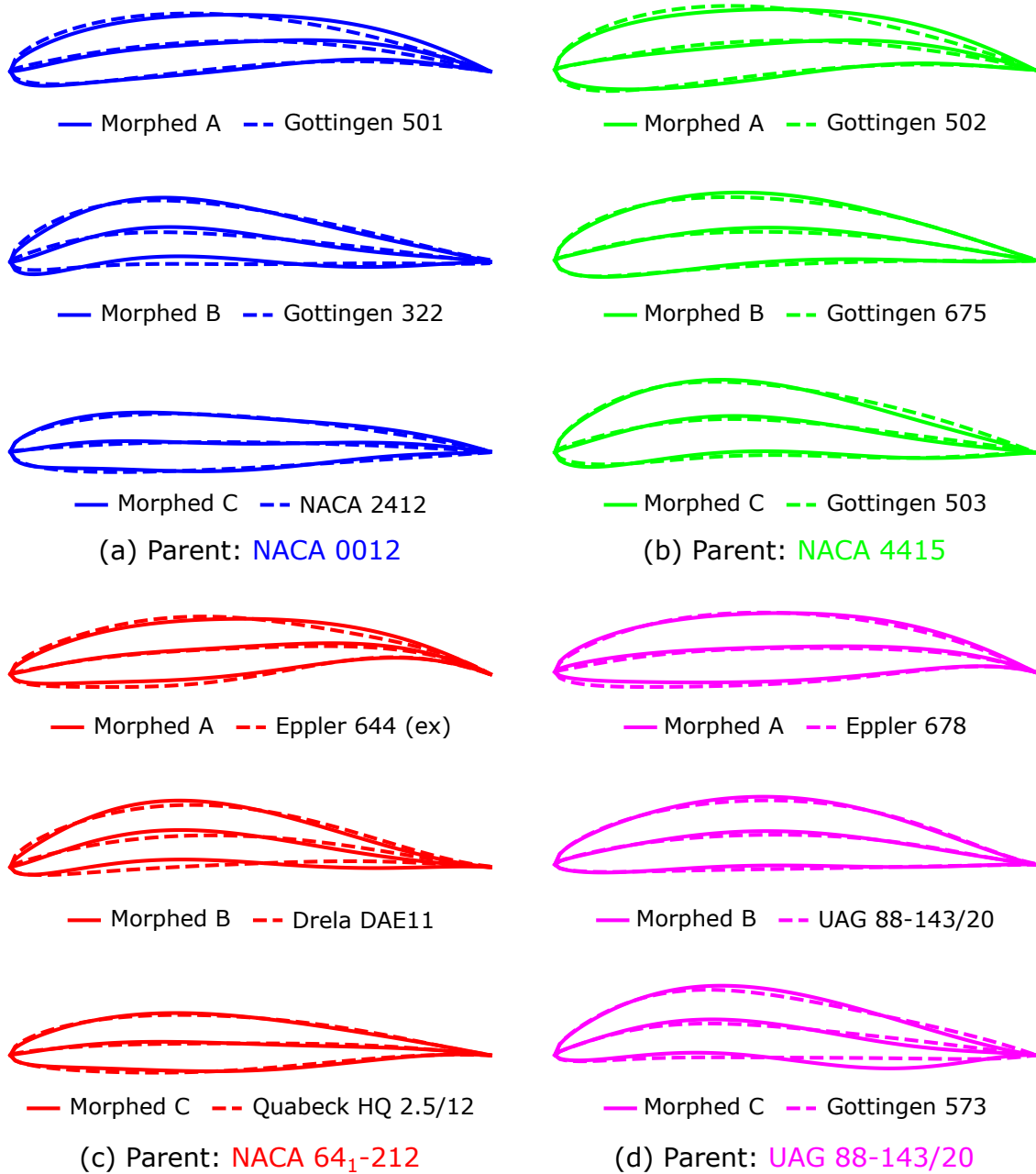
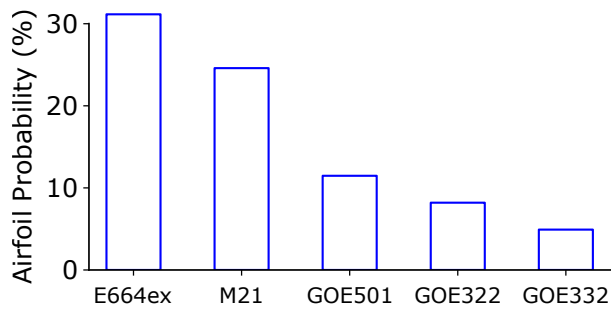
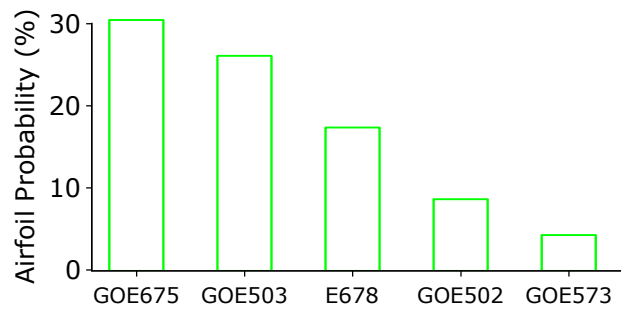


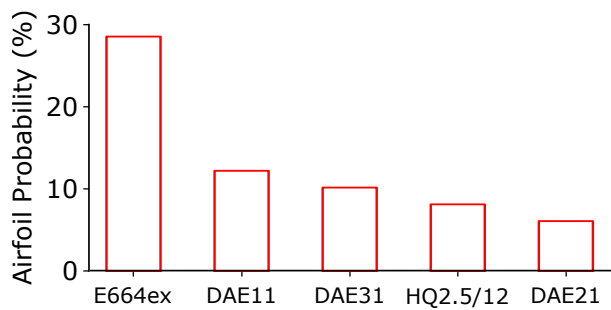
Figure 6.8: Cluster centers of te non-dominated surfaces and airfoils with the most significant degree of similarity for each concept.



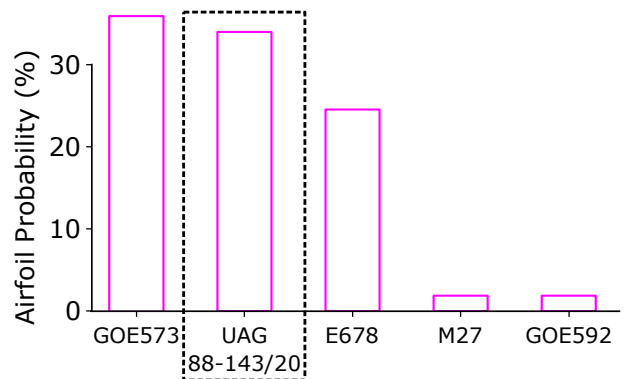
(a) Parent: **NACA 0012**



(b) Parent: **NACA 4415**



(c) Parent: **NACA 64₁-212**



(d) Parent: **UAG 88-143/20**

Figure 6.9: Probability mass function for similar airfoils for the support vectors of the four evaluated concepts.

6.3 Comments

This chapter shows that parametric optimization is an effective tool for optimizing a flight performance objective function over a range of parameters, making it a valuable method for optimizing morphing structures. Specifically, P3GA is a reliable method to optimize the aerodynamic performance of a structurally consistent airfoil coupled with an aerodynamic solver. This accuracy, coupled with the decreased runtime compared to traditional methods [174], supports the use of parametric optimization over conventional optimization methods for solving morphing problems.

The two-parameter non-dominated surface describing the lift-to-drag ratios of morphing NACA 0012, NACA 4415, NACA 64₁-212, and UAG 88-143/20 airfoils are compared to those from non-morphing baseline designs, quantifying the improvement from morphing technologies. Morphing airfoils achieve similar or better performance across changing operational conditions than fixed, specialized airfoils. Overall, there is not a strong correlation between the aerodynamic performance of a parent airfoil and the calculated non-dominated surface. Structural constraints and initial OML constrain the feasible morphed shapes due to the structurally consistent framework.

The evaluated airfoils are ranked according to concept selection and expected value principles. The selected airfoil depends on the utilized metric, maximum lift-to-drag ratio vs expected lift-to-drag ratio. Fixed airfoils can also have superior performance over a morphing airfoil, demonstrating that morphing is not always necessary. Nevertheless, concept selection is a suitable method to procedurally define the optimal parent airfoil for an aircraft class or mission, or even to determine if morphing is more advantageous than utilizing an aerodynamically favorable airfoil.

7. FINITE-DEFLECTION REVERSION BEAM THEORY

The proposed structurally consistent parameterization method in Chapter 5 considers kinematic constraints when generating deformed shapes, leading to geometrically feasible configurations for most shape coefficient combination inputs. However, the approach does not provide a unique solution for the convex problem of a structure under load as shown in Fig. 7.1. Therefore, there must be an affine transformation M that relates the applied loads \mathbf{L} to the deformed position \mathbf{r} or geometric coefficients \mathbf{a} in an injective fashion; hence:

$$M(\mathbf{L}) \rightarrow \mathbf{r}(\mathbf{a}). \quad (7.1)$$

Such a relation is proposed in this chapter by including kinematics of finite-beam deflections, constitutive models, and other assumptions to form the governing equations. Because no assumptions are made regarding the bending moments and geometry, a general beam model is developed. The proposed framework is implemented for a two-dimensional cross section of the airfoil skin. The current model does not allow for embedded skin actuators (cf. Chapter 3) but enables modeling of skins subject to various loads and actuators and an extension to actuators is proposed. Therefore, it can be utilized as an alternative or an improvement to the structurally consistent method of Chapter 6.

For a given set of applied loads:

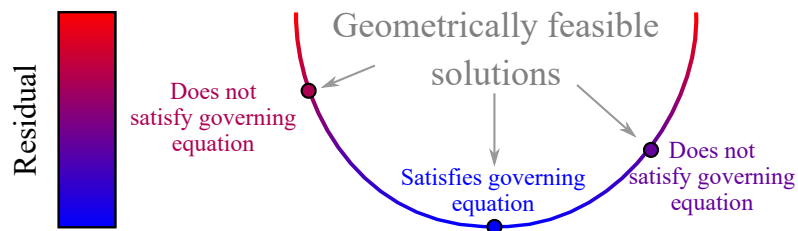


Figure 7.1: Distinction between a geometrically feasible solution and the stable solution under specific loads.

For sake of clarity, Fig. 7.2 is provided as a reference to the various variables utilized in this chapter. Keeping with the previous nomenclature for structurally consistent airfoils (Chapter 4), the term *child* and *parent* are used to denote deformed and undeformed for this chapter.

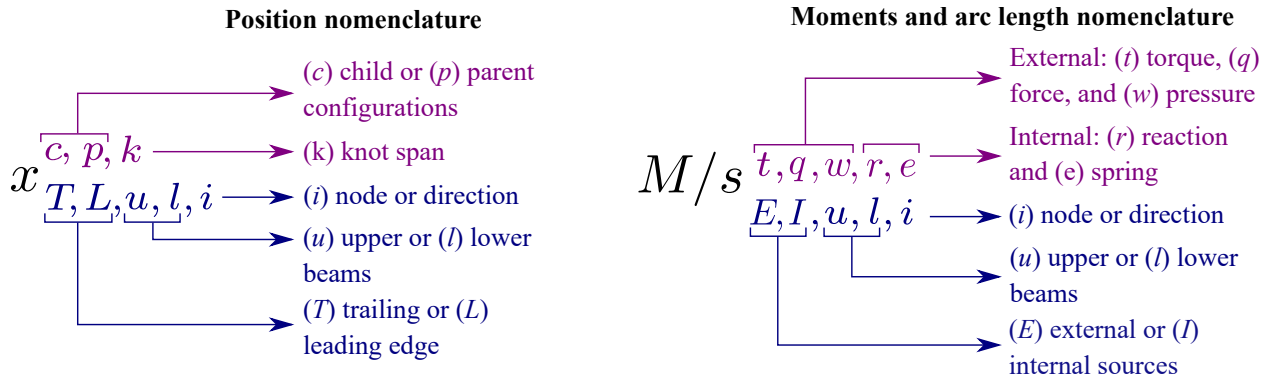


Figure 7.2: Nomenclature regarding superscripts and subscripts utilized for any variable in this chapter (e.g., x , M , and s)

7.1 Overview

7.1.1 Motivation

As depicted in Fig. 7.3, a universal parameterization method for Computer-Aided Design (CAD), structural analysis, and fluid analysis is required to guarantee higher accuracy for analyses of high-performance aeronautical vehicles and more intuitive geometry manipulation. The traditional structural analysis method of Finite-Element Analysis (FEA) is not utilized herein except for result verification. The new universal representation is inspired by the work from Hughes and co-authors [184] on Isogeometric Analysis (IGA). However, IGA can only be utilized for parameterization methods with specific properties (e.g., subdomains, denoted as “patches”, where shape function requirements are satisfied [184, 185]). Therefore, IGA requires parameterization methods (e.g., NURBS) that are not:

- efficient (i.e., introduce large number of degrees of freedom), and

- intuitive (i.e., the NURBS coefficients have no physical meaning).

In this chapter, a method to solve the boundary value problem of a thin beam undergoing large deflections is proposed for any *parameterization technique*.



Figure 7.3: Traditional methodology vs. universal parameterization methodology, where EBM stands for Euler-Bernoulli method. A universal parameterization method enables higher accuracy analysis without approximating the topology with a mesh of low-order piecewise polynomials.

7.1.2 Case studies

The overarching goal is to develop a structural model that can be utilized for arbitrary geometries and loads such as airfoil sections. Different set of requirements are solved in increasing order of complexity to achieve this goal. For each set of requirements, a different category of beam model is developed. The following three categories of beam problems depicted in Fig. 7.4, each with a respective set of case studies (A, B, and C), are analyzed:

- (A) Spline element beam: consists of a beam represented by one continuous polynomial, usually a CST. This is the most limiting case as concentrated forces and torques can only be applied at the free end, and no boundary conditions can be imposed along the beam. This case study is also evaluated for a power series to demonstrate that the proposed method is not restricted to CST equations.
- (B) Spline beam: consists of a beam represented by a spline, usually a CST spline. It consists of m spline element beams connected at knots Ξ , leveraging the properties of the spline element beam, but allowing for bending moment discontinuities at the knots from concentrated forces and torques.

(C) Multi-beam assembly: consists of two spline beams, denoted as *upper* and *lower*, interacting with each other through hinged spars, actuators, and springs. The model leverages the previous two beam categories and allows the modeling of systems similar to a skinned aerodynamic structure.

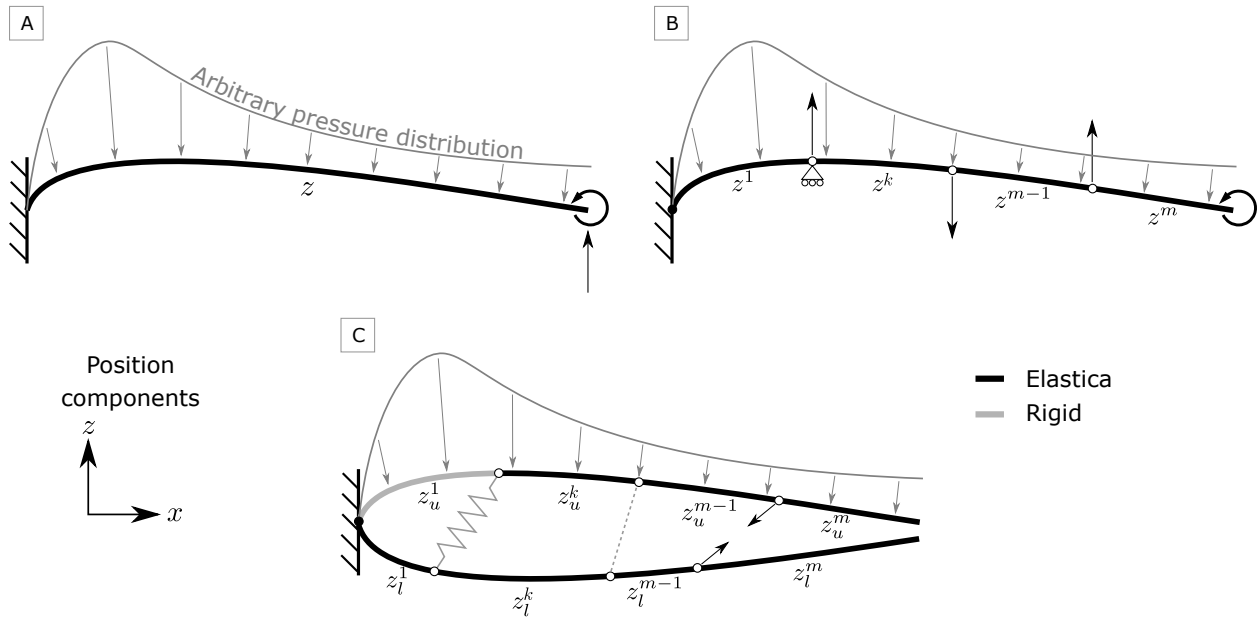


Figure 7.4: The different categories of beam models studied in this chapter: (A) spline element beam, (B) spline beam, and (C) multi-beam assembly. (A) requires C^0 pressure distributions, while (B) and (C) do not. (C) includes incorporates the interactions between different beams.

7.2 Finite-deflection Euler-Bernoulli derivation

Curvilinear beam theory is an active field of study with methodologies continually being developed since 1945 and papers continue to be published in the topic [64–66, 186–203]. Beam models can be derived in multiple ways, including three more common methods [204]: Newtonian method based on the free body diagram [186], variational method [58], and variational asymptotic method [187]. The first two are *ad hoc* methods that include various kinematic assumptions (e.g., the Euler-Bernoulli assumptions), leveraging the knowledge that the engineer has of the problem.

The variational asymptotic method has the merits of the variational method without using *ad hoc* assumptions. Since the steps utilized for defining the general Euler-Bernoulli governing equation are well-established, a Newtonian methodology is utilized. The assumptions considered for the beam model in this chapter are:

- *Finite deflections*: most engineers are familiar with the beam derivation that assumes small deflections. As a consequence, the component of the displacement parallel to the beam is typically neglected, and all governing equations are depicted in a Cartesian coordinate system ($i_i \in [1, 2, 3]$) as a function of x -coordinates as shown in Fig. 7.5. A morphing skin, however, is subject to large rotations and deflections, making the small deflection assumption unsuitable. Therefore, finite deflections are assumed, and a curvilinear reference frame ($g_i \in [1, 2, 3]$) is utilized that is a function of the arc length coordinate s along the beam neutral line. The curvilinear coordinate system also consists of coordinate β that denotes the distance along the normal of the neutral line for a specific arc length s . The relation between arc length s and Cartesian coordinates x and z is given by [205]:

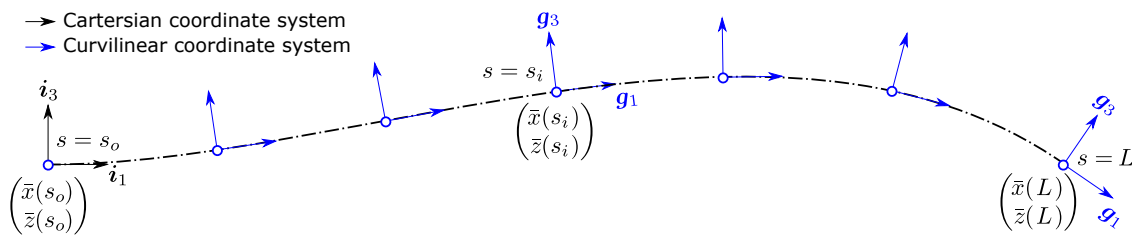


Figure 7.5: Curvilinear and Cartesian coordinate systems for bending beam.

$$s = \int_0^x \sqrt{1 + \left(\frac{dz}{dx}(\chi)\right)^2} d\chi. \quad (7.2)$$

In the study of finite deflections and curved geometries, it is convenient to define two other

geometric quantities. The first is the beam angle ϕ related to the following Cartesian coordinates derivatives: [196]

$$\cos \phi = \frac{dx}{ds}, \quad (7.3)$$

$$\sin \phi = \frac{dz}{ds}, \quad (7.4)$$

and the second is the radius of curvature ρ defined via the relationship to the curvature κ as: [196]

$$\kappa(s) = \frac{1}{\rho(s)} = \frac{d\phi}{ds}(s) = \frac{\frac{d^2z}{dx^2}(s)}{\left[1 + \left(\frac{dz}{dx}(s)\right)^2\right]^{3/2}}. \quad (7.5)$$

- *Euler-Bernoulli*: for most aerospace applications, the aircraft skin thickness is orders of magnitude smaller than the arc length or chord. Therefore, the Euler-Bernoulli assumption, where cross sections perpendicular to the reference neutral line remain perpendicular for all deformed configurations, is acceptable. As such, the position vector $\mathbf{r}(s, \beta)$ is the linear combination of the position vector of the neutral line $\bar{\mathbf{r}}(s)$ and the distance β from the neutral line along the normal \mathbf{n} as shown in Fig. 7.6. Therefore [206]:

$$\mathbf{r}(s) = \begin{pmatrix} x(s) \\ z(s) \end{pmatrix} = \begin{pmatrix} \bar{x}(s) + \beta n_1(s) \\ \bar{z}(s) + \beta n_2(s) \end{pmatrix} = \bar{\mathbf{r}}(s) + \beta \mathbf{n}(s), \quad (7.6)$$

where

$$\mathbf{n}(s) = \begin{pmatrix} n_1(s) \\ n_2(s) \end{pmatrix} = \begin{pmatrix} -\frac{dz}{ds}(s) \\ \frac{dx}{ds}(s) \end{pmatrix}. \quad (7.7)$$

Thus, the position vector can be reformulated as:

$$\begin{pmatrix} x(s) \\ z(s) \end{pmatrix} = \begin{pmatrix} \bar{x}(s) - \beta \frac{dz}{ds}(s) \\ \bar{z}(s) + \beta \frac{dx}{ds}(s) \end{pmatrix}. \quad (7.8)$$

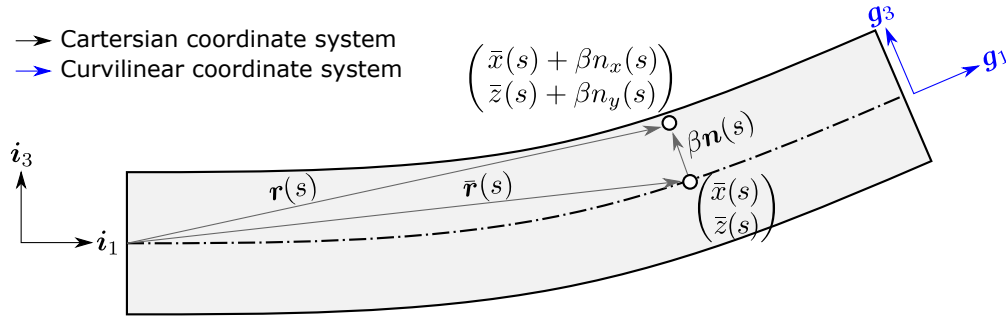


Figure 7.6: Definitions of position vectors for the beam.

- *Elastica*: strains along the curvilinear neutral axis are assumed to be small and the beam is assumed to be experiencing pure bending. The arc length L of the curvilinear neutral axis is constant for all deformed configurations. Because the arc length coordinate s is the same for the child (deformed) and parent (undeformed) (cf. Chapter 4 for definitions of the parent and child configurations), the position vectors for both configurations are a function of the same arc length coordinate:

$$\begin{pmatrix} x^c(s) \\ z^c(s) \end{pmatrix} = \begin{pmatrix} \bar{x}^c(s) - \beta \frac{dz^c}{ds}(s) \\ \bar{z}^c(s) + \beta \frac{dx^c}{ds}(s) \end{pmatrix}, \quad (7.9)$$

$$\begin{pmatrix} x^p(s) \\ z^p(s) \end{pmatrix} = \begin{pmatrix} \bar{x}^p(s) - \beta \frac{dz^p}{ds}(s) \\ \bar{z}^p(s) + \beta \frac{dx^p}{ds}(s) \end{pmatrix}, \quad (7.10)$$

and the displacement is given by:

$$\mathbf{u}(s) = \begin{pmatrix} x^c(s) \\ z^c(s) \end{pmatrix} - \begin{pmatrix} x^p(s) \\ z^p(s) \end{pmatrix}. \quad (7.11)$$

Regarding additional geometric metric properties, the beam angles for child and parent configurations are defined as ϕ^c and ϕ^p while ρ^c and ρ^p are the radii of curvature for the child and parent configurations.

- *Only transverse loads:* in the most general form, the contributions to the bending moment are generated by an arbitrary pressure distribution $W(s)$, concentrated forces Q , and discrete bending moments (torques) T . The resultant bending moment is composed of contributions from forces internal $M_I(s)$ and external $M_E(s)$ to the assembly such that:

$$M(s) = M_I(s) + M_E(s), \quad (7.12)$$

where M_I is a summation of the moments from reactions forces M^r and elastic springs M^e :

$$M_I(s) = M^e(s) + M^r(s), \quad (7.13)$$

and these two moments components resultant from beam interactions as will be discussed in the next section. When only one beam is considered, $M(s) = M_E(s)$. $M_E(s)$ is a linear combination of moment contributions from torques $M^t(s)$, forces $M^q(s)$, and pressures $M^w(s)$, and it is given by:

$$M_E(s) = M^t(s) + M^w(s) + M^q(s). \quad (7.14)$$

The discrete bending moments can take place anywhere along the beam, originating from torque springs, torque tube actuators, or others. Other papers that develop finite deflection

beam models only consider one torque at the end of an element or the whole beam, but such a simplification is not herein assumed. Instead, n^t concentrated moments T^k are considered at arc length coordinates s^t . Modified from Zhang *et al.* [196], the resultant contribution is :

$$M^t(s) = \sum_{k=1}^{n^t} \langle s^{t,k} - s \rangle^0 T^k, \quad (7.15)$$

where $\langle \cdot \rangle^0$ is the Macaulay bracket notation for a unit step [207] (i.e., if the parenthetical expression is negative, the output is zero; otherwise, the output is one).

Non-uniform pressure distributions along the arc length are expected for the skin of the aircraft. Previous papers simplified the pressure distribution as uniform or linearly distributed pressures, but that is not possible herein. Instead, an arbitrary pressure distribution $W(s)$ is assumed. The pressure distribution can be rotational (i.e., load angle with neutral line is constant for all deformed configurations) depending on the value of parameter γ . the pressure distribution is aligned with the original undeformed vertical direction if $\gamma = 0$ or aligned with the normal $\mathbf{n}(s)$ for any child configuration. Modified from Rao and Rao [201], the contributions to the bending moment along the out-of-plane axis \mathbf{i}_2 are:

$$M^w(s) = \int_s^L [W(\chi) \bar{\mathbf{n}}(\chi) \times \mathbf{d}(s, \chi)] \cdot \mathbf{i}_2 d\chi, \quad (7.16)$$

where the vector $\bar{\mathbf{n}}(s)$ is the pressure orientation ($\bar{\mathbf{n}}(s) = \mathbf{n}(s)$ if $\gamma = 1$) and the vector $\mathbf{d}(s, \chi)$ denotes the distance from an arc length s to any other point along the neutral line with arc-length χ . Both vectors are given by:

$$\mathbf{d}(s, \chi) = \begin{pmatrix} x^c(\chi) - x^c(s) \\ z^c(\chi) - z^c(s) \end{pmatrix}, \quad (7.17)$$

$$\bar{\mathbf{n}}(s) = \begin{pmatrix} -\cos(\gamma\phi^c(s)) \\ \sin(\gamma\phi^c(s)) \end{pmatrix}. \quad (7.18)$$

Finally, concentrated transverse loads on the beam are expected from various sources such as actuators or structural weights. Similar to torques, previous finite beam models only consider one force per element or beam. Because an aircraft skin is subject to various load sources such as from the internal structure, the same assumption is not made. The possibility of n^q concentrated loads \mathbf{Q} applied at arc lengths s^q is considered. Modified from Mutyalarao *et al.* [208], the contribution to the bending moment distribution along the out-of-plane direction \mathbf{i}_2 :

$$M^q(s) = \sum_{k=1}^{n^q} \langle s^{q,k} - s \rangle^0 [\mathbf{Q}^{c,k} \times \mathbf{d}(s, s^{q,k})] \cdot \mathbf{i}_2. \quad (7.19)$$

The initial load vector $\mathbf{Q}^{p,k}$ has magnitude Q^k and angle θ^k relative to the inertial horizontal orientation at arc length $s^{q,k}$. The orientation of the load is held constant if $\gamma = 0$. If the load is rotational ($\gamma = 1$), the load vector $\mathbf{Q}^{p,k}$ is rotated by angle ϕ^k that is the difference between the child beam angle $\phi^{c,k}$ and the parent beam angle $\phi^{p,k}$ at arc length $s^{q,k}$. The general equation for load \mathbf{Q}^k is:

$$\mathbf{Q}^k = \mathbf{R}\mathbf{Q}^{p,k} = Q^k \mathbf{R} \begin{pmatrix} \sin \theta^k \\ \cos \theta^k \end{pmatrix} = Q^k \begin{bmatrix} \cos \beta \phi^k & -\sin \beta \phi^k \\ \sin \beta \phi^k & \cos \beta \phi^k \end{bmatrix} \begin{pmatrix} \sin \theta^k \\ \cos \theta^k \end{pmatrix}. \quad (7.20)$$

- *Infinitesimal strain:* despite the finite deflections, material obeys linear elasticity and is only subject to small strains. As such, the non-linear component of the Green-Lagrangian strain tensor [209] can be neglected. Considering all the assumptions, the governing equation for finite beams, as shown by Frisch-Fay [186], is:

$$M(s) = -\bar{E}I \left(\frac{1}{\rho^c(s)} - \frac{1}{\rho^p(s)} \right), \quad (7.21)$$

where \bar{E} is the equivalent Young Modulus, I is the beam moment of inertia, and EI is

known as the flexural rigidity of the beam [196]. Considering that E is the material Young Modulus and ν is the Poisson ratio, $\bar{E} = E$ for plane stress and $\bar{E} = E/(1 - \nu^2)$ for plane strain [210]. All the illustrative results for this chapter are for a thin beam sections, so plane stress is assumed. However, for an aircraft skin, plane strain should be assumed.

Depending on the beam model, it is convenient to write Eq. 7.21 as a function of beam angles of parent and child configurations, ϕ^P and ϕ^c . Utilizing the definition of the radius of curvature (Eq. 7.5), the governing equation is formulated as follows [186]:

$$M(s) = -EI \left(\frac{d\phi^c}{ds}(s) - \frac{d\phi^p}{ds}(s) \right). \quad (7.22)$$

7.2.1 Simplifications

The derived general equation for Euler-Bernoulli can be unfamiliar to most engineers but can be simplified to a more familiar format if certain assumptions are made. First, if the initial geometry is a straight beam, we have that the parent curvature radius $\rho^p(s) \rightarrow \infty$ for $s \in [0, L]$. Therefore [186]:

$$M(s) = -EI \frac{1}{\rho^c(s)}. \quad (7.23)$$

Shell and curved beam theory utilized in FEA often assume that the radius for each element is constant. Therefore, the child curvature radius $\rho^c(s) = \rho$ and:

$$M(s) = -\frac{EI}{\rho}. \quad (7.24)$$

Moreover, if only small deflections are considered, the second derivative of the z -component of the displacement (i.e., $d^2z/dx^2 \ll 1$ and the horizontal component of the displacement can be small and are not considered in the formulation. Since the arc length derivative $ds/dx = 1$, Eq. 7.23 can be formulated in the following more familiar format as a function of Cartesian coordinate x [210]:

$$M(x) = -EI \frac{d^2z^c}{dx^2}(x). \quad (7.25)$$

While useful in demonstrating the equivalency of this approach to more commonly used methods, these simplified beam models are *not* utilized throughout the remainder of this chapter.

7.3 Methodology

There are other finite deflection beam models with associated solvers that utilize the same assumptions from section 7.2 for specific initial geometries and loads [64–66, 186–203]. However, as shown in Table 7.1, the current body of literature lacks a beam model that allows for arbitrary initial geometry and loads. Therefore, a new method is proposed by this chapter that satisfies this requirement and utilizes a *universal parameterization method*. Since multiple features of the proposed model are inspired by previous work, a short summary of existing methods is discussed before introducing the new methodology.

7.3.1 Previous methods

Five aspects are of interest regarding existing methods: permitted initial geometry, permitted loading conditions, category of free variables, applicable solvers, and required discretization. Existing shortcomings will form the motivations for the developments demonstrated in this chapter.

		Loads				Number of papers
		Forces	Distributed pressure	Discrete moments	Arbitrary	
Initial geometry	Straight	[65, 66, 186–196]	[186, 189, 190, 192, 198–200]	[186–188, 191, 196]	[66, 201]	
	Polar	[186, 191, 197]	[186]	[186, 191, 197]	-	
	Arbitrary	[64, 202, 203]	[202]	-	-	

Table 7.1: A review of implementations of beam theory.

1. *Initial geometry*: the majority of studies regarding finite deflection beams consider that the

initial geometry is straight (see Eq. 7.23) [65, 66, 186–196, 200, 201] or of a constant radius (see Eq. 7.24) [66, 201]. The latter is by far the most common in engineering applications given fabrication constraints and their load-carrying efficiencies; they are also the only initial geometries that possess analytical solutions for specific conditions [186, 187, 190, 196, 200]. Finally, a more general approach for geometry is possible [64, 202, 203], with the framework developed by Hampton *et al.* [64] being utilized in this work.

2. *Loading conditions*: the majority of studies solve for a concentrated force at the free end of a straight [65, 66, 186–196], constant radius curved [186, 191], and arbitrarily curved [66, 201] beam. However, there are no existing models for discrete bending moments and arbitrary bending moment distributions (e.g., a combination of concentrated loads and linearly distributed pressures). Moreover, except for the work from Rao and Rao [201], no methods consider rotational loads. Therefore, all available methods limit arbitrary admissible geometries, portraying only a fraction of possible loading conditions.
3. *Free variables*: the general governing equation for Euler-Bernoulli is commonly solved for the following three free variables: beam angle ϕ , displacement u , and coefficients \mathbf{A} of a power series. Solving for displacements is widely implemented for other models such as small deflection beams. Still, it is uncommon for finite deflection beams as it leads to non-linear second-order differential equations. Beam angle ϕ is the most common method for finite deflections (see Eq. 7.22) as the governing equation is a first-order differential equation and has analytical solutions for specific cases. Moreover, the beam angle ϕ can be approximated by a power series (i.e., the reversion method) where polynomial coefficients \mathbf{A} must be determined. All three methods require additional processes to calculate the deformed parameterization (i.e., angle integration, linear superposition, and/or regression methods). Therefore, no approach provides a true analytical relation between Cartesian coordinates of the neutral line and a set of coefficients \mathbf{A} .
4. *Solvers*: except for a restricted category of beam problems with analytical solutions [186,

187, 190, 196, 200], most beam problems can only be solved numerically. Most authors arrange the governing equations in a system of first-order differential equations and implement a fourth-order Runge-Kutta method [189, 192, 193, 199, 201]. Conversely, the governing equation can also be solved via complete and incomplete elliptical integration [194–196]. Other less popular techniques include the Shooting method [198, 203], and the Projection algorithm [211].

Outside of the domain of finite beams, the Weighted-Residual and Ritz methods are common means to solve partial differential equations [58]. Both methods approximate the displacement by a polynomial series and generate a system of equations that can be solved for the polynomial coefficients. The methods require that the power series satisfy certain requirements (e.g., polynomial order), lead to a non-linear system of equations that needs to be solved via Newton’s method for finite deflections of arbitrary geometries, and require additional processes to determine the geometry of the shape configuration. For such reasons, an alternative general method inspired by the aforementioned methods is utilized.

5. *Discretization*: Independent of the method, any beam with discontinuous bending moment distribution benefits from discretization as will be later shown. The chain algorithm, similar to FEA, discretizes elastic members into small linearized elements, but, unlike FEA, elements are analyzed in succession (i.e., from the fully fixed end to the free end) and hence inversion of the overall stiffness matrix is avoided [191]. Campanile and Hasse [197] proposed a circle-arc method that uses a similar discretization technique as in the chain algorithm but approximates the deflection configuration of each element by a circular arc.

7.3.2 The proposed reversion method

There has not been located in the existing literature any finite deflection model that allows for arbitrary initial geometry and loads and a universal geometric representation of all deformed geometries, as shown in Fig. 7.7. A method that incorporates all these features provides a potentially intuitive tool to design engineers and can be incorporated into the design of morphing

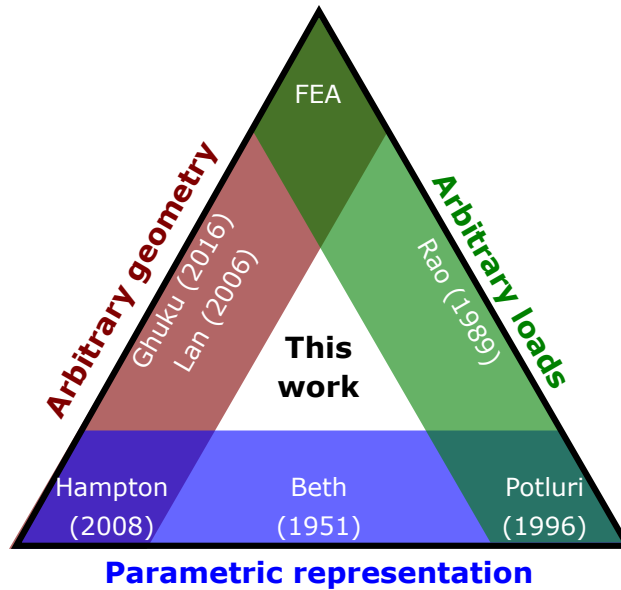


Figure 7.7: A summary of methods from Table 7.1 that consider a combinations of the following: arbitrary initial geometry, arbitrary loads, and parametric representation. Previous publication only consider up to one or two of these attributes, but this work considers the synthesis of all three.

structures. Therefore, a new approach that combines elements from power series, chain algorithm, and conservation of angular momentum is proposed.

For an arbitrary moment, the bending discontinuities can take place at the arc length locations Ξ , also known as the knots for a spline. In cases where the bending moment is continuous or approximately continuous, a non-piecewise parameterization method can be utilized. A piecewise representation is necessary to represent arbitrary loads as will be depicted in Fig. 7.19 as one CST cannot accurately represent discontinuous bending moments. The degrees of freedom of the parameterization method are denoted by coefficients A^c for the child and A^p for the parent.

The kinematic constraints that will be discussed in the next section will be shown to restrict the array of independent shape coefficients a^c and a^p to be subsets of all possible child and parent shape coefficients A^c and A^p . Therefore, the parent (x^p, z^p) and child (x^c, z^c) coordinates can be written as functions of the independent variables sets for splines (cf. Chapter 3 for the mathematical formulation of splines) as*:

*Semicolons are utilized to distinguish individual variables (left), and parameters (right).

$$z^c(s) = z(s; \mathbf{a}^c, \Xi), \quad (7.26)$$

$$z^p(s) = z(s; \mathbf{a}^p, \Xi). \quad (7.27)$$

Consequently, the Euler-Bernoulli equation for large deflections and arbitrary geometries (Eq. 7.21) can be rewritten as:

$$M(s, \mathbf{a}^c) = g(s, \mathbf{a}^c) + r(s), \quad (7.28)$$

where r is the residual due to the approximate z function and g is has terms dependent on the arc length, geometry, and material properties as defined by:

$$g(s) = EI \left[\frac{1}{\rho^c}(s; \mathbf{a}^c, \Xi) - \frac{1}{\rho^p}(s; \mathbf{a}^p, \Xi) \right]. \quad (7.29)$$

The total residual along the neutral line of the beam is:

$$\mathbb{R}(\mathbf{a}^c) = \int_0^L r(s) ds = \int_0^L [M(s, \mathbf{a}^c) - g(s, \mathbf{a}^c)] ds. \quad (7.30)$$

The values of \mathbf{a}^c that minimize the total residual \mathbb{R} represent the stable solution of a convex problem as they approximately satisfies conservation of linear momentum. Ideally, the minimal performance \mathbb{R}^* is zero or close to zero for the correct solution. Moreover, kinematic restrictions are imposed via equality constraints ω (e.g., case studies C). Therefore, the problem statement is formulated as:

$$\begin{aligned} \mathbb{R}^* &= \min_{\mathbf{a}^c} \mathbb{R}(\mathbf{a}^c), \\ \text{subject to:} & \end{aligned} \quad (7.31)$$

$$\omega(\mathbf{a}^c) = \mathbf{0}.$$

In the case of a multi-beam assembly, $\mathbf{a}^c = \{\mathbf{a}_u^c, \mathbf{a}_l^c\}$ and the objective function is the norm of the residual of each beam (\mathbb{R}_u and \mathbb{R}_l):

$$\mathbb{R} = \sqrt{(\mathbb{R}_u^2 + \mathbb{R}_l^2)}. \quad (7.32)$$

For all examples, a gradient-based optimizer known as the Sequential Least Squares Programming (SQLSP) algorithm [212] is implemented where the Jacobian:

$$\mathbf{J} = \frac{\partial \mathbb{R}(\mathbf{a}^c)}{\partial \mathbf{a}^c}, \quad (7.33)$$

is calculated via finite differences. Potentially, the Jacobian terms could have analytical solutions if linearized, but the calculation is not trivial as the bending moments cannot be decoupled from geometry properties for large deflections (Eqs. 7.16-7.15) and the non-linear relation between Cartesian coordinates and the arc length (Eq. 7.2). Although this work focuses on CST equations, the problem statement is valid regardless of the parameterization method.

7.3.3 Kinematic constraints and boundary conditions

Because the proposed approach utilizes shape coefficients as independent variables, boundary conditions are imposed based on their geometric implications. Dirichlet boundary conditions (prescribed values for $z(s)$ along the domain boundary) lead to a decrease in the number of independent shape coefficients by imposing kinematic constraints on the parameterization method itself. The analytical solutions for constrained degrees of freedom are derived in this section. As the method is not restricted to one geometric parameterization method, the constraints are formulated in a general format that is relevant for all parameterization methods as well as for CST equations. The following eight constraints are considered:

1. *Fixed root*: the beam root is fully fixed for all examples. The constant vertical coordinate and slope at the root are defined as z_0 and slope z'_0 (for most examples $z_0 = 0$ and $z'_0 = 0$);

thus,

$$z(s = 0) = z_0, \quad (7.34)$$

$$\frac{dz}{dx}(s = 0) = z'_0. \quad (7.35)$$

When CST equations are utilized as the parameterization technique, this corresponds to the following solutions for the parameterized coordinate ζ and the zeroth shape coefficient of the first spline element A_0^1 (Eq. 4.31):

$$\zeta_L^1 = z_0/c^1, \quad (7.36)$$

$$A_0^1 = -\zeta_T + \frac{z_0}{c^1} + z'_0. \quad (7.37)$$

2. *Free end*: the bending moment at the beam free end is zero if no torque T_s is applied at arc length coordinate $s = L$, corresponding to knot arc length Ξ^m . From the Euler-Bernoulli equation for large deflections and arbitrary geometries (Eq. 7.21):

$$\frac{T_s}{EI} = \frac{1}{\rho^{c,m}} - \frac{1}{\rho^{p,m}}, \quad (7.38)$$

$$\rho^{c,m} = \frac{EI\rho^{p,m}}{T_s + EI}. \quad (7.39)$$

If torque at the free end is zero, $T_s = 0$, then the radius of curvature between child and parent configurations are the same, $\rho^{c,m} = \rho^{p,m}$. Based on the radius of curvature equation at $\psi = 1$ (Eq. B.15) and the free end constraint (Eq. 7.39), the following relation is defined for the m -th spline element:

$$\frac{2nA_{n-1}^{c,m} - 2(N_1 + n)A_n^{c,m}}{c^{c,m} [1 + (-A_n^{c,m} + \zeta_T^{c,m} - \zeta_L^{c,m})^2]^{3/2}} = \frac{2nA_{n-1}^{p,m} - 2(N_1 + n)A_n^{p,m}}{c^{p,m} [1 + (-A_n^{p,m} + \zeta_T^{p,m} - \zeta_L^{p,m})^2]^{3/2}}, \quad (7.40)$$

and solving for the n -th child shape coefficient of the m -th spline element $A_n^{c,m}$:

$$A_n^{c,m} = \frac{1}{N_1 + n} \left\{ nA_{n-1}^{c,m} + [nA_{n-1}^{p,m} - (N_1 + n)A_n^{p,m}] \frac{c^{c,m}}{c^{p,m}} \left[\frac{1 + (-A_n^{c,m} + \zeta_T^{c,m} - \zeta_L^{c,m})^2}{1 + (-A_n^{p,m} + \zeta_T^{p,m} - \zeta_L^{p,m})^2} \right]^{3/2} \right\}. \quad (7.41)$$

3. *Rigid leading edge*: for airfoil applications, the region near the leading edge tends to be stiffer than the rest of the skin because of structural reinforcement, and it can be assumed rigid. Previously for structurally consistent airfoils (see Chapter 4), where a single CST was utilized, this imposition leads to a constant leading edge radius at arc length coordinate $s = 0$. However, helicopter blades and other structures are likely to be rigid for the whole region corresponding to the D-section. Therefore, a rigid leading edge section can be imposed by fixing the coefficients for the first spline element (i.e., $k = 1$). Therefore,

$$A_i^{c,1} = A_i^{p,1} \quad \forall i \in \{0, \dots, n\}. \quad (7.42)$$

As a consequence of a rigid leading edge section, the bending moment at the knot arc length Ξ^1 is discontinuous and only C^1 continuity is imposed even if the remainder of the beam is C^2 continuous.

4. C^0 continuity: The beam consists of a single component. As such, all relevant geometries are assumed to be C^0 continuous. Therefore the following is true for the parent and child configurations for any parameterization method:

$$z^{k-1}(\Xi^k) = z^k(\Xi^k) \quad \forall k \in \{1, \dots, m\}. \quad (7.43)$$

For CST equations (see Eq. 4.33), the rigid leading edge constraints for parent and child configurations are given by:

$$\zeta_L^k = \frac{c^{k-1}}{c^k} \zeta_T^{k-1} \quad \forall k \in \{1, \dots, m\}. \quad (7.44)$$

5. C^1 continuity: Aerodynamic outer mold lines are smooth surfaces; discontinuities increase drag and can initiate laminar to turbulent transition and should be avoided. The aerodynamically relevant geometries considered herein are assumed to be C^1 continuous. Therefore, the following is valid for any parameterization method:

$$\frac{dz^{k-1}}{dx}(s^k) = \frac{dz_k}{dx}(s^k) \quad \forall k \in \{1, \dots, m\}. \quad (7.45)$$

For CST equations (see Eq. 4.34), the C^1 continuity constraint at the knots is imposed for parent and child configurations by:

$$\zeta_T^k = -\zeta_L^{k-1} - A_n^{k-1} + \zeta_T^{k-1} + \zeta_L^k - A_0^k \quad \forall k \in \{1, \dots, m\}. \quad (7.46)$$

6. C^2 continuity: except for applied torques, the bending moment in Eq. 7.21 is a C^0 continuous function. From the same equation (or Eq. 7.25), the second derivative of the vertical position must also be C^0 continuous at all arc length coordinates except for rigid components. Therefore, C^2 continuity conditions are assumed for the position for all locations of the child configuration that the bending moment is C^0 continuous. The parent configuration has no bending moments applied, so C^2 continuity is always assumed. Therefore, the following is valid:

$$\frac{d^2 z^{k-1}}{dx^2}(s^k) = \frac{d^2 z_k}{dx^2}(s^k) \quad \forall k \in \{1, \dots, m\}. \quad (7.47)$$

For CST equations, (see Eq. 4.34), the kinematic constraints are imposed for parent and child configurations by:

$$\frac{1}{c^{k-1}} [nA_{n-1}^{k-1} - (N_1 + n)A_n^{k-1}] = \frac{1}{c^k} [-(n+1)A_0^k + nA_1^k], \quad (7.48)$$

and solving for the 0-th shape function for spline element k (i.e., the beam is composed of

m spline elements), A_0^k :

$$A_0^k = \frac{1}{n+1} \left\{ nA_1^k - \frac{c^k}{c^{k-1}} [nA_{n-1}^{k-1} - (N_1 + n)A_n^{k-1}] \right\}. \quad (7.49)$$

7. *Elastica*: as mentioned before (third assumption in Section 7.2) the beams here considered are inextensible along the neutral line. The mathematical implication to the spline is that the arc length L^k is preserved for spline beam elements similar to structurally consistent airfoils. As a consequence:

$$L^{c,k} = L^{p,k}. \quad (7.50)$$

From the definition of arc length (Eq. 7.2), the constraint is imposed by calculating chord $c^{c,k}$ for each beam region that satisfies:

$$\int_0^{c^{c,k}} \sqrt{1 + \left(\frac{dz}{dx}(\chi; \mathbf{A}^c) \right)^2} d\chi = \int_0^{c^{c,p}} \sqrt{1 + \left(\frac{dz}{dx}(\chi; \mathbf{A}^p) \right)^2} d\chi. \quad (7.51)$$

8. *Displacement boundary conditions*: any knot to which a constraint on a displacement degree of freedom is applied experiences a reaction force or moment. Because of the suggested solution approach (see Eq. 7.31), the bending moment distribution together with resulting reaction forces must be calculated. This calculation is atypical for FEA and similar methods as reaction forces are usually only calculated at post-processing. Therefore, a methodology to calculate reaction forces from kinematic constraints is introduced.

Such kinematic constraints might include boundary conditions (e.g., pinned root) or connections to attached rigid bodies (e.g., spars as is Chapter 5). The arc length coordinates s^r where displacements can be constrained are included in the set of knots Ξ ($s^r \in \Xi$). The x -component of the reaction forces is neglected because of the small influence compared to the z -component. This assumption is valid for all the explored case studies, but could be limiting to certain applications. From Eq. 7.19, the generated moment from n^r reaction forces R^k is:

$$M^r(s) = \sum_{k=1}^{n^r} \langle s^{r,k} - s \rangle^0 R^k (x(s^{r,k}) - x(s)) . \quad (7.52)$$

To determine the values of the reaction forces R^k , the governing equation (Eq. 7.21) can be rewritten as follows:

$$M^w(s) + M^t(s) + M^q(s) + M^e(s) + \sum_{k=1}^{n^r} \langle s^{r,k} - s \rangle^0 (x(s^{r,k}) - x(s)) R^k = g(s) , \quad (7.53)$$

Rearranging, the following relation is valid at any arc length s for any configuration A^c :

$$\sum_{k=1}^{n^r} \langle s^{r,k} - s \rangle^0 (x(s^{r,k}) - x(s)) R^k = g(s) - M^w(s) - M^t(s) - M^q(s) - M^e(s) . \quad (7.54)$$

Eq. 7.54 is valid for any arc length coordinate and can be sampled along the neutral line to form a system of equations with n^r unknown reaction forces. The number of independent sampled points is denoted N . If $N < n^r$, the system is underdefined and cannot be solved. If $N = n^r$ the system of equations is invertible, but the selection of sampled points is arbitrary and could bias the solutions. If $N > n^r$ the system of equations is overdefined and can be solved via a least-squares algorithm. Therefore, the reaction forces are calculated from an overdefined system of equations $n^r \times N$. The definition of the sampling N will be discussed in Section 1.4 as it also pertains to the stability of the solution.

Other boundary conditions such as simply supported locations or interactions with other beams can be incorporated through constraints or other parameter dependencies, which is discussed in future sections.

Considering all the boundary conditions imposed on the shape coefficients, the number of configuration variables depends on the number of rigid edges, torques applied, or C^2 continuous knots. Moreover, the number of coefficients necessary to define the parent geometry is not the same

as the number of degrees of freedom for the child geometries because of the free end boundary condition. Table 7.2 provides a summary of the number of shape coefficients for parent and child geometries where n is the order of the polynomial, m is the number of polynomial domains, and t is the number of discrete locations to which a concentrated torque or simply supported boundary condition is applied.

Table 7.2: Number of degrees of freedom to define a parent geometry \mathbf{a}^p and child configuration \mathbf{a}^c . Because of the imposed constraints, the number of degrees of freedom vary according to the imposed continuity at the knots. n is the order of the polynomial, m is the number of polynomial domains, and t is the number of locations with an applied torque.

	Number of degree of freedom	
	$\dim(\mathbf{a}^p)$	$\dim(\mathbf{a}^c)$
C^1 continuous beam	$(n + 1)m$	$(n + 1)m$
C^2 continuous beam	$nm + 1$	$nm + t$
C^2 continuous beam with Rigid LE	$nm + 1$	$n(m - 1) + t$

7.3.4 Beam interactions

The OML of the airfoil can be simplified as two beams, *upper* and *lower*, connected at specific knot locations. Each beam has distinct parameterization equations and positions coordinates for each beam is attributed as (x_u, z_u) and (x_l, z_l) . The beams can interact via the following components: hinged rigid spars, hinged springs, and hinged actuators. These interactions do not change the number of design variables or how the geometry is defined but affect the problem statement and bending moment distributions. As depicted in Fig. 7.8, all interactions can be classified regarding the relationship between forces $Q^{p,k}$ and $Q^{c,k}$ (first introduced in Eq. 7.15) as well as the lengths $l^{p,k}$ and $l^{c,k}$. A summary of each interaction is herein provided.

Three different beam interactions are studied to represent situational differences between the relation between the beam and the attached internal component. In aerospace, the thin skin is less stiff than internal structures (e.g., ribs and spars); hence, the internal components can be considered as hinged rigid bodies compared to the compliant skin. However, if the stiffness of an internal

components of the same order of magnitude or lower than the skin (e.g., a leaf-beam suspension), the internal structure can be modeled as a hinged linear spring. Finally, if the internal component is not a structural component but instead it exerts a coupled load without kinematically constraining the beam, it can be simplified to a hinged actuator.

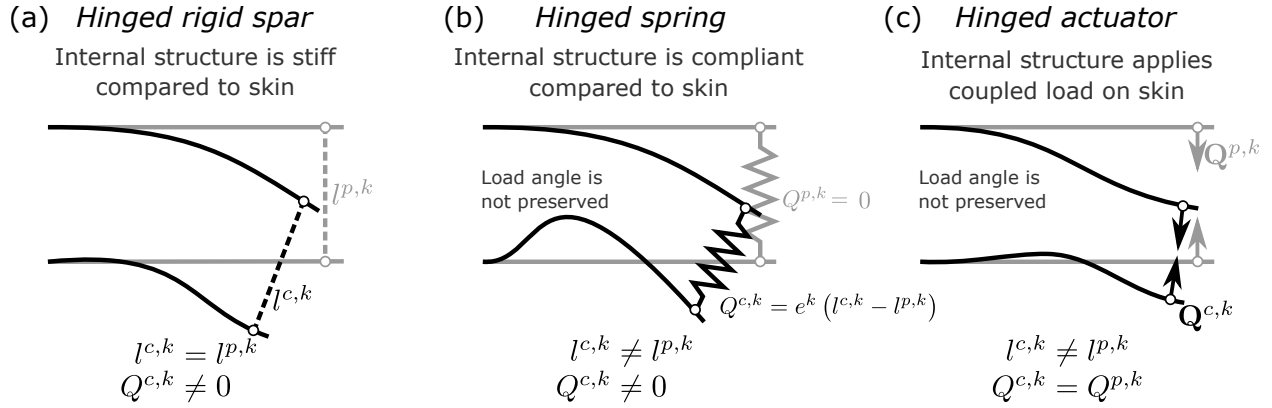


Figure 7.8: Interactions between beams. For all three investigated interactions, the relation between reaction forces and lengths for parent and children configuration differ.

1. The length of the components is preserved for child and parent configurations for rigid spars ($l^{p,k} = l^{c,k}$). The length is defined as:

$$l^{p,k} = \sqrt{(x_u^{p,k} - x_l^{p,k})^2 + (z_u^{p,k} - z_l^{p,k})^2}, \quad (7.55)$$

$$l^{c,k} = \sqrt{(x_u^{c,k} - x_l^{c,k})^2 + (z_u^{c,k} - z_l^{c,k})^2}, \quad (7.56)$$

and the angle between the spar and the beams is not preserved as depicted in Fig. 7.9(a). The child geometry defines the magnitude and direction of the reaction forces, but the length is determined by the parent geometry. Moreover, a rigid spar generates an additional reaction

force at both beams with the same magnitude but opposing directions because of the conservation of linear momentum. Therefore, the reaction forces for the upper and lower surfaces at knot k are defined as:

$$\mathbf{R}_u^k = -\mathbf{R}_l^k, \quad (7.57)$$

the moment generated by the opposing reaction force is still calculated via Eq. 7.52 and the following equality constraint ω is imposed on the momentum residual minimization (cf. Eq. 7.31):

$$\omega^k = |l^{c,k} - l^{p,k}|. \quad (7.58)$$

2. If the internal structure has stiffness on the same order of magnitude as the beam or cross section of the skin, the interaction between both beams can occur through hinged springs as depicted in Fig. 7.8(b). n^e springs with stiffness e^k can be applied at knots s^e . The resultant bending moment from spring components along the out-of-plane axis i_2 is given by:

$$M^e(s) = \sum_{k=1}^{n^e} \langle s^{e,k} - s \rangle^0 [\mathbf{Q}^{e,k} \times \mathbf{d}(s, s^{e,k})] \cdot \mathbf{i}_2, \quad (7.59)$$

where \mathbf{d} is the distance vector from arc length s to $s^{e,k}$ (cf. Eq. 7.17),

$$\mathbf{Q}^{e,k} = e^k (l^{c,k} - l^{p,k}) \begin{pmatrix} x_u^{c,k} - x_l^{c,k} \\ z_u^{c,k} - z_l^{c,k} \end{pmatrix}. \quad (7.60)$$

3. In some applications such as morphing airfoils [122], actuators can connect the beams and generate force without imposing kinematic restrictions (e.g., $l^{p,k} = l^{c,k}$). Therefore, the hinged actuators can be modeled as coupled force vectors where the magnitude is constant,

but the direction and length are defined by the child geometry as depicted in Fig. 7.8(c), rotating as the structure rotates to maintain actuator alignment. From the conservation of linear momentum, the force vectors acting on each beam are related by:

$$Q_u^k = -Q_l^k. \quad (7.61)$$

7.4 Implementation

The implementation of the proposed methodology benefits from efficient algorithms and a general framework to allow for various loading and initial geometries; it must provide reliable results. A framework that satisfies all three is here described via pseudocode. Although the implementation is specific to CST equations, any parameterization method can be utilized as will be shown in Section 1.5.1. For the purposes of illustration, the following three beam models are considered in increasing order of complexity: spline beam element ($m = 1$), the CST spline beam (beam component with $m > 1$), and the multi-beam assembly. The more complex models utilize the simpler models as a foundation, as shown in Fig. 7.9, allowing for robustness and an intuitive flow of information as the implementation is developed and demonstrated.

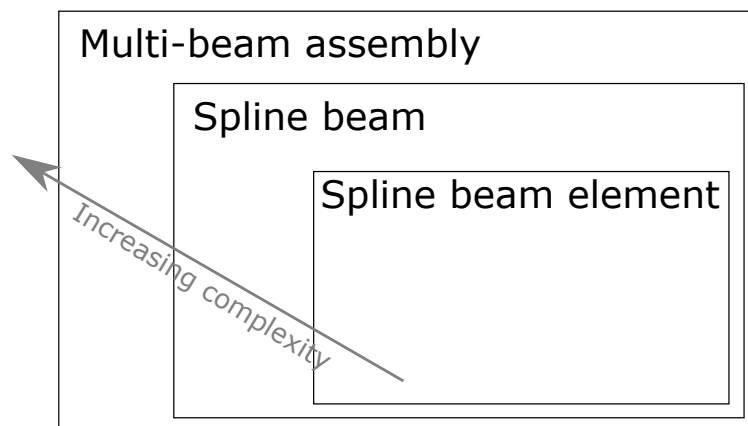


Figure 7.9: Nested beam models.

7.4.1 Spline beam element and spline beam

To efficiently calculate integrals along the neutral line (e.g., Eq. 7.30) as well as track the displacements (see Eq. 7.11), a quadrature with N integration points along the neutral line is defined. The integration points are *not* necessary for geometric representation nor are they related to the number of free variables (as in FEA) but are necessary for numerical integration. As multiple integrations are necessary for each configuration, it is efficient to store geometric properties along the mesh for reuse. Each region k of the beam over which a continuous CST function is used can have an arbitrary number of integration points N^k . As such, the total number of integration points is:

$$N = \sum_{k=1}^m N^k - m + 1. \quad (7.62)$$

The distribution of integration points for each region can be uniformly distributed based on the radius of curvature ρ , Cartesian coordinate x , or arc length s . The latter is here utilized for all examples. An example is provided in Fig. 7.10 to illustrate the differences between integration points s and the knots Ξ .

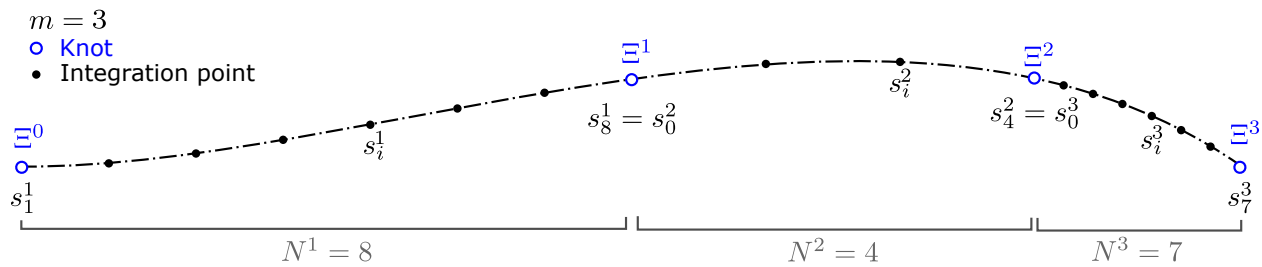


Figure 7.10: An example of a beam with four knots and varying number of integration points per spline beam element.

The defined quadrature is utilized for multiple operations such as the integral of the residual

via trapezoidal rule (cf. Eq. 7.30): †

$$\mathbb{R}(\mathbf{A}^c) \approx \frac{1}{2} \sum_{j=0}^{N-1} (s_{j+1} - s_j) (r(s_j, \mathbf{A}^c) + r(s_{j+1}, \mathbf{A}^c)) , \quad (7.63)$$

and to calculate the arc length (Eq. 7.2) for specific coordinate x_j :

$$s_j = \sum_{p=1}^j \frac{1}{2} (x_p - x_{p-1}) \left(\frac{ds_p}{dx} + \frac{ds_{p-1}}{dx} \right) . \quad (7.64)$$

When utilizing Eq. 7.64 to calculate x_j for a new \mathbf{a}^c , the value of ds_j/dx is at first unknown as it is dependent on x_j . The equation is reformulated as follows such that it can be solved via fixed-point iteration for x_j :

$$\begin{aligned} s_j &= \frac{1}{2} (x_j - x_{j-1}) \left(\frac{ds_j}{dx} + \frac{ds_{j-1}}{dx} \right) + \sum_{p=1}^{j-1} \frac{1}{2} (x_p - x_{p-1}) \left(\frac{ds_p}{dx} + \frac{ds_{p-1}}{dx} \right) , \\ x_j &= x_{j-1} + \frac{2s_j - \sum_{p=1}^{j-1} (x_p - x_{p-1}) \left(\frac{ds_p}{dx} + \frac{ds_{p-1}}{dx} \right)}{\left(\frac{ds_j}{dx} + \frac{ds_{j-1}}{dx} \right)} . \end{aligned} \quad (7.65)$$

The details regarding the implementation of the methodology and any other relevant calculations are portrayed in Boxes 7.1-7.4. The core of the algorithm is depicted in Box 7.1 while the algorithms for calculating dependent shape coefficients are in Box 7.2, for geometric states are in Box 7.3, and for moments are in Box 7.4. The residual for each case is calculated, whereas the optimization will utilize the current set of objective values to determine the next design variable or if the optimization converged. Convergence is achieved when the variation of the objective function between two iterations is less than 10^{-6} .

†For specific boundary conditions (e.g., the non-zero slope at the root) and class coefficients ($N_1 = 0.5$), there are singularities at the bounds that result in an improper integral [213]. The singularity can be mediated by separating the integral into two components, unbound and bound, such that the unbound component can be analytically solved and the bound component is a proper integral. This decomposition is necessary for implementing the framework to arbitrary geometries at the root but was not utilized for any of the case studies and is thus omitted.

Box 7.1: Main algorithm for CST and CST spline beam models.

Initialize with $\mathbf{a}^c = \mathbf{a}^p$

1. Parent

- a. Calculate dependent shape coefficients and knot positions using Box 7.2

$$\mathbf{a}^p \rightarrow \{\mathbf{A}^p, \zeta_L^p, \zeta_T^p\}$$

- b. Determine geometric states using Box 7.3

$$\{\mathbf{A}^p, \zeta_L^p, \zeta_T^p\} \rightarrow \left\{ \mathbf{r}^p, \frac{d\mathbf{r}^p}{ds}, \mathbf{P} \right\}$$

2. Child

- a. Calculate dependent shape coefficients and knot positions using Box 7.2

$$\mathbf{a}^c \rightarrow \{\mathbf{A}^c, \zeta_L^c, \zeta_T^c\}$$

- b. Determine geometric states using Box 7.3

$$\{\mathbf{A}^c, \zeta_L^c, \zeta_T^c\} \rightarrow \left\{ \mathbf{r}^c, \frac{d\mathbf{r}^c}{ds}, \boldsymbol{\rho}^c \right\}$$

3. Calculate moment distribution components (Eq. 7.12) via Box 7.4

$$M(s) = M^q(s) + M^w(s) + M^t(s) + M^r(s)$$

4. Calculate residual (Eq. 7.63)

$$\mathbb{R}(\mathbf{a}^c) \approx \sum_{j=0}^{N-1} \frac{1}{2} (s_{j+1} - s_j) [M(s_j, \mathbf{a}^c) - g(s_j, \mathbf{a}^c) + M(s_{j+1}, \mathbf{a}^c) - g(s_{j+1}, \mathbf{a}^c)]$$

where (Eq. 7.29) gives:

$$g(s; \mathbf{a}^c) = EI \left[\frac{1}{\rho^c}(s; \mathbf{a}^c) - \frac{1}{\rho^p}(s; \mathbf{a}^p) \right]$$

5. Calculate Jacobian based on finite differences

6. Optimizer calculates next \mathbf{a}^c based on Jacobian

7. Repeat steps 2-6 until optimization converges

Box 7.2: Algorithm to calculate dependent variables for CST spline ($m \neq 1$) and CST ($m = 1$) beams.

Calculate dependent shape coefficients and knot positions

For $k = 1, \dots, m$ (initial guess $c^{c,k} = c^{p,k}$):

If $k = 1$ and child configuration and rigid:

$$\mathbf{A}^{c,k} = \mathbf{A}^{p,k}$$

else:

$$\mathbf{A}_i^{c,k} = \mathbf{a}_{(k-1)n+i}^c \quad \forall i \in [1, n]$$

a. If $k > 1$, C^2 (Eq. 7.49) continuity conditions are imposed:

$$A_0^k = \frac{1}{n+1} \left\{ nA_1^k - \frac{c^k}{c^{k-1}} [nA_{n-1}^{k-1} - (N_1 + n)A_n^{k-1}] \right\}$$

b. If $k = 1$, boundary conditions $\zeta(0)$ and $\zeta'(0)$ (Eq. 7.37) are imposed:

$$\zeta_L^1 = z_0/c_1$$

$$A_0^1 = -\zeta_T + \frac{z_0}{c_1} + z_0'$$

else, C^0 (Eq. 7.44) and C^1 (Eq. 7.46) continuity conditions are imposed:

$$\zeta_L^k = \frac{c^{k-1}}{c^k} \zeta_T^{k-1}$$

$$\zeta_T^k = -\zeta_L^{k-1} - A_n^{k-1} + \zeta_T^{k-1} + \zeta_L^k - A_0^k$$

c. If $k = m$ and child configuration, free end (Eq. 7.41) conditions are imposed:

$$A_n^c = \frac{1}{N_1 + n} \left\{ nA_{n-1}^c + [nA_{n-1}^p - (N_1 + n)A_n^p] \frac{c^c}{c^p} \left[\frac{1 + (-A_n^c + \zeta_T^c - \zeta_L^c)^2}{1 + (-A_n^p + \zeta_T^p - \zeta_L^p)^2} \right]^{3/2} \right\}$$

d. If child configuration, calculate chord $c^{c,k}$ (Eq. 7.51):

$$\int_0^{c^{c,k}} \sqrt{1 + \left(\frac{dz}{dx}(\chi; \mathbf{A}^{c,k}) \right)^2} d\chi = \int_0^{c^{p,k}} \sqrt{1 + \left(\frac{dz}{dx}(\chi; \mathbf{A}^{p,k}) \right)^2} d\chi$$

e. If child configuration, iterate steps a-d until chord converges

Box 7.3: Algorithm to determine parent and child geometries for CST spline ($m \neq 1$) and CST element ($m = 1$) beams.

Calculate geometric states

For $j = 1, \dots, N$ (initial guess $x_j^c = x_j^p$ for child and $x_j^p = s_j$ for parent):

- a. Determine k such that $\Xi^{k-1} \leq s_j < \Xi^k$ and calculate ψ_j^k (Eq. 4.30)[‡]

$$\psi_j^k = \frac{x(s_j) - x(\Xi^{k-1})}{c^k}$$

- b. Calculate arc length derivatives regarding x (Eq. 7.2)

$$\frac{ds_j}{dx} = \sqrt{1 + \left(\frac{d\zeta_j^k}{d\psi^k}\right)^2}$$

where (Eq. B.4)

$$\frac{d\zeta_j^k}{d\psi^k} = C^k(\psi_j^k) \sum_{i=0}^n A_i^k S_i(\psi_j^k) \left(\frac{i - n - N_2^k}{1 - \psi_j^k} + \frac{N_1^k + i}{\psi_j^k} \right) + \zeta_T^k$$

$$C^k(\psi_j^k) = (\psi_j^k)^{N_1^k} (1 - \psi_j^k)^{N_2^k}$$

$$S_i(\psi_j^k) = \left[\frac{n!}{i!(n-i)!} (\psi_j^k)^i (1 - \psi_j^k)^{n-i} \right]$$

- c. calculate horizontal component x_j by fixed-point iteration to Eq. 7.65

$$x_j = x_{j-1} + \frac{2s_j - \sum_{p=1}^{j-1} (x_p - x_{p-1}) \left(\frac{ds_p}{dx} + \frac{ds_{p-1}}{dx} \right)}{\left(\frac{ds_j}{dx} + \frac{ds_{j-1}}{dx} \right)}$$

- d. Repeat a-c until x_j converges

- e. Calculate vertical component z_j using Eq. 4.31

$$z_j = c^k \zeta^k(\psi_j^k)$$

- f. Calculate angles if load is rotational using Eq. 7.4

$$\sin \phi_j = \left(\frac{ds_j}{dx} \right)^{-1} \quad \cos \phi_j = \frac{d\zeta_j}{d\psi} \left(\frac{ds_j}{dx} \right)^{-1}$$

- g. Calculate second derivative of parameterized vertical component using Eq. B.5

$$\frac{d^2 \zeta_j^k}{dx^2} = C^k(\psi) \sum_{i=0}^n A_i^k S_i \left[\left(\frac{N_1^k + i}{\psi_j^k} + \frac{i - n - N_2^k}{1 - \psi_j^k} \right)^2 - \frac{N_1^k + i}{(\psi_j^k)^2} + \frac{i - n - N_2^k}{(1 - \psi_j^k)^2} \right]$$

- h. Calculate radius curvature using Eq. (7.5)

$$\frac{1}{\rho_j^c} = \frac{1}{c^k} \frac{d^2 \zeta_j^k}{d\psi^2} \left[1 + \left(\frac{d\zeta_j^k}{d\psi} \right)^2 \right]^{-1/2}$$

Box 7.4: Algorithm to determine bending moments.

Calculate moment components

a. Calculate contribution due to torques M^t via Eq. 7.15:

$$M^t(s_j) = \sum_{i=1}^{n_t} \langle s^{t,k} - s_j \rangle^0 T_i$$

b. Calculate contribution due to pressure M^w via Eq. 7.16:

$$M^w(s_j) = \sum_{i=j}^{N-1} \frac{1}{2} (s_i - s_{i+1}) (m_i + m_{i+1})$$

where:

$$m_i = W(x_i) \{ \cos(\beta\theta_i) [x_i - x_j] - \sin(\beta\theta_i) [z_i - z_j] \}$$

For $j = 1, \dots, N$:

c. Calculate contribution due to forces M^q via Eq. 7.19:

$$M^q(s) = \sum_{k=1}^{n^q} \langle s^{q,k} - s_j \rangle^0 [\mathbf{Q}^{c,k} \times \mathbf{d}(s_j, s^{q,k})] \cdot \mathbf{i}_2.$$

where:

$$\mathbf{Q}^k = Q^k \begin{bmatrix} \cos \beta\phi^k & -\sin \beta\phi^k \\ \sin \beta\phi^k & \cos \beta\phi^k \end{bmatrix} \begin{pmatrix} \sin \theta^k \\ \cos \theta^k \end{pmatrix}.$$

$$\mathbf{d}(s_j, s^{q,k}) = \begin{pmatrix} x^c(s^{q,k}) - x^c(s_j) \\ z^c(s^{q,k}) - z^c(s_j) \end{pmatrix}$$

d. Calculate reaction forces R_i via Eq. 7.54:

$$\sum_{k=1}^{n^r} \langle s^{r,k} - s_j \rangle^0 (x(s^{r,k}) - x(s_j)) R^k = g(s_j) - M^w(s_j) - M^t(s_j) - M^q(s_j) - M^e(s_j)$$

e. Calculate M^r via Eq. 7.52:

$$M^r(s) = \sum_{k=1}^{n^r} \langle s^{r,k} - s_j \rangle^0 R^k (x(s^{r,k}) - x(s_j))$$

7.4.2 Multi-beam assembly

Implementation of the proposed approach for a multi-beam assembly is similar to solving the upper and lower beams simultaneously (Box 7.5) via inclusion of spar reactions or spring forces in Box 7.6, and the calculation of equality constraint ω (Eq. 7.58). The reaction and spring forces are only calculated for the upper beam. In contrast, the forces or moment distributions for the lower beam are related to the upper equivalents via Eqs. 7.57 and 7.61. Following the calculation of the bending moment and geometric states, the residual for each beam and the objective function are determined (Box 7.1). Based on the objective and constraint values, the optimizer will define the next set of design variables or if the algorithm has converged. If there are reaction forces, the Levenber-Marquardt algorithm is implemented to calculate them [214].

Box 7.5: Algorithm for coupled CST spline beams.

Initialize with $\mathbf{a}_u^c = \mathbf{a}_u^p$ and $\mathbf{a}_l^c = \mathbf{a}_l^p$

1. Parent

a. Upper beam: implement procedure from Box 7.1(1)

$$\{\mathbf{A}_u^p\} \rightarrow \{\mathbf{r}_u^p, \boldsymbol{\rho}_u^p\}$$

b. Lower beam: implement procedure from Box 7.1(1)

$$\{\mathbf{A}_l^p\} \rightarrow \{\mathbf{r}_l^p, \boldsymbol{\rho}_l^p\}$$

c. Calculate distance between constrained knots for parent configuration

For $k = 1, \dots, m^c$:

$$l^{p,k} = \sqrt{\left(x_u^{p,k} - x_l^{p,k}\right)^2 + \left(z_u^{p,k} - z_l^{p,k}\right)^2}$$

2. Child

a. Upper beam: implement procedure from Box 7.1(2-4) and Box 7.6

$$\{\mathbf{a}_u\} \rightarrow \{\mathbf{r}_u^c, \boldsymbol{\rho}_u^c, \mathbb{R}_u\}$$

b. Lower beam: implement procedure from Box 7.1(2-4) and Box 7.6

$$\{\mathbf{a}_l\} \rightarrow \{\mathbf{r}_l^c, \boldsymbol{\rho}_l^c, \mathbb{R}_l\}$$

c. Calculate distance between constrained knots for child configuration

For $k = 0, \dots, m$:

$$l^{c,k} = \sqrt{\left(x_u^{c,k} - x_l^{c,k}\right)^2 + \left(z_u^{c,k} - z_l^{c,k}\right)^2}$$

3. Calculate constraints

For $k = 1, \dots, m$:

$$\omega^k = l^{c,k} - l^{p,k}$$

4. Calculate total residual

$$\mathbb{R} = \sqrt{(\mathbb{R}_u^2 + \mathbb{R}_l^2)}$$

5. Calculate Jacobian via finite differences

6. Optimizer calculates next \mathbf{a}_u and \mathbf{a}_l based on Jacobian and constraints $\boldsymbol{\omega}$

7. Repeat steps 2-5 until optimizer converges

Box 7.6: Main algorithm to determine the solution of a multi-beam assembly.

Calculate external moment components M_E

For $j = 1, \dots, N$:

a. If *upper* beam, calculate moment M^e if there are spring elements via Eq. 7.6:

$$M^e(s) = \sum_{k=1}^{n^e} \langle s^{e,k} - s_j \rangle^0 [\mathbf{Q}^{e,k} \times \mathbf{d}(s_j, s^{e,k})] \cdot \mathbf{i}_2,$$

where:

$$\mathbf{Q}^{e,k} = e^k (l^{c,k} - l^{p,k}) \begin{pmatrix} x_u^{c,k} - x_l^{c,k} \\ z_u^{c,k} - z_l^{c,k} \end{pmatrix}$$

where:

$$l^{p,k} = \sqrt{(x_u^{p,k} - x_l^{p,k})^2 + (z_u^{p,k} - z_l^{p,k})^2}$$

$$l^{c,k} = \sqrt{(x_u^{c,k} - x_l^{c,k})^2 + (z_u^{c,k} - z_l^{c,k})^2}$$

else moment M_l^e is given by Eq. 7.54:

$$M_u^e = -M_l^e$$

b. If *lower* beam, connected reaction forces R_j are (Eq. 7.57):

$$R_l^k = -R_u^k$$

else calculate reaction forces via Eq. 7.61:

$$\sum_{k=1}^{n^r} \langle s^{r,k} - s_j \rangle^0 R^k [x(s^{r,k}) - x_j] = g(s_j) - M^w(s_j) - M^t(s_j) - M^q(s_j) - M^e(s_j)$$

c. Calculate M^r via Eq. 7.52:

$$M^r(s_j) = \sum_{k=1}^{n^r} \langle s^{r,k} - s_j \rangle^0 R^k (x(s^{r,k}) - x(s_j))$$

7.5 Case studies

Multiple case studies are evaluated for the developed beam formulations to demonstrate the versatility and robustness of the proposed framework that does not exist in currently existing beam models. Three sets of case studies are explored for: (A) a spline beam element, (B) a spline beam, and (C) a multi-beam assembly. An example of each case study is depicted in Fig. 7.11. A total of 20 case studies for CST basis and nine for power series parameterization are evaluated. Each case study is utilized to verify the different features of the framework, with the nature of the studies approaching that of morphing airfoil sections as features are added. All case studies are validated against known solutions from either analytical solutions, experiments [189,201,202], or FEA. The root mean square error in the deformed position ϵ is utilized to quantify the difference between the novel solutions and the reference.

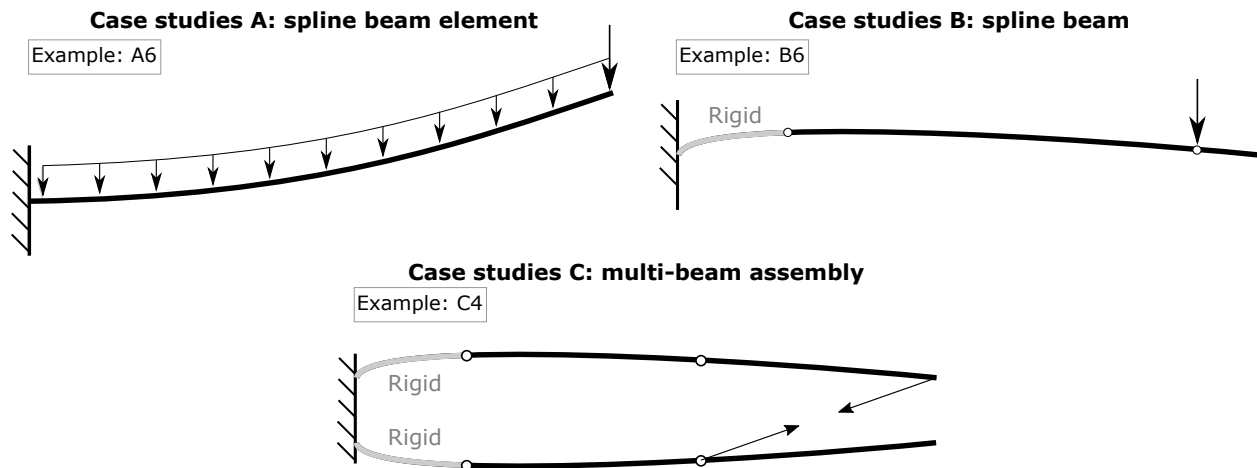


Figure 7.11: Schematics of loads, boundary conditions, and initial geometries for an example from each case study.

7.5.1 Case studies A: beam spline element

Case studies A consider parameterizations with only one spline beam element. Therefore, all domains are C^n continuous (n being the order of the polynomial) and no discontinuities of the

bending moment are possible. Although it is the simplest implementation of the proposed formulation, all demonstrated capabilities are pertinent for more complex case studies such as beam splines and assemblies. Six case studies with variants for varying loads are selected to demonstrate reliable responses for finite deflections, concentrated loads, linear pressure distributions, rotational loads, and initially curved geometries. Features of each case are depicted in Table 7.3 and the respective schematics are found in Fig. 7.12.

Table 7.3: All explored features for case studies A.

		Finite deflections	Concentrated load	Linear pressure	Rotational load	Initially curved
Case studies	A1		✓			
	A2			✓		
	A3	✓	✓	✓		
	A4	✓		✓	✓	
	A5	✓	✓			✓
	A6	✓	✓	✓		✓

Case studies A are first evaluated for a power series to demonstrate that the methodology is generalizable to any parametric representation. While still imposing length preservation to calculate x , the vertical component z is given by:

$$z = \sum_{i=2}^n A_i x^i, \quad (7.66)$$

where A_i are the shape coefficients and $A_0 = A_1 = 0$ because of the fixed boundary conditions (Eq. 7.37).

The solutions for all cases utilizing the power series are provided in Fig. 7.13. All the low residual solutions have a low root mean square error regarding the reference; hence, the results are in agreement with known solutions. The same study is implemented for a CST basis as summarized in Fig. 7.14 with similar results. When comparing the residual and RMSE for both parameterization methods in Table 7.4, the advantage of CST basis over a power series is not evident as

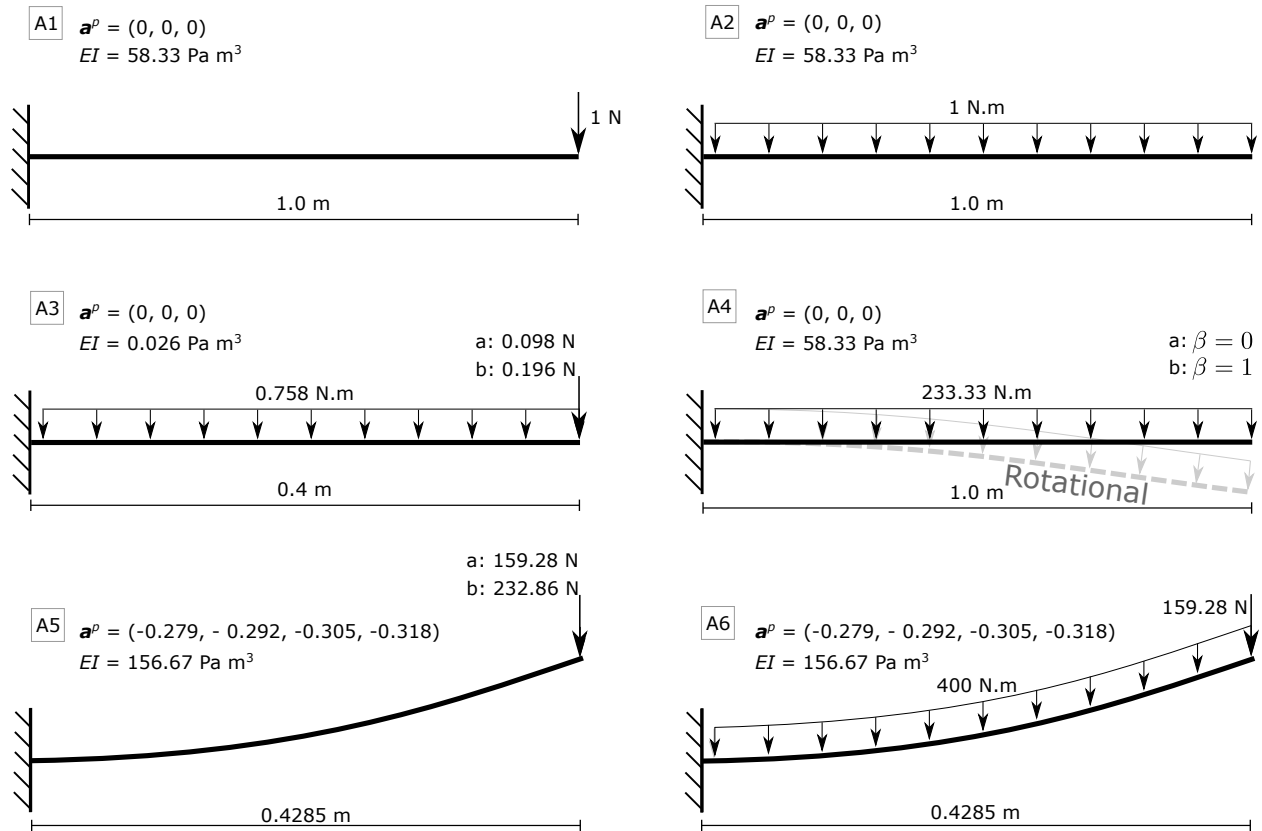


Figure 7.12: Schematics of loads, boundary conditions, and initial geometries considered in case studies A. Studies A3-A6 result in finite deflections.

only initially straight beams as both metrics have the same order of magnitude. However, CST equations have improved accuracy for initially curved configurations (e.g., case study A5).

Table 7.4: Residual and RMSE for case studies A with power series and CST.

	Residual		RMSE		References
	Power series	CST	Power series	CST	
Case studies					
A1	1.3×10^{-6}	1.5×10^{-7}	5.2×10^{-7}	2.9×10^{-8}	Euler-Bernoulli, FEA
A2	9.4×10^{-7}	2.9×10^{-6}	2.3×10^{-7}	4.6×10^{-7}	Euler-Bernoulli
A3a	7.5×10^{-3}	6.8×10^{-3}	4.7×10^{-4}	3.8×10^{-4}	Experiment [189]
A3b	4.7×10^{-2}	1.3×10^{-2}	1.2×10^{-3}	3.3×10^{-4}	Experiment [189]
A4a	3.0×10^{-2}	1.1×10^{-2}	2.1×10^{-3}	2.9×10^{-3}	Experiment [201]
A4b	2.7×10^{-2}	1.8×10^{-2}	2.0×10^{-3}	2.6×10^{-3}	Experiment [201]
A5a	1.1×10^{-2}	8.2×10^{-4}	1.5×10^{-3}	1.5×10^{-3}	Experiment [202]
A5b	1.6×10^{-2}	1.1×10^{-3}	1.2×10^{-3}	7.4×10^{-4}	Experiment [202]
A6	5.0×10^{-3}	6.5×10^{-4}	6.8×10^{-5}	7.1×10^{-5}	FEA

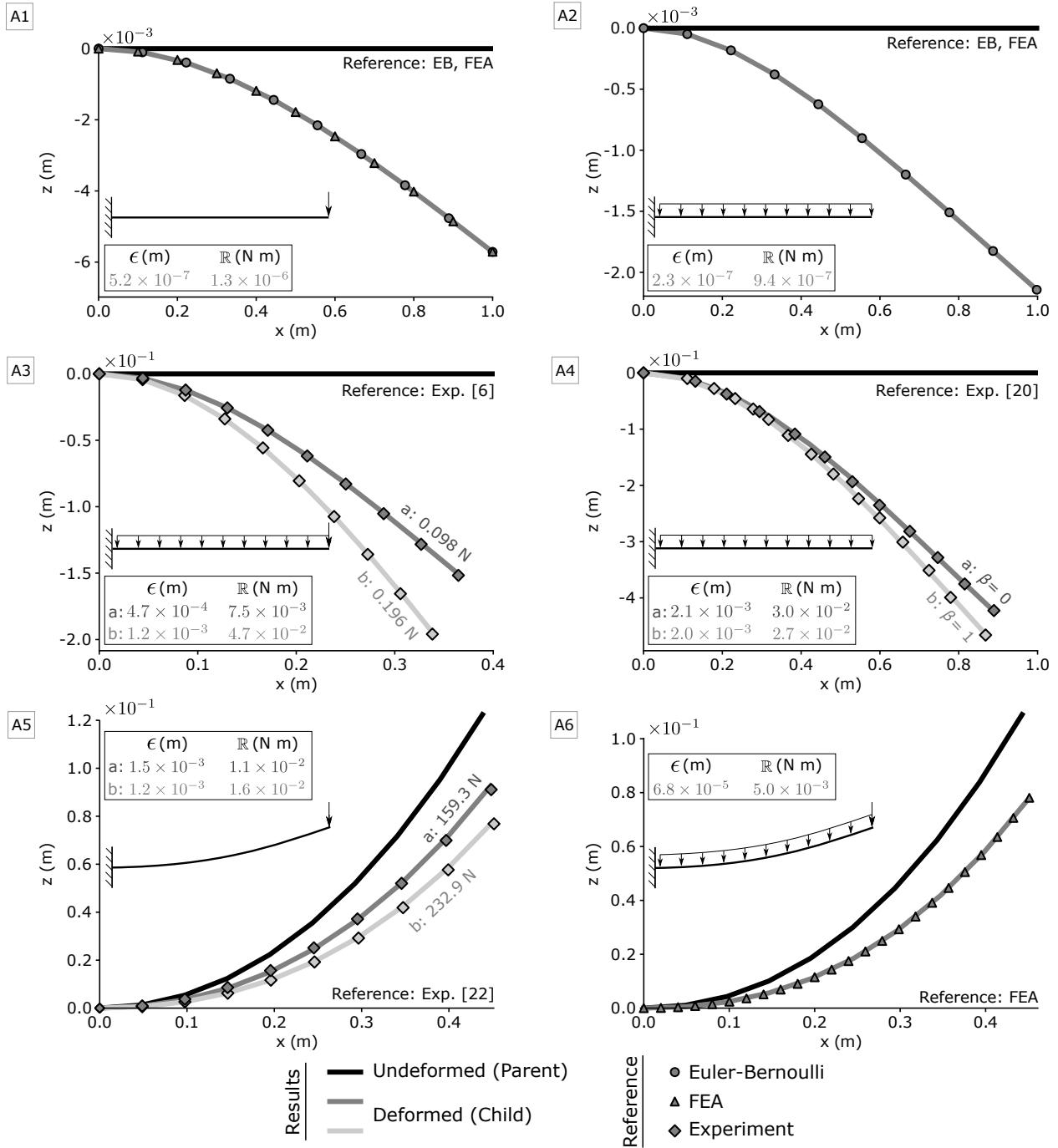


Figure 7.13: Results of case studies A with a power series basis. All case studies returned low RMSE ϵ and residuals \mathbb{R} with no error exceeding 0.43% of the maximum deflection magnitude.

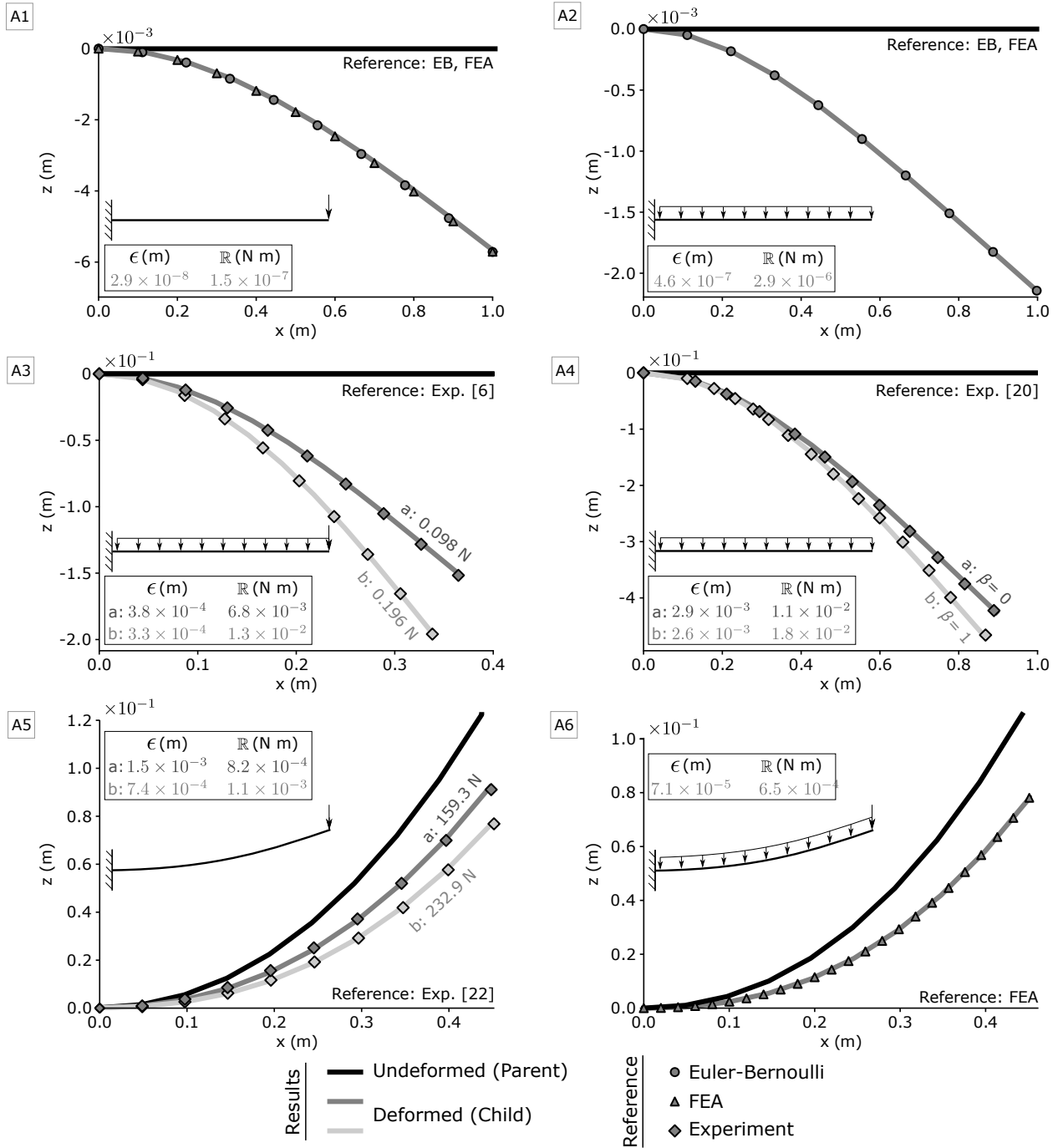


Figure 7.14: Results of case studies A with CST basis. All case studies returned low RMSE ϵ and residuals \mathbb{R} with no error exceeding 0.53% of the maximum deflection magnitude.

7.5.2 Case studies B: CST spline beam

For the next case studies, power series are not considered and only a CST spline beam is evaluated. Six case studies are evaluate to demonstrate the following features: concentrated loads at any location of the beam, arbitrary pressure distributions, reaction forces, applied torques, rigid components, and initially curved geometries. The features of each case are summarized in Table 7.5 and the respective schematics in Fig. 7.15. Note the progression toward a morphing airfoil section.

Table 7.5: All explored features for case studies B.

	Concentrated loads	Linear pressure	Reaction force	Discrete moments	Initially curved	Rigid component
B1	✓					
B2	✓	✓				
B3			✓			
B4			✓	✓		
B5	✓				✓	
B6	✓				✓	✓

The stable solutions for all case studies are in agreement with the known solutions for each problem as shown in Fig. 7.16. Residuals up to 2.8×10^{-3} N m can provide accurate solutions with root mean square error of 5.9×10^{-4} m.

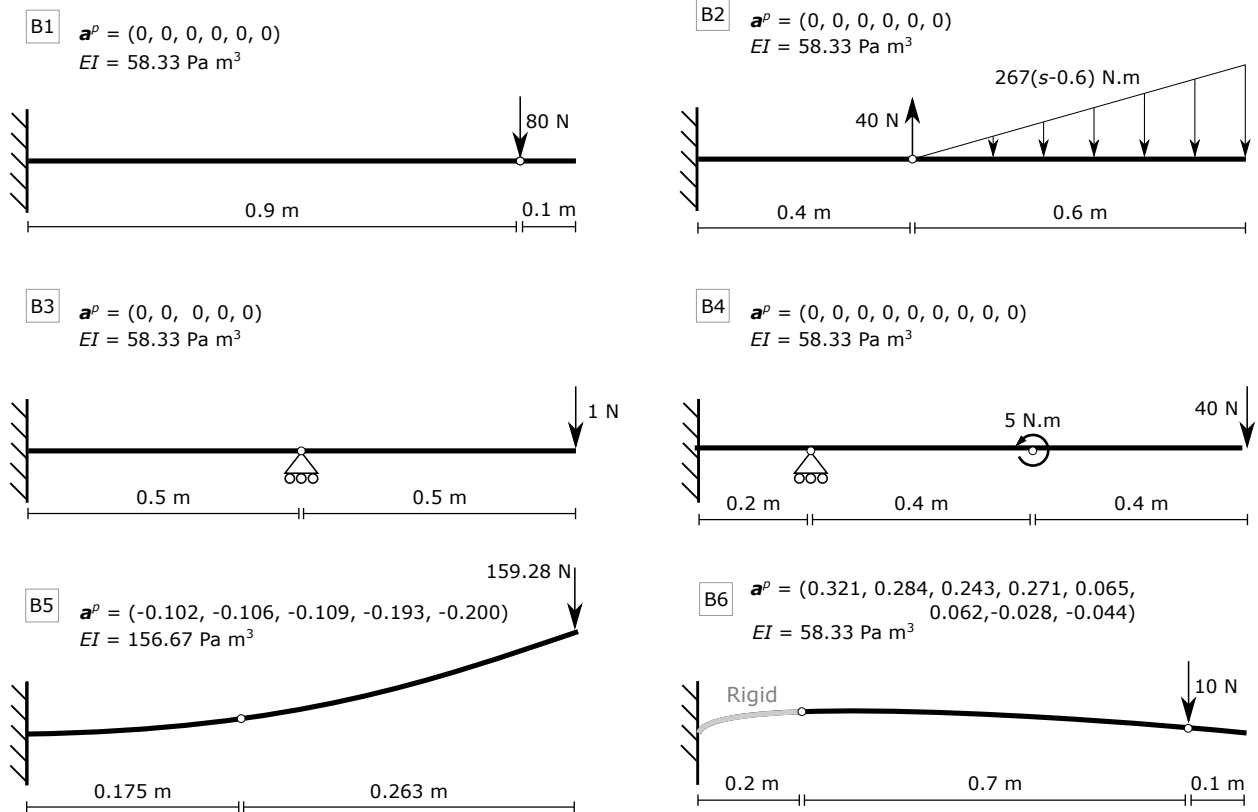


Figure 7.15: Schematics of loads, boundary conditions, and initial geometries for case studies B (independent shape coefficients are depicted).

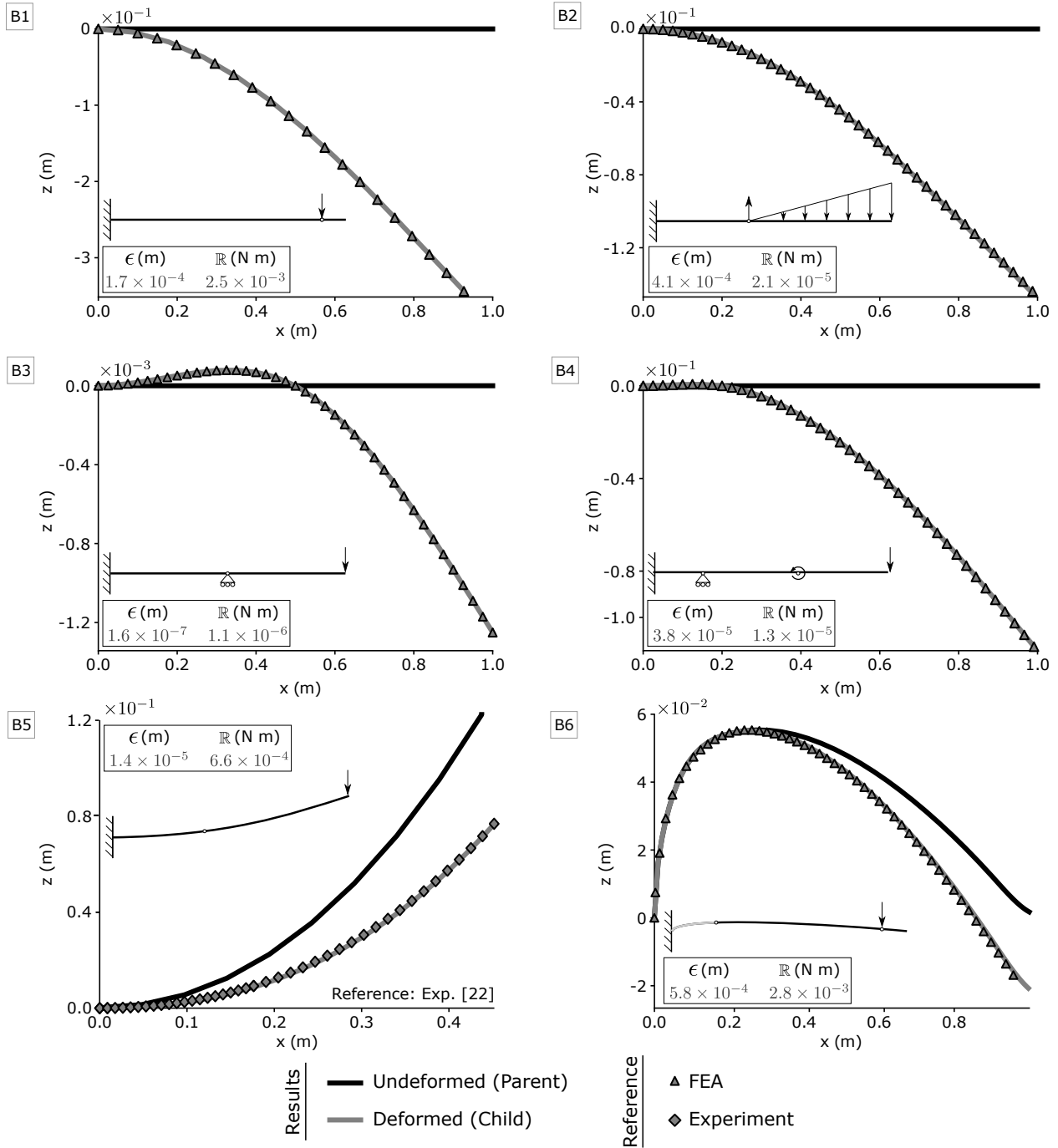


Figure 7.16: Results of case studies B with CST basis. All case studies returned low RMSE ϵ and residuals \mathbb{R} with no error exceeding 0.05% of the maximum deflection magnitude.

7.5.3 Case studies C: multi-beam assembly

The last set of case studies verifies the performance of multi-beam assemblies with various types of beam interactions and initial geometries as depicted in Table 7.6 and Fig 7.18. Similar to the previous case studies, all results agree with FEA as depicted in Fig. 7.18, demonstrating that this method is reliable for structures that begin to represent categories of morphign airfoil sections.

Table 7.6: All explored features for case studies C.

Case studies	Coupled force	Spring element	Reaction force	Rigid component	Initially curved
	C1	✓	✓		
C2			✓		
C3	✓		✓		
C4	✓			✓	✓

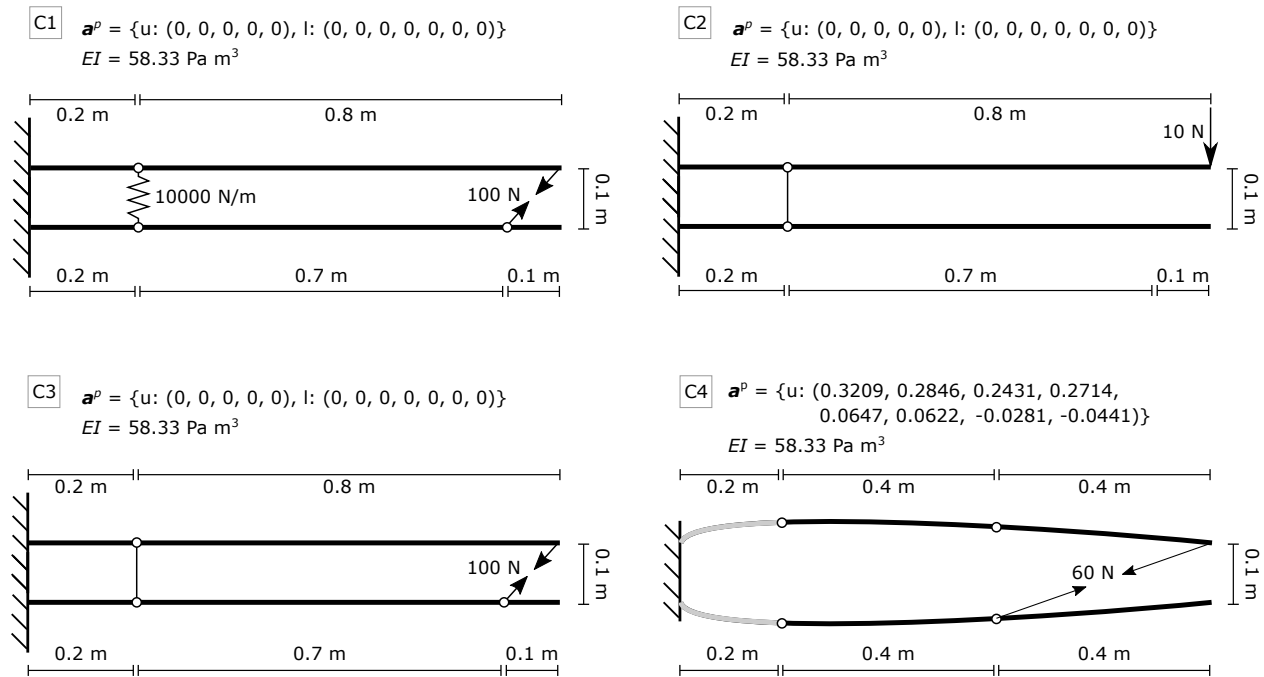


Figure 7.17: Schematics loads, boundary conditions, and initial geometries of case studies C.

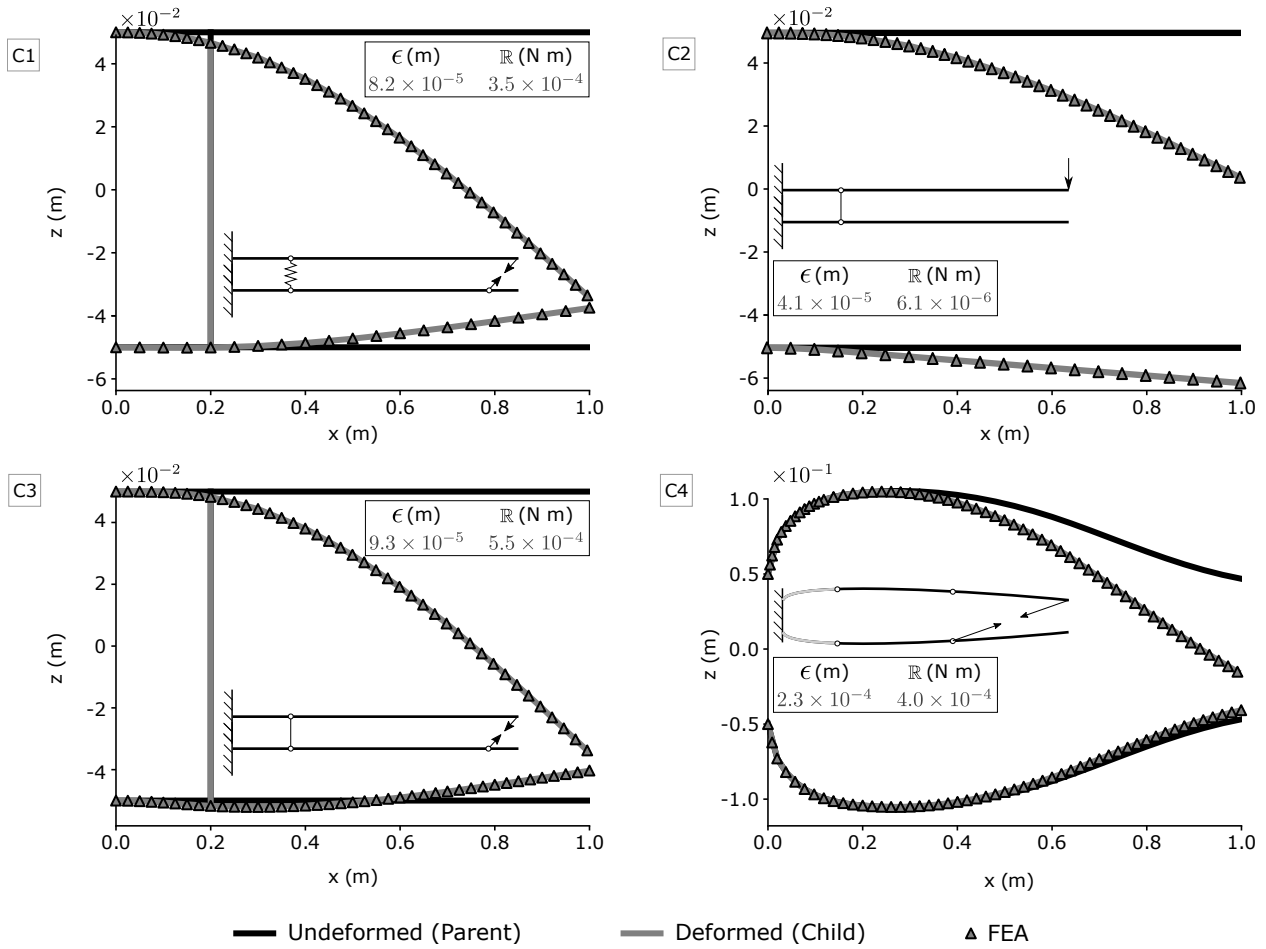


Figure 7.18: Results of case studies C with CST basis. All case studies returned satisfactory RMSE ϵ and residuals \mathbb{R} with no error exceeding 0.37% of the maximum deflection magnitude.

A final example is evaluated utilizing one spline element for each beam and two spline elements as shown Fig. 7.19. As previously mentioned, the piecewise representation is necessary to represent arbitrary loads as one CST cannot accurately represent discontinuous bending moments. The error at $s = 0.2$ m also leads to an incorrect estimation of the reaction force; further deteriorating the correct bending moment distribution. Note that the RMSE ϵ for both cases are of the same magnitude despite the incorrect moment distributions and increased residual \mathbb{R} when utilizing one spline element.

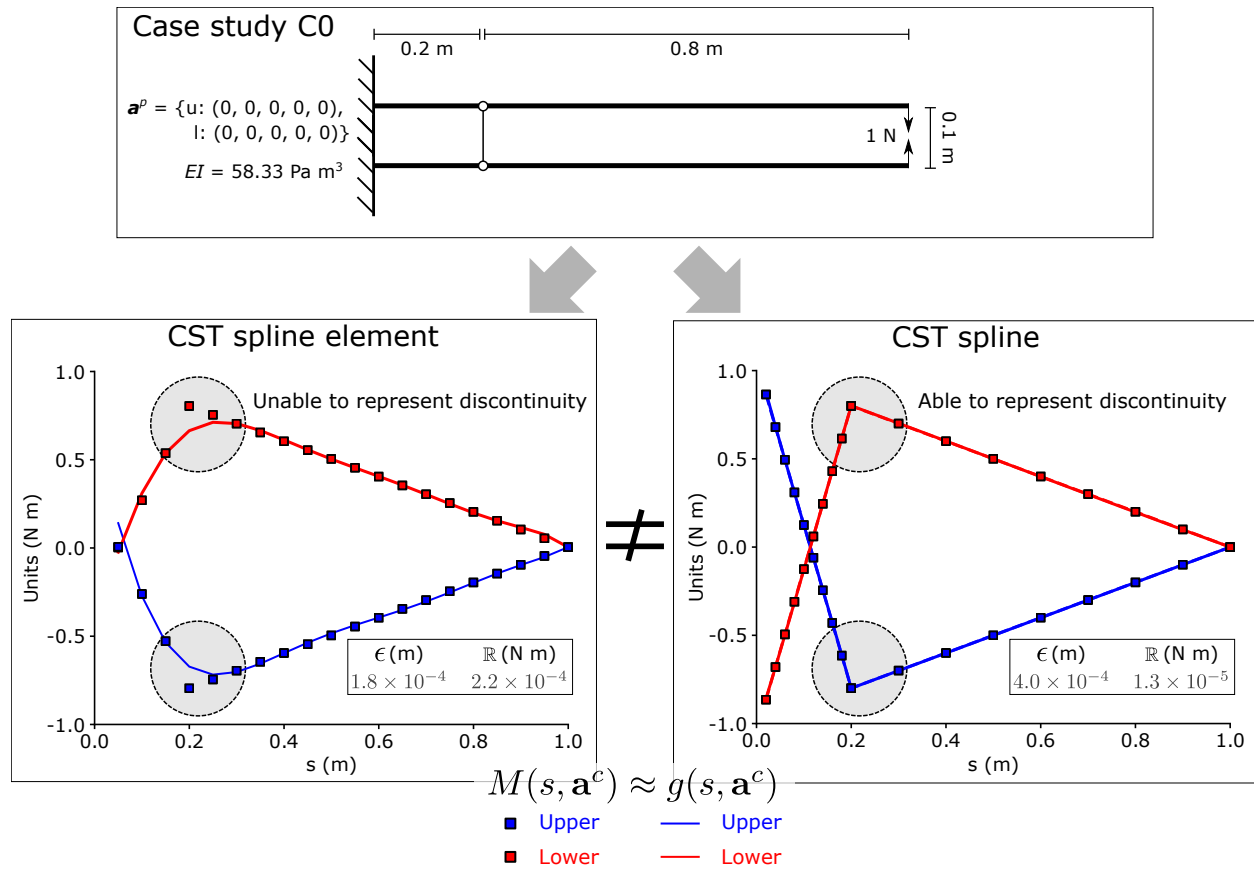


Figure 7.19: Motivation to utilize CST spline for beam representation in lieu of a single CST. The highlighted regions demonstrates that a single spline element is unable to capture the discontinuous bending moment. The bending moments differ at the root because the reaction force calculation is dependent on the geometric representation as will be shown in Section 7.3.4.

7.6 Comments

The skins of morphing wings, if they have constant cross sections and are morphed uniformly along the span (cf. Chapter 4) can be simplified as 2-D beams subject to a number of distributed and discrete boundary conditions and internal constraints undergoing finite deflections. There are no existing beam models that satisfy all desirable characteristics while allowing for a universal parameterization for CAD and structural analysis. Therefore, a geometry- and mechanics-based method has been demonstrated that it satisfies conservation of linear momentum to determine the stable solution of a beam or assembly of beams that satisfy all kinematic constraints.

In increasing complexity, the model is developed for a spline element beam, a spline beam, and a multi-beam assembly. Kinematic constraints are imposed directly on shape coefficients to decrease the number of degrees of freedom or as equality constraints penalizing solutions. In total, the physical responses of 20 case studies are verified with existing solutions utilizing CST, CST splines, and power series as basis functions. Overall, the proposed method reliably determines the correct solution for arbitrary initial geometries and loads for any parameterization method.

Because of the generality of the proposed model, it can be coupled with other components or further improved. While an elastica is assumed (i.e., linear elastic material model and length preserving beam formulation), the theory of an extensible elastica [215] could be incorporated. Therefore, it would enable the utilization of the structurally consistent framework from Chapter 5 with the energy minimization. Moreover, the curvilinear Euler-Bernoulli beam equations can be generalized into the curvilinear Kirchhoff-Love shell theory [206]; hence, the 3D CST equations from Chapter 4 could be utilized as the universal representation of a morphing skin; this is proposed as a highly enabling extension for other researches. Finally, the non-linear constitutive behaviors such as those of shape memory alloys (Chapter 2) could be incorporated instead of assuming linear elasticity, allowing the modeling of a morphing wing with embedded SMA components.

8. CONCLUSIONS AND FUTURE WORK

The goal of this dissertation is to explore bio-inspired applications that leverage geometric and material non-linearities and to develop tools that enable design explorations for these unorthodox problems. In Section 1.6, the six goals of this study were outlined and led to the discussions in Chapters 2-7. The following two sections specify the conclusions and future work for each goal.

8.1 Summary and conclusions

Considering the previously mentioned challenges in the development of morphing structures, the following contributions are made:

- (i) *Shape memory alloys as artificial muscles*: Muscle constitutive behavior plays a critical role in understanding animal locomotion [75] as well as developing efficient bipedal locomotion [103]. In our effort to explore the design domain of artificial muscles, SMA components are incorporated in a novel bipedal locomotion model as a stiffness-controlled spring element. The tunable spring compliance adds a mechanism that can increase or decrease the amount of energy delivered to or dissipated from locomotion, changing robot gait. This adaptivity is expected to benefit other applications beyond bipedal locomotion. As the work-loop response of the humerotriceps is the same as that of other muscles used for flying, this multifunctional mechanism could aid the design of other bio-inspired devices. It may provide biological insight regarding the design of more efficient engineering systems while also providing engineering insight into movement and coordination in biological systems that cannot be easily directly measured (e.g., bird wings) [74].
- (ii) *Experimental study of camber morphing wing*: In the context of aerospace engineering, morphing structures are useful in their ability to change the OML while improving or maintaining certain aerodynamic performance metrics. Skin-based morphing is of particular interest in that it minimizes installation volume. SMAs have a high force to volume ratio that makes them a suitable choice for skin-based morphing. The concept of a morphing wing with com-

posite SMA actuators embedded in the skin is proposed, modeled, fabricated, and tested as an alternative to increasing aircraft aerodynamic performance. The various manufactured platforms and ensuing wind tunnel tests demonstrate that the concept can be tuned to meet application requirements, is controllable in various environmental conditions, and leads to reproducible results regardless of platform size and number of actuators. Experimental results include a 40% lift increase and a 3.5% deflection relative to the chord.

(iii) *Parameterization of multi-component aircraft assembly*: a physically meaningful and efficient parameterized representation is developed for an accurate depiction of already existing aircraft. The main restriction to the development of commercial supersonic transport (SST) is the noise intrinsic to sonic booms. Small changes to the OML of an SST can lead to noise decrease for specific flight conditions. However, aeroacoustic performance improvement may not be maintained for off-design flight conditions. A concept to overcome this design dilemma is a morphing aircraft that changes shape to tune performance according to flight conditions. To accurately represent the geometry of a morphing aircraft and of already existing aircraft, a modified 3D CST method is proposed. The schema is adapted according to the desired structure to be represented (e.g., fuselage and wing). Through boolean operations and analytical intersection calculations, parts are precisely combined to generate an assembly (e.g., aircraft). The tool is benchmarked utilizing the JAXA wing body. A CST spline is also proposed to increase the versatility of CST equations, which are intended for modeling morphing wings. It is shown that the improved parameterization can accurately describe general SST concepts and possibly other geometries of interest.

(iv) *Development of structurally consistent morphing wing models*: Camber morphing of the wing OML may improve aerodynamic performance and reduce noise emissions for some aircraft. However, not all OMLs are obtainable from a given reference configuration as the extent to which the OML can deform is restricted by both the reference airfoil shape and wing internal structure. The CST parameterization method is modified for the first time to con-

sider the kinematics of a morphing airfoil with rigid internal structure, providing structurally consistent CST equations. Skin-based actuators and certain assumptions regarding the internal structure are stipulated. Accurate kinematically feasible deformed configurations are rapidly calculated without the need for structural analysis or consideration of actuation technology, enabling rapid iterative preliminary design optimization. The kinematic relations are accurate for moderate deformations (strains $\leq 4\%$) while still providing good estimates for larger deformations when comparing to FEA results.

- (v) *Optimization of morphing wings for subsonic flight conditions*: Morphing structures can allow significant improvements in performance by optimally changing shape across varying conditions. A critical barrier to the design of morphing structures is the challenge of determining how optimal shapes change as a function of the many operating conditions that affect optimality. Traditional engineering optimization techniques are able to determine an optimal shape only for one condition or an aggregation over operating conditions (i.e., optimizing average performance). Parametric optimization is an alternative approach that can solve a family of related optimization problems simultaneously. Herein the analysis of the design of a structurally consistent camber morphing wing is performed for civil utility subsonic aircraft applications using parametric optimization techniques. The approach combines rigorous consideration of structural constraints via CST equations with the Predictive Parametric Pareto Genetic Algorithm (P3GA), an algorithm for nonlinear multi-parametric optimization. The system is tuned to maximize lift-to-drag ratio, a key metric for aircraft flight range. The process is repeated for multiple concepts (i.e., different parent airfoils) and ranked based on expected and maximum lift-to-drag ratios. Results show that morphing always increases performance and allows reconfiguration between existing airfoils, but that it is not necessary for all aircraft. The concept selection algorithm shows that there are fixed airfoils that could have performance equivalent or superior to a morphing configurations depending on the application.

(vi) *Development of a finite beam method with universal parameterization*: the optimization results motivate the development of a finite beam method for arbitrary geometries and loads for any parameterization method. Currently, no existing method satisfies the aforementioned requirements. A new curvilinear beam method is developed inspired by isogeometric analysis and the Ritz method that satisfies all requirements. Case studies for power series, CST, and CST spline as a basis are verified with known solutions. Overall, the method provides reliable solutions as function of shape coefficients, providing a universal representation between topology and structural analysis.

8.2 Future work

Considering the previously mentioned challenges in the development of morphing structures, the following future work is proposed:

- (i) *Shape memory alloys as artificial muscles*: the main focus of the bi-pedal locomotion study was to evaluate the effect between the electrical and mechanical stimuli for only one cycle (i.e., period of time between landing of the same robot end point). The transient response of the gait under varying electrical stimuli for multiple cycles was not explored. Future work could explore this rich design domain and develop control laws that explore the multifunctional response. Finally, the numerical results for the bi-pedal robot need to be experimentally verified despite previous experimental verification of the isolated actuators.
- (ii) *Experimental study of camber morphing wing*: a key product of the camber morphing wing study is a six-foot composite prototype with twelve actuators. Only an open-loop control is implemented in Chapter 3 and all the actuators are imposed to the same current. However, future studies could modify the platform setup to allow for closed-loop control of the separate actuators, leading to a greater design domain. The morphed configurations would include the previously studied camber morphing, but could also include twisting and varying camber morphing along the span.
- (iii) *Parameterization of multi-component aircraft assembly*: the CST splines are developed for

a two-dimensional domain but can be expanded to three dimensions. The 3D CST equations can incorporate splines (e.g., knots in two directions in the parameterized domain), allowing for a more versatile parameterization method that can incorporate taper and other geometric discontinuities.

- (iv) *Development of structurally consistent morphing wing models*: the structurally consistent framework was developed for camber morphing and was restricted to two dimensions. The framework can be expanded to three dimensions, allowing for other structural constraints for other components such as ribs. This would allow for varying internal structures as well as other modes of morphing such as twist or span morphing.
- (v) *Optimization of morphing wings for subsonic flight conditions*: the operating conditions are incorporated into the expected value in Chapter 6 to generate a metric that returns the best airfoil for a Cessna 172. This procedure can be repeated for other aircraft without having to run a parametric optimization. Moreover, cases with an additional parameter (e.g., altitude) or additional objective function (e.g., power) could also be studied. The resultant volume in hyperdimensional space cannot be easily visualized, and a concept selection algorithm becomes necessary to determine a dominant solution.
- (vi) *Development of a finite beam method with universal parameterization*: since Euler-Bernoulli beams can be generalized to Kirchoff-Love shell theory, the new beam model can also be generalized to shells. Moreover, non-linear constitutive response and structurally consistent frameworks can also be incorporated in the framework. If coupled with an aerodynamic tool, a similar study to Chapter 6 can be performed, determining the optimal kinematically and mechanically correct morphed solution for each flight condition.

REFERENCES

- [1] B. Sanders, F. E. Eastep, and E. Forster, “Aerodynamic and Aeroelastic Characteristics of Wings with Conformal Control Surfaces for Morphing Aircraft,” *Journal of Aircraft*, vol. 40, pp. 94–99, Jan. 2003.
- [2] I. Ordaz and W. Li, “Adaptive Aft Signature Shaping of a Low-Boom Supersonic Aircraft Using Off-Body Pressures,” American Institute of Aeronautics and Astronautics, Jan. 2012.
- [3] P. B. Leal, M. A. Savi, and D. J. Hartl, “Aero-structural optimization of shape memory alloy-based wing morphing via a class/shape transformation approach,” *Proceedings of the Institution of Mechanical Engineers, Part G: Journal of Aerospace Engineering*, vol. 232, pp. 2745–2759, Dec. 2018.
- [4] A. F. Arrieta, O. Bilgen, M. I. Friswell, and P. Ermanni, “Modelling and configuration control of wing-shaped bi-stable piezoelectric composites under aerodynamic loads,” *Aerospace Science and Technology*, vol. 29, pp. 453–461, Aug. 2013.
- [5] P. B. C. Leal, H. R. Stroud, and D. J. Hartl, “Design and fabrication of a shape memory-based bio-inspired morphing wing,” in *VIII ECCOMAS Thematic Conference on Smart Structures and Materials (SMART)*, 2017.
- [6] A. M. Pankonien, K. Duraisamy, C. T. Faria, and D. Inman, “Synergistic Smart Morphing Aileron: Aero-structural Performance Analysis,” American Institute of Aeronautics and Astronautics, Jan. 2014.
- [7] G. Molinari, A. F. Arrieta, and P. Ermanni, “Aero-Structural Optimization of Three-Dimensional Adaptive Wings with Embedded Smart Actuators,” *AIAA Journal*, vol. 52, pp. 1940–1951, Sept. 2014.
- [8] P. B. C. Leal, M. A. Savi, and D. J. Hartl, “Aero-structural optimization of shape memory alloy-based wing morphing via a class/shape transformation approach,” *Proceedings*

of the Institution of Mechanical Engineers, Part G: Journal of Aerospace Engineering, p. 095441001771619, July 2017.

- [9] Y. Liu, C. Yang, and X. Song, "An airfoil parameterization method for the representation and optimization of wind turbine special airfoil," *Journal of Thermal Science*, vol. 24, pp. 99–108, Apr. 2015.
- [10] V. Sripawadkul, M. Padulo, and M. Guenov, "A Comparison of Airfoil Shape Parameterization Techniques for Early Design Optimization," in *13th AIAA/ISSMO Multidisciplinary Analysis Optimization Conference*, American Institute of Aeronautics and Astronautics, Sept. 2010.
- [11] B. Kulfan, "Recent Extensions and Applications of the "CST" Universal Parametric Geometry Representation Method," in *7th AIAA Aviation Technology, Integration and Operations Conference (ATIO)*, American Institute of Aeronautics and Astronautics, Sept. 2007.
- [12] P. B. C. Leal, C. L. Bertagne, and D. J. Hartl, "Aero-structural Optimization of Shape Memory Alloy-based Wing Morphing via a Class/Shape Transformation Approach," in *23rd AIAA/AHS Adaptive Structures Conference*, American Institute of Aeronautics and Astronautics, 2015.
- [13] D. Lagoudas, D. Hartl, Y. Chemisky, L. Machado, and P. Popov, "Constitutive model for the numerical analysis of phase transformation in polycrystalline shape memory alloys," *International Journal of Plasticity*, vol. 32-33, pp. 155–183, may 2012.
- [14] S. M. Mirvakili and I. W. Hunter, "Artificial Muscles: Mechanisms, Applications, and Challenges," *Advanced Materials*, vol. 30, no. 6, pp. 1–28, 2018.
- [15] K. M. Schmoller and A. R. Bausch, "Similar nonlinear mechanical responses in hard and soft materials," *Nature Materials*, vol. 12, pp. 278–281, apr 2013.
- [16] M. H. Dickinson, "How Animals Move: An Integrative View," *Science*, vol. 288, pp. 100–106, apr 2000.

- [17] S. M. Swartz, K. S. Breuer, and D. J. Willis, “Aeromechanics in aeroecology: flight biology in the atmosphere,” *Integrative and Comparative Biology*, vol. 48, pp. 85–98, nov 2007.
- [18] C. Harvey, V. B. Baliga, P. Lavoie, and D. L. Altshuler, “Wing morphing allows gulls to modulate static pitch stability during gliding,” *Journal of the Royal Society Interface*, vol. 16, no. 150, 2019.
- [19] K. Ghose, T. K. Horiuchi, P. S. Krishnaprasad, and C. F. Moss, “Echolocating Bats Use a Nearly Time-Optimal Strategy to Intercept Prey,” *PLoS Biology*, vol. 4, p. e108, apr 2006.
- [20] A. K. Stowers, L. Y. Matloff, and D. Lentink, “How pigeons couple three-dimensional elbow and wrist motion to morph their wings,” *Journal of The Royal Society Interface*, vol. 14, p. 20170224, Aug. 2017.
- [21] D. D. Chin, L. Y. Matloff, A. K. Stowers, E. R. Tucci, and D. Lentink, “Inspiration for wing design: how forelimb specialization enables active flight in modern vertebrates,” *Journal of The Royal Society Interface*, vol. 14, p. 20170240, June 2017.
- [22] S. Barbarino, O. Bilgen, R. M. Ajaj, M. I. Friswell, and D. J. Inman, “A Review of Morphing Aircraft,” *Journal of Intelligent Material Systems and Structures*, vol. 22, pp. 823–877, June 2011.
- [23] J. J. Joo, C. R. Marks, L. Zientarski, and A. J. Culler, “Variable Camber Compliant Wing - Design,” American Institute of Aeronautics and Astronautics, Jan. 2015.
- [24] F. Previtali, A. F. Arrieta, and P. Ermanni, “Double-walled corrugated structure for bending-stiff anisotropic morphing skins,” *Journal of Intelligent Material Systems and Structures*, vol. 26, pp. 599–613, Mar. 2015.
- [25] T. Yokozeki, A. Sugiura, and Y. Hirano, “Development of Variable Camber Morphing Airfoil Using Corrugated Structure,” *Journal of Aircraft*, vol. 51, pp. 1023–1029, May 2014.
- [26] U. Icardi and L. Ferrero, “Preliminary study of an adaptive wing with shape memory alloy torsion actuators,” *Materials & Design*, vol. 30, pp. 4200–4210, Dec. 2009.

- [27] F. Previtali, T. Delpero, A. Bergamini, A. Arrieta, and P. Ermanni, “Extremely Anisotropic Multi-functional Skin for Morphing Applications,” in *23rd AIAA/AHS Adaptive Structures Conference*, AIAA SciTech, American Institute of Aeronautics and Astronautics, Jan. 2015.
- [28] P. B. Leal, H. Stroud, E. Sheahan, M. Cabral, and D. J. Hartl, “Skin-based camber morphing utilizing shape memory alloy composite actuators in a wind tunnel environment,” American Institute of Aeronautics and Astronautics, Jan. 2018.
- [29] O. Bilgen, K. B. Kochersberger, D. J. Inman, and O. J. Ohanian, “Novel, Bidirectional, Variable-Camber Airfoil via Macro-Fiber Composite Actuators,” *Journal of Aircraft*, vol. 47, pp. 303–314, Jan. 2010.
- [30] D. S. Ramrakhyani, G. A. Lesieutre, M. I. Frecker, and S. Bharti, “Aircraft Structural Morphing using Tendon-Actuated Compliant Cellular Trusses,” *Journal of Aircraft*, vol. 42, pp. 1614–1620, Nov. 2005.
- [31] N. M. Ursache, A. J. Keane, and N. W. Bressloff, “Design of Postbuckled Spinal Structures for Airfoil Camber and Shape Control,” *AIAA Journal*, vol. 44, pp. 3115–3124, Dec. 2006.
- [32] B. K. S. Woods, I. Dayyani, and M. I. Friswell, “Fluid/Structure-Interaction Analysis of the Fish-Bone-Active-Camber Morphing Concept,” *Journal of Aircraft*, vol. 52, pp. 307–319, Jan. 2015.
- [33] A. Airoidi, M. Crespi, G. Quaranti, and G. Sala, “Design of a Morphing Airfoil with Composite Chiral Structure,” *Journal of Aircraft*, vol. 49, pp. 1008–1019, July 2012.
- [34] D. Coutu, V. Brailovski, and P. Terriault, “Promising Benefits of an Active-Extrados Morphing Laminar Wing,” *Journal of Aircraft*, vol. 46, pp. 730–731, Mar. 2009.
- [35] E. Torenbeek, *Synthesis of Subsonic Airplane Design*. Springer Science & Business Media, 1982.
- [36] FAA, “Federal Aviation Regulations (FARS, 14cfr), Part 25, Section 147 - Directional and lateral control,” 2002.

- [37] J. D. Anderson, *Fundamentals of Aerodynamics*. Anderson series, New York: McGraw-Hill, 5th ed ed., 2011.
- [38] J. Valasek, ed., *Morphing aerospace vehicles and structures*. AIAA progress series, Reston, VA: John Wiley & Sons, 2012.
- [39] J. Hájek, ed., *Parameterization of Airfoils and Its Application in Aerodynamic Optimization*. WDS'07 Proceedings of Contributed Papers, Part I, Praha, Czech Republic: Matfyzpress, 2007. OCLC: 254739455.
- [40] H. Sobieczky, "Parametric Airfoils and Wings," in *Recent Development of Aerodynamic Design Methodologies* (K. Fujii and G. S. Dulikravich, eds.), vol. 65, pp. 71–87, Wiesbaden: Vieweg+Teubner Verlag, 1999.
- [41] J. Lepine, J.-Y. Trepanier, and F. Pepin, "Wing aerodynamic design using an optimized NURBS geometrical representation," in *38th Aerospace Science Meeting and Exhibit*, American Institute of Aeronautics and Astronautics, Jan. 2000.
- [42] R. M. Hicks and P. A. Henne, "Wing Design by Numerical Optimization," *Journal of Aircraft*, vol. 15, pp. 407–412, July 1978.
- [43] J. Ferguson, "Multivariable curve interpolation," *Journal of the ACM (JACM)*, vol. 11, no. 2, pp. 221–228, 1964.
- [44] T. Zhao, Y. Zhang, H. Chen, Y. Chen, and M. Zhang, "Supercritical wing design based on airfoil optimization and 2.75d transformation," *Aerospace Science and Technology*, vol. 56, pp. 168–182, Sept. 2016.
- [45] SungKi Jung, Won Choi, L. S. Martins-Filho, and F. Madeira, "An Implementation of Self-Organizing Maps for Airfoil Design Exploration via Multi-Objective Optimization Technique," *Journal of Aerospace Technology & Management*, vol. 8, pp. 193–202, Apr. 2016.
- [46] E. Tandies and E. Assareh, "Inverse design of airfoils via an intelligent hybrid optimization technique," *Engineering with Computers*, vol. 33, pp. 361–374, July 2016.

- [47] E. Gillebaart and R. De Breuker, “Low-fidelity 2d isogeometric aeroelastic analysis and optimization method with application to a morphing airfoil,” *Computer Methods in Applied Mechanics and Engineering*, vol. 305, pp. 512–536, June 2016.
- [48] B. Kulfan, “New Supersonic Wing Far-Field Composite-Element Wave-Drag Optimization Method,” *Journal of Aircraft*, vol. 46, pp. 1740–1758, Sept. 2009.
- [49] A. M. Morris, C. B. Allen, and T. C. S. Rendall, “High-fidelity aerodynamic shape optimization of modern transport wing using efficient hierarchical parameterization,” *International Journal for Numerical Methods in Fluids*, vol. 63, pp. 297–312, May 2010.
- [50] J. A. Cottrell, T. J. Hughes, and Y. Bazilevs, *Isogeometric Analysis: Toward Integration of CAD and FEA*. Wiley, 2009.
- [51] D. J. Benson, Y. Bazilevs, E. De Luycker, M.-C. Hsu, M. Scott, T. J. R. Hughes, and T. Be-lytschko, “A generalized finite element formulation for arbitrary basis functions: From isogeometric analysis to XFEM,” *International Journal for Numerical Methods in Engineering*, pp. n/a–n/a, 2010.
- [52] V. P. Nguyen, C. Anitescu, S. P. Bordas, and T. Rabczuk, “Isogeometric analysis: An overview and computer implementation aspects,” *Mathematics and Computers in Simulation*, vol. 117, pp. 89–116, Nov. 2015.
- [53] W. M. Lai, D. Rubin, and E. Krempf, *Introduction to continuum mechanics*. Amsterdam ; Boston: Butterworth-Heinemann/Elsevier, 4th ed ed., 2010.
- [54] Z. Friedman and J. B. Kosmatka, “An accurate two-node finite element for shear deformable curved beams,” *International Journal for Numerical Methods in Engineering*, vol. 41, pp. 473–498, Feb. 1998.
- [55] J. N. Reddy, *An introduction to nonlinear finite element analysis*. Oxford ; New York: Oxford University Press, 2004. OCLC: ocm53156584.

- [56] A. Arbind and J. N. Reddy, "A one-dimensional model of 3-D structure for large deformation: a general higher-order rod theory," *Acta Mechanica*, vol. 229, pp. 1803–1831, Apr. 2018.
- [57] E. A. Peraza Hernandez, B. Kiefer, D. J. Hartl, A. Menzel, and D. C. Lagoudas, "Analytical investigation of structurally stable configurations in shape memory alloy-actuated plates," *International Journal of Solids and Structures*, vol. 69-70, pp. 442–458, Sept. 2015.
- [58] J. N. Reddy, *Energy principles and variational methods in applied mechanics*. New York: J. Wiley, 2nd ed ed., 2002.
- [59] W. S. Slaughter, *Linearized Theory of Elasticity*. Boston: Birkhauser Boston, 2002. OCLC: 958524517.
- [60] O. A. Bauchau and J. I. Craig, *Structural analysis: with applications to aerospace structures*. No. v. 163 in Solid mechanics and its applications, Dordrecht ; New York: Springer, 2009. OCLC: ocn472487575.
- [61] E. A. Peraza Hernandez, D. J. Hartl, and D. C. Lagoudas, *Active Origami: Modeling, Design, and Applications*. Cham: Springer International Publishing, 2019.
- [62] E. A. Peraza Hernandez, D. J. Hartl, E. Akleman, and D. C. Lagoudas, "Modeling and analysis of origami structures with smooth folds," *Computer-Aided Design*, vol. 78, pp. 93–106, Sept. 2016.
- [63] Y. Kumar, "The Rayleigh-Ritz method for linear dynamic, static and buckling behavior of beams, shells and plates: A literature review," *Journal of Vibration and Control*, vol. 24, pp. 1205–1227, Apr. 2018.
- [64] R. D. Hampton, M. J. Leamy, P. J. Bryant, and N. Quraishi, "Deformation and flexibility equations for curved, end-loaded, planar elastica," *AIAA Journal*, vol. 46, no. 2, pp. 356–363, 2008.
- [65] R. A. Beth and C. P. Wells, "Finite deflections of a cantilever-strut," *Journal of Applied Physics*, vol. 22, no. 6, pp. 742–746, 1951.

- [66] P. Potluri, J. Atkinson, and I. Porat, “Large deformation modelling of flexible materials,” *Journal of the Textile Institute*, vol. 87, no. 1, pp. 129–151, 1996.
- [67] K. Lane and D. Marshall, “A Surface Parameterization Method for Airfoil Optimization and High Lift 2d Geometries Utilizing the CST Methodology,” American Institute of Aeronautics and Astronautics, Jan. 2009.
- [68] R. P. Liem, J. R. Martins, and G. K. Kenway, “Expected drag minimization for aerodynamic design optimization based on aircraft operational data,” *Aerospace Science and Technology*, vol. 63, pp. 344–362, Apr. 2017.
- [69] G. K. W. Kenway and J. R. R. A. Martins, “Multipoint High-Fidelity Aerostructural Optimization of a Transport Aircraft Configuration,” *Journal of Aircraft*, vol. 51, pp. 144–160, Jan. 2014.
- [70] E. Galvan and R. J. Malak, “P3ga: An algorithm for technology characterization,” *Journal of Mechanical Design*, vol. 137, no. 1, p. 011401, 2015.
- [71] C. Nam, A. Chattopadhyay, and Y. Kim, “Application of shape memory alloy (SMA) spars for aircraft maneuver enhancement,” in *SPIE’s 9th Annual International Symposium on Smart Structures and Materials*, pp. 226–236, International Society for Optics and Photonics, 2002.
- [72] D. J. Maglieri, P. J. Bobbitt, K. J. Plotkin, K. P. Shepherd, P. G. Coen, and D. M. Richwine, “Sonic boom: Six decades of research,” 2014.
- [73] D. D. Chin, L. Y. Matloff, A. K. Stowers, E. R. Tucci, and D. Lentink, “Inspiration for wing design: how forelimb specialization enables active flight in modern vertebrates,” *Journal of The Royal Society Interface*, vol. 14, p. 20170240, jun 2017.
- [74] B. Baliga, I. Szabo, and D. L. Altshuler, “Range of motion in the avian wing is strongly associated with flight behavior and body mass,” *Science Advances*, vol. 5, no. 10, 2019.
- [75] J. S. Theriault, J. W. Bahlman, R. E. Shadwick, and D. L. Altshuler, “Work loop dynamics of the pigeon (*Columba livia*) humerotriceps demonstrate potentially diverse roles for

- active wing morphing,” *The Journal of Experimental Biology*, vol. 222, no. 7, p. jeb195578, 2019.
- [76] Y. Bar-Cohen, “Biomimetics—using nature to inspire human innovation,” *Bioinspiration & Biomimetics*, vol. 1, pp. P1–P12, mar 2006.
- [77] R. K. Josephson, “Mechanical Power output from Striated Muscle during Cyclic Contraction,” *Journal of Experimental Biology*, vol. 114, pp. 493–512, 1985.
- [78] A. M. Gabaldón, F. E. Nelson, and T. J. Roberts, “Mechanical function of two ankle extensors in wild turkeys: Shifts from energy production to energy absorption during incline versus decline running,” *Journal of Experimental Biology*, vol. 207, no. 13, pp. 2277–2288, 2004.
- [79] G. S. Sawicki, B. D. Robertson, E. Azizi, and T. J. Roberts, “Timing matters: Tuning the mechanics of a muscle-tendon unit by adjusting stimulation phase during cyclic contractions,” *Journal of Experimental Biology*, vol. 218, no. 19, pp. 3150–3159, 2015.
- [80] E. I. Saavedra Flores, M. I. Friswell, and Y. Xia, “Variable stiffness biological and bio-inspired materials,” *Journal of Intelligent Material Systems and Structures*, vol. 24, pp. 529–540, mar 2013.
- [81] C. T. Farley, J. Glasheen, and T. A. McMahon, “Running springs: speed and animal size,” *The Journal of experimental biology*, vol. 185, pp. 71–86, 1993.
- [82] R. Blickhan, “The spring-mass model for running and hopping,” *Journal of Biomechanics*, 1989.
- [83] Z. Gan, Y. Yesilevskiy, P. Zaytsev, and C. D. Remy, “All common bipedal gaits emerge from a single passive model,” *Journal of the Royal Society Interface*, vol. 15, no. 146, 2018.
- [84] N. Smit-Anseeuw, R. Gleason, R. Vasudevan, and C. D. Remy, “The Energetic Benefit of Robotic Gait Selection-A Case Study on the Robot RAMone,” *IEEE Robotics and Automation Letters*, vol. 2, no. 2, pp. 1124–1131, 2017.

- [85] W. Xi, Y. Yesilevskiy, and C. D. Remy, “Selecting gaits for economical locomotion of legged robots,” *International Journal of Robotics Research*, vol. 35, no. 9, pp. 1140–1154, 2016.
- [86] E. A. Peraza Hernandez, D. J. Hartl, and D. C. Lagoudas, “Structural Mechanics and Design of Active Origami Structures,” in *Active Origami*, pp. 331–409, Cham: Springer International Publishing, 2019.
- [87] A. L. Hof, “Scaling gait data to body size,” *Gait and Posture*, vol. 4, no. 3, pp. 222–223, 1996.
- [88] B. D. Robertson and G. S. Sawicki, “Exploiting elasticity: Modeling the influence of neural control on mechanics and energetics of ankle muscle-tendons during human hopping,” *Journal of Theoretical Biology*, vol. 353, pp. 121–132, 2014.
- [89] D. Lagoudas, *Shape memory alloys: modeling and engineering applications*. New York: Springer US, jan 2008.
- [90] P. B. Leal and M. A. Savi, “Shape memory alloy-based mechanism for aeronautical application: Theory, optimization and experiment,” *Aerospace Science and Technology*, vol. 76, pp. 155–163, may 2018.
- [91] S. Enemark, M. A. Savi, and I. F. Santos, “Nonlinear dynamics of a pseudoelastic shape memory alloy system - Theory and experiment,” *Smart Materials and Structures*, vol. 23, no. 8, 2014.
- [92] B. C. Chang, J. A. Shaw, and M. A. Iadicola, “Thermodynamics of shape memory alloy wire: Modeling, experiments, and application,” *Continuum Mechanics and Thermodynamics*, vol. 18, no. 1-2, pp. 83–118, 2006.
- [93] W. W. Daniel, *Applied Nonparametric Statistics.*, vol. 34. Houghton Mifflin, 1978.
- [94] M. A. Kazemi Lari, A. D. Dostine, J. Zhang, A. S. Wineman, and J. A. Shaw, “Robotic jellyfish actuated with a shape memory alloy spring,” in *Bioinspiration, Biomimetics, and Bioreplication IX*, no. March, p. 2, SPIE, mar 2019.

- [95] A. Villanueva, C. Smith, and S. Priya, “A biomimetic robotic jellyfish (Robojelly) actuated by shape memory alloy composite actuators,” *Bioinspiration and Biomimetics*, vol. 6, no. 3, 2011.
- [96] B. Kim, M. G. Lee, Y. P. Lee, Y. Kim, and G. Lee, “An earthworm-like micro robot using shape memory alloy actuator,” *Sensors and Actuators, A: Physical*, vol. 125, no. 2, pp. 429–437, 2006.
- [97] C. Pfeiffer, C. Mavroidis, K. DeLaurentis, and M. Mosley, “Shape memory alloy actuated robot prostheses: initial prototypes,” *American Society of Mechanical Engineers, Bioengineering Division (Publication) BED*, vol. 43, pp. 145–146, 1999.
- [98] B. C. dos Santos and M. A. Savi, “Nonlinear dynamics of a nonsmooth shape memory alloy oscillator,” *Chaos, Solitons and Fractals*, vol. 40, no. 1, pp. 197–209, 2009.
- [99] K. Radkhah, *Advancing Musculoskeletal Robot Design for Dynamic and Energy-Efficient Bipedal Locomotion*. PhD thesis, 2013.
- [100] S. Davis, *Viewpoint: Bigdog, the rough-terrain quadruped robot*, vol. 39. IFAC, 2013.
- [101] J. Ahn and N. Hogan, “A Simple State-Determined Model Reproduces Entrainment and Phase-Locking of Human Walking,” *PLoS ONE*, vol. 7, no. 11, pp. 1–11, 2012.
- [102] M. W. Spong, J. K. Holm, and D. Lee, “Passivity - Based control of bipedal locomotion,” *IEEE Robotics and Automation Magazine*, vol. 14, no. 2, pp. 30–40, 2007.
- [103] F. Iida, Y. Minekawa, J. Rummel, and A. Seyfarth, “Toward a human-like biped robot with compliant legs,” *Robotics and Autonomous Systems*, vol. 57, no. 2, pp. 139–144, 2009.
- [104] M. Hutter, C. Gehring, M. Bloesch, M. A. Hoepflinger, C. D. Remy, and R. Siegwart, “Starleth: A compliant quadrupedal robot for fast, efficient, and versatile locomotion,” *Adaptive Mobile Robotics - Proceedings of the 15th International Conference on Climbing and Walking Robots and the Support Technologies for Mobile Machines, CLAWAR 2012*, pp. 483–490, 2012.

- [105] M. A. Daley and A. Birn-Jeffery, “Scaling of avian bipedal locomotion reveals independent effects of body mass and leg posture on gait,” *Journal of Experimental Biology*, vol. 221, no. 10, 2018.
- [106] J. R. Usherwood, T. Y. Hubel, B. J. Smith, Z. T. Self Davies, and G. Sobota, “The scaling or ontogeny of human gait kinetics and walk-run transition: The implications of work vs. peak power minimization,” *Journal of Biomechanics*, vol. 81, pp. 12–21, 2018.
- [107] A. M. Fredriks, S. Van Buuren, W. J. Van Heel, R. H. Dijkman-Neerincx, S. P. Verloove-Vanhorick, and J. M. Wit, “Nationwide age references for sitting height, leg length, and sitting height/height ratio, and their diagnostic value for disproportionate growth disorders,” *Archives of Disease in Childhood*, vol. 90, no. 8, pp. 807–812, 2005.
- [108] Y. Wu, J. K. Yim, J. Liang, Z. Shao, M. Qi, J. Zhong, Z. Luo, X. Yan, M. Zhang, X. Wang, R. S. Fearing, R. J. Full, and L. Lin, “Insect-scale fast moving and ultrarobust soft robot,” *Science Robotics*, vol. 4, p. eaax1594, jul 2019.
- [109] D. C. Lagoudas, D. A. Miller, L. Rong, and P. K. Kumar, “Thermomechanical fatigue of shape memory alloys,” *Smart Materials and Structures*, vol. 18, no. 8, 2009.
- [110] B. Haghgouyan, C. Hayrettin, T. Baxevanis, I. Karaman, and D. C. Lagoudas, “Fracture toughness of NiTi—Towards establishing standard test methods for phase transforming materials,” *Acta Materialia*, vol. 162, pp. 226–238, 2019.
- [111] M. Ilton, M. Saad Bhamla, X. Ma, S. M. Cox, L. L. Fitchett, Y. Kim, J. sung Koh, D. Krishnamurthy, C. Y. Kuo, F. Z. Temel, A. J. Crosby, M. Prakash, G. P. Sutton, R. J. Wood, E. Azizi, S. Bergbreiter, and S. N. Patek, “The principles of cascading power limits in small, fast biological and engineered systems,” *Science*, vol. 360, no. 6387, 2018.
- [112] S. Enemark and I. F. Santos, “Rotor-bearing system integrated with shape memory alloy springs for ensuring adaptable dynamics and damping enhancement - Theory and experiment,” *Journal of Sound and Vibration*, 2016.

- [113] T. E. Higham, A. A. Biewener, and J. M. Wakeling, “Functional diversification within and between muscle synergists during locomotion,” *Biology Letters*, vol. 4, no. 1, pp. 41–44, 2008.
- [114] J. Shaw, L. Izu, and Y. Chen-Izu, “Mechanical Analysis of Single Myocyte Contraction in a 3-D Elastic Matrix,” *PLoS ONE*, vol. 8, no. 10, 2013.
- [115] N. T. George, S. Sponberg, and T. L. Daniel, “Temperature gradients drive mechanical energy gradients in the flight muscle of *Manduca sexta*,” *Journal of Experimental Biology*, vol. 215, pp. 471–479, feb 2012.
- [116] J. W. Bahlman, V. B. Baliga, and D. L. Altshuler, “Flight muscle power increases with strain amplitude and decreases with cycle frequency for small birds,” *Journal of Experimental Biology*, 2020.
- [117] A. P. Willmott and C. P. Ellington, “The mechanics of flight in the hawkmoth *Manduca sexta* I. Kinematics of hovering and forward flight,” *Journal of Experimental Biology*, vol. 200, no. 21, pp. 2705–2722, 1997.
- [118] B. T. Lester, T. Baxevanis, Y. Chemisky, and D. C. Lagoudas, “Review and perspectives: shape memory alloy composite systems,” *Acta Mechanica*, vol. 226, pp. 3907–3960, Dec. 2015.
- [119] S. Bansmer, N. Buchmann, R. Radespiel, R. Unger, M. Haupt, P. Horst, and R. Heinrich, “Aerodynamics and Structural Mechanics of Flapping Flight with Elastic and Stiff Wings,” in *Nature-Inspired Fluid Mechanics* (C. Tropea and H. Bleckmann, eds.), vol. 119, pp. 331–354, Berlin, Heidelberg: Springer Berlin Heidelberg, 2012.
- [120] T. Liu, K. Kuykendoll, R. Rhew, and S. Jones, “Avian Wing Geometry and Kinematics,” *AIAA Journal*, vol. 44, pp. 954–963, May 2006.
- [121] P. C. Withers, “An aerodynamic analysis of bird wings as fixed aerofoils,” *Journal of Experimental Biology*, vol. 90, no. 1, pp. 143–162, 1981.

- [122] J. K. Strelec, D. C. Lagoudas, M. A. Khan, and J. Yen, “Design and implementation of a shape memory alloy actuated reconfigurable airfoil,” *Journal of Intelligent Material Systems and Structures*, vol. 14, no. 4-5, pp. 257–273, 2003.
- [123] G. Song, B. Kelly, and B. N. Agrawal, “Active position control of a shape memory alloy wire actuated composite beam,” *Smart Materials and Structures*, vol. 9, no. 5, p. 711, 2000.
- [124] A. Villanueva, C. Smith, and S. Priya, “A biomimetic robotic jellyfish (Robojelly) actuated by shape memory alloy composite actuators,” *Bioinspiration & Biomimetics*, vol. 6, p. 036004, Sept. 2011.
- [125] C. A. Rogers, “Active vibration and structural acoustic control of shape memory alloy hybrid composites: Experimental results,” *The Journal of the Acoustical Society of America*, vol. 88, pp. 2803–2811, Dec. 1990.
- [126] J. A. Balta, F. Bosia, V. Michaud, G. Dunkel, J. Botsis, and J.-A. Manson, “Smart composites with embedded shape memory alloy actuators and fibre Bragg grating sensors: activation and control,” *Smart Materials and Structures*, vol. 14, pp. 457–465, Aug. 2005.
- [127] J. Schrooten, V. Michaud, J. Parthenios, G. C. Psarras, C. Galiotis, R. Gotthardt, J.-A. Manson, and J. Van Humbeeck, “Progress on composites with embedded shape memory alloy wires,” *Materials transactions*, vol. 43, no. 5, pp. 961–973, 2002.
- [128] K.-t. Lau, L.-m. Zhou, and X.-m. Tao, “Control of natural frequencies of a clamped–clamped composite beam with embedded shape memory alloy wires,” *Composite Structures*, vol. 58, no. 1, pp. 39–47, 2002.
- [129] P.-L. Ko, F.-L. Chang, C.-H. Li, J.-Z. Chen, I.-C. Cheng, Y.-C. Tung, S.-H. Chang, and P.-C. Lin, “Dynamically programmable surface micro-wrinkles on PDMS-SMA composite,” *Smart Materials and Structures*, vol. 23, p. 115007, Oct. 2014.
- [130] S. Choi, J. J. Lee, D. C. Seo, and S. W. Choi, “The active buckling control of laminated composite beams with embedded shape memory alloy wires,” *Composite structures*, vol. 47, no. 1, pp. 679–686, 1999.

- [131] J.-E. Bidaux, J.-A. E. Månson, and R. Gotthardt, “Active Stiffening of Composite Materials by Embedded Shape-Memory-Alloy Fibres,” *MRS Proceedings*, vol. 459, Jan. 1996.
- [132] SAES, “SmartFlex Wires,” tech. rep.
- [133] A. WK55902, “New Test Method for Mechanical Uniaxial Constant Force Thermal Cycling of Shape Memory Alloys,” *ASTM International*, 2017.
- [134] A. V. Popov, L. T. Grigorie, R. M. Botez, M. Mamou, and Y. Mébarki, “Closed-Loop Control Validation of a Morphing Wing Using Wind Tunnel Tests,” *Journal of Aircraft*, vol. 47, pp. 1309–1317, July 2010.
- [135] M. S. Selig, ed., *Summary of low speed airfoil data*. Virginia Beach, Va: SoarTech Publications, 1995.
- [136] R. Velázquez and E. E. Pissaloux, “Modelling and temperature control of shape memory alloys with fast electrical heating,” *Int J Mech Control*, vol. 13, pp. 1–8, 2012.
- [137] K. Ikuta, M. Tsukamoto, and S. Hirose, “Shape memory alloy servo actuator system with electric resistance feedback and application for active endoscope,” in , *1988 IEEE International Conference on Robotics and Automation, 1988. Proceedings*, pp. 427–430 vol.1, Apr. 1988.
- [138] N. Ma, G. Song, and H.-J. Lee, “Position control of shape memory alloy actuators with internal electrical resistance feedback using neural networks,” *Smart Materials and Structures*, vol. 13, pp. 777–783, Aug. 2004.
- [139] P. Moghadas, R. Malak, and D. Hartl, “Reinforcement Learning for Control of a Shape Memory Alloy Based Self-Folding Sheet,” p. V05BT08A044, ASME, Aug. 2015.
- [140] “NI Educational Laboratory Virtual Instrumentation Suite II Series (NI ELVISTM II Series) User Manual,”
- [141] K. J. Åström and T. Häggglund, *Advanced PID Control*. ISA - The Instrumentation, Systems and Automation Society, 2006.

- [142] R. S. Sutton and A. G. Barto, *Reinforcement learning: an introduction*. Adaptive computation and machine learning, Cambridge, Mass: MIT Press, 1998.
- [143] V. Mnih, K. Kavukcuoglu, D. Silver, A. Graves, I. Antonoglou, D. Wierstra, and M. Riedmiller, “Playing Atari with Deep Reinforcement Learning,” *arXiv preprint arXiv: {...}*, pp. 1–9, 2013.
- [144] H. van Hasselt, A. Guez, and D. Silver, “Deep Reinforcement Learning with Double Q-learning,” 2015.
- [145] T. Schaul, J. Quan, I. Antonoglou, and D. Silver, “Prioritized Experience Replay,” pp. 1–21, 2015.
- [146] V. Mnih, A. P. Badia, M. Mirza, A. Graves, T. P. Lillicrap, T. Harley, D. Silver, and K. Kavukcuoglu, “Asynchronous Methods for Deep Reinforcement Learning,” *arXiv*, vol. 48, pp. 1–28, 2016.
- [147] V. Mnih, K. Kavukcuoglu, D. Silver, A. a. Rusu, J. Veness, M. G. Bellemare, A. Graves, M. Riedmiller, A. K. Fidjeland, G. Ostrovski, S. Petersen, C. Beattie, A. Sadik, I. Antonoglou, H. King, D. Kumaran, D. Wierstra, S. Legg, and D. Hassabis, “Human-level control through deep reinforcement learning,” *Nature*, vol. 518, no. 7540, pp. 529–533, 2015.
- [148] T. P. Lillicrap, J. J. Hunt, A. Pritzel, N. Heess, T. Erez, Y. Tassa, D. Silver, and D. Wierstra, “Continuous control with deep reinforcement learning,” *arXiv preprint arXiv:1509.02971*, pp. 1–14, 2015.
- [149] Y. Duan, X. Chen, J. Schulman, and P. Abbeel, “Benchmarking Deep Reinforcement Learning for Continuous Control,” *ICML, arXiv:1604.06778 [cs.LG]*, p. 14, 2016.
- [150] J. R. Usherwood, J. A. Cheney, J. Song, S. P. Windsor, J. P. J. Stevenson, U. Dierksheide, A. Nila, and R. J. Bomphrey, “High aerodynamic lift from the tail reduces drag in gliding raptors,” *Journal of Experimental Biology*, vol. 223, 02 2020. jeb214809.

- [151] P. B. Leal, T. White, V. G. Goecks, J. Valasek, and D. J. Hartl, “Experimental and computational assessment of a shape memory alloy based morphing wing incorporating linear and non-linear control,” American Institute of Aeronautics and Astronautics, Jan. 2018.
- [152] a. M. U. F. Standard Test Methods for Flexible Cellular Materials Slab, Bonded, *D3574-17*. ASTM International.
- [153] R. Glaser and V. Caccese, “Experimental methods to determine in-plane material properties of polyurethane-coated nylon fabric,” *Journal of the Textile Institute*, vol. 104, pp. 682–698, July 2013.
- [154] M. F. Ashby, *Materials selection in mechanical design*. Burlington, MA: Butterworth-Heinemann, 4th ed ed., 2011.
- [155] B. Pan, K. Qian, H. Xie, and A. Asundi, “Two-dimensional digital image correlation for in-plane displacement and strain measurement: a review,” *Measurement Science and Technology*, vol. 20, no. 6, p. 062001, 2009.
- [156] C. Goidescu, H. Weleman, C. Garnier, M. Fazzini, R. Brault, E. Péronnet, and S. Mistou, “Damage investigation in CFRP composites using full-field measurement techniques: Combination of digital image stereo-correlation, infrared thermography and X-ray tomography,” *Composites Part B: Engineering*, vol. 48, pp. 95–105, May 2013.
- [157] A. Chrysochoos, B. Berthel, F. Latourte, A. Galtier, S. Pagano, and B. Wattrisse, “Local energy analysis of high-cycle fatigue using digital image correlation and infrared thermography,” *The Journal of Strain Analysis for Engineering Design*, July 2008.
- [158] M. Drela, *XFOIL 6.9 User Primers*. MIT AERO and Astro, Harold Youngren, Aircraft, Incl, 2001.
- [159] SC/Tetra, “User’s Manual,” 2015.
- [160] A. Ueno, M. Kanamori, and Y. Makino, “Multi-fidelity Low-boom Design Based on Near-field Pressure Signature,” American Institute of Aeronautics and Astronautics, Jan. 2016.

- [161] P. B. C. Leal and D. J. Hartl, “Structurally Consistent Class/Shape Transformation Equations for Morphing Airfoils,” *Journal of Aircraft*, pp. 1–12, Oct. 2018.
- [162] R. T. Farouki, “The Bernstein polynomial basis: A centennial retrospective,” *Computer Aided Geometric Design*, vol. 29, pp. 379–419, Aug. 2012.
- [163] J. E. Hurtado, *Kinematic and Kinetic Principles*. Aug. 2016.
- [164] G. Mei and J. C. Tipper, “Simple and Robust Boolean Operations for Triangulated Surfaces,” *arXiv:1308.4434 [cs]*, Aug. 2013. arXiv: 1308.4434.
- [165] S. Bansmer, N. Buchmann, R. Radespiel, R. Unger, M. Haupt, P. Horst, and R. Heinrich, “Aerodynamics and structural mechanics of flapping flight with elastic and stiff wings,” in *Nature-Inspired Fluid Mechanics*, pp. 331–354, Springer, 2012.
- [166] D. P. Huttenlocher, G. A. Klanderman, and W. J. Rucklidge, “Comparing images using the Hausdorff distance,” *IEEE Transactions on Pattern Analysis and Machine Intelligence*, vol. 15, pp. 850–863, Sept. 1993.
- [167] S. F. Frisken, “Efficient Curve Fitting,” *Journal of Graphics Tools*, vol. 13, pp. 37–54, Jan. 2008.
- [168] L. Schumaker, *Spline functions: basic theory*. Cambridge University Press, 2007.
- [169] B. K. S. Woods and M. I. Friswell, “Preliminary investigation of a fishbone active camber concept,” in *ASME 2012 Conference on Smart Materials, Adaptive Structures and Intelligent Systems*, pp. 555–563, American Society of Mechanical Engineers, 2012.
- [170] P. B. C. Leal, R. Patterson, and D. J. Hartl, “Design optimization toward a shape memory alloy-based bio-inspired morphing wing,” in *25th AIAA/AHS Adaptive Structures Conference*, American Institute of Aeronautics and Astronautics, Jan. 2017.
- [171] C. A. Mattson and A. Messac, “Concept Selection Using s-Pareto Frontiers,” *AIAA Journal*, vol. 41, pp. 1190–1198, June 2003.

- [172] R. J. Malak and C. J. J. Paredis, “Using Parameterized Pareto Sets to Model Design Concepts,” *Journal of Mechanical Design*, vol. 132, no. 4, p. 041007, 2010.
- [173] D. J. Hartl, E. Galvan, R. J. Malak, and J. W. Baur, “Parameterized Design Optimization of a Magnetohydrodynamic Liquid Metal Active Cooling Concept,” *Journal of Mechanical Design*, vol. 138, p. 031402, Jan. 2016.
- [174] E. Galvan, R. J. Malak, D. J. Hartl, and J. W. Baur, “Performance assessment of a multi-objective parametric optimization algorithm with application to a multi-physical engineering system,” *Structural and Multidisciplinary Optimization*, vol. 58, pp. 489–509, Aug. 2018.
- [175] P. B. C. Leal, J. Weaver-Rosen, R. J. Malak Jr, and D. J. Hartl, “Aerodynamic Advantages of Utilizing Structurally Consistent Camber Morphing Wings Across Changing Flight Conditions in Lightweight Aircraft,” in *ASME 2018 Smart Materials, Adaptive Structures and Intelligent Systems Conf*, (San Antonio, TX, USA), The American Society of Mechanical Engineers, 2018.
- [176] K. Deb, A. Pratap, S. Agarwal, and T. Meyarivan, “A fast and elitist multiobjective genetic algorithm: NSGA-II,” *IEEE transactions on evolutionary computation*, vol. 6, no. 2, pp. 182–197, 2002.
- [177] E. Galvan, C. Hsiao, S. Vermillion, and R. Malak, “A Parallel Approach for Computing the Expected Value of Gathering Information,” *SAE International Journal of Materials and Manufacturing*, vol. 8, Apr. 2015.
- [178] D. M. Tax and R. P. Duin, “Support vector domain description,” *Pattern recognition letters*, vol. 20, no. 11-13, pp. 1191–1199, 1999.
- [179] C. Kasnakoglu, “Investigation of multi-input multi-output robust control methods to handle parametric uncertainties in autopilot design,” *PloS one*, vol. 11, no. 10, p. e0165017, 2016.
- [180] L. Rokach and O. Maimon, “Clustering methods,” in *Data mining and knowledge discovery handbook*, pp. 321–352, Springer, 2005.

- [181] I. H. Abbott and A. E. V. Doenhoff, *Theory of Wing Sections, Including a Summary of Airfoil Data*. Courier Corporation, 1959.
- [182] A. M. Pankonien, L. Gamble, C. Faria, and D. J. Inman, “Synergistic Smart Morphing Alleron: Capabilities Identification,” American Institute of Aeronautics and Astronautics, Jan. 2016.
- [183] J. M. Weaver-Rosen, P. B. C. Leal, D. J. Hartl, and R. J. Malak, “Parametric optimization for morphing structures design : application to morphing wings adapting to changing flight conditions,” *Structural and Multidisciplinary Optimization*, vol. 62, pp. 2995–3007, 2020.
- [184] J. A. Cottrell, T. J. R. Hughes, and Y. Bazilevs, *Isogeometric Analysis*. Chichester, UK: John Wiley & Sons, Ltd, aug 2009.
- [185] J. N. Reddy, *Introduction to the finite element method*. McGraw-Hill Education, 2019.
- [186] R. Frisch-Fay, “Flexible Bars,” 1962.
- [187] C. Y. Wang, “Large deflections of an inclined cantilever with an end load,” *International Journal of Non-Linear Mechanics*, vol. 16, no. 2, pp. 155–164, 1981.
- [188] F. Ma and G. Chen, “Modeling large planar deflections of flexible beams in compliant mechanisms using chained beam-constraint-model,” *Journal of Mechanisms and Robotics*, vol. 8, no. 2, 2016.
- [189] L. Chen, “An integral approach for large deflection cantilever beams,” *International Journal of Non-Linear Mechanics*, vol. 45, no. 3, pp. 301–305, 2010.
- [190] M. Sathyamoorthy, *Nonlinear Analysis of Structures*. CRC Press, 1998.
- [191] T. C. Hill and A. Midha, “A graphical, user-driven newton-raphson technique for use in the analysis and design of compliant mechanisms,” *Journal of Mechanical Design, Transactions of the ASME*, vol. 112, no. 1, pp. 123–130, 1990.
- [192] J. T. Holden, “On the finite deflections of thin beams,” *International Journal of Solids and Structures*, vol. 8, no. 8, pp. 1051–1055, 1972.

- [193] M. H. Ang Jr., W. Wei, and L. Teck-Seng, "On the Estimation of the Large Deviations Spectrum," in *Proceedings of IECON '93 - 19th Annual Conference of IEEE Industrial Electronics*, vol. 3, (Maui, Hi), pp. 1604–1609, 1993.
- [194] T. Beléndez, C. Neipp, and A. Beléndez, "Large and Small Deflection Analysis of a Cantilever Beam," *European Journal of Physics*, vol. 23, pp. 371–379, 2002.
- [195] K. E. Bisshopp and D. C. Drucker, "Large deflection on cantilever beams," *International Journal of Non-Linear Mechanics*, vol. 15, no. 3, p. 272, 1945.
- [196] A. Zhang and G. Chen, "A comprehensive elliptic integral solution to the large deflection problems of thin beams in compliant mechanisms," *Journal of Mechanisms and Robotics*, vol. 5, no. 2, pp. 1–10, 2013.
- [197] L. F. Campanile and A. Hasse, "A simple and effective solution of the elastica problem," *Proceedings of the Institution of Mechanical Engineers, Part C: Journal of Mechanical Engineering Science*, vol. 222, no. 12, pp. 2513–2516, 2008.
- [198] P. Szablewski and R. Korycki, "Shape Determination of Elastica Subjected to Bending by Means of Displacements," *Fibres and Textiles in Eastern Europe*, vol. 24, no. 6, pp. 138–142, 2016.
- [199] T. M. Wang, "Non-linear bending of beams with uniformly distributed loads," *International Journal of Non-Linear Mechanics*, vol. 4, no. 4, pp. 389–395, 1969.
- [200] F. V. Rohde, "Deflections of a Cantilever Beam With," no. 2, pp. 337–338, 1952.
- [201] B. N. Rao and G. V. Rao, "Large deflections of a cantilever beam subjected to a rotational distributed loading," *Forschung im Ingenieurwesen*, vol. 55, no. 4, pp. 116–120, 1989.
- [202] S. Ghuku and K. Nath Saha, "A theoretical and experimental study on geometric nonlinearity of initially curved cantilever beams," *Engineering Science and Technology, an International Journal*, vol. 19, no. 1, pp. 135–146, 2016.

- [203] C. C. Lan and K. M. Lee, “Generalized shooting method for analyzing compliant mechanisms with curved members,” *Journal of Mechanical Design, Transactions of the ASME*, vol. 128, no. 4, pp. 765–775, 2006.
- [204] W. Yu, “Beam Models,” 2012.
- [205] S. Ghuku and K. N. Saha, “Large deflection analysis of curved beam problem with varying curvature and moving boundaries,” *Engineering Science and Technology, an International Journal*, vol. 21, no. 3, pp. 408–420, 2018.
- [206] D. Schöllhammer and T. P. Fries, “Kirchhoff–Love shell theory based on tangential differential calculus,” *Computational Mechanics*, vol. 64, no. 1, pp. 113–131, 2019.
- [207] J. M. Gere and B. J. Goodno, *Mechanics of materials*. Stamford, CT: Cengage Learning, 8th ed ed., 2013.
- [208] M. Mutyalarao, D. Bharathi, and B. N. Rao, “On the uniqueness of large deflections of a uniform cantilever beam under a tip-concentrated rotational load,” *International Journal of Non-Linear Mechanics*, vol. 45, no. 4, pp. 433–441, 2010.
- [209] W. M. Lai, D. Rubin, and E. Krempl, *Introduction to continuum mechanics*. Butterworth-Heinemann, 2009.
- [210] T. Haukaas, “Euler-bernoulli beams,” *University of British Columbia*, 2012.
- [211] D. Brander, J. A. Bærentzen, A. S. Fisker, and J. Gravesen, “Bézier curves that are close to elastica,” *CAD Computer Aided Design*, vol. 104, pp. 36–44, 2018.
- [212] J. Nocedal and S. J. Wright, “Sequential quadratic programming,” *Numerical optimization*, pp. 529–562, 2006.
- [213] G. Flynn, “Numerical Methods for Improper Integrals,” *The College Mathematics Journal*, vol. 26, no. 4, pp. 284–291, 1995.
- [214] J. J. Moré, “The levenberg-marquardt algorithm: implementation and theory,” in *Numerical analysis*, pp. 105–116, Springer, 1978.

- [215] A. Magnusson, M. Ristinmaa, and C. Ljung, “Behaviour of the extensible elastica solution,” *International Journal of Solids and Structures*, vol. 38, no. 46-47, pp. 8441–8457, 2001.
- [216] M. Tabesh, B. Lester, D. Hartl, and D. Lagoudas, “Influence of the latent heat of transformation and thermomechanical coupling on the performance of shape memory alloy actuators,” in *Proceedings of the ASME 2012 Conference on Smart Materials, Adaptive Structures and Intelligent Systems*, pp. 1–12, 2012.

APPENDIX A

DERIVATION OF ACTUATION FREQUENCY TO BODY MASS RATIO

A relation between the maximum actuation frequency of an SMA spring located at the robot leg and the body mass of the bi-pedal robot is derived based on conservation of linear momentum and energy. During the stride, the robot weight and ground reaction force, equivalent to the elastic spring force, counter each other with the maximum load on the SMA springs taking place at approximately 50% of the stride. In that instance, the elastic force is aligned with gravity, and the *conservation of linear momentum* considering the spring stiffness definition (Eq. ??) and stretch $\delta_l = (l_l - l_o)/l_o$ is:

$$Mg = \frac{Gr}{4NC^3} \delta_l l_o, \quad (\text{A.1})$$

solving for the wire radius r :

$$r = \frac{4NMgC^3}{G\delta_l l_o}. \quad (\text{A.2})$$

A second equation is derived from *conservation of energy* by making three assumptions. The maximum frequency of an SMA is dominated by the cooling period. Considering that the heating period is at most an order of magnitude less than cooling, the heating phase is neglected for calculating actuation frequency. Moreover, heat contributions from phase transformations are neglected as all studied cases only had partial phase transformation. Finally, thermal expansion is neglected as the temperature ranges are not significant. Conservation of energy [216] considering the three assumptions reduces to governing equation to Newton's cooling law. The solution to the equation for cooling a wire at initial temperature T_i to final temperature T_f at ambient temperature T_∞ is:

$$T_f = (T_i - T_\infty)e^{-\frac{h}{\rho c} \Delta t} + T_\infty \quad (\text{A.3})$$

where c is the SMA heat capacity, Δt is the time necessary to cool down the specimen, and h is the heat transfer coefficient. h is a function of the wire radius, the Nusselt number Nu , and the fluid

thermal conductivity k such that:

$$h = \frac{k \text{Nu}}{2r}. \quad (\text{A.4})$$

Solving Newton's cooling law, Eq. A.3, for Δt and considering the definition of the convection coefficient, the actuation frequency is given by:

$$f = \frac{1}{\Delta t} = -\frac{k \text{Nu}}{2\rho c r} \left[\ln \frac{T_f - T_\infty}{T_i - T_\infty} \right]^{-1}. \quad (\text{A.5})$$

Finally, the definition of radius from conservation of linear momentum, Eq. A.2, is incorporated in the actuation frequency equation from conservation of energy to derive the following final relation:

$$f = \frac{A}{M}, \quad (\text{A.6})$$

where

$$A = -\frac{G}{8\rho c g} \frac{k \text{Nu} \delta_l l_o}{NC^3} \left[\ln \frac{T_f - T_\infty}{T_i - T_\infty} \right]^{-1}. \quad (\text{A.7})$$

The typical ranges for each parameter are provided in the Supplementary Information documents.

The lower and upper bounds for coefficient A are 4×10^{-7} and 9×10^3 kg.

APPENDIX B

CST DERIVATIVES

From Eq. , the relationship between dimensional coordinate z and non-dimensional coordinate ζ is

$$z = c\zeta . \quad (\text{B.1})$$

From the previous equation, the following definitions are derived between non-dimensional and dimensional derivatives:

$$\frac{dz}{dx} = \frac{d\zeta}{d\psi} , \quad (\text{B.2})$$

and

$$\frac{d^2z}{dx^2} = \frac{1}{c} \frac{d^2\zeta}{d\psi^2} . \quad (\text{B.3})$$

The first and second derivatives in the $\psi - \zeta$ non-dimensional domain are given by:

$$\frac{d\xi_P}{d\psi} = C(\psi) \sum_{i=0}^n A_i S_i(\psi) \left(\frac{i - n - N_2}{1 - \psi} + \frac{N_1 + i}{\psi} \right) + \zeta_T , \quad (\text{B.4})$$

$$\frac{d^2\xi_P}{d\psi^2}(\psi) = C(\psi) \sum_{i=0}^n A_i S_i \left[\left(\frac{N_1 + i}{\psi} + \frac{i - n - N_2}{1 - \psi} \right)^2 - \frac{N_1 + i}{\psi^2} + \frac{i - n - N_2}{(1 - \psi)^2} \right] . \quad (\text{B.5})$$

These have components at the denominator that cause singularities if numerically evaluated at the $\psi = 0$ and $\psi = 1$.. However, the derivatives have finite solutions for most cases if limits are evaluated, the form the equations below are the derivative values as it approaches the possible singularity. A non-exhaustive list is here presented based on the fact that they are utilized in the model. The equations are derived for classical CST, but can be also valid for any domain of a CST spline.

B.1 First derivative

For any class coefficients N_1 and N_2 , as $\psi \rightarrow 0^+$, the first derivative is:

$$\lim_{\psi \rightarrow 0^+} \frac{d\zeta}{d\psi}(\psi) = A_0 N_1 \psi^{N_1-1} + \zeta_T - \zeta_L, \quad (\text{B.6})$$

and if $N_1 = 1$

$$\lim_{\psi \rightarrow 0^+} \frac{d\zeta}{d\psi}(\psi) = A_0 + \zeta_T - \zeta_L. \quad (\text{B.7})$$

For any class coefficients N_1 and N_2 , as $\psi \rightarrow 1^-$, the first derivative is:

$$\lim_{\psi \rightarrow 1^-} \frac{d\zeta}{d\psi}(\psi) = A_0 N_1 \psi^{N_1-1} + \zeta_T - \zeta_L, \quad (\text{B.8})$$

and if $N_2 = 1$

$$\lim_{\psi \rightarrow 1^-} \frac{d\zeta}{d\psi}(\psi) = -A_n + \zeta_T - \zeta_L. \quad (\text{B.9})$$

B.2 Second derivative

Except for the case where $N_1 = N_2 = 1$, all second derivatives are singular at $\psi \rightarrow 0^+$ and $\psi \rightarrow 1^-$.

For $\psi \rightarrow 0^+$, $N_1 = 0.5$, and $N_2 = 1$ the second derivative is

$$\lim_{\psi \rightarrow 0^+} \frac{d^2\zeta}{d\psi^2}(\psi) = \frac{1}{2\psi^{3/2}} [-2(n+1)A_0\psi - 0.5A_0 + 5n\psi], \quad (\text{B.10})$$

and if $N_1 = 1$:

$$\lim_{\psi \rightarrow 0^+} \frac{d^2\zeta}{d\psi^2}(\psi) = -2(n+1)A_0 + 2nA_1. \quad (\text{B.11})$$

For $\psi \rightarrow 1^-$ and $N_2 = 1$:

$$\lim_{\psi \rightarrow 1^-} \frac{d^2\zeta}{d\psi^2}(\psi) = 2nA_{n-1} - 2(N_1 + n)A_n. \quad (\text{B.12})$$

B.3 Curvature radius

Despite the singularities for the second derivatives, the curvature radius is not singular at the bounds. For $\psi \rightarrow 0^+$ and $N_2 = 1$

$$\lim_{\psi \rightarrow 0^+} \frac{1}{\rho}(\psi) = \frac{N_1 - 1}{A_0^2 N_1^2 c}, \quad (\text{B.13})$$

and if $N_1 = 0.5$

$$\lim_{\psi \rightarrow 0^+} \frac{1}{\rho}(\psi) = -\frac{2}{A_0^2 c}. \quad (\text{B.14})$$

For $\psi \rightarrow 1^-$ and $N_2 = 1$

$$\lim_{\psi \rightarrow 1^-} \frac{1}{\rho}(\psi) = \frac{2nA_{n-1} - 2(N_1 + n)A_n}{c[1 + (-A_n + \zeta_T - \zeta_L)^2]^{3/2}}. \quad (\text{B.15})$$